

**Advancing THz-Security Imager
by using Digital Image Processing-Methods at the Hardware Level**

vorgelegt von
Diplom-Physiker, Diplom-Kaufmann
Sven Augustin
geb. in Wriezen

von der Fakultät II - Mathematik und Naturwissenschaften
der Technischen Universität Berlin
zur Erlangung des akademischen Grades

Doktor der Naturwissenschaften
- Dr. rer. nat. -

genehmigte Dissertation

Promotionsausschuss:

Vorsitzende: Prof. Dr. rer. nat. Janina Maultzsch
Gutachter: Prof. Dr. rer. nat. Heinz-Wilhelm Hübers
Gutachter: Prof. Dr.-Ing. habil. Viktor Krozer

Tag der wissenschaftlichen Aussprache: 06. November 2015

Berlin 2015



Advancing THz-Security Imager by using Digital Image Processing-Methods at the Hardware Level



Author:
Sven AUGUSTIN

Supervisor:
Heinz-Wilhelm HÜBERS



- Version - November 22, 2015
FINAL VERSION

ABSTRACT

THz-Imager are a promising alternative for improving security, e.g. in public transport. This work addresses some of the major problems THz-security imager suffer from when deployed as a means for the stand-off detection of hidden threats. The text starts with analyzing the scenario of stand-off detection and threats likely encountered therein. It is then shown how THz-imager are used in this detection scenario and also why the use of THz-radiation is a good and promising choice. The main components of a THz-imager are named and examined leading to the main problems this technology suffers from. Which are shown to be; first the necessity for mechanical scanning, second poor depth of focus and resolution and third the long measurement times needed. All the aforementioned problems are demonstrated using a THz-security imager designated **Integrated Security Monitor-Imager**, named after the project it was developed for. The ISM-imager constitutes the THz-part of the Integrated Security Monitor. One possible solution to the problems 1-3 is presented in this thesis. The chosen approach is the use of methods common to digital image processing. The new paradigm in this is the usage of these common methods NOT on the digital level after the image acquisition, but ALREADY during image acquisition at the hardware level.

This NEW PARADIGM becomes possible with the help of devices known as THz-Spatial Light Modulators. SLMs have been used in the visible region of the electromagnetic spectrum for decades but are not readily available for the THz-region. The contribution of this work to the advancement of THz-security imaging stems from reinventing/expanding established methods to the THz-region. In doing so at least two obstacles have had to overcome. First, the THz-region of the electromagnetic spectrum is known as the Quasioptic-region because many optical methods no longer work straightforwardly in this part of the spectrum. The second obstacle is that also methods and devices from the radiowave spectral region are no longer straightforwardly applicable.

Although some of the fundamentals were there, they had to be expanded -reinvented- for the THz-region and this is the innovative contribution of this work, trying to contribute to a CHANGE OF PARADIGM FOR THZ-SECURITY IMAGING by implementing the aforementioned ideas. The (reinvented) methods range from HARDWARE EDGE-DETECTION over HARDWARE PHASE-SHIFT DETECTION and HARDWARE CALIBRATED IMAGING to COMPRESSED SENSING using a THz-SLM. In this the notion behind Compressed Sensing just to acquire the relevant information with as little overhead as possible is key in the understanding of the new imaging paradigm presented here. Therefore, the theory and application of Compressed Sensing is a major topic in this work. In order to adapt the aforementioned methods, some of their physical properties had to be examined for and with Quasioptic-techniques. The results are presented in this thesis namely chapter 6. To promote efficient reading every sub-chapter of chapter 6 is structured in scientific paper format and can be read as a standalone text. The thesis then concludes with a brief analysis of the results presented and discusses some advantages offered by the newly implemented techniques. In this, the final outlook chapter shows possibilities for a sustainable advancement of THz-imager/THz-imaging in the future.

Author's Note

The work presented here is focused on the imaging process in the THz-region of the electromagnetic spectrum. It concentrates on the detection of hidden threats that are concealed under clothing. It is written by a physicist with an electrical engineering background and because of that, both views are incorporated in the text. It is the author's opinion, that the subject of THz-imaging itself can not solely be placed as either part of physics or of the engineering disciplines. It contains by nature parts of both. Namely signal and image processing aspects on one hand as well as details on the properties of semiconductors and THz-radiation on the other hand, to name but a small portion of the topics involved. For me the question arose, whether this is an engineering dissertation or one of physics. The choice was to write this text as a physics dissertation, although it contains only little fundamental physics research.

To guide the reader through the text, sign posting is used in every chapter. So, every chapter starts with a paragraph set in italic letters to distinguish it from the rest of the text. The information given therein is just a description of the content of the respective chapter and contains no information needed to understand the text. To speed-up the reading process those paragraphs can be skipped without fear of missing crucial information. The information given in these paragraphs also contains tips about each section in the respective chapter that can be used to enable a more efficient reading process.

As already stated, the goal of this text is to give an understanding of THz-imager and their shortcomings. From their emergence over key components and issues in their usage to new and very recent developments for their improvement. The author hopes to provide the readers with some new ideas by reading this text.

Sven Augustin

Acknowledgments

My thanks and appreciation go first to my supervisor Prof. Dr. Heinz-Wilhelm Hübers for supporting me and my work even in tough times. Without his support this work would not have been possible. Special thanks goes also to Michael Greiner-Bär. Without his competent help, advice and guidance some would have been lost in a maze of contradicting options (even me sometimes). I also want to thank Jan Hieronymus, Philipp Neumaier, Heiko Richter, Franziska Hanke, Fanny Hamann, Mathias Ziegler and Klaus Morgenstern.

The thanks to my family and friends goes, of course, without saying. Without them and their support this thesis would not have been completed and I would not be able to stand (literally) and appreciate its outcome. So, my warmest regards go to James, Rosi, Kristy, Mathias, Oliver and Elinor.

Contents

ABSTRACT	3
Author's Note	4
Acknowledgments	5
Contents	6
 I Theoretical Part	 9
1 Introduction	10
1.1 The Need for Security	11
1.2 Why THz-Imager?	13
1.3 Spatial Light Modulators	19
1.4 THz-Imager and Compressed Sensing	22
References Chapter 1	28
2 Theoretical Basics of THz-Imaging	30
2.1 The Quasioptic nature of THz-radiation	31
2.2 THz-imaging modalities	34
2.3 The passive imaging modality	36
2.3.1 Signals in passive THz-imaging - Temperature Resolution	38
2.3.2 The Scanning Optics – Spatial Resolution . . .	43
2.3.3 The scene	49
2.4 The active imaging modality	50
2.4.1 Frequency Modulated Continuous Wave THz- Imaging	50
2.4.2 Illumination scenarios	52
2.4.3 The effects of polarization	53
2.5 Software scanning	55

References Chapter 2	56
3 Theoretical Basics of Compressed Sensing	58
3.1 Introducing Compressed Sensing for THz-imaging	59
3.2 Compressed Sensing Dictionaries for THz-Imaging	64
3.3 The pros and cons of a specific Φ	67
3.4 Compressed Sensing Reconstruction Algorithms . .	70
3.4.1 Orthogonal Matching Pursuit (OMP) - Greedy algorithms	72
3.4.2 Basis Pursuit (BP) - l_1 - algorithms	73
3.4.3 Specialized THz-reconstruction algorithms .	74
3.5 Compressed Sensing and Single-Pixel THz-Imaging	74
3.5.1 THz-Spatial Light Modulators	77
3.6 Compressed Sensing for improved image Reconstruction of THz-images	79
References Chapter 3	82
4 A few Words on Image Processing	86
4.1 The classical Image Processing Paradigm	87
4.2 Image processing techniques and the optimal digital-image pixel size	88
4.3 What is hardware image processing?	92
4.4 The information content of THz-images	96
References Chapter 4	100
II Experimental Part	102
5 ISM-Imager System Evaluation	103
5.1 System Description	104
5.2 System Characterization	107
5.2.1 Characterization of the Tx/Rx-system	107
5.2.2 Characterization of the ISM-imager	113
5.3 Passive mode	115
5.3.1 Temperature Resolution	116
5.3.2 Spatial Resolution	118
5.4 Active mode	119
5.4.1 Tx–Rx crosstalk	123
5.4.2 Polarization effects	125
5.4.3 Off-axis illumination	127
5.5 Chapter summary	129

6 Experimental Results	130
6.1 The experimental starting point – Passive Imaging with the ISM Imager	131
6.2 CS-based reconstruction of passive THz-Images . .	141
6.2.1 CS-based reconstruction of passive THz-Images - Results interpretation	152
6.3 Introducing the Lock-In Phase Space	153
6.3.1 Lock-In Phase Space - Results interpretation .	163
6.4 Multinary Lock-In Phase Space	164
6.4.1 Multinary Lock-In Phase Space - Results interpretation	182
6.5 Developing a THz-SLM	183
6.5.1 Design	183
6.5.2 Optical Switching	186
6.5.3 THz-SLM imaging using CS-techniques . . .	189
6.5.4 Developing a THz-SLM - Results interpretation	194
6.6 Chapter summary	195
7 Conclusions and New Developments	196
7.1 Active vs. Passive THz-Imaging	197
7.2 Hardware vs. Software Scanning	197
7.3 Lock-In Phase Space vs. Lock-In Intensity Space . .	198
7.4 Hardware vs. Software Image Processing	198
7.5 THz-Imaging vs. THz-Imaging with CS	199
7.6 Spatial undersampling vs. Information content . . .	199
7.7 SNR vs. Scanning Time	200
8 Outlook	201
8.1 Using Compressed Sensing with a THz-SLM for THz-security Imaging	202
8.2 3D-THz-SLM	203
8.3 Towards BRDF enhanced THz-security imaging . .	205
Summary - Contributions of this Thesis	206
Own Publications	211
A Appendix	215
A.1 Motivation of the Radiometer equation	215
A.2 Classification of blurring kernels	216
A.3 Passive THz-images and their acquisition parameters	217
A.4 CS-based reconstruction beam model parameters .	219

Part I

Theoretical Part

Introduction

Contents

1.1	The Need for Security	11
1.2	Why THz-Imager?	13
1.3	Spatial Light Modulators	19
1.4	THz-Imager and Compressed Sensing	22

This chapter introduces the concept of THz-security imaging to the reader. It shows circumstances of its development process and the reasons for introducing this new, special branch of security imaging to the world in general. This chapter also picks up the notion of the Bodyscanner (“Nacktschanner” in German) and points out the problems THz-scanners have faced and are still facing because of the introduction of this notion into the public awareness.

In the first section, “The Need for Security”, a brief history of the events that led to the new importance of security imaging as an imaging domain is given, including its major milestones and issues. This will directly lead to the question “Why THz-imagers” are used and it will be addressed in the second section of the chapter. This part of the chapter also gives a brief overview of the state-of-the-art in THz-imaging and how this thesis connects to previous research in the field. The third section then gives a short introduction of the concept of Spatial Light Modulators (SLMs) including a few application examples, which will clarify the importance these devices have had for the imaging disciplines in the past. It also introduces the concept of a THz-SLM, which is a key concept in this thesis. This part will show how THz-SLMs can offer one possible solution to the issues faced by THz-imagers today. To conclude this chapter the concept of Compressed Sensing (CS) is introduced to the reader, which exactly, as its name suggests, reduces (compresses) the data acquisition process so that only information that is needed (necessary) is acquired. This new technique becomes possible because of Spatial Light Modulators. Its benefits for THz-imaging are briefly pointed out and the promises and difficulties it holds for THz-imaging are addressed.

The entire chapter reflects the multidisciplinary approach, with the discussion of technical as well as social issues and their connection, promoted by the Helmholtz Research School on security Technologies, this author’s graduate school. To promote efficient reading, readers just interested in the technical details may safely skip this chapter, entirely.

1.1 The Need for Security

“The Need for Security” is one of the basic prerequisites for human development/motivation [16]. After the Second World War, Germany/GDR was, as a country, not involved in any open war and hence has enjoyed a long period of peace. The situation became even more stable with the end of the Cold War and the reunion of the two German countries. So one could conclude, that “the Need for Security” was pretty much satisfied for almost all Germans. But starting with the (tragic) events of September 11th 2001 in the USA and the subsequent bombings in Madrid 2004 and London 2005, a different threat to “the Need for Security” became evident: terrorism.

Although the aforementioned acts of terrorism were carried out abroad, they also had an effect on Germany, Germans and their way of living. Let us briefly recall the events in the USA, Madrid and London to better understand these effects¹.

Terrorism is not a problem created in modern times. The essence of terrorism was conveyed already by Sun Tzu² who allegedly stated, “kill one, frighten ten thousand.” In the events that took place on September 11 2001, a few hijackers who boarded planes like ordinary passengers, assumed control of four planes and then crashed them into prominent targets like the Pentagon and the World Trade Center. During the attacks of March 11 2004, in Madrid, the railway system was targeted. In this case, four trains were targeted with ten explosive devices hidden in backpacks that were planted in the trains. The last of the aforementioned events is the attack on London’s Underground at July 7 2005. On this day four suicide bombers detonated four explosive devices. Three devices were detonated, in three subway trains and one device was detonated on a Londoner bus.

The three described events were merely picked to demonstrate the common pattern most modern terrorist attacks exhibit. They do not represent a complete list of terrorist events in modern times nor are the events not presented any less horrible. But starting with 9/11, the notion of “war against terrorism” was coined. Thus, regardless of peacetime, the threat of lethal attacks invaded the normal lives of many ordinary citizens, even in Germany. The “war against terrorism” was and is fought on an entirely new battlefield in the midst of normal people who are not soldiers. In the terrorist attacks mentioned earlier the terrorists targeted mass transportation systems like subways, rail roads and airplanes. Most casualties were non-combatants on their way to work or other private destinations. In light of this new kind of war, how can “the Need for Security” still be addressed? This in turn translates to the questions how THz-security imaging can help to improve security and what is the scenario in which it is implemented. This scenario is illustrated in the following image (figure (1.1)).

¹Information about these terror attacks taken from [13].

²supposedly 544-496 BC

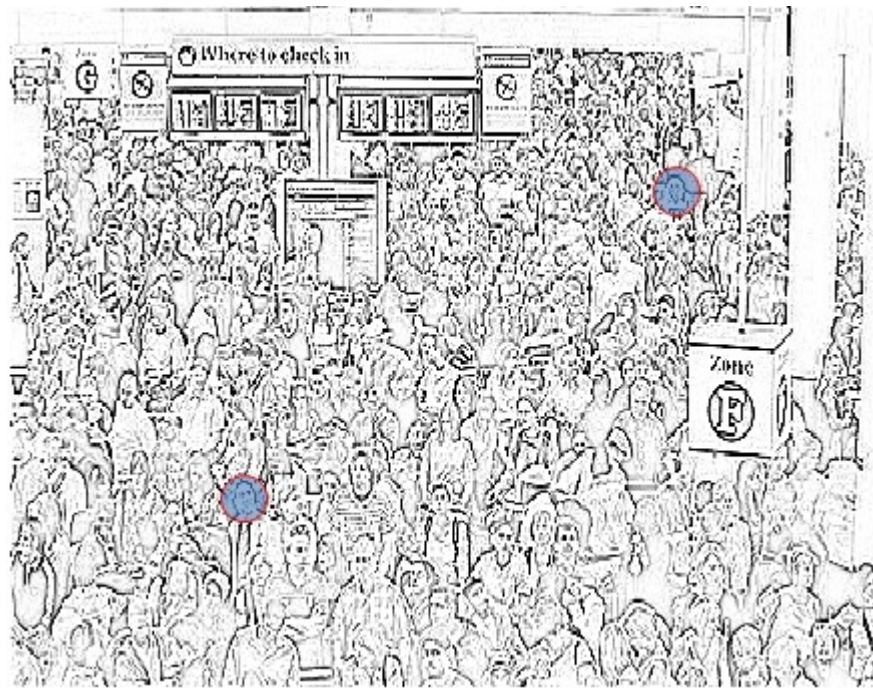


Figure 1.1: Potential scenario for THz-security imaging

The image shows a situation frequently encountered when using mass transportation systems like planes, railroads, buses, etc. This scenario assumes terrorists (red circles) among ordinary passengers. Here the terrorists would be armed with some sort of concealed weapon. Thus, the “the Need for Security” can be addressed by detecting these hidden threats. Before 9/11, metal detectors and random checks of passengers were considered sufficient security at airports, while for subways and other mass transportation systems almost no security checks were/are conducted. From a technical point of view, the question can be raised, how “the Need for Security” can be addressed? One possible solution is to make the hidden threats visible. This, in turn, would suggest the usage of an imaging technology of some kind. According to the scenario of figure (1.1), the field of view of the imaging device would lie a few meters from the device itself and would have a depth of focus of a few meters as well. Also, because the threats to be detected would be hidden under some sort of obscurant (clothing, fabric, etc.), the people in the field of view would have to be “stripped off” their clothing. This makes THz-radiation a promising tool for the aforementioned imaging task because it can penetrate many optical obscurants without being harmful to people in the scene³. Although THz-radiation is a promising tool for the detection of hidden threats, its ability to see through optical obscurants caused a different issue, the “Bodyscanner issue”. After this phrase was coined, it was one of the main reasons that prevented such a technology from finding widespread use most of all (but not

³More details on THz-radiation are given in the next section.

limited) in Germany (“Nacktscanner-Problematik”)⁴. The illustration of the scenario in figure (1.1) also already points out one possible solution of the Bodyscanner-issue. The detection of contours and contours alone offers this possible solution because this way no privacy invading details can ever be shown. At this point it is also important to distinguish between the hardware and software level. If the detection of contours/edges is done at the software level then potentially privacy invading images exist on some level of the digital processing chain but if the detection of edges is done at the hardware level, privacy violation is not possible (details on this subject are given in section (6.3) - Introducing the Lock-In phase space).

To summarize the scenario: Terrorists carrying hidden threats (weapons, explosives, etc.) under clothing or hidden in bags use public transportation systems or access security sensible areas amidst ordinary people. The task is to identify these terrorists with as little privacy invasion as possible. For this imaging task a technology is needed which is able to “see through” optical obscurants and provides a field of view of a few meters with a depth of focus of a few meters as well. The next section will give reasons why THz-radiation is a promising choice as an imaging technology in this scenario.

1.2 Why THz-Imager?

As with every imaging technology, there are two different ways to image a scene of interest. The imaging can be done in an active or in a passive way. In passive mode only natural radiation is coming from the scene and is then detected. This natural radiation can be emitted from objects in the scene or is reflected from natural sources (e.g. the sun). In active mode artificial sources are used to illuminate the scene. These two modi are also useable for THz-imaging⁵.

The energy equivalence $h_{PI} \cdot \nu = k_B \cdot T$ shows that the energy of photons in this part of the electromagnetic spectrum is of the same order of magnitude as plasma frequencies or molecular rotations and even temperatures in the range of everyday life experience ($-10^\circ\text{C} - 100^\circ\text{C}$). Because of that, when considering THz-radiation, one normally speaks about temperatures and the change in temperature⁶. Also, the designation of THz-region varies. It is more a question of definition than fact. In this thesis the spectral region between 300 GHz and 3 THz will be considered the THz-region⁷. Having introduced the aforementioned definitions and concepts, to answer the question why THz-imager are a good and promising choice for the detection of hidden threats in the scenario introduced in the previous section, choices have to be made first. Namely to decide whether to use active or passive mode and at what

⁴See e.g. <http://www.spiegel.de/reise/aktuell/flughafen-sicherheit-politiker-entsetzt-ueber-geplante-nacktscanner-a-586083.html>.

⁵Details can be found in [3]

⁶This is just a habit of convenience like in spectroscopy everybody is using wave numbers even so it is not a unit of the SI-system.

⁷This is sometimes also referred to as the sub-millimeter region of the electromagnetic spectrum. This definition for THz-region is adopted since this part of the electromagnetic spectrum is particularly suited for security imaging. Often the part of the electromagnetic spectrum between 100 GHz and 10 THz is considered the THz-region. This definition is particularly suited for spectroscopic applications.

frequency to operate.

The first decision active mode vs. passive mode is not as straightforward as it seems at first glance. The initial guess would be that the signal-to-noise ratio (SNR) for the detection of objects in the scene could be made adjustable at will in active mode and would only depend on the output power of available sources. But the SNR is not the whole truth when it comes to the detection of hidden threats. To be able to detect hidden objects with a high detection probability, the achieved contrast in the acquired images is more important than the SNR alone. To come to a profound decision, all contributing parts have to be taken into account. Equation (1.1) lists all contributing fractions⁸

$$T_D = \epsilon(\theta, \varphi, r) \cdot T_{eff} + s(\theta, \varphi, r) \cdot T_S + t(\theta, \varphi, r) \cdot T_B \quad (1.1)$$

In equation (1.1), T_D denotes the detected temperature coming from the scene, comprised of the effective temperature T_{eff} weighted with the emissivity of the object $\epsilon(\theta, \varphi, r)$, the scattered/reflected temperature T_S , which is scattered back from the object and multiplied with the scattering coefficient $s(\theta, \varphi, r)$. The last contribution is from the temperature of the background T_B modified by the transmittance of the object $t(\theta, \varphi, r)$. All three contributions are modified by a function because ϵ , s and t (their measured values) depend on the direction and distance to the detector⁹.

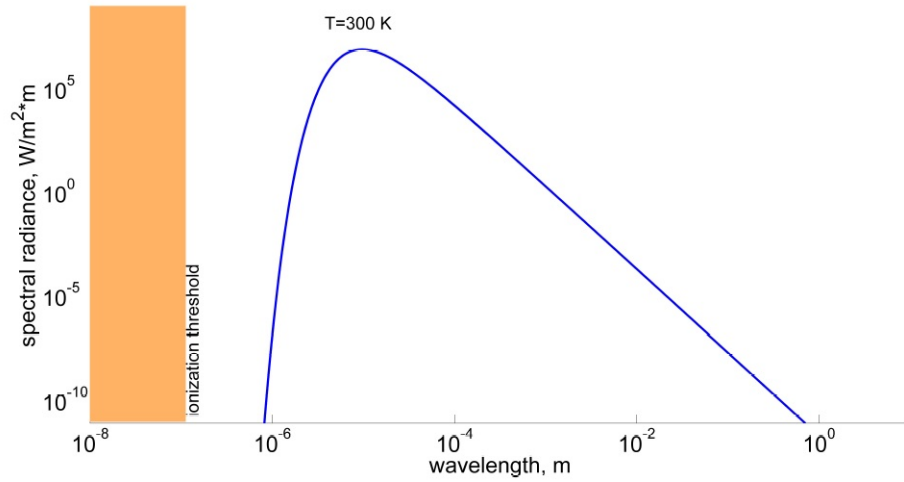


Figure 1.2: Spectral Emission according to Planck's law for a blackbody with a temperature of 300 K.

⁸Equation (1.1) is valid in the active as well as in the passive regime but all temperatures are effective temperatures instead of physical temperatures, due to absorption. Also, the dominant fraction changes when changing the regime and it also considers only the steady-state case, where no change in object temperature happens (anymore).

⁹It is also important to consider the effects of polarization, which gives two functions respectively for the two independent polarizations \parallel and \perp .

In a passive regime, the dominant component that yields contrast in the scene (see equation (1.1)) is the physical temperature T , which is dominated by the emissivity of the object $\epsilon(\theta, \varphi, r)$ ¹⁰. In this regime, the radiation emitted from objects in the scene is approximated by Planck's law with the temperature of objects around 300 K (ambient temperature). Figure (1.2) illustrates this. Here it is shown that the peak emission appears in the infrared-region of the spectrum. In the passive regime the consideration, therefore, leaves imaging in the IR-region, the microwave-region, the submillimeter-region, the millimeter-region and part of the radiowave-region as possible candidates for passive security imaging. Because the maximum emission appears in the IR-region, it could be suspected that the IR-region is best suited for this kind of imaging. But before a reasonable decision can be made all important factors for the successful detection of hidden threats have to be taken into account. To identify the most important factors, let us consider again the scenario from the previous section, which was exemplified in Figure (1.1). The scenario shows that weapons or explosives are likely to be hidden under clothing or stashed in backpacks or other kind of luggage. In most cases the scene of interest is a few meters away from the detector so the radiation has not only to penetrate optical obscurants (clothing, luggage), but also a few meters of atmosphere, which also can have a significant attenuating effect (see Figure (1.3)).

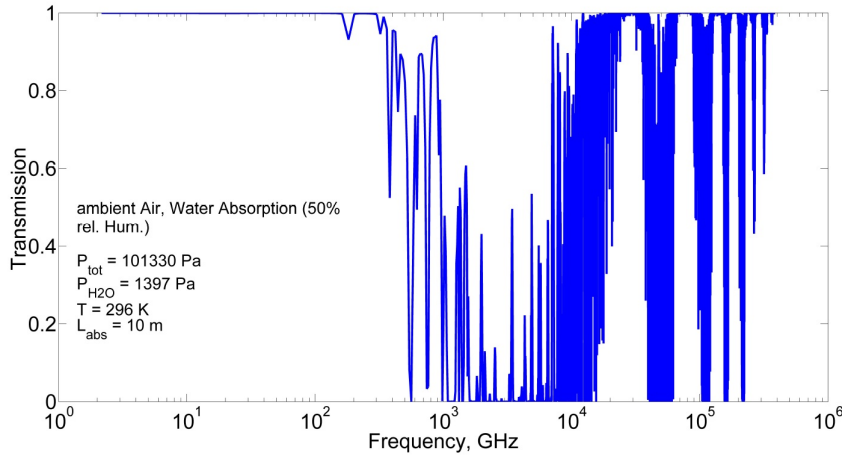


Figure 1.3: Transmission through 10 m of atmosphere. Conditions for the simulation are indicated in the figure inset.

After traveling through the obscurants and the few meters of atmosphere, the attenuated radiation has to be detected with sufficient temperature- and spatial resolution to make the hidden threats¹¹ visible. The answer which one of the aforementioned technologies should be chosen as means for the imaging process is (like always) a trade-off between conflicting goals. As a rule of thumb, the longer the wavelength of the used radiation the better the transmittance

¹⁰Is the passive imaging conducted outdoors, the reflection of the cold sky will have a significant contribution to the contrast in the scene.

¹¹What is sufficient resolution (see discussions in section (2.3.1) and section (2.3.2))?

through obscurants and the atmosphere on one hand and on the other hand there are considerations about the size of the imager, which will be larger for larger wavelength¹² and produce images with diminished spatial resolution. Also depending on the chosen wavelength, the expenditures for the required hardware soon soar sky high and so the “war against terrorism” becomes a “battle of materials”¹³. There still is one more issue that needs to be taken into account, the “Bodyscanner issue”. Because of the high quality images necessary for the detection of hidden threats, the acquired high-resolution, clothing penetrating images were and still are considered a privacy intrusion (see Figure (1.4) image (a) as an example).

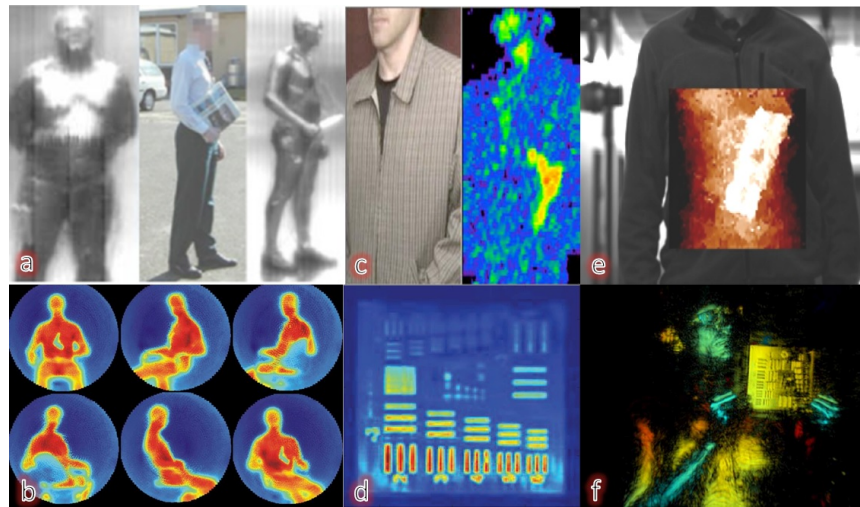


Figure 1.4: Example Bodyscanner, image (a) taken from [4], image (b) taken from [18], image (c) taken from [12], image (d) taken from [15], image (e) taken from [8], image (f) taken from [1].

The usual solution for this problem is to acquire the high resolution images and estrange them for presentational matters. However, on some level of the imaging- and digital image processing chain, the high resolution and potentially privacy invading images exist. To find a real solution for this contradiction, which seems to have no possible solution, a shift in thinking, a transition from a classical paradigm to a new paradigm is necessary. In the classical imaging paradigm a hardware front end of some sort acquires images, which are digitally processed afterwards.

A new paradigm now states that some sort of processing is already done on the hardware level, for example, edge detection. Since the experiments considered here will implement processing on the hardware level, this also is a point of consideration for the imaging frequency to choose. The specific pros and

¹²This is another rule of thumb. Concepts like Superresolution, phased arrays and synthetic apertures provide ideas that are exclusions to this rule.

¹³Some readers might think that this is just a melodramatic saying and they may be right. But nevertheless it is also true. Research groups all over the world spend 100th of 1000th of Euros on building next generation THz-security scanners (e.g. [17]).

cons, of the respective spectral region that were discussed in this section are summarized in Table (1.1).

Table 1.1: Summary of the different spectral regions pros and cons for passive/active security imaging.

	Transmittance ^{70%}	Resolution ^{5%}	Size ^{5%}	Cost ^{5%}	Processing ^{15%}	RESULT
Infrared	+	++++	++++	+++	++++	36%
Far-Infrared	++	+++	++	++	+	48%
Submillimeter	+++	++	++	++	+	64%
Millimeter	++++	+	+	++++	+	79%

Consider the summary of Table (1.1) as a hint towards finding the right choice for the spectral region in which security imaging is done. Although the chosen main criteria can in some way be objectified, the choice for the values of the weights appears to be rather random. From the discussion in this and the previous section it seems necessary to appoint the highest weight to the ability of the used radiation to penetrate the obscurants likely encountered. The weights for the resolution criterion, the size criterion as well as the cost criterion appear to be secondary, because there is no way to change the physical property of transmittance but the other criteria can be changed simply by engineering ingenuity (as far as resolution and size are concerned). The cost criterion simply reflects the maturity and commercialization of the underlying technology¹⁴. The last criterion of Table (1.1) reflects the present capability to do some sort of processing, while still on the hardware level. This criterion was weighted with 15% as it enables concepts like edge detection, Superresolution, Compressed Sensing, etc. almost everything that is possible in Software, to be implemented already on the hardware level. The capability to do image processing while still on the hardware level has the potential to advance and in some cases already has advanced imaging (in the VIS/NIR region) as we know it (see e.g. [7]). This will be explained in more detail during the rest of this thesis.

But what about the other imaging modality of active security imaging? As already mentioned, on one hand the SNR in this modality can be adjusted to the situation at hand over a wide range. On the other hand the image contrast is affected by problems with Speckles, crosstalk, multipath propagation and polarization effects (to name just the most severe effects). Possible solutions do exist but the situation in active imaging becomes much more complex than the passive mode. To arrive at a well-founded decision what imaging modality and what imaging frequency can be used again table (1.1) provides a hint. A quick look at the state-of-the-art is also helpful.

Interest in the application of millimeter- and submillimeter wave imaging for security tasks rose with the maturity of underlying technologies, such as monolithic microwave integrated circuits (MMIC), already in the mid 1900s. Early attempts mainly focused on passive millimeter wave systems [2]. With the success and maturity of radar-systems, an approach was made to adapt such system technology to passive security imaging tasks. Early systems used low GHz frequencies for the detection of hidden threats. Soon attempts were made to increase the used frequency. With the higher frequency a better spatial resolution was achieved at the cost of transmittance through obscurants [19].

¹⁴The 94 GHz technology, for example, has already been in use for decades.

The achievable image quality and visibility of hidden objects was very good (see Fig. (1.4) image (a)). Such imagery was measured outdoors where reflections of the cold sky provided a considerable temperature difference/contrast. For indoor measurements the contrast was substantially reduced, making passive measurements with hidden object detection a challenge. To increase image contrast, the illumination with artificial sources was attempted [4]. The success promoted further research efforts in the field. The two development directions in THz-imaging for security applications, namely the passive and active imaging modality are both pursued with renewed vigor today, thanks to the advancement of the technologies involved.

In the case of passive imaging, a prominent example that illustrates the state-of-the-art is the THz-camera developed at the IPHT in Jena. It operates in the atmospheric window around 0.35 THz and uses a detector array that is integrated in a closed-cycle cryocooler. The optical system employs a Cassegrain-type telescope and fast mechanical scanning with the secondary mirror of the telescope. With this system, it is possible to acquire a THz-image at a stand-off distance of 3-10 m with a spatial resolution of 1-2 cm. It has a field of view (FoV) of 2 m x 1 m and is able to scan its FoV at 25 frames per second [14]. An example image is shown in Fig. (1.4) image (b)¹⁵.

For an active THz security scanner a number of different approaches were/are pursued in order to combat the myriad of difficulties encountered in this modality. Early attempts used gas lasers for illumination in lack of compact, powerful sources. Due to the large FoV necessary for security imaging, such systems needed also appropriate scanning optics making them bulky and slow. An example for such an early active security imager is found in [12] and an example image is shown in Fig. (1.4) image (c). With the increasing maturity of solid-state multiplier based sources powerful and compact sources became available, making the use of gas lasers obsolete. These new kind of sources are electronically tunable over a small frequency range, allowing frequency modulation techniques to be implemented. The frequency modulated continuous wave (FMCW) technique uses range information to combat Speckles, spurious noise and multipath propagation problems [9] (see Fig. (1.4) image (d) for an example.). The next generation of active security imagers uses FMCW techniques in combination with digital beam-forming [1] or synthetic aperture radar (SAR) [15] improving their compactness even further. Fig. (1.4) image (e,f) contains sample images for these two examples.

In conclusion the passive imaging modality is straightforwardly implementable and is advantageous because of its simplicity and the lack of problems with e.g. polarization effects, multipath propagation, Speckles, etc. However, it has the serious drawback of a limited SNR, which can only be increased by improving the detection capabilities of the employed detection system. This in turn is very costly and also limited by background radiation. The other modality of active security imaging is not limited in its SNR but has to deal with serious implementation difficulties. It is this authors opinion that for the imaging scenario depicted in Fig. (1.1) only an active solution is plausible. But this text is trying to contribute to the notion of digital image processing

¹⁵The image shown here, illustrates early imagery (2008) acquired with the IPHT camera. At the time this thesis was written, an advanced version of the camera was in use, which was able to produce passive images with video capability.

at the hardware level. For that new methods and techniques are needed. The investigation of such techniques is more efficient in a passive imaging modality because it provides a better setting for this kind of investigation since it does not suffer from the myriad of problems, which occur as mentioned before, in the active imaging modality. For all the stated reasons why to pick THz-imager or, to be more specific, the region around 1 mm wavelength for the passive imaging in this investigation and the context of the security scenario introduced in the previous section; a wavelength of 1 mm has very good properties as far as the transmittance of obscurants is concerned. The resolution of acquired images is high even in a basic scanning scheme. The antenna size and hardware costs are still manageable. One of the most important points for choosing submillimeter radiation, is the potential to study new methods that incorporate digital image processing methods while still on the hardware level. This thesis will give results for such a method that potentially offers a solution for the “Bodyscanner problem” and in extension allows measurements in the Lock-In phase space. Processing on the hardware level becomes possible because of devices known as Spatial Light Modulators (SLM). A few necessary basic information on SLMs will be given in the next section.

1.3 Spatial Light Modulators

The most basic information to give on SLMs is to define the underlying concept. A Spatial Light Modulator is a device that is capable of altering a property of an incident beam of electromagnetic radiation (amplitude/intensity, phase or polarization) as a function of spatial coordinates¹⁶ and time. In short, the function of an SLM can be described by its transfer function, which is some function $f(\cdot)$ of two spatial variables and time. This transfer function is acting on and thereby changing an input light beam transforming it into an output beam:

$$\mathcal{H}(x, y, t) = f(x, y, t) \quad (1.2)$$

This leads straightforwardly to a categorization of different SLM-designs. The first distinction is between analog and digital SLMs. When the value of the transfer function \mathcal{H} varies in quantized amounts, when one of the spatial variables or the time assumes specific values, the SLM is said to be digital. Otherwise, when the value of \mathcal{H} varies continuously with every change of x , y or t , the SLM is called analog. The next level of distinction is the way in which the change in the transfer function of the SLM is controlled. This can be done whether optically, mechanically or electrically/electronically.

In this categorization, the final level is the way in which the transfer function itself is modulated. Is the modulation partially or globally meaning, if always the entire transfer function is changed or just parts of it. Since all physi-

¹⁶This thesis is mainly concerned with 2D-SLMs that are a function of 2 spatial coordinates but also gives a short outlook on the design and application possibilities of 3D-SLMs.

cal processes take a finite time until their completion¹⁷, this intended change leads directly to the first performance parameter of a specific SLM-design, its switching time T_S . It states the time for the SLM to complete a change in the targeted light property, commanded by its control signals. Another important performance parameter is the degree of modulation \mathcal{M} , which describes the degree of change in the light property that was actually achieved by the control signals. It can be described by equation (1.3), which states that the depth of modulation \mathcal{M} is 100% minus the ratio of I_{ON} by I_{OFF} , which describe the light property I with the control signals ON and OFF respectively.

$$\mathcal{M} = 100 \cdot \left(1 - \frac{I_{ON}}{I_{OFF}} \right) \quad (1.3)$$

In this T_S and \mathcal{M} are not the only parameters of importance. There are also the size, the power consumption, operating conditions, etc. But T_S and \mathcal{M} are the most important performance parameters, for the subject of interest here. Since many SLM-designs suffer from unwanted memory-effects one parameter shall in addition be mentioned. It is the degree of reproducibility \mathcal{R} . Its value describes how accurately, under the same conditions, a value of \mathcal{H} can be reproduced. The categorization of SLM-designs introduced above is summarized in Figure (1.5). In the figure two design possibilities are highlighted. These two design categories will be examined in greater detail in this thesis.

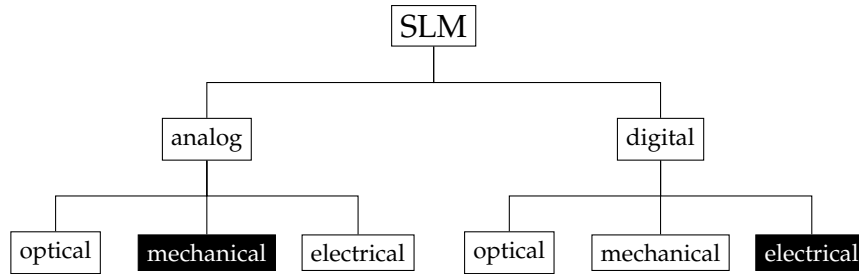


Figure 1.5: Categorization of SLM-designs.

To better understand the importance and function of SLMs a few application examples will be helpful. One of the simplest SLMs or rather a precursor is a transparency on an overhead projector. The situation and the derived block diagram are shown in Figure (1.6).

¹⁷This statement is true on the macroscopic level but has exceptions on the quantum level, e.g. quantum leaps and quantum entanglement.

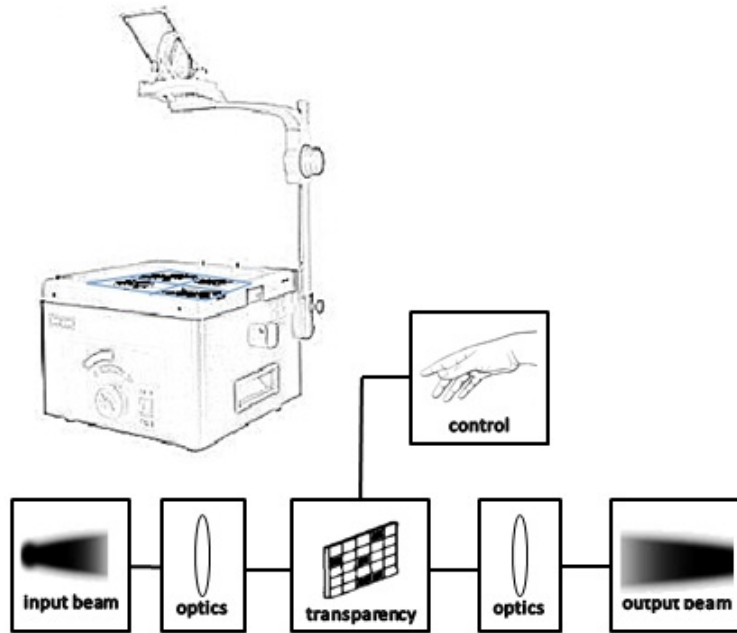


Figure 1.6: Schematic drawing of an overhead projector with a transparency as an example for a precursor for SLMs and the derived block diagram.

The beam of an optical light source in the overhead projector is changed by some optical elements so that the input beam is formed to best achieve the predefined performance. The light beam then passes through the transparency, which modulates the beam and transforms it into another beam. This beam is then again shaped by the output optics of the projector. From the schematic drawing and from the functional description just given, the block diagram of Figure (1.6) is derived.

All SLM-designs follow this block diagram, with varying implementations for the “transparency block” and the “control block”, depending on the category they are in (refer again to Figure (1.5)). A very straightforward extension of an overhead projector is the diascope with mounted slides and slide trays as “transparency block”. In this the modulation caused by the mounted slides is related to the transfer function \mathcal{H} of this very simple SLM. The change of a mounted slide can be achieved with a push of a button, which is electrically transmitted and then mechanically implemented. Therefore, a diascope can be categorized as a mechanical, analog SLM-design¹⁸. To extend the fundamental idea of an overhead projector even further, the SLM-design can be equipped with the automation- and flexibility-potential offered by a modern computer. Such a SLM-design is known as a beamer¹⁹. It can be categorized as a digital

¹⁸A simple diascope is used during the experiments for this thesis, to implement a first design for a THz-SLM.

¹⁹Another distinction of SLM designs is whether they work in transmission or reflection mode.

SLM-design that is controlled by electrical/electronic signals.

Many of the methods introduced in this thesis could be implemented much more effectively if a powerful tool like a THz-beamer (THz-SLM)²⁰ working in transmission or reflection mode would be available. Because of the perceived significance of THz-SLMs for the next generation of THz-imager, after implementing the proposed methods of this thesis with conventional means, the last of the experimental part of the thesis is devoted to the development of a working prototype of a THz-SLM.

The conventional SLM-designs mentioned above use chopping devices (rotating mirrors) as "transparency blocks". Other SLM-designs that will also be mentioned in this thesis are: Faraday rotators, which act on the polarization of the input beam and modulate this light property. Also a Decoherencer will be briefly examined. This SLM-design changes the light property of coherence.

All of these designs are neither as flexible nor as effective a SLM as a THz-beamer would be. But the proposed methods of this thesis were still implementable on the ISM-imager. One exception is the Compressed Sensing method. Preliminary measurements were conducted with the THz-SLM prototype. But the setup was still too large to incorporate it into the ISM-imager. The significance of Compressed Sensing for the next generation of THz-imager can not be overestimated. This will be briefly introduced in the last section of this introductory chapter.

1.4 THz-Imager and Compressed Sensing

The idea of Compressed Sensing or better to say its roots are actually at least as old as the Second world war. The fundamental idea was published by Dorfman in 1943 ([10]). He introduced a more efficient way of finding defective members in a large population. Motivated by the detection of flawed entities in a manufacturing process, his ideas were applied to disease testing of large human populations. Through the use of *group testing* techniques not every member of a large population had to be examined but still the condition of every member in the population was determined without error (perfect reconstruction). Even in this simple form the possibilities for the reduction of effort was in some cases as high as more than 90% (see Figure (1.7)):

Simple beamer always work in transmission mode. However, digital light processing (DLP) beamer use devices known as Digital Micromirror Devices (DMD), which are mirror arrays that allow for SLM-designs in reflection mode. A DMD is an essential part in the THz-SLM developed during this thesis.

²⁰The difference between a SLM and a beamer is just whether the source of the incident beam is added to the design in question. In this text both labels are treated as synonyms.

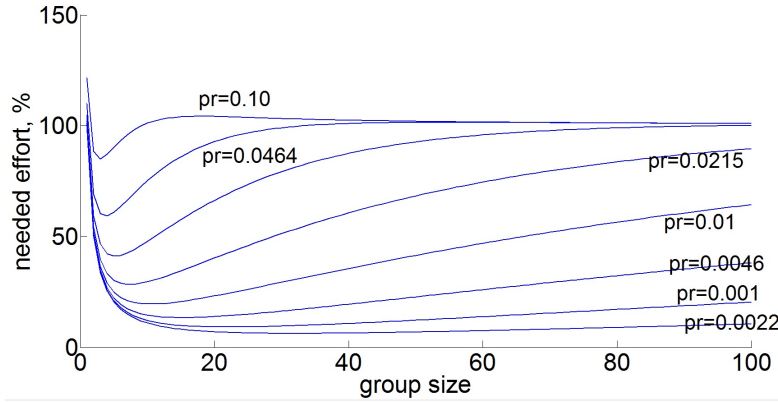


Figure 1.7: Depiction of the reduction in effort achievable with the simple group testing technique proposed by Dorfman. pr is the prevalence rate in the population of 1,000,000 entities.

From Figure (1.7) it is obvious that the achievable reduction depends in some cases very sensitively on the choice for the group size²¹. This crude first attempt of compressing the amount of data and reducing the effort needed to acquire it, led to the formulation of the new technique that was coined Compressed Sensing or Compressive Sampling or Compressed Sampling²². As long as there is sufficient sparsity in the signal of interest, meaning that only a few entries in the signal vector are non-zero elements, perfect reconstruction of the entire population is achievable with considerable less effort. These ideas were refined starting in the early years of this century. The field of Compressed Sensing started out as a more efficient way to retrieve messages (information) that were corrupted by noise or some other interference during transmission [5]. Later, the potential of CS was also recognized in other areas above all in imaging. In imaging the term Compressed Sensing is synonymous with analog-to-information conversion.

To understand this notion have a look at Figure(1.8). Here, an example THz-image and its wavelet decomposition in some wavelet basis is shown. Visible in the histogram is that most of the wavelet coefficients have values close to zero. Most of the information content of the image is contained in the relative few wavelet coefficients with large values. To compress the image by using, for example the JPEG2000 protocol, the coefficients with values lower than a certain threshold value are ignored. Using this protocol, the resulting image is shown in Figure (1.9):

²¹As explained in the chapter on the basics of Compressed Sensing, this is related to the mask properties used for CS-imaging.

²²Compressed Sensing was introduced in the famous paper of Candes and Tao, [6].

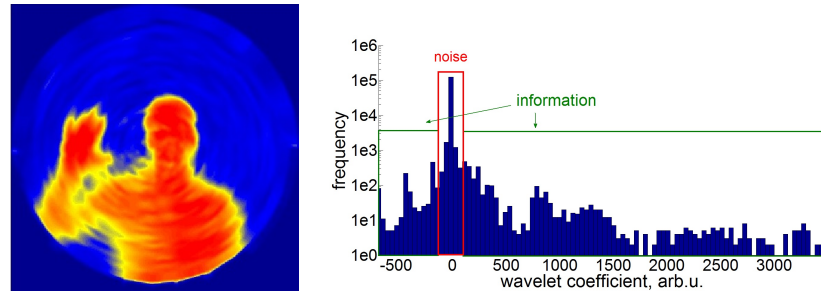


Figure 1.8: Example THz-image (left) and histogram of wavelet coefficients (right).

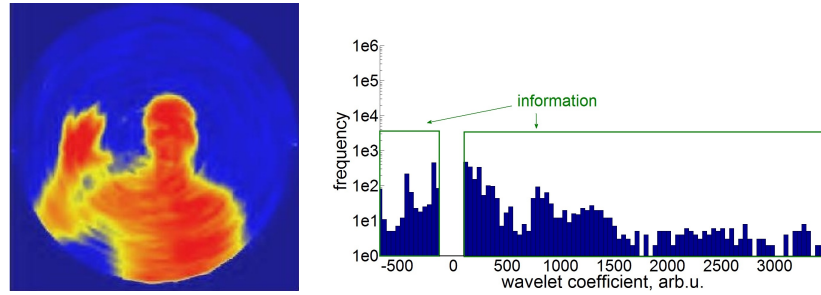


Figure 1.9: Compressed Example THz-image (left) and histogram of the wavelet coefficients used for reconstruction (right).

Depending on the chosen wavelet basis, the compression of the example image is of the order of 85%. The JPEG protocol works after the image acquisition is done. Now imagine a digital camera. Here millions and millions of pixels are acquired and most of them are thrown away afterwards (according to the JPEG-protocol). Compressed Sensing on the other hand acquires directly the image pixels that are significant, the information in the image. *CS acquires images already in their compressed form.* That is why CS is the embodiment of the ideas presented in this thesis - in one sentence, the merging of the software with the hardware level. To illustrate the concept of Compressed Sensing a little bit more, an experiment known as the Single Pixel Camera shall be briefly presented [11]. One of the outlooks of the research done for this thesis, is the development of a THz-Single Pixel Camera (a THz-beamer with only one detector for image detection).

A schematic setup of the Single Pixel Camera (SPC) is presented in Figure (1.10)²³.

²³Details can be found in [11].

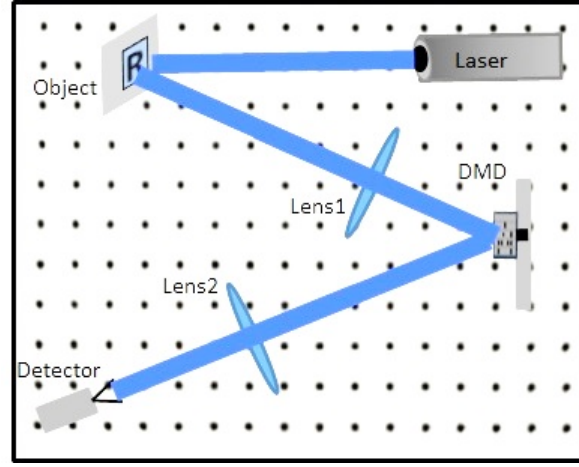


Figure 1.10: Schematic Setup of the VIS-Single Pixel Camera.

The SPC works like an optical computer evaluating inner products of the light being reflected from the object x and test functions generated by the DMD ϕ_m ²⁴. The DMD is the SLM of the SPC design. The function of the SPC can be mathematically described by Equation (1.4).

$$y[n] = \langle x | \phi_m(n) \rangle \quad (1.4)$$

In the SPC the entire scene (object) is illuminated by the laser source. The reflected radiation is mapped onto the DMD by lens1. The DMD then reflects only certain pixel via lens2 onto the detector. The detector, therefore, measures (integrates) the product of the test function $\phi_m(n)$ and the radiation coming from the scene x . In this, m is the number of the used test function and n is the number of pixels/mirrors the DMD contains. So, the DMD is multiplying $x \cdot \phi_m$ and also discretizing the product (the mirror array called DMD is therefore a digital SLM). The advantages and disadvantages of the SPC are summarized in Table (1.2).

Table 1.2: Advantages and Disadvantages of the Single pixel Camera.

ADVANTAGE		DISADVANTAGE	
measurement time	↓	entire scene	
resolution	↑	illumination necessary	✓
DLP capability			
on the hardware level	✓		

²⁴As already mentioned, the DMD is a micro mirror array in which every mirror is addressable with a computer. The notion of the SPC as optical computer using the DMD is also introduced in [11].

The most obvious advantage of a CS-scanning scheme is that, if just one detector is available, the measurement time is substantially reduced in comparison to a raster scan (see Figure (1.11)²⁵). Other advantages listed in Table (1.2) are increased resolution, since Superresolution becomes possible when using an SLM. Also other DLP capabilities become accessible on the hardware level, like edge detection, object detection, etc. The disadvantage of a CS scanning scheme is just that at all times, the entire scene has to be illuminated, which wastes the power emitted in inactive

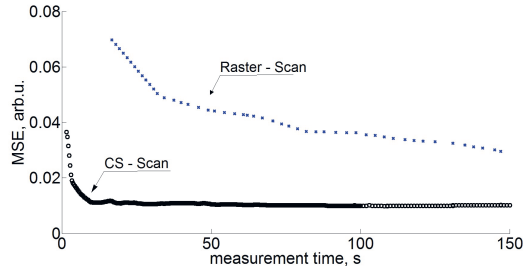


Figure 1.11: Test measurement with the SPC of the object in Figure (1.10).

pixel. This is unproblematic when sufficient power, for the illumination of the scene, is available. To advance THz-imager, the idea inspired by the SPC now was to adapt the CS scanning scheme for THz-imaging. The possible advantages for THz-imaging are even more promising than for VIS-radiation.



Figure 1.12: Schematic representation of the idea of Digital Light Processing in the THz-region. Shown is a digital THz-SLM (its "transparency block") whose pixel can be controlled individually by a computer.

Why is that? Because in the THz-region one detector pixel still costs a few thousand € and raster scanning or spiral scanning schemes are ubiquitous. Large pixel number THz-cameras will probably not be available for many years (at least not as sensitive ones). Due to the large wavelength in the THz-region, THz-cameras that work at a few meter distance from the scene tend to be rather bulky, meaning rather large THz-optics is necessary. The combina-

tion of a single or just a few detectors with large mechanical scanners makes the necessary scanning process difficult and slow. A CS scanning scheme promises scanning without moving large mechanical parts. The ideas of digital image processing (DIP) on the hardware level realized by DLP-methods and their *thinking outside the box* use as demonstrated in Compressed Sensing and the SPC inspired the work done for this thesis. The ideas are summed up in Figure (1.12) which will act as a continuous reminder of the "leitmotif" for this thesis.

²⁵Reproduced after [11].

To see this more clearly let us briefly recapitulate the ideas presented in this chapter.

This introductory chapter outlined the scenario in which THz-imaging would be most effective showing that the detection of hidden threats from a stand-off distance of a few meters is a situation often encountered in security imaging. It was shown that THz-radiation is a valuable imaging tool in this scenario. The direction for advancing THz-imager outlined in this introduction suggests the use of Spatial Light Modulators. When using SLMs it becomes possible to employ methods known to Digital Image Processing, that are normally bound to the software level, already on the hardware level, during image acquisition. The possibilities of this DLP technique are almost endless. Much that can be implemented as an algorithm on a computer will be translatable by the SLM into the hardware domain²⁶. This thesis will present only a few methods that are possible, like edge detection, detection in the phase domain, thresholding, custom signal quantization, etc. In this, the method of Compressed Sensing plays a very prominent role since it is the embodiment of this aforementioned change in how imaging is done (as shown in the example of the single pixel camera). This concludes the introduction and the overview what is discussed in the remainder of the text. The next three chapters now give the necessary scientific background information to support the ideas presented in this thesis.

²⁶The notion of an optical computer is, in this author's opinion, very helpful for the understanding of many of the ideas presented in this thesis.

References Chapter 1

- [1] S. S. Ahmed, A. Schiessl, and L.-P. Schmidt, "A novel fully electronic active real-time imager based on a planar multistatic sparse array," *IEEE Transactions on Microwave Theory and Techniques*, vol. 59, no. 12, pp. 3567–3576, 2011.
- [2] R. Appleby, K. A. Krapels, and N. A. Salmon, "The history of passive millimetre-wave imaging at qinetiq," in *SPIE Europe Security and Defence*, ser. SPIE Proceedings. SPIE, 2008, pp. 711 702–711 702–7.
- [3] R. Appleby and R. N. Anderton, "Millimeter-wave and submillimeter-wave imaging for security and surveillance," *Proceedings of the IEEE*, vol. 95, no. 8, pp. 1683–1690, 2007.
- [4] R. Appleby and H. B. Wallace, "Standoff detection of weapons and contraband in the 100 ghz to 1 thz region," *IEEE Transactions on Antennas and Propagation*, vol. 55, no. 11, pp. 2944–2956, 2007.
- [5] E. J. Candes, J. Romberg, and T. Tao, "Robust uncertainty principles: exact signal reconstruction from highly incomplete frequency information," *IEEE Transactions on Information Theory*, vol. 52, no. 2, pp. 489–509, 2006.
- [6] E. J. Candes and T. Tao, "Decoding by linear programming," *IEEE Transactions on Information Theory*, vol. 51, no. 12, pp. 4203–4215, 2005.
- [7] M. P. Christensen, G. W. Euliss, M. J. McFadden, K. M. Coyle, P. Milojkovic, M. W. Haney, van der Gracht, Joeseeph, and R. A. Athale, "Active-eyes: an adaptive pixel-by-pixel image-segmentation sensor architecture for high-dynamic-range hyperspectral imaging," *Applied Optics*, vol. 41, no. 29, p. 6093, 2002.
- [8] K. B. Cooper, R. J. Dengler, N. Llombart, A. Talukder, A. V. Panangadan, C. S. Peay, I. Mehdi, P. H. Siegel, M. Anwar, N. K. Dhar, and T. W. Crowe, "Fast high-resolution terahertz radar imaging at 25 meters," in *SPIE Defense, Security, and Sensing*, ser. SPIE Proceedings. SPIE, 2010, pp. 76 710Y–76 710Y–8.
- [9] K. B. Cooper, R. J. Dengler, N. Llombart, B. Thomas, G. Chattopadhyay, and P. H. Siegel, "Thz imaging radar for standoff personnel screening,"

- IEEE Transactions on Terahertz Science and Technology*, vol. 1, no. 1, pp. 169–182, 2011.
- [10] R. Dorfman, “The detection of defective members of large populations,” *The Annals of Mathematical Statistics*, vol. 14, no. 4, pp. 436–440, 1943.
 - [11] M. F. Duarte, M. A. Davenport, D. Takhar, J. N. Laska, Ting Sun, K. F. Kelly, and R. G. Baraniuk, “Single-pixel imaging via compressive sampling,” *IEEE Signal Processing Magazine*, vol. 25, no. 2, pp. 83–91, 2008.
 - [12] T. M. Goyette, J. C. Dickinson, K. J. Linden, W. R. Neal, C. S. Joseph, W. J. Gorveatt, J. Waldman, R. Giles, W. E. Nixon, and L. P. Sadwick, “1.56 terahertz 2-frames per second standoff imaging,” in *Integrated Optoelectronic Devices 2008*, ser. SPIE Proceedings. SPIE, 2008, pp. 68 930J–68 930J–11.
 - [13] M. R. Habermeld and A. v. Hassell, *A new understanding of terrorism: Case studies, trajectories and lessons learned*. New York and London: Springer, 2009.
 - [14] E. Heinz, T. May, D. Born, G. Zieger, A. Brömel, S. Anders, V. Zakosarenko, T. Krause, A. Krüger, M. Schulz, F. Bauer, H.-G. Meyer, N. A. Salmon, and E. L. Jacobs, “Development of passive submillimeter-wave video imaging systems for security applications,” in *SPIE Security + Defence*, ser. SPIE Proceedings. SPIE, 2012, p. 854402.
 - [15] Jinshan Ding, M. Kahl, O. Löffeld, and P. H. Bolivar, “Thz 3-d image formation using sar techniques: Simulation, processing and experimental results,” *IEEE Transactions on Terahertz Science and Technology*, vol. 3, no. 5, pp. 606–616, 2013.
 - [16] A. H. Maslow, “A theory of human motivation,” *Psychological Review*, vol. 50, no. 4, pp. 370–396, 1943.
 - [17] T. May, E. Heinz, K. Peiselt, G. Zieger, D. Born, V. Zakosarenko, A. Brömel, S. Anders, and H.-G. Meyer, “Next generation of a sub-millimetre wave security camera utilising superconducting detectors,” *Journal of Instrumentation*, vol. 8, no. 01, p. P01014, 2013.
 - [18] T. May, G. Zieger, S. Anders, V. Zakosarenko, M. Starkloff, H.-G. Meyer, G. Thorwirth, E. Kreysa, J. O. Jensen, H.-L. Cui, D. L. Woolard, and R. J. Hwu, “Passive stand-off terahertz imaging with 1 hertz frame rate,” in *SPIE Defense and Security Symposium*, ser. SPIE Proceedings. SPIE, 2008, pp. 69 490C–69 490C–8.
 - [19] G. N. Sinclair, R. Appleby, P. R. Coward, S. Price, and R. M. Smith, “Passive millimeter-wave imaging in security scanning,” in *AeroSense 2000*, ser. SPIE Proceedings. SPIE, 2000, pp. 40–45.

Theoretical Basics of THz-Imaging

Contents

2.1	The Quasioptic nature of THz-radiation	31
2.2	THz-imaging modalities	34
2.3	The passive imaging modality	36
2.3.1	Signals in passive THz-imaging - Temperature Resolution	38
2.3.2	The Scanning Optics – Spatial Resolution	43
2.3.3	The scene	49
2.4	The active imaging modality	50
2.4.1	Frequency Modulated Continuous Wave THz-Imaging	50
2.4.2	Illumination scenarios	52
2.4.3	The effects of polarization	53
2.5	Software scanning	55

This chapter presents the necessary physical basics for the understanding of this thesis. It starts at the most fundamental level, the radiation itself. In the first section it describes the peculiarities encountered when dealing with THz-radiation and introduces this region of the electromagnetic spectrum as the Quasioptic-region. The second section then turns to the specific application of THz-radiation at hand, namely THz-imagers and investigates the main components of them, following the path of the radiation through the imaging system. The focus in this section will be on stand-off imagers, meaning the image acquisition from a distance of a few meters. It also looks at the two imaging modalities in more detail, building upon the differences of the active- and the passive modality already given in the first chapter.

The next section then establishes the physical limits of a passive imaging system by introducing the concepts of temperature- and spatial resolution, their interdependence and the conditions for their applicability. The section "Temperature resolution" is focused on one of the most important equations when dealing with THz-imagers, the Radiometer equation. The section about "The Scanning Optics" uses concepts from system theory to build a bridge from the physical limits of an imaging system to the pictures it produces. The last few sections focus on the active imaging modality and its differences to the passive modality. The fourth section introduces the method of

frequency modulated continuous wave (FMCW) imaging as a means to combat many of the problems encountered in the active mode. It will also hint at the problems that artificial radiation produces because of its high degree of polarization. The chapter then concludes with a first detailed look at the software scanning technique, which, in contrast to hardware scanning, promises a possible solution for the scenario exemplified in figure (1.1) section (1.1).

2.1 The Quasioptic nature of THz-radiation

THz-radiation, or to be more specific submillimeter-radiation, just describes electromagnetic radiation with a wavelength of ≈ 1 mm. What makes the submillimeter-region special is the combination of maturity of the underlying technologies and some physical properties of the radiation in this region of the electromagnetic spectrum. Consider the representation of figure (2.1). It shows the submillimeter-region in between the radiowave-region and the VIS/IR-region. In addition, the emission of

a blackbody at 300 K is shown. The electromagnetic radiation of the radiowave-region on one side is characterized by a rather large wavelength in regard to systems operating in this part of the spectrum. That also means that diffraction plays a very important role. On the other end in the VIS/IR part the wavelength is small compared to the system size. In

turn, this means that diffraction effects play almost no role in this part of the spectrum. Thus, in the submillimeter-region diffraction is a factor that has to be taken into account. If we consider the two extremes, the radiowave-region on one hand and the VIS/IR-region on the other hand, then it is understandable that the THz-region adapts methods of both to its special needs. THz-imager are distributed systems, consisting of individual parts that need to be connected to form the system THz-imager as a whole. The parts of a distributed system in the radiowave-region are connected using cables, waveguides, strip lines, etc. depending on the exact frequency and bandwidth of the respective system. Losses increase with increasing frequency. At THz-frequencies (in the Submillimeter-region) propagation losses in dedicated conduits are so high that such means of propagation are not suitable for distributed systems. On the other end, in the VIS/IR-region, distributed systems face similar problems because of the even higher frequencies in this part of the electromagnetic spectrum. Unlike the radiowave-region in the VIS/IR-region no dedicated conduits are used to connect the parts of a distributed system. In this region the solution

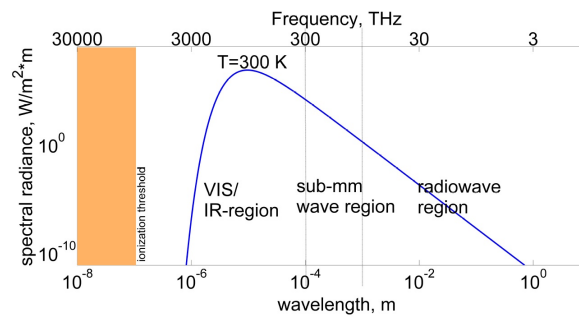


Figure 2.1: THz-region in between the VIS/IR and radio-wave region.

is to use free space propagation to channel radiation from one part to another.

Hence the name Quasioptic-region. Here, the properties of the used radiation are in between radiation properties in the radiowave region and the VIS/IR-region. The frequency is so high that only free-space propagation provides a viable option for the connection of the parts of a distributed system. On the other hand the frequency is too low (wavelength is too large) to pay no attention to diffraction effects. Therefore, the Quasioptical-region is only quasi optical because, like in the optic-region, free space propagation is used but the limit $\lambda \rightarrow 0$ is not applicable. The Quasioptical approximation for the propagation of a collimated beam is given by equation (2.1).

$$R = z + \frac{1}{z} \left(\frac{\pi \cdot \omega_0^2}{\lambda} \right)^2 \quad \omega = \omega_0 \left[1 + \left(\frac{\lambda \cdot z}{\pi \cdot \omega_0^2} \right)^2 \right]^{0.5} \quad (2.1)$$

Equation (2.1) consists of two parts since the beam parameter derived from the paraxial wave equation is a complex quantity¹. The real part of the beam parameter is identified with the radius of curvature R of the beam. It depends on the distance z (without loss of generality the z -axis was chosen as the direction of propagation and the position of the source was chosen as origin of the coordinate system $z = 0$). Here, λ is the wavelength of the respective radiation and ω is the beam radius. In turn, ω_0 characterizes the minimum of the beam radius and is called the beam waist. The beam radius is defined as the value at which the intensity in the beam drops to $(1/e)^2$ relative to its on-axis value. Figure (2.2) illustrates the change in radius of curvature and beam radius with changing distance z from the source.

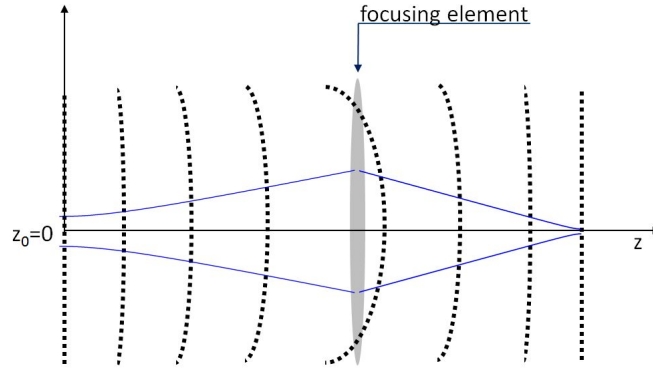


Figure 2.2: Beam propagation of a Quasioptical beam according to equation (2.1). The blue lines indicate the change of the beam radius and the dotted lines, in turn, indicate the change in radius of curvature.

¹See [4] pp. 9 - 17 for details.

In figure (2.2) the blue lines indicate the change in beam radius with increasing distance $z - z_0$ from the source. The dotted lines, in turn, show the radius of curvature (phase fronts) at different positions along the line of beam propagation. It is noteworthy that at the positions of the beam waist (position of the source and focus point of the focusing element) the radius of curvature reaches infinity and the phase fronts are flat (plane wave). It is also important to consider the validity conditions of equation (2.1). It is derived from the **reduced wave equation**, which depends on the approximation that the variation along the axis of propagation (due to diffraction effects) is small over distances of the order of a wavelength. Also, the variation on the axis of propagation has to be small compared to the variation perpendicular to this direction. The second approximation is also called the **paraxial approximation**. The validity of this approximation limits the applicability of all the Quasioptic equations given in this section. The paraxial approximation is valid as long as the beam divergence is not above 30° (restated after [4]). Some effects of deviations from the aforementioned conditions of validity of the paraxial approximation are discussed in [8].

The simplest mathematical function that solves the (axially symmetric) paraxial wave equation is a Gaussian function. That means the beam (the fundamental mode) can be described according to equation (2.2).

$$I = I_0 \cdot \exp\left(\frac{-2 \cdot r^2}{\omega^2}\right) \quad (2.2)$$

Here, I denotes the intensity of the beam, r describes the distance from the axis of propagation and I_0 is the maximum intensity at the center of the beam ($r = 0$). In a distributed Quasioptical-system the beam propagates and passes the different system components. As indicated by equation (2.1) the beam needs to be collimated already after a few cm of free space propagation. Otherwise the beam size becomes too large for most Quasioptical-system components. Also, because of the large wavelength of ≈ 1 mm, diffraction effects become more and more pronounced with increasing beam size. As a rule of thumb it usually is acceptable to commit to a truncation of $4 \cdot \omega$ by optical elements or apertures in the path of the beam propagation. With a truncation of four times the beam radius 99.97% of the power in the fundamental Gaussian mode is included in the truncated beam.

As already discussed, since free space propagation is mostly chosen for distributed Quasioptical-systems, the system size only remains manageable if the beam is focused after only a few cm of free space propagation. Refractive focusing elements in the Quasioptic-region are made from dielectric materials. Therefore, the overall lens design is similar to lenses from the optical region but because of the large wavelength the requirements for the quality of lenses are easier to meet. Even a surface quality of $\lambda/100$, which requires surface roughness below this limit, is met even by direct machining. On one hand there are refractive focusing elements and on the other hand reflective optical components can be used to focus Quasioptical-beams. Like in the optic-region, metallic mirrors are used in this case. The advantage of the relaxed surface quality conditions in Quasioptics now produces a disadvantage if metallic components are introduced in the system. Metallic surfaces are almost perfect reflectors (at the order of 99.99%) and result in unwanted reflections in the

system setup. The unwanted reflected parts of the beam interfere with one another and because of the large coherence length in this part of the spectrum (see e.g. [10]) produce standing waves. Because of the interference parts of the beam show largely enhanced or reduced values severely distorting the system response. Due to the standing wave property, the interference is not changing with time distorting the system response the entire time of the measurement. Especially severe is the situation if the measurement is the acquisition of an image. The interference superelevation can cause extremely high values in the image limiting contrast and visibility. Also, large values in the image can be caused at image positions where no object is present in the scene. To demonstrate the situation, the following image shows the measurement of a metallic Siemensstar with a test imaging setup².

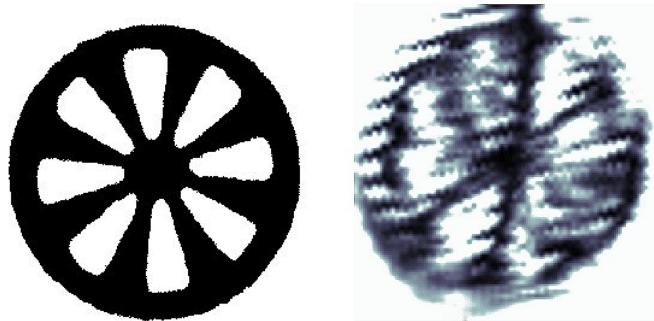


Figure 2.3: Digital camera image of a metallic Siemensstar (left) and THz-image (right) exemplifying standing waves and image artifacts encountered in Quasioptical-imaging.

Here, figure (2.3) serves only to exemplify the problems standing waves cause for Quasioptic-imaging. In the figure the standing waves are visible as fringe-like structures. When compared with the digital camera image the THz-image shows no clear edges and detection artifacts³. In conclusion, some of the peculiarities of the Quasioptic-region just introduced as well as the presence or possibility for the appearance of standing waves have to be taken into account when designing a Quasioptic-imaging system. The make-up of such systems will be discussed in the next section.

2.2 THz-imaging modalities

As already discussed in the previous chapter, the two imaging modalities, namely active and passive imaging, differ from a system point of view only by an artificial source⁴. Here, the two imaging modalities are examined in a stand-off security imaging background. To make the description of the

²The details on the test setup will be presented in in section (6.5.1).

³Some of the artifacts are also due to diffraction effects. See the detailed discussion in section (6.5.1).

⁴Depending on the illumination scenario, a few additional optical components like a beam splitter, lenses, mirrors, etc., might be necessary. Here such optical components are treated as part

beam propagation introduced in the last section more illustrative in a stand-off imaging background, the confocal distance or Rayleigh range is introduced in equation (2.3).

$$z_c = \frac{\pi \cdot \omega_0^2}{\lambda} \quad (2.3)$$

The Rayleigh range can be used to make an easy distinction between the "near field" and the "far field" and also to introduce the concept of depth of focus for Quasioptical-imaging. In figure (2.4) the beam radius over distance z , normalized to the Rayleigh range and the beam waist, is plotted (top row). In the bottom row two cases for different beam waists ω_0 are plotted in absolute units.

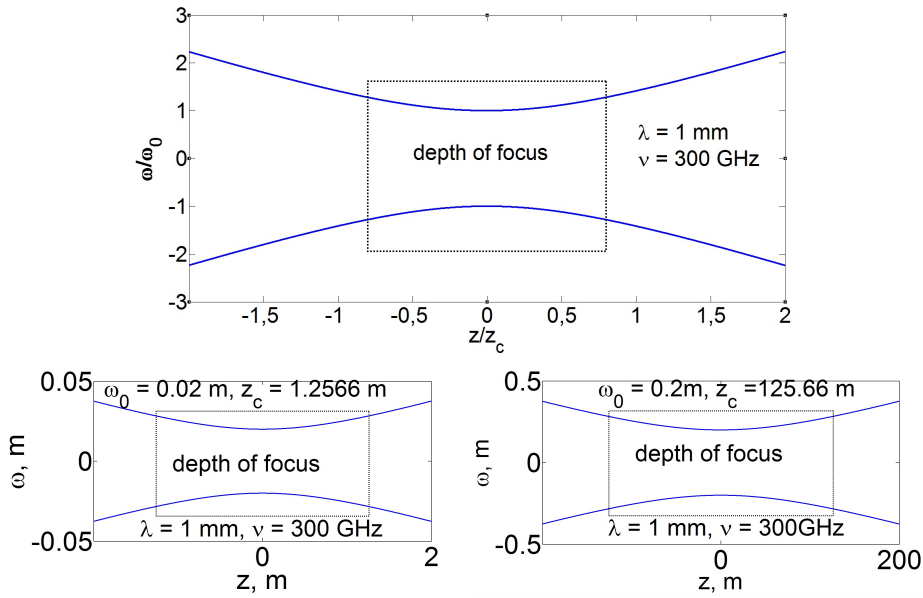


Figure 2.4: Beam propagation of a Quasioptical beam normalized to z_c and ω_0 (top row) and in absolute units for differing ω_0 (bottom row). Observable is the increasing depth of focus with increasing ω_0 .

The limit $z \ll z_c$ is called the "near field" and the limit $z \gg z_c$ is called the "far field". In the region up to the Rayleigh distance the beam radius is almost constant ($\omega(z_c) = \sqrt{2} \cdot \omega_0$). That is why the identification of z_c as the depth of focus (DoF) is straightforward. As can be seen from figure (2.4 bottom row) in absolute units, the DoF increases quadratically with increasing ω_0 . The standard approach for stand-off imaging now is to have a scanning telescope that focuses the Quasioptical-beam to a small spot size (waist) at a distance of a few meters. With the details on beam propagation just discussed it is understandable that this approach results in only a narrow DoF. This is one

of the source component. Different illumination scenarios as well as the effects of polarization are briefly considered in section (2.4).

limitation of the hardware scanning approach. Nonetheless, it is the state-of-the-art in THz-imaging for both imaging modalities. The differences of the two modalities and the details of the system designs will now be briefly considered starting with the passive imaging modality. After this discussion a few details and differences on the software scanning approach will be briefly introduced as well.

2.3 The passive imaging modality

The passive imaging modality uses no artificial source to illuminate the scene. It just uses the radiation coming from objects in the scene and the radiation that originates from natural sources (e.g. the sun) and is reflected of objects in the scene. The fraction of radiation being emitted from the objects in the scene is under normal conditions ($15^\circ\text{C} < T_{Amb} < 30^\circ\text{C}$) larger than the reflection from natural sources. This can be easily understood by considering the temperatures involved. Persons in the scene have temperatures around 37°C , which is larger than T_{Amb} under normal conditions. Concealed objects on the other hand may have temperatures close to body temperature, which would make them difficult to detect. This is the main drawback of the passive modality, the limited SNR. The emitted signal power from objects in the scene can not be increased (it is limited by their respective temperatures). As a reminder, the detected temperature T_D given by equation (1.1) from the introduction section (1.2) is reproduced⁵.

$$T_D = \underbrace{\epsilon(\theta, \varphi, r) \cdot T_{eff}}_{(1)} + \underbrace{s(\theta, \varphi, r) \cdot T_S}_{(2)} + \underbrace{t(\theta, \varphi, r) \cdot T_B}_{(3)} \quad (1.1)$$

As discussed there, the detected temperature at the detection component (T_D) (see below) consists mainly of three parts. The effective temperature of objects in the scene (T_{eff}) multiplied by their respective emissivity function $\epsilon(\theta, \varphi, r)$, the scattered temperature (T_S) multiplied with the scattering function $s(\theta, \varphi, r)$ and the transmitted background temperature T_B multiplied by the transmission function $t(\theta, \varphi, r)$. For the passive imaging modality (indoors) component (1) has the most significant contribution to the detected temperature. As a starting point for the investigation of the main components of THz-imager, it is helpful to consider passive imaging outdoors where also component (2) of equation (1.1) has a non-negligible contribution. Imaging outdoors makes the situation also more comparable to the later discussed active imaging modality. The reason why component (2) is non-negligible for passive imaging outdoors is the cold sky background, which provides significant contrast as shown in the following image.

⁵Please also keep in mind that equation (1.1) should only be considered in the steady-state case.

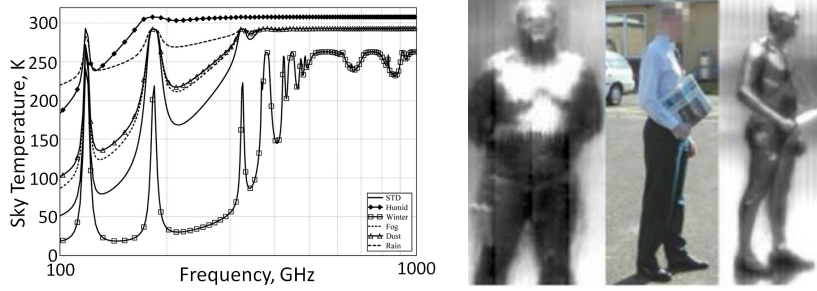


Figure 2.5: Sky temperature for different frequencies (left) and example image at 94 GHz taken outdoors. Both, the image and the representation of the sky temperatures were taken from [1].

Depending on the conditions outdoors (temperature, humidity, etc.) and the frequency used, the temperature difference to objects in the scene (persons) can be as high as 300 °C. In the image on the RHS of figure (2.5) the reflection of the cold sky from the concealed metallic knife is extremely bright (glint effect). Not only does the sky provide a very cold natural illumination source but also is the reflectivity of metal almost unity. The reflectivity is implicit in the scattering coefficient $s(\theta, \varphi, r)$ of equation (1.1). It is the fraction of $s(\theta, \varphi, r)$ that follows the additional condition $\theta_{incident} = \theta_{outgoing}$. The cold sky provides an almost homogeneous illumination with many incident directions. That is another advantage of passive THz-imaging outdoors. The fact that the cold sky illumination provides for many incident angles is an important point that also provides valuable insight for illumination scenarios in the active imaging modality. This will be briefly discussed in more detail in section (2.4.2)⁶. At this point it is helpful to derive a general block diagram for stand-off imagers.

Already introduced were the telescope and the detection system component. Also mentioned were the scene, which we treat here as belonging to the system and the illumination source (source component). Here, the categorization that is illustrated in figure (2.6) is adopted. This categorization is not the only categorization imaginable but shall be the guideline for the assessment presented here.

⁶As mentioned before, images like the one shown in figure (2.5) caused the notion "Bodyscanner". However, the ability to see through visually opaque objects should, for the evaluations of this thesis, be seen with regard to contents discussed above.

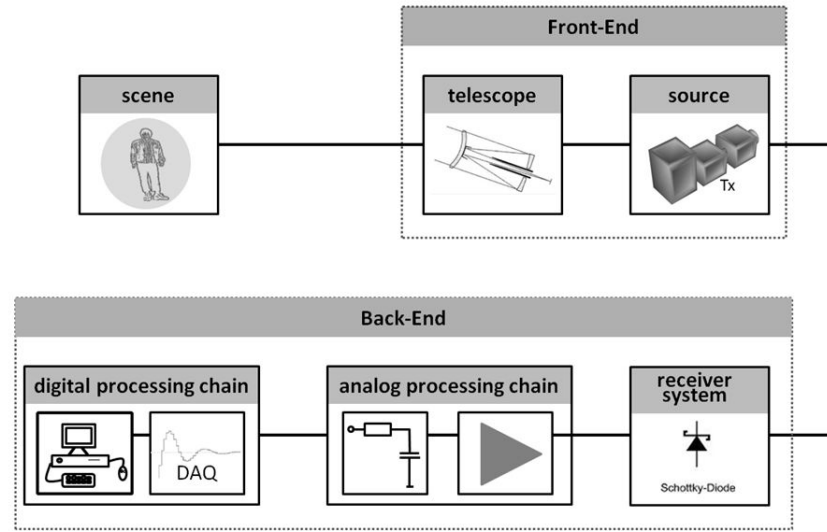


Figure 2.6: Generic block diagram for THz-imagers.

The block diagram shown in figure (2.6) is generic in the sense that the components listed therein are components in most THz-imager systems, active or passive⁷. Every component is considered in more detail following the reversed path of the radiation. It is also helpful to consider first what signal to expect from objects in the scene.

2.3.1 Signals in passive THz-imaging - Temperature Resolution

All objects emit THz-radiation according to their temperature. Planck's law describes the emitted radiation of an ideal blackbody and is a good first approximation for all objects encountered in (passive) THz-imaging. The emitted thermal radiation is statistical in nature. The wave trains are independent of each other with statistically varying frequency and phase. Due to the independent and erratic behavior of the phase, thermal radiation is highly depolarized radiation. The lack of a distinct polarization makes thermal radiation easily processable on the level of the front-end (for details see e.g. [5]).

The processing usually involves refractive- and/or reflective optical elements. Refractive optical elements, on one hand, mostly have no effect on the polarization of the radiation involved, whereas reflective elements tend to rotate the direction of polarization⁸. Since thermal radiation is statistical radiation, only temporal averages provide information about the processed radiation and possible objects in the scene. Usually only the radiation intensity is accessible for detection. The detected intensity in turn is proportional to the

⁷The terms front-end and back-end are used ambiguously in the literature. Here, the (optical) front-end is mainly dealing with the free space propagation of the signals coming from the scene and the (electronic) back-end processes the electronic signals until an image is formed. The conversion is done in the receiver, which is counted as part of the back-end.

⁸The effects of electric/magnetic fields and anisotropic media in the propagation path, as well as details on the rotation of the axis of polarization, will be briefly discussed in section (2.4.3).

power delivered to the antenna of the detector system. It can be shown (see e.g. [5]) that the power detected by detector system can be written as a linear function of the antenna temperature (T) as shown in equation (2.4).

$$P_D = k_B \cdot T \cdot \Delta\nu \quad (2.4)$$

Equation (2.4) is identical to the equation that describes the noise power dissipated in an electrical resistor at impedance matching. It states that the detected power P_D is proportional to the temperature of the resistor T . The proportionality factor is the bandwidth $\Delta\nu$ multiplied by Boltzmann's constant k_B . In the context of the detection of electromagnetic radiation, equation (2.4) means that the radiation resistance of the receiving antenna (detector system antenna) is equivalent to a noise temperature (antenna temperature)⁹. The antenna temperature is under ideal conditions identical to the temperature of the detected object (T_D in equation (1.1)). Deviations from the ideal conditions may occur because of the non-ideal antenna characteristic and attenuation due to the atmosphere (mainly water vapor). From equation (2.4) it can be seen that the detected power goes up when the temperature of the object rises ($T \uparrow$) or when the detection bandwidth is increased ($\Delta\nu \uparrow$). Since the temperatures of objects in the scene are given (in passive mode), the detected signal strength can only be increased by increasing the bandwidth of the detection system.

That is the reason why the passive imaging modality is extremely limited and is unlikely (in this author's opinion) to offer a viable solution for the imaging scenario depicted in figure (1.1). Even with hundreds of thousands of € spend, a passive THz-security camera still lacks sufficient detection capability. To better understand the abilities of a passive security imager, the signals at different points of the back-end shall now be analyzed and an equation describing the sensitivity limit is derived. The examination follows the path of the block diagram shown in figure (2.6) and starts at the beginning of the back-end. An example signal at this point is depicted in the time domain, in the frequency domain¹⁰ respective power spectral density and as intensity/amplitude histogram in figure (2.7).

⁹The fact that on one hand T is interpreted as the temperature of a resistor and on the other hand as the temperature of a detection system antenna are essentially only two different views of the same physical occurrence, the propagation of electromagnetic energy. In one view, it appears as electrical current in ideal dedicated conduits and in another view, it appears as electromagnetic radiation in the form of free-space propagation.

¹⁰Fourier analysis of stochastic signals that have unlimited signal energy is not valid. It is given here only as a general description without relation to the SI unit system.

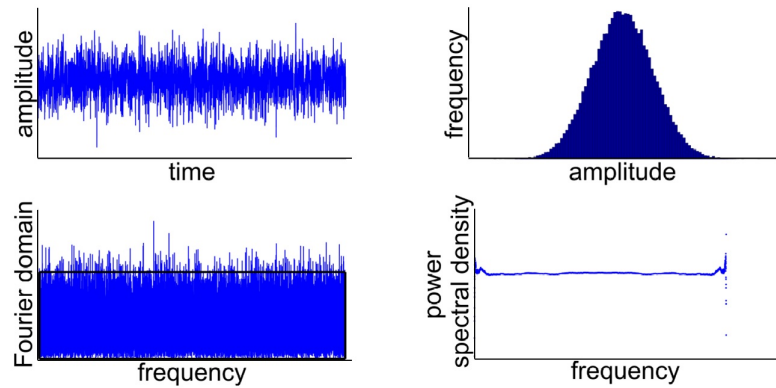


Figure 2.7: Signal at the input of the back-end in passive THz-imaging. The signal in the time domain (left-top) is stochastic in nature. In the Fourier domain (left-bottom) therefore results an almost constant spectrum (white noise). Its amplitude values follow approximately a Gaussian distribution (right-top) with a constant power spectral density (right-bottom).

It can be assumed from Figure (2.7) that the bandwidth of the incoming radiation is large in comparison to the used local oscillator frequency (LO-frequency) of the receiver¹¹. It can also be seen from the graphs in figure (2.7) that the intensity values follow a Gaussian distribution, which makes the incoming signal a good approximation of Gaussian noise (white noise). As a next step in the analog processing chain the incoming signal needs to be amplified before it can be digitized. In the heterodyne process the input signal is shifted in the frequency domain to an intermediate frequency (IF). The choice for the IF is heavily influenced by the technological maturity of the underlying devices (mixer, amplifier, etc.). Basically, at the present level of technology, the signal after the mixer can be regarded as very broadband (almost infinite) bandwidth with regard to the LO-frequency. The limiting factor in regard to the output signal bandwidth is introduced by the amplifier following the mixer. To get better noise performance of the back-end system, the first amplifier following the mixer is implemented as an active bandpass filter but still the first amplifier determines the global noise performance of the back-end (see e.g. [5] pp. 119-122). The signal in the time and frequency domain as well as its intensity distribution are shown in figure (2.8).

¹¹For this examination the use of a heterodyne receiver system is assumed. Details on such systems are discussed in section (5.2).

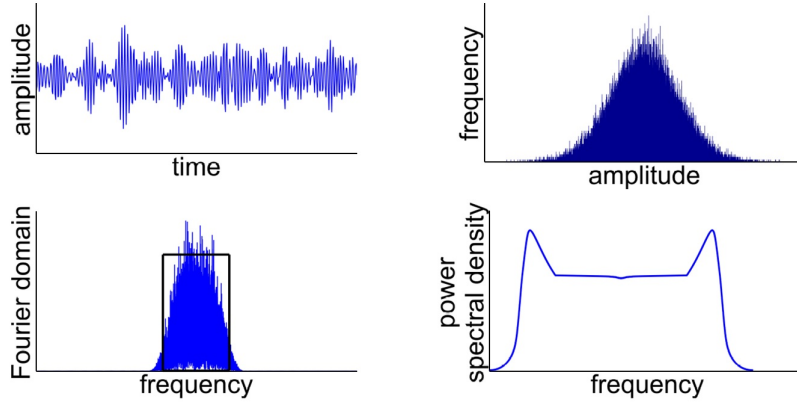


Figure 2.8: Signal after amplification in the back-end of a generic passive THz-imager. The signal in the time domain (left-top) is stochastic with a superimposed modulation. The Fourier domain shows the band limitation by the amplifier transfer function (left-bottom). The amplitude values still follow approximately a Gaussian distribution (right-top) but the power spectral density is no longer constant (right-bottom).

It can be seen from figure (2.8) that the band limited signal after the first amplifier still has a Gaussian intensity distribution limited by the amplifier transfer function. Following equation (2.4), it can be seen that the band limitation severely diminishes the power of an incoming signal. It also is one main factor for the decrease in sensitivity of a passive THz-imager (see consequent discussion below). Following the path of the radiation through the block diagram of figure (2.6), the radiation now enters the actual detector. We assume here a power rectifying detector with a quadratic response (current-voltage characteristic). The detector simultaneously acts as rectifier and integrator. After the detector the signal is sampled and digitized using data acquisition (DAQ) devices¹². The mathematical description of the signal behind the detector is given as follows in equation (2.5)

$$U_D = \alpha \cdot P_D \quad (2.5)$$

Equation (2.5) describes only the low frequency response of the detector output signal. The integration time τ of the integrator is the main factor in determining its frequency response. The output signal of the back-end is proportional to the detected THz-power emitted by objects in the scene and U_D also follows approximately a Gaussian distribution. The output signal of the back-end is exemplified in figure (2.9).

¹²At this point it should be mentioned that the integration can also be done digitally. The digital integration would offer additional benefits. However, the commercially available hardware is not well-suited for this approach. CS here also offers potential for improved hardware.

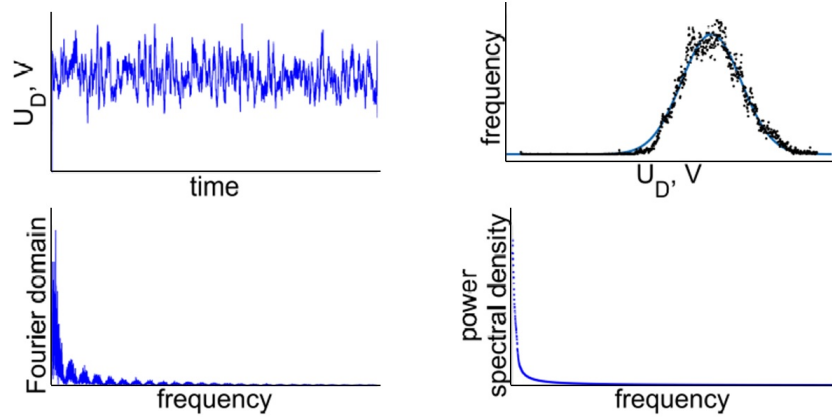


Figure 2.9: Signal at the output of the back-end. The signal $U_D(t)$ in the time domain (left-top) is integrated over some integration time τ . The Fourier domain shows artifacts from the integrator transfer function (left-bottom). Also in this case, the amplitude values follow (approximately see fit) a Gaussian distribution (right-top). The power spectral density shows the additional band limitation by the integrator (right-bottom).

The interesting question now is how the width of this distribution can be quantified. This leads directly to the sensitivity limit/temperature resolution of a THz-imager. The answer to the question how the temperature resolution can be quantified is given by the so called **Radiometer equation** and given in equation (2.6).

$$\Delta T = \frac{T_{sys}}{\sqrt{2 \cdot \Delta\nu \cdot \tau}} \quad (2.6)$$

A motivation for the derivation of equation (2.6) is given in section (A.1). The Radiometer equation provides a limit for the achievable temperature resolution. It can be interpreted straightforwardly. T_{sys} is the noise temperature of the entire system (THz-imager). Equation (2.6) then determines what signal (ΔT) is detectable with 67% certainty when a given system noise temperature T_{sys} , detection bandwidth $\Delta\nu$ and integration time τ are the system parameters.

A descriptive explanation of equation (2.6) is that if $\Delta T/T_{sys}$ is interpreted as the relative standard deviation of the random (Gaussian) variable T , its value is according to statistical theory characterized by $1/\sqrt{N}$ with N , the number of measurements. The number of measurements now is in the case of a passive (THz)-imager given by $\Delta\nu \cdot \tau$, which leads to equation (2.6)¹³. Figure (2.10) illustrates the situation described above.

¹³The factor $\frac{1}{\sqrt{2}}$ is caused by the non-ideal characteristic of the integrator (RC-element)

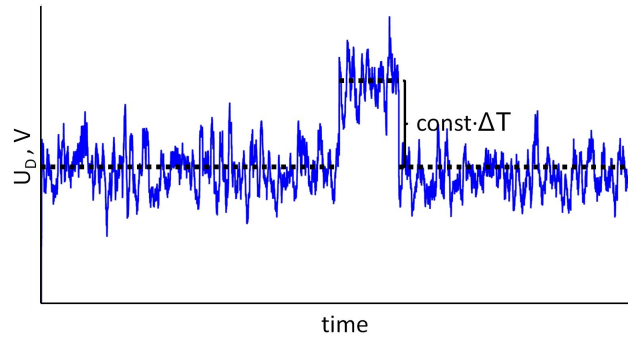


Figure 2.10: Example detection situation described by the Radiometer equation.

Objects in the scene are only detectable if objects in scene cause a shift of the average value that is large enough, in comparison to the system noise fluctuations. The minimal size of the required shift is in turn given by the Radiometer equation. However, as already mentioned, the temperature resolution limit of the Radiometer equation is not achievable due to atmospheric losses, antenna losses and the scanning process etc. The losses due to the atmosphere can not be influenced by the design of the imager. The losses due to the imager antenna (the telescope) and the scanning process itself will be briefly discussed in the next section.

2.3.2 The Scanning Optics – Spatial Resolution

The field-of-view (FoV) of a THz-imager has to be mapped onto the detection system. This is done by the (scanning) optics¹⁴. There are two limit cases to the mapping process depending on the number of detectors in the detection system. The first limit case is given when no scanning is necessary to map the entire FoV. The second when scanning, whether hardware- or software scanning, is necessary to map the FoV. In the first case the detection system consists of multiple detectors. The actual number and placement of these detectors mainly determines the achievable spatial resolution. The second limit case is realized when the detection system consists of only one detector. In this case the achievable spatial resolution depends on the properties of the (scanning) telescope and the pattern that is used to scan the field of view. It should be mentioned that in between these limit cases different combinations of number of detectors and scanning patterns are in use. In this thesis the focus is on the single detector case.

The single detector case is usually named the single-pixel case and it is of such importance because multi-pixel cameras are still an emerging technology in the THz-region and at present not readily available (see e.g. [2]). Also some single-pixel detectors achieve sensitivities that are orders of magnitude superior

¹⁴The scanning optics includes all necessary elements to transform a beam coming from the scene into a beam entering the detection system.

(measured by their noise equivalent power) than multi-pixel cameras¹⁵. The scanning patterns in the single-pixel case also vary between two extreme cases. On one hand there is the raster scan. In this well-known scanning scheme the FoV is overlaid with an rectangular raster of positions and at every raster position the signal from the scene is measured. In this scanning scheme the scanning telescope comes to a complete stop at every position in the raster. This scanning process provides very accurate mapping but it is also very slow. As a compromise between accuracy and speed, measurements can be taken "on the fly". In this mode of the raster scan the scanner/scanning telescope only comes to a full stop at the end of the zig-zag pattern. The raster scan motion with the two mentioned modi is illustrated in figure (2.11).

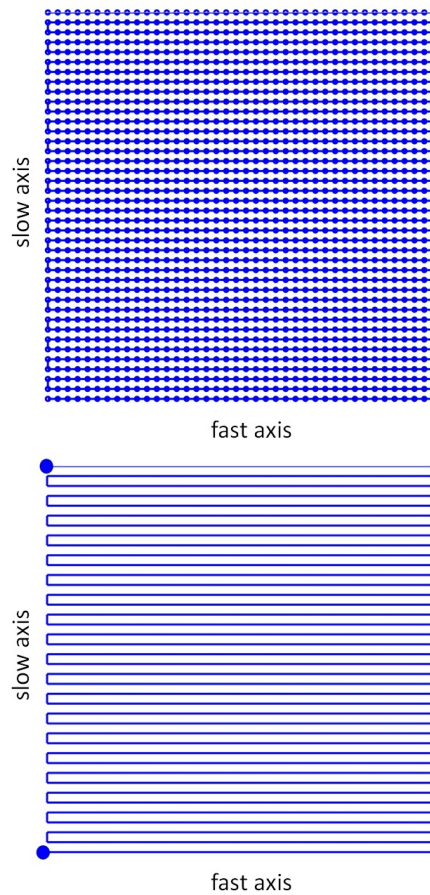


Figure 2.11: Scan patterns of a simple raster scan (top) and an "on the fly" raster scan (bottom). Stops during the scan are indicated as circles. The asymmetric axes are labeled fast respective slow axis depending on the movement along each axis in the scanning pattern.

¹⁵This advantage in sensitivity makes the single-pixel approach significant even for future developments when THz multi-pixel cameras will reach maturity.

Then, on the other hand, for a large FoV of a few square meters raster-scanning even in "on the fly" mode is still too slow. For these cases, a scanning motion that comes to a complete stop only at the beginning and at the end of the scanning process and also minimizes the slowing due to changes in direction is used. An efficient way to cover a large FoV in this way is a spiral motion. This in turn limits the FoV to a circular area. Other scanning motions exist which lead to different area shapes for the FoV and also different deviations from the ideal mapping (aberrations). Here, we limit the discussion to the spiral scanning motion and briefly discuss what aberrations develop because of the scanning process.

Many different spiral forms exist, like Euler's spiral, Fermat's spiral, logarithmic spiral, etc. For the discussion here, only the simplest form, the so called Archimedean-spiral, is of interest. The fundamental equation that describes an Archimedean-spiral in polar coordinates is given by equation (2.7).

$$r = \alpha + \beta \cdot \theta \quad (2.7)$$

Here, r denotes the radius of the spiral and θ denotes the polar angle in the scanning plane. α, β are constants that directly link the radius to the polar angle, which causes the radius to increase linearly with θ . This in turn has major implications for the mapping process. Depending on the scanning velocity ω , which is introduced here as an angular velocity ($\theta = \omega \cdot t$), the mapping of the FoV is not temporally equidistant. What this means is shown in figure (2.12).

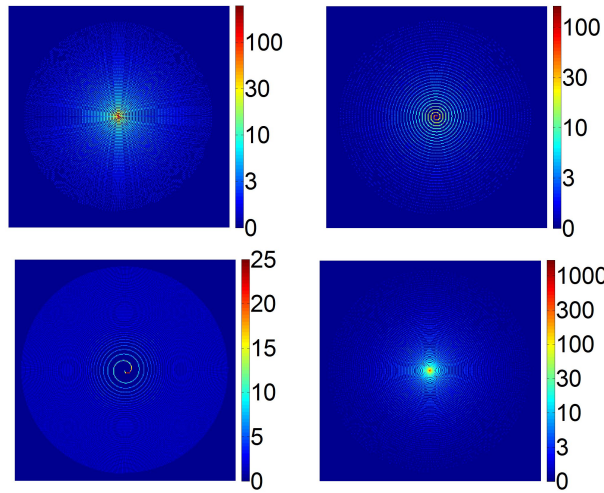


Figure 2.12: Different scanning patterns and the resulting sampling of the FoV. Depending on the chosen pixel size, certain pixels are sampled multiple times. The number of times a specific pixel is sampled is indicated in the images with a respective color code. The top row shows two different scanning schemes of an Archimedean-spiral with constant angular velocity ω , which is identical to a linearly increasing β . Top-left with β_a and top-right with $\beta_b = 2 \cdot \beta_a$. The bottom row shows the results of a non-constant β . Bottom-left $\beta \cdot \theta = \omega \cdot \sqrt{t}$ and bottom right $\beta \cdot \theta = \omega \cdot t^2$.

In figure (2.12), different scanning situations are shown. In the top row different scanning patterns with constant angular velocity ω are depicted. This is equivalent with β increasing linearly. In the bottom row ω is still constant but β is not linear anymore. The effect on r is shown in figure (2.13).

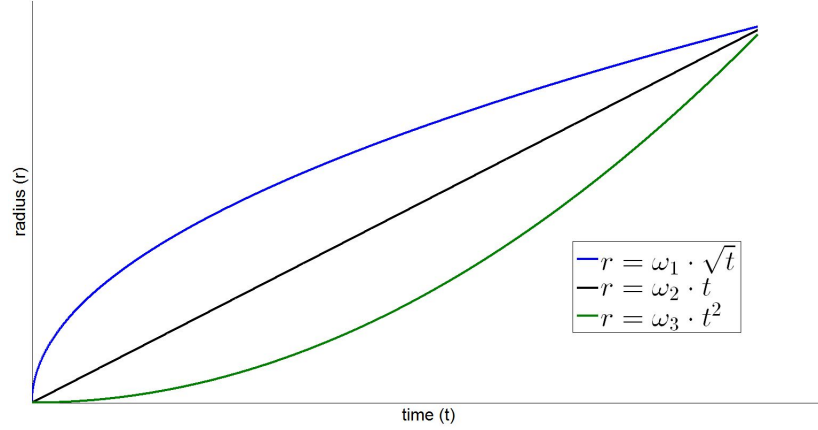


Figure 2.13: Change of the radius (r) for different choices of β .

The choice for β directly affects the number of traces that cover the FoV. The number of traces in turn is directly connected to the amount of undersampling that is incurred during image acquisition (see figure (2.12) again)¹⁶. The term undersampling, as it is introduced here, means the area that is covered during image acquisition. When this area is smaller as the nominal FoV undersampling occurs¹⁷. Details on the coverage of the FoV, the generated beam size by the telescope and a few other important telescope properties will be briefly discussed now. Details on the connection between beam size and the optimal size for a digital pixel¹⁸ are also discussed in section (4.2).

The choice of a telescope design is motivated by many reasons. There is the optical mapping quality (distortions, aberrations), light (THz) collecting power, on-axis or off-axis design, etc. Telescopes have been in use in the visible part of the spectrum for centuries. As discussed earlier, the properties and materials used for refractive optical elements are different in the THz- and VIS-region. However, since metallic objects have an index of reflection of almost unity in both regions, telescope designs based on reflective elements are very similar in the VIS- and THz-region. Only the size has to be adapted in order to compensate for the much larger wavelength in the THz-region (to avoid diffraction effects). Possible telescope designs include Cassegrain- and Cassegrain-type¹⁹ designs, Gregorian-designs, Schmidt-designs, etc. Every

¹⁶The choice for β also directly affects the number of pixels in the generated THz-images. For the generation of every image pixel a specific interval of the acquisition time is used. This time is called time-per-pixel and plays an important role throughout this text.

¹⁷A detailed discussion on this subject can be found in section (4.2)

¹⁸This topic is also closely related to the optimal choice of the parameters α , β and ω .

¹⁹The main feature that distinguishes a Cassegrain telescope from a Cassegrain-type telescope are the shapes of the primary and secondary mirror, which deviate from the classical Cassegrain

telescope design has advantages as well as disadvantages. The best telescope design does not exist. Here, we focus on the Cassegrain-(type) design. Maybe one of the most appealing reasons why to focus on this design is that it is an on-axis design²⁰. The on-axis property makes handling this telescope type a lot easier allowing for a better optical alignment. A large center bore allows for the on-axis property and it is an identifying feature of a Cassegrain/Cassegrain-type telescope design. It is also the main drawback of all Cassegrain-type telescopes because it introduces a central blockage in the optical path. Figure (2.14) shows the schematic setup of a classic Cassegrain telescope.

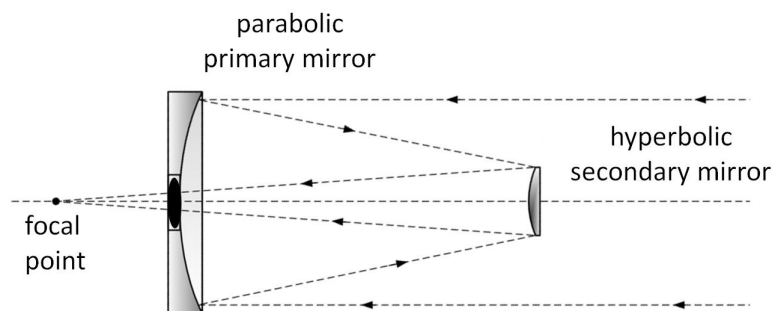


Figure 2.14: Schematic diagram of a classical Cassegrain telescope. Its identifying feature is a center bore, which is also present in Cassegrain-type designs. The main difference between Cassegrain and Cassegrain-type designs is the shape of their respective primary and secondary mirrors.

The FoV is (in the hardware scanning mode) scanned by rotating and tilting the secondary mirror of the Cassegrain-type telescope. This motion introduces image artifacts because of the changing conditions during the imaging process. A few affected figures of merit are given in the list below. These important telescope properties and their changing values during the imaging process have to be considered:

- aperture efficiency
- directivity
- radiation pattern (side lobes)
- edge taper/spill over/central blockage

The details on these figures of merit are a subject of antenna/telescope theory and are here not given. However, their influence and connection to the imaging

design for Cassegrain-type designs (see figure (2.14)).

²⁰Off-axis Cassegrain designs exist as well under the name Schiefspiegler. But these Schiefspiegler designs are very uncommon and use tilted mirrors to deviate the optical path away from the optical axis (avoid shadow casting by the secondary mirror). Here, we treat the Cassegrain-(type) telescope as on-axis design and pay no regard to the uncommon Schiefspiegler.

process shall be briefly discussed.

The aperture efficiency describes the fraction of the power that is collected by the antenna aperture compared to the power collected by a perfect antenna having the same physical size. It, therefore, has a direct relation to the SNR during the imaging process. The directivity and radiation pattern are in turn directly connected to the image quality. A low directivity, respectively a radiation pattern having considerable side lobes, also produces considerable image artifacts [14]. The change of the radiation pattern during the imaging process results in beams with ever increasing side lobes while approaching the rim in the FoV. The last figure of merit describes the influence of the finite antenna size on the performance of the telescope. The concepts of edge taper, spill over and the influence of the central blockage are schematically depicted in figure (2.15).

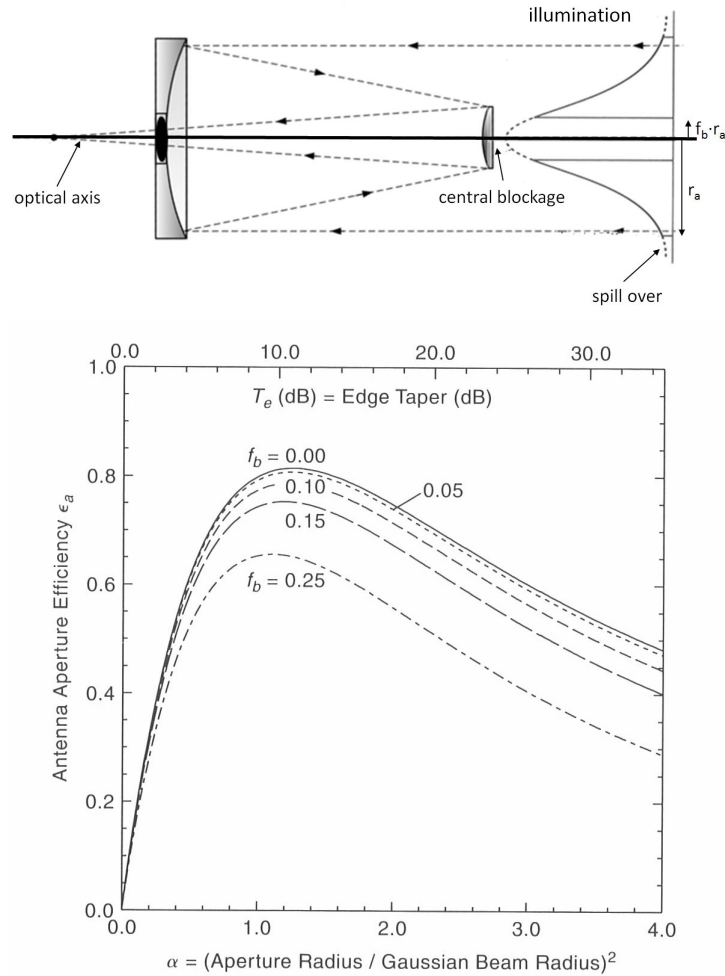


Figure 2.15: Changing aperture efficiency depending on the choice for the size of the central blockage. Drawings taken from [4].

As figure (2.15) shows, there is an optimal choice for the geometric telescope parameters (e.g. f_b the fraction of the primary mirror with radius r_a , which is blocked by the central blockage) as far as aperture efficiency is concerned. A derived figure of merit from this choice is the edge taper. It gives the relative power density at the radius r_e and is given by equation (2.8).

$$T_e(r_e) = -2 \cdot \exp \frac{r_e^2}{\omega_a^2} \quad (2.8)$$

In equation (2.8), ω_a describes the beam radius at the aperture plane. The edge taper, the aperture efficiency and the spill over are, therefore, directly connected figures of merit and can not be optimized separately as is visible in figure (2.15).

In summary, a Cassegrain-type telescope can be used as on-axis optics. Hence the detection system can be placed on the optical axis (at the focus point) and therefore no grazing of incoming or outgoing radiation is incurred. The on-axis property allows for very compact imager designs, a better and easier alignment as well as less optical aberrations [15]. These advantages of a Cassegrain-type design do not come without a price, the central blockage. A considerable amount of radiation is blocked by it reducing the aperture efficiency. The details on how much power is lost because of it depend on the exact geometry of the primary and secondary mirror of the Cassegrain-type design and the mode the imager is operated in (details can be found in [4] pp. 130-133). For the imaging task that is of interest here, the advantages outweigh the disadvantages and therefore a Cassegrain-type telescope was chosen as telescope for the ISM-imager²¹. Following the path of the radiation, the telescope now determines the position of the scene. This will be briefly discussed in the next section.

2.3.3 The scene

As already mentioned, the properties of the telescope determine the properties of the scene. The term scene is somewhat vague, so this section should start out with a definition. The word literally means something seen by a viewer, a view or prospect²². In the context of THz-imagers it means a scene is a view seen (imaged) by a THz-imager. To be a little more rigid with the term, the definition of the optimal scene shall also contain properties of the imager. Since the spatial resolution that can be achieved depends on the distance to the imager, the optimal scene is defined to be the view with the optical axis in the middle of the optimal scene and at a distance where the best spatial resolution can be achieved (distance of the beam waist). The border of the optimal scene in the plane at the waist distance away from the imager is then given by the field-of-view of the imager. Figure (2.16) illustrates the aforementioned situation.

²¹The particularities of the ISM-imager telescope will be discussed in section (5.2).

²²Cited after THE FREE DICTIONARY (<http://www.thefreedictionary.com>).

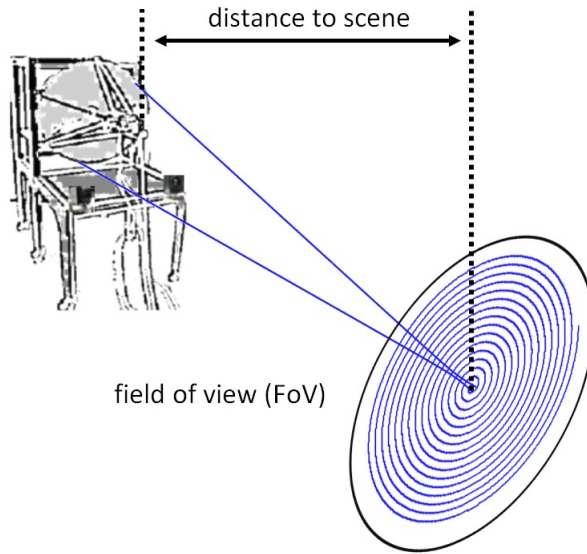


Figure 2.16: Illustration of the (optimal) scene.

With the definition of the scene, the reversed path of the radiation has reached the source of the radiation. As discussed earlier, in passive mode objects in the scene emit THz-radiation or reflect/scatter it from natural sources. The general behavior of THz-imagers in active mode is similar to the situation described in section (2.3). The differences between the two modi will be briefly discussed in the next section.

2.4 The active imaging modality

The difference between the active and passive imaging modality is the introduction of artificial sources (one or more) into the imaging setting. The block diagram of figure (2.6) remains (almost) unchanged. However, the radiation from artificial sources has certain distinctions from natural radiation that are pertinent for the understanding of this imaging modality. It was already discussed that due to the artificial illumination the SNR is no longer limited, like in the passive mode. Unlike illumination from the sun/sky most artificial sources are a very directional means of illumination, introducing a dependence on the specific illumination scenario. The artificial radiation is often highly polarized radiation and because of its coherence property (the coherence length spans several meters), Speckle and standing wave phenomena are prone to arise. A few of the aforementioned peculiarities will be briefly discussed in this section.

2.4.1 Frequency Modulated Continuous Wave THz-Imaging

The technique of Frequency Modulated Continuous Wave (FMCW) THz-imaging is used to combat some of the issues the active imaging modality is faced with. FMCW provides range resolution and this enables it to acquire

pseudo-3D (2.5D) THz-imagery. With the additional range information problems like multipath propagation, standing waves and Speckle-effects, etc. can be reduced. The technique itself relies on the variation of the CW illumination. The resulting frequency difference to the received signal, due to the path the emitted radiation has traveled before being scattered back to the receiver (different illumination scenarios might be useful, see next section), provides the aforementioned range resolution. A block diagram of a possible FMCW setup is shown in figure (2.17).

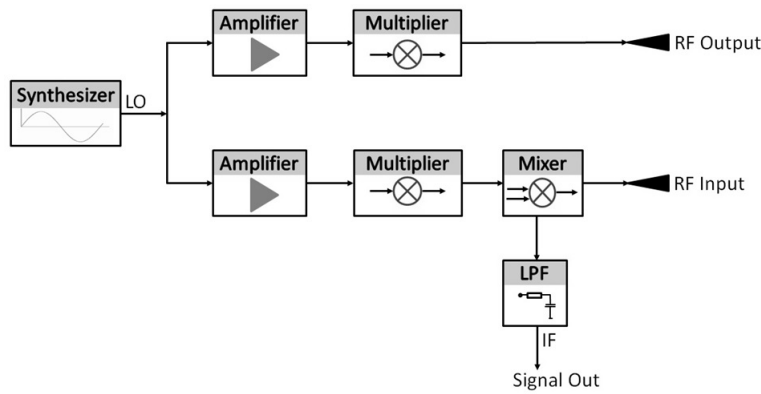


Figure 2.17: Schematic block diagram of a version of homodyne frequency modulated continuous wave radar (FMCW-radar).

Figure (2.17) shows a version of a FMCW-radar implementation called homodyne FMCW-radar. Homodyne²³ refers to the fact that the signal to be detected and the local oscillator (LO) signal originate from the same source. This assures a phase-locking between the signal and the LO-frequency. In the block diagram the synthesizer signal is amplified and its frequency is multiplied to the appropriate range. The detection is achieved by mixing the signal coming from the scene with the LO-signal. The frequency at the synthesizer is modulated using, e.g., a sawtooth pattern. A path difference arises because the signal from the scene has to travel from the imager to the scene and back. The two signals at the mixer (the LO-signal and the signal from the scene) have different frequencies and the signal after the mixing and low-pass filtering (LPF) contains range information encoded in its frequency. For more details on the FMCW-technique see e.g. [7]. In short the FMCW-technique acts as a spatial filter, filtering out unwanted radiation that is distinguishable from wanted radiation due to its time of flight. With this technique, even cross-talk between receiver (Rx) and transmitter (Tx) is distinguishable. Although FMCW addresses many issues in active imaging, it is not the solution to all. One problem still remaining is the very directional illumination in this modality, which is discussed now²⁴.

²³Homodyne derived from homo = same and dyne = power.

²⁴Although FMCW-imaging could not be used as an imaging technique in this thesis, many of the problems encountered during the PHD-time can be ameliorated with this technique. It is this author's opinion, that the use of the FMCW-technique in combination with some of the novel techniques presented in this thesis could contribute to the advancement of THz-imaging.

2.4.2 Illumination scenarios

In passive mode the radiation emitted by objects in the scene itself or the reflection of radiation coming from the sun/sky is the source of the detected signals. This in turn produces images that appear to have a smooth contrast change over the entire image. However, with artificial illumination the origin of the radiation is mostly a compact and small source (or sources). This in turn means that the radiation often comes from a distinct direction. This produces contrast jumps in images and Speckle effects, which are regions in the image with very high contrast in regard to surrounding image regions (see e.g. figure (2.18)). To be more exact, the Speckle phenomenon arises because of the coherent nature of artificial THz sources in combination with the high directivity and the large wavelength when compared to the encountered surface roughness. For details on the phenomenon of Speckle in THz-imaging see, e.g., [10] and for mm-wave imaging see, e.g., [6].

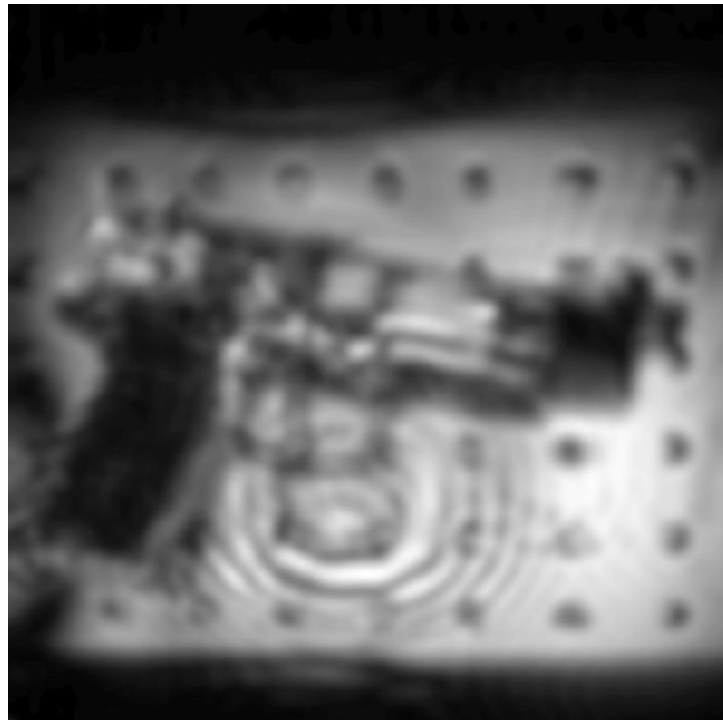


Figure 2.18: Example active THz-image exhibiting Speckle and rapid contrast changes. Image taken from [11].

A way to combat such effects is to choose more elaborate illumination scenarios²⁵.

²⁵Also, the portion of radiation that is scattered back and can be detected by the receiver depends on the scattering material and the angles (incident, outgoing) involved. Details are studied in the framework of the bidirectional reflectance distribution function (BRDF). An introduction to the subject can be found in [13].

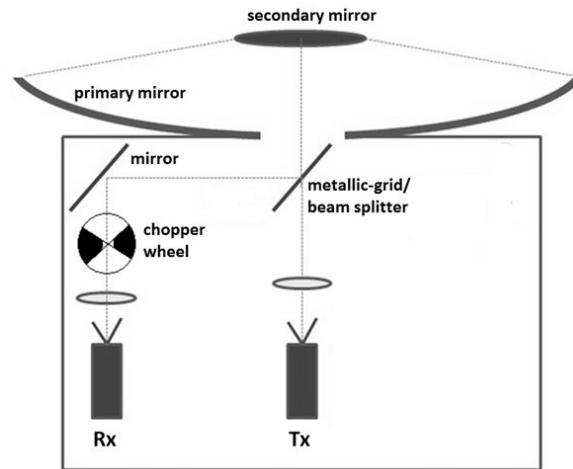


Figure 2.19: Implementation example of a single source on-axis illumination using a Cassegrain-(type) telescope. The chopper wheel in the image hints to the use of Lock-in detection but is not essential for a single source illumination scenario.

Better illumination scenarios would be the illumination with multiple sources or the illumination with an incoherent source. The goal is to mimic the illumination by the sun/sky. Here, one problem is that at present powerful, incoherent sources do not exist in the THz-region. Also, due to the fact that the scattering of THz-radiation from directional, artificial sources in the atmosphere is by far not as efficient as for THz-radiation coming from the sun, the radiation from artificial sources would still retain a strong directional characteristic.

A possible solution would be the usage of a Decoherencer (a diffuser deliberately destroying the coherence of the radiation), one implementation example of a SLM. A Decoherencer is a device that uses reflection/scattering of rough surfaces to destroy the phase relationship between neighboring wave trains (for an example see [10]). Such technology/devices are not commercially available at the moment and only exist as lab prototypes. In the process of randomizing the phase relationship the polarization of the radiation is also destroyed, which also has beneficial effects for the imaging process as discussed in the next section.

2.4.3 The effects of polarization

The polarization of the radiation used for THz-imaging is of such importance because many optical components have an effect on it. Also, in a distributed THz-system radiation is, if not transmitted via free-space, transferred using waveguides and emitted into free-space using antennae. As is known from the theory of waveguides and antennae, waveguides as well as antennae have a strong dependency on the polarization. The situation becomes especially complicated when mechanical scanning using reflective elements (see again the section on the Scanning Optics (2.3.2)) is involved. Since, even simple reflective elements (mirrors) rotate the polarization vector (see figure (2.20) for

an example, reproduced after [3]). The details of the rotation of polarization, involving (three) metallic mirrors are discussed in [12] and reference given therein.

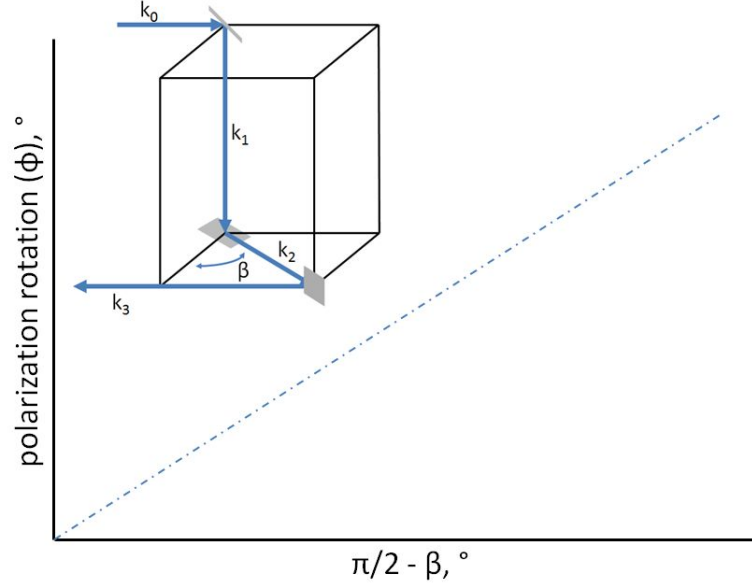


Figure 2.20: Example for a metallic three mirror polarization rotator reproduced after [3].

Also, since THz-beams tend to be rather large, they can not be treated as rays and have a varying state of polarization over their diameter. This makes processing and accurate detection of THz-beams a challenge. To compensate for the changing state of polarization, at least two possibilities exist. The changing state of polarization can be measured and the measured change then used as input for calibration procedures. The second approach would be the use of a Faraday rotator [9]. It can be used to reverse the rotation of the polarization vector. The particularities when dealing with polarization in a THz-system are rather complicated and shall here not be discussed further. However, without consideration and compensation of the polarization rotation, no accurate THz-image acquisition is possible. This in turn means that the (almost) unpolarized nature of radiation encountered in the passive mode is an advantage for this imaging modality. This makes the passive imaging modality very well-suited for the testing of new imaging techniques, without interference from polarization effects. Since, many of the novel techniques presented in this thesis involve at least three reflections (mirrors) using the ISM-imager, the main part of this thesis deals with the passive imaging modality. However, a few experiments also demonstrate the effects of the rotation of polarization just discussed, for the special case of the ISM-imager.

After the theoretical basics of the hardware scanning approach were discussed in the previous sections, the last section of this chapter briefly introduces the concept of software scanning.

2.5 Software scanning

To summarize the concepts introduced so far, the hardware scanning approach seems unlikely (in this author's opinion) to offer a solution for the imaging task introduced in section (1.1) and illustrated in figure (1.1). The hardware scanning approach is too slow, bulky and costly (because of the scanning telescope). In addition, it only offers a narrow depth of focus for spatial resolutions below 1 cm. The software scanning approach now offers the possibility to scan a scene of interest without movement of any mechanical elements. This offers tremendous opportunities. As discussed in this chapter, without having to move mechanical parts, the imaging process is potentially faster and the needed telescope is cheaper to manufacture. Also, the software scanning approach would allow for an easier processing of the radiation's polarization. A possible software scanning design is shown in figure (2.21).

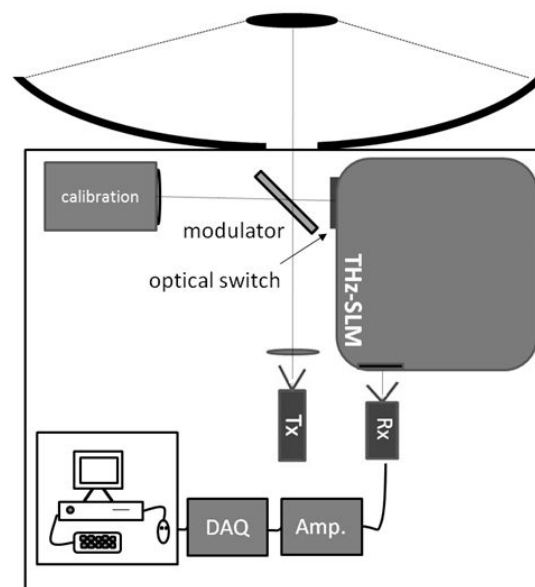


Figure 2.21: Possible software scanning design for the passive and the active imaging modality

The most critical design-component is a THz spatial light modulator (THz-SLM). Only with such devices (see again section 1.3) software scanning is possible. At present, such designs are emerging for the THz-region. In this author's opinion, software scanning designs offer a possible solution for the imaging task introduced in section (1.1) and illustrated in figure (1.1). In combination with the young and fast developing theoretical framework of Compressed Sensing (CS), it seems possible that a solution to the imaging task of section (1.1) and figure (1.1) can be found. The introduction to the necessary CS-basics as well as the theoretical fundamentals on the combination of CS using THz-SLMs (including details on the design presented in figure (2.21)) will be given in the next chapter.

References Chapter 2

- [1] R. Appleby and H. B. Wallace, "Standoff detection of weapons and contraband in the 100 ghz to 1 thz region," *IEEE Transactions on Antennas and Propagation*, vol. 55, no. 11, pp. 2944–2956, 2007.
- [2] M. Bauer, S. Boppel, A. Lisauskas, V. Krozer, and H. G. Roskos, "Real-time cmos terahertz camera employing plane-to-plane imaging with a focal-plane array of field-effect transistors," in *Infrared, Millimeter, and Terahertz Waves (IRMMW-THz), 2013 38th International Conference on*, 2013, pp. 1–2.
- [3] E. J. Galvez and P. M. Koch, "Use of four mirrors to rotate linear polarization but preserve input output collinearity. ii," *Journal of the Optical Society of America A*, vol. 14, no. 12, p. 3410, 1997.
- [4] P. F. Goldsmith, *Quasioptical systems: Gaussian beam quasioptical propagation and applications*, ser. IEEE Press/Chapman & Hall Publishers series on microwave technology and RF. Piscataway and NJ: IEEE Press, 1998.
- [5] O. Hachenberg and B. Vowinkel, *Technische Grundlagen der Radioastronomie*. Mannheim [u.a.]: Bibliogr. Inst., 1982.
- [6] I. Jaeger, J. Stiens, L. Zhang, S. Islam, G. Koers, and R. Vounckx, "Comparison of speckle reduction diversity tools for active millimeter-wave imaging," *Journal of the Optical Society of America A*, vol. 25, no. 7, p. 1716, 2008.
- [7] B. Kapilevich, Y. Pinhasi, R. Arusi, M. Anisimov, D. Hardon, B. Litvak, and Y. Wool, "330 ghz fmcw image sensor for homeland security applications," *Journal of Infrared, Millimeter, and Terahertz Waves*, vol. 31, no. 11, pp. 1370–1381, 2010.
- [8] D. H. Martin and J. W. Bowen, "Long-wave optics," *IEEE Transactions on Microwave Theory and Techniques*, vol. 41, no. 10, pp. 1676–1690, 1993.
- [9] M. Martinelli, "A universal compensator for polarization changes induced by birefringence on a retracing beam," *Optics Communications*, vol. 72, no. 6, pp. 341–344, 1989.

- [10] D. T. Petkie, "Multimode illumination in the terahertz for elimination of target orientation requirements and minimization of coherent effects in active imaging systems," *Optical Engineering*, vol. 51, no. 9, p. 091604, 2012.
- [11] D. T. Petkie, F. C. d. Lucia, C. Castro, P. Helminger, E. L. Jacobs, S. K. Moyer, S. Murrill, C. Halford, S. Griffin, and C. Franck, "Active and passive millimeter and sub-millimeter-wave imaging," in *European Symposium on Optics and Photonics for Defence and Security*, ser. SPIE Proceedings. SPIE, 2005, pp. 598 918–598 918–8.
- [12] L. L. Smith and P. M. Koch, "Use of four mirrors to rotate linear polarization but preserve input–output collinearity," *Journal of the Optical Society of America A*, vol. 13, no. 10, p. 2102, 1996.
- [13] J. C. Stover, *Optical scattering: Measurement and analysis*, 3rd ed., ser. SPIE Press monograph. Bellingham and Wash. (1000 20th St. Bellingham WA 98225-6705 USA): SPIE, 2012, vol. PM224.
- [14] J. Tsao and B. D. Steinberg, "Reduction of sidelobe and speckle artifacts in microwave imaging: the clean technique," *IEEE Transactions on Antennas and Propagation*, vol. 36, no. 4, pp. 543–556, 1988.
- [15] R. N. Wilson, *Reflecting telescope optics*. Berlin and London: Springer, 1996.

Theoretical Basics of Compressed Sensing

Contents

3.1	Introducing Compressed Sensing for THz-imaging	59
3.2	Compressed Sensing Dictionaries for THz-Imaging	64
3.3	The pros and cons of a specific Φ	67
3.4	Compressed Sensing Reconstruction Algorithms	70
3.4.1	Orthogonal Matching Pursuit (OMP) - Greedy algorithms	72
3.4.2	Basis Pursuit (BP) - l_1 - algorithms	73
3.4.3	Specialized THz-reconstruction algorithms	74
3.5	Compressed Sensing and Single-Pixel THz-Imaging	74
3.5.1	THz-Spatial Light Modulators	77
3.6	Compressed Sensing for improved image Reconstruction of THz-images	79

This chapter presents the necessary theoretical basics of Compressed Sensing (CS). It explains the idea behind this new data acquisition paradigm and discusses the key concepts involved. The first section gives a mathematical introduction of CS and examines the conditions for its beneficial application. The second section discusses dictionaries. The dictionary is an essential CS-concept and the choice of a dictionary influences the performance of a CS-based software scanning scheme. Another important CS-concept is discussed in section three, the reconstruction algorithms. Different approaches are introduced and examined using several performance indicators. Section four gives an overview of the state-of-the-art in single-pixel imaging and discusses the merits it especially offers for THz-imaging. The last section of this chapter discusses the potential of CS as a means for the detection of image features from a reduced set of measurements. This is connected to the concepts of image reconstruction as will be discussed in this section.

3.1 Introducing Compressed Sensing for THz-imaging

Compressed Sensing or Compressive Sampling or Compressed Sampling is a new way to acquire digital data. In the context of this text, CS can also be thought of as a special, very efficient form of software scanning. In this, the CS-paradigm refers to a compressive data acquisition scheme that explicitly exploits the intrinsic structure of signals, in a non-adaptive fashion. CS is applicable in the active as well as the passive imaging modality. It is chosen to introduce it in an active imaging modality, in transmission geometry. The extension to a reflection geometry and a passive imaging modality is straightforward and discussed later in the text.

A schematic implementation of a CS scheme in active mode with a transmission geometry is shown in figure (3.1).

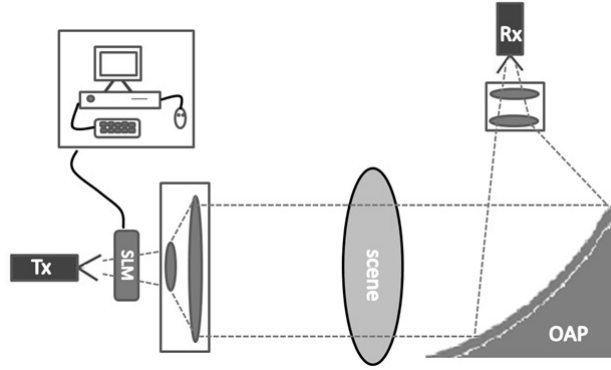


Figure 3.1: Schematic CS setting in active mode and transmission geometry.

One important feature of the imaging setting of figure (3.1) is that the THz-radiation source (Tx) illuminates the entire scene (\vec{x}) with a parallel beam during the measurement time¹. The illumination is spatially modulated using a THz-SLM and for each discrete modulation a measurement (y_i) of the transmitted radiation is taken. For the optical components diffractive as well as refractive elements can be used. The transmission setup of figure (3.1) employs a separate telescope for the illumination of the scene and for the collection of the radiation that passes through the scene. The imaging process in the CS-setting of figure (3.1) can be described in mathematical form by equation (3.1).

$$\vec{y} = \Phi \cdot \vec{x} \quad (3.1)$$

In equation (3.1), Φ describes the spatial modulation in the illumination of the Tx by the THz-SLM². Each row of Φ is denoted ϕ_i and is given by a different discrete modulation pattern, also called a mask. The masks can be easily

¹The scene is mapped onto a rectangular matrix, which is then serialized into a vector representation, to make the equations easier readable.

²In subsequent sections, it will be discussed that Φ actually contains information on the entire imaging setup.

visualized by transforming the row-vectors ϕ_i into matrices using a suitable reshape procedure³. One example is shown in figure (3.2).

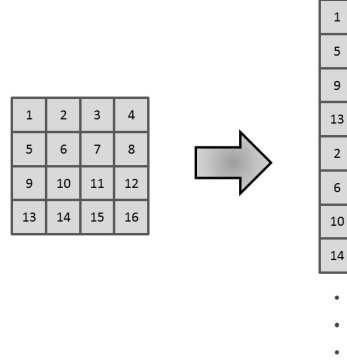


Figure 3.2: Reshape procedure to visualize the relationship between masks (a matrix representation of ϕ_i) and ϕ_i the row vectors of Φ .

Φ , seen as modulation matrix, contains all aspects of the illumination, including the quality of the optical mapping. Due to different effects, deviations from the theoretical modulation arise and must be taken into account. An important feature of the CS-approach is that these deviations can even be beneficial to the imaging performance, as long as the deviations are known⁴. This somewhat counter intuitive fact stems from an underlying fundamental concept of CS, the *incoherence* property. Different names for this property exist like coherence, mutual-coherence, incoherence, etc. Essentially incoherence is a measure of correlation between two basis. The basis Φ used to measure the signal and the basis Ψ in which the signal representation is most dense. That means that Φ describes the properties of the measurement process itself and the other basis, Ψ , describes properties of the signal⁵. In a CS-approach both views, the signal view and the measurement system view, are intimately connected. A good notion is to think of both bases as the two sides of a coin, you cannot have one without the other. To clarify the meaning of this notion, equation (3.1) is expanded into equation (3.2).

$$\vec{y} = \Phi \cdot \vec{x} = \underbrace{\Phi \cdot \Psi}_A \cdot \vec{\alpha} \quad (3.2)$$

As can be seen from equation (3.2), the extension of equation (3.1) introduced the expansion of the signal \vec{x} in an alternate domain. The expansion coefficients are named $\vec{\alpha}$. As mentioned before, in the basis Ψ the signal \vec{x} has a very dense

³The reshape procedure is determined by the size of the scene. One example procedure would be to build the matrix by dividing ϕ_i in sections the width of the scene and then adding them column by column until the matrix is formed (MATLAB reshape procedure).

⁴Even the introduction of pseudo-randomness via the just presented reshape-procedure might be beneficial for the CS-reconstruction.

⁵The basis property for Φ, Ψ is not a necessary condition. A relaxed condition would be to choose Φ, Ψ as mathematical frames.

representation, meaning \vec{a} has only a few significant entries. Both views, the signal view as well as the measurement view will be discussed in detail in the following sections. A CS-based imaging approach now achieves good performance when the two bases involved exhibit low correlation, when they are incoherent. The incoherence between the two bases Φ and Ψ is measured using the definition of equation (3.3).

$$\mu(\Phi, \Psi) = \sqrt{n} \cdot \max_{k,l} |\langle \phi_k, \psi_l \rangle| \quad (3.3)$$

In the definition of equation (3.3) n denotes the dimensionality of the vector space that is spanned by the basis vectors and the indicis k, l denote the elements of Φ and Ψ respectively. This means that the incoherence measures the similarity of the basis Φ to the basis Ψ . The similarity is quantified with the scalar product of the pair of basis vectors that exhibits the maximum correlation between each other. It can be shown that $\mu(\Phi, \Psi) \in [1, \sqrt{n}]$. A small μ means that the two bases Φ and Ψ are very dissimilar, which supports the performance of a CS measurement. Performance in this context means on one hand that it is possible to acquire the whole signal (an image in the context considered here) with less measurements, with the same resolution as if the signal would be acquired with the Nyquist-rate. On the other hand, with a CS-approach it is also possible to acquire a signal with the Nyquist-rate achieving a higher resolution compared to Nyquist sampling⁶. As mentioned before, for a good performance of a CS-approach a low $\mu(\Phi, \Psi)$ value is one prerequisite. To get a grasp of incoherence, a few examples are helpful. Let us consider for Φ the spike basis/pixel basis, $\phi_{m,n}(x, y) = \delta(x - m, y - n)$ and for Ψ the Fourier basis, $\psi_{o,p} = \frac{1}{\sqrt{n}} e^{j2\pi o \cdot x/n} \cdot e^{j2\pi p \cdot y/n}$. This bases pair has an incoherence value $\mu(\Phi, \Psi)$ of 1. This example pair is encountered in a classical Nyquist sampling situation. Another example would be to chose Ψ from a wavelet family and Φ from the noiselet family. This pair is quite interesting because noiselets have many favorable properties for SLM-based imaging e.g. pseudo-randomness and they exhibit a low $\mu(\Phi, \Psi)$ value with many different wavelet families.

The details on the incoherence property, its benefits for a CS measurement approach and the connection to the measurement matrix Φ will be discussed in the next section. Before these particularities are discussed another important CS-concept shall be introduced, the notion of sparsity. As already mentioned above, sparsity is an inherent property of the signal \vec{x} ("the other side of the coin"). The sparsity gives the number of non-zero elements in a signal of length n . Mathematically speaking, sparsity is defined using definition (3.4).

$$S_{\vec{x}}^{\Psi} = S = \|\vec{x}\|_0 \quad (3.4)$$

The symbol $\|\cdot\|_0$ characterizes the l_0 -Norm, which counts the number of non-zero elements. The superscript in definition (3.4) refers to the fact that the

⁶Nyquist sampling refers to the classical sampling approach where a signal is sampled uniformly with a sampling rate that is at least twice as high as the largest frequency in the signal (band limited signals). If the signal of interest is not band limited (like natural pictures) an anti-aliasing filter must be introduced prior to the acquisition (artificial band limitation).

number of non-zero elements depends on the basis Ψ in which the signal \vec{x} is displayed. The importance of sparsity in a CS-framework cannot be overestimated. In one form or another, the signal sparsity limits the achievable performance within a CS-scheme. The discovery of bases which allow for a sparse representation of the signal \vec{x} (sparse domains) is therefore of tremendous importance (see e.g. [37]). Figure (3.3) demonstrates the concept of sparse domains.

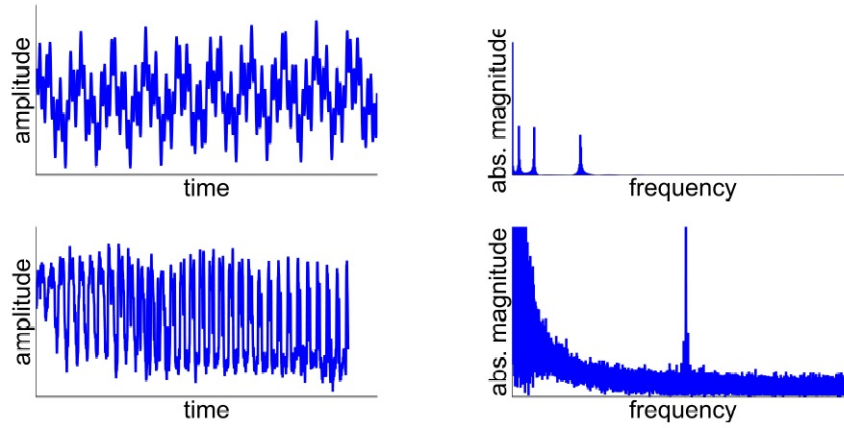


Figure 3.3: Exemplifying sparsity (sparse domains), top row artificial signal spike domain (left) and Fourier domain (right), bottom row measured THz-image signal spike domain (left) and Fourier domain (right).

The artificial signal shown in the top row of figure (3.3) strikingly demonstrates the dependency of the sparsity property on the signal basis. In the spike domain almost all signal values are non-zero values although many small signal values exist. In comparison to the Fourier domain, here, only a few signal components are non-zero and all other components are exactly zero. The bottom row of figure (3.3) demonstrates a problem with the definition in equation (3.4). Real signals never approach exactly zero due to noise and the digital nature of the acquired signals (see the bottom right of figure (3.3), which shows the signal in the bottom left in the Fourier domain).

To adapt equation (3.4) to this property of real signals, thresholding is introduced in the definition. This means that absolute signal values below a chosen fraction of the signal maximum are treated as zero values. The threshold is thereby dependent on the noise level and the acquisition process. Also, by thresholding signal components carrying actual information can be influenced or altered. The direct connection between Φ the measurement basis and Ψ the basis of representation in a CS-scanning scheme allows efficient analog-to-information conversion but also holds the risk of dismissing seemingly unimportant signal components. See figure (3.4) for a demonstration of this fact⁷.

⁷The design of efficient CS-procedures that measure the signal \vec{x} with 100% fidelity is the subject of intense research.

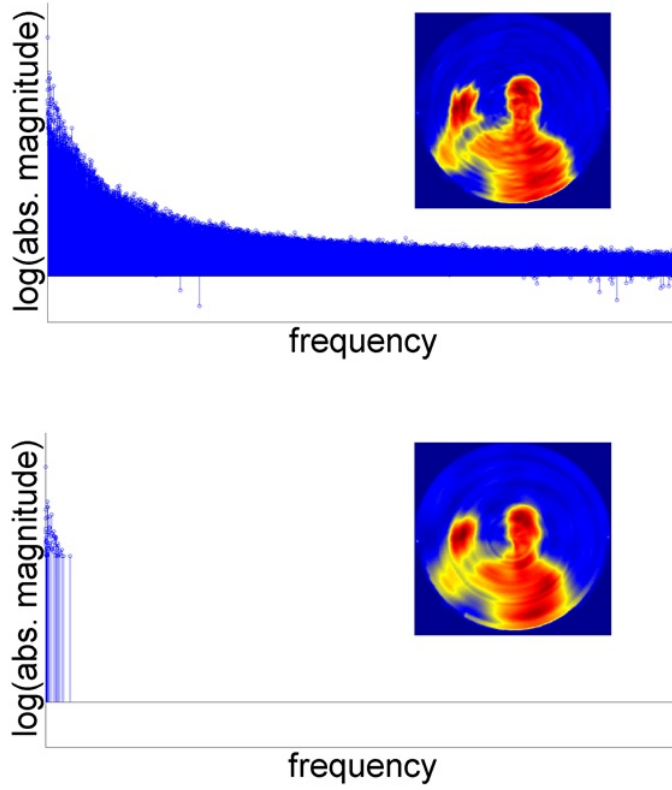


Figure 3.4: Demonstration of the connection between Φ and Ψ and the sensitivity to information loss. THz-image and full Fourier spectrum (Top). Thresholded Fourier spectrum and resulting THz-image (bottom).

Shown in figure (3.4) are two versions of the same THz-image. The original image with its full Fourier-spectrum is shown in the top half of figure (3.4). As can be seen on the logarithmically-scaled spectrum, in the Fourier domain the signal \vec{x} is not sparse (no zero components). When thresholding is performed on the signal spectrum the signal is artificially sparsified. This is shown in the bottom half of figure (3.4). As can be seen there, the image is distorted and details are lost. The practice of filtering just described is a common method in digital image processing. The important difference in a CS-setting now is that when the measurement matrix Φ is tuned according to the expected sparsity in the signal \vec{x} , the details visible in the original image will never be measured and cannot be added by signal processing after the measurement. The ability to do signal processing during image acquisition (on the hardware level) is one of the most important advantages of a CS-scanning scheme. What is shown by the example in figure (3.4) is that the choice for Φ and Ψ is crucial and must be carefully analyzed to avoid unnecessary information loss. The details on the

analysis are given in the next section starting with the details about Ψ ⁸.

3.2 Compressed Sensing Dictionaries for THz-Imaging

The assumption made here is that \vec{x} the image/signal in question is essentially sparse in some domain Ψ . That means that \vec{x} can be well-approximated by a small superposition of vectors $\psi_l \in \mathbb{R}^n$ taken from a given finite set $\{\psi_l\}$. This finite set is called a dictionary. The most intuitive domain for the representation of THz-images is the spike domain. A simple example that shall serve as a test image during this section is shown in figure (3.5).



Figure 3.5: Test image with black indicating zero values and white indicating one values.

The image in figure (3.5) is easily interpretable. It can be determined that the sparsity of the test image in the spike domain is $S_{\vec{x}}^{\delta(x,y)} = 95$. Noteworthy is that the test image in the spike domain is binary. There it contains only two values that can be represented using the numbers zero and one and no additional noise components. For THz-imaging applications, applying CS-methods, domains Ψ are of interest that present the THz-image with the highest sparsity possible⁹. To improve the sparsity, it seems reasonable to try (again) a Fourier transform-based dictionary first. The transformed test image (MATLAB fft2-method) is shown in figure (3.6).

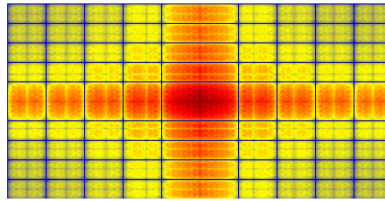


Figure 3.6: Absolute values of the Fourier-transformed test image (MATLAB fft2-method).

⁸One simple way to avoid information loss induced by sparsifying the signal \vec{x} is to incorporate a progressive JPEG-like scheme into the CS algorithm meaning to keep on measuring until the image quality change reveals no further details.

⁹The maximum sparsity is related to the information content of the respective THz-images. The details on this relation will be discussed in the next chapter.

After transforming into the Fourier domain the image data is complex and no longer binary. As a result the sparsity is not increased but reduced. Usually, the Fourier domain is able to give a very descriptive and concise signal representation. As a sparse domain in CS-based THz-imaging it is, in the case of the test image, not a suitable domain¹⁰. However, it is known that natural images can be represented very efficiently in a wavelet basis (see e.g. [34]). The “hunt” for sparse domains is more a question of experience than analytical reasoning. A more scientific approach compared to the heuristic approach just presented is pursued in the sub-field of dictionary learning (see e.g. [37]). For the considerations presented in this text the heuristic approach has to suffice. The considerations on the signal representation in a sparse domain makes a modification of equation (3.1) necessary. The original signal/image \vec{x} is represented in a sparse domain Ψ with coefficients α . This leads to equation (3.2), which is reproduced here for further discussion.

$$\vec{y} = \Phi \cdot \vec{x} = \underbrace{\Phi \cdot \Psi}_A \cdot \vec{\alpha} \quad (3.2)$$

Equation (3.2) is, as mentioned before, the full formalism describing the CS-approach. It describes the inseparable relation between the hardware level represented by Φ and the software level represented by Ψ . The matrix A has to be optimized to achieve the optimal performance with a CS-scanning approach. The CS-approach always works when the sparsity in the signal of interest is sufficiently high. The notion of what is sufficiently high sparsity is clarified by the theorem presented in equation (3.5) (details are discussed in e.g. [9]).

$$\|\vec{\hat{x}} - \vec{x}\|_2 \leq C_0 \cdot \|\vec{x} - \vec{x}_{S_x^\Psi}\|_1 / \sqrt{S_x^\Psi} \quad \text{and} \quad \|\vec{\hat{x}} - \vec{x}\|_1 \leq C_0 \cdot \|\vec{x} - \vec{x}_{S_x^\Psi}\|_1 \quad (3.5)$$

The symbols $\|\cdot\|_1$ and $\|\cdot\|_2$ in equation (3.5) characterize the l_1 -norm and l_2 -norm respectively. \vec{x}_S characterizes a version of the vector \vec{x} with all but the S -largest components set to zero. The conclusions from equation (3.5) are of huge importance. It states that for signals that are really S -sparse (without thresholding) the reconstruction using the measurement procedure following equation (3.2) is 100% exact. This holds true for the case where differences are measured using the l_2 -norm as well as for the l_1 case. The more important conclusion is derived for signals \vec{x} that are not S -sparse. For this case equation (3.5) states that the reconstructed signal $\vec{\hat{x}}$ deviates from the original signal \vec{x} in both norms with an error that is smaller than the difference between the original signal \vec{x} from its S -sparse version \vec{x}_S where all other components than the S -largest components are forced to zero. The astonishing fact in equation (3.5) is that the S -largest signal components do not need to be known in advance and that the bounds of equation (3.5) are deterministic, they involve no probabilities (see [7] p. 6 for a discussion of the implications of equation (3.5)).

To understand the necessary conditions for equation (3.5) to hold true, the

¹⁰One interesting alternative would be to consider sampling in the Fourier domain (Φ) and choose a different Ψ with small coherence ($\mu \approx 1$).

restricted isometry property (RIP) needs to be introduced. The definition of the RIP is given in equation (3.6).

$$(1 - \delta_S) \cdot \|\vec{x}\|_2^2 \leq \|A \cdot \vec{x}\|_2^2 \leq (1 + \delta_S) \cdot \|\vec{x}\|_2^2 \quad (3.6)$$

Equation (3.6) defines the isometry constant δ_S for a measurement matrix A and sparsity S . In that δ_S is the smallest number that satisfies equation (3.6). When equation (3.6) holds, A approximately preserves the Euclidean length of S -sparse signals (cited after [7]). The RIP-constant is encountered in the necessary conditions for equation (3.5). It follows (for details see the discussion in [9] on the RIP) that equation (3.5) holds true if $\delta_{2S} \leq \sqrt{2} - 1$ and the RIP is satisfied for δ_{2S} . At this point an example demonstrating the facts presented in this section should help to clarify the details. For this example consider again the test image (figure (3.5)), which is sampled according to a CS-scheme with reduced number of measurements, as indicated in figure (3.7).

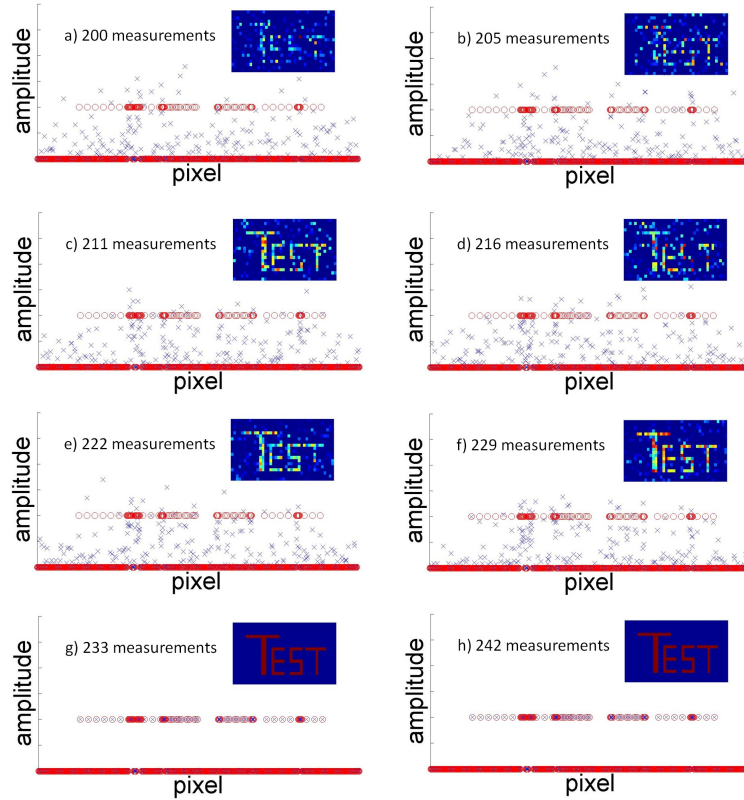


Figure 3.7: CVX reconstructed test image with varying number of measurements. Ψ is chosen as the Fourier domain and Φ is constructed out of random Bernoulli masks.

The example of figure (3.7)¹¹ demonstrates the possibility of recovering a sparse signal from a significantly reduced set of measurements (the test image has 800 pixel and a sparsity of 95). The conditions for a successful recovery are as presented in this section the sparsity of the signal, the incoherence of Φ , Ψ and the RIP property of the measurement matrix. As the example shows, the recovery works with only a fraction of the required measurements of a classical raster scanning approach. However, as is visible in figure (3.7) c) and d), the recovery is influenced by the pseudo-random character of the masks¹². This adds a statistical aspect to the recovery procedure (for details see simulation study below). The example also demonstrates the mutual dependence of Φ , Ψ , RIP and the sparsity. These properties not only determine by how much the number of necessary measurements can be reduced, they also crucially determine all performance aspects of a CS-scanning scheme. For example, it can be shown [7] that the number of necessary measurements m is given by condition (3.7).

$$m \geq C \cdot \mu(\Phi, \Psi)^2 \cdot S_{\vec{x}}^{\Psi} \cdot \log n \quad (3.7)$$

As a rule of thumb, the necessary number of measurements m is approximately $4 \times S_{\vec{x}}^{\Psi}$. This number of measurements is sufficient to recover the signal with overwhelming probability. In a practical situation the influence of the measurement noise level diminishes the reconstruction probability to some extent. Still, for a successful recovery with a high probability of success, it is the first goal to identify the sparse domains in which the signal \vec{x} can be represented by only a few components. After that the incoherence property and the RIP impose some conditions on Φ . However, the degree of freedom in the choice of Φ is still high. The pros and cons of a specific choice are briefly discussed now.

3.3 The pros and cons of a specific Φ

Other than the incoherence condition and the RIP, the choice of Φ is also limited by the measurement process itself. Measurements can only be carried out in the spike-domain or in the Fourier domain. Also, the measurement setup determines whether it is possible to sample the signal in a real-valued or complex-valued manner.

So, the measurement system limits the choice for Φ but the degree of freedom is still high. On the next level it must be chosen if Φ is designed adaptively or non-adaptively to the measurement signal. The initial CS-approach was to sample a signal \vec{x} non-adaptively. In this case the matrix Φ is designed (the matrix entries are chosen) from a random distribution like the Gaussian distribution, the Bernoulli distribution, etc. The non-adaptive sampling with random matrices is a concept that is opposite to the classical Nyquist sampling. The non-adaptive sampling was already illustrated in the brief example of the last section. It used the test image of figure (3.5) and sampled it with pseudo-random Bernoulli masks..

¹¹In the figure it is also noticeable that the reconstruction algorithm recovers values between 0 and 1 although the signal \vec{x} is a binary signal.

¹²Since the RIP of the pseudo-randomly chosen masks is not as good in case d) as in case c), the visible image quality is worse with even more measurements. This is due to the pseudo-random procedure for choosing Φ (see simulation study in the next section for details).

In the test image the sparsity (in the spike-domain) is as mentioned before $S_{\vec{x}}^{\delta(x,y)} = 95$ at a signal length of $\vec{x}_{testimage} = 800$. At this point it is worth noting that although the spike-domain is, for the test image signal a sparse domain, it is easily affected by measurement noise. The focus on this domain usually leads to a reduced imaging performance, namely an increased number m of necessary measurements or a reduced image quality. This point is addressed in robustness considerations within the CS framework (see e.g. [20], [8] and references given therein). However, to illustrate the random character of the sampling, figure (3.8) illustrates the signals encountered for case f) of the example shown in figure (3.7) .

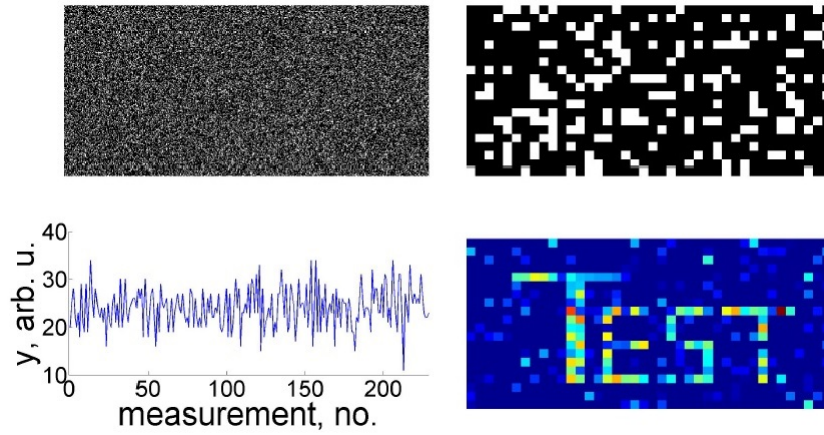


Figure 3.8: Signals encountered in case f) of the example presented in the last section. Top row matrix Φ (left) and example mask $\phi_{100} = \Phi(100, :)$. Bottom row measurement vector \vec{y} left and reconstructed image \vec{x} .

Figure (3.8) shows the matrix Φ (top row left) one row of Φ (a so called mask ϕ_j) in the top row on the RHS. The bottom row shows the measurement vector \vec{y} and the reconstructed image \vec{x} . According to the measurement procedure of equation (3.1) every row of Φ is multiplied with the vector of the scene \vec{x} (just to use the terminology already introduced and to show the relationship between CS and THz-imaging) and the result is achieved by component-wise summation (scalar product of ϕ_j and \vec{x}). Spoken directly, this procedure measures (assigns a value) to the similarity of every ϕ_j with the scene \vec{x} . This is how the measurement vector \vec{y} is constructed. In a non-adaptive scanning scheme the scene \vec{x} can be represented by a variety of different signals. It can be shown that in this sampling scenario (non-adaptive case) the sampling with random matrices and l_1 -minimization is a near-optimal sensing strategy (see e.g. [7], [10]).

Since the matrix Φ is constructed from pseudo-randomly selected matrix elements of a specific distribution, a probability component is added to the sensing process. The randomly chosen matrices Φ vary in their performance in regard to the RIP and coherence property. Therefore, sampling with a specific Φ might not work as good as expected (see again figure (3.7) case d)). Here,

two strategies are possible. The first strategy would be to store an optimal Φ (for a variety of signals \vec{x}) in a look-up table and then use this optimal Φ for all measurements afterwards. The second strategy would be to draw a new Φ for every measurement and simply accept the performance variations. To demonstrate the extent of these variations, figure (3.9) presents an excerpt of a performance simulation study done by this author¹³. The study uses again the test image but uses $\Psi = \mathbb{1}$ to not distort the results. As simulation environment the Matlab software for Disciplined Convex Programming (CVX-toolbox) was chosen (see <http://cvxr.com/cvx/> for details).

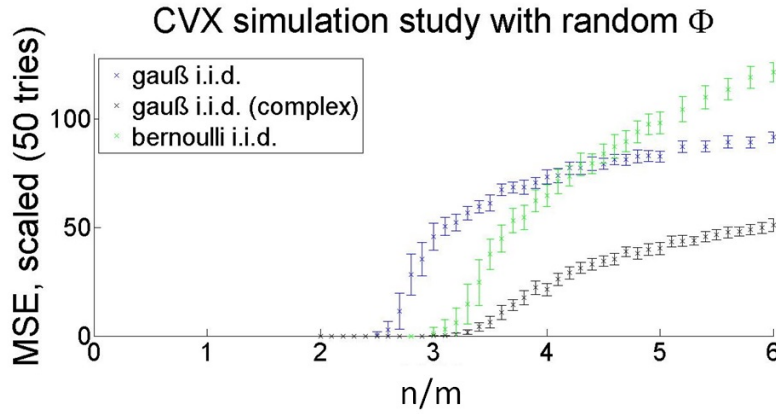


Figure 3.9: Performance study with random Φ .

In the simulation study, for every number of measurements m , a random Φ was drawn out of a respective distribution and the signal reconstructed from the generated measurements. This was done 50 times for each m and the errors for each draw were measured using the mean squared error (MSE) from the original test image. The results are given in figure (3.9) and show the variations of the reconstruction, introduced by the pseudo-random character of Φ . For the different distributions a characteristic behavior, when changing m is visible that is different for the binary distribution (Bernoulli distribution) and multinary distributions like the Gaussian distribution. The details of the change in the characteristic may also depend on the reconstruction algorithm used but are not yet fully understood. The main point of argumentation is visible in figure (3.9) by the size of the error bars, which reflect the variations in the reconstruction quality due to the pseudo-random nature of each Φ .

The other extreme for the considerations regarding Φ is the design of an adaptive matrix. This means that a priori knowledge about the signal (or the class of signals that shall be measured) is used in the design of Φ . For example, if it is known in advance that the signal that shall be measured is a binary signal. This a priori knowledge can then be used for the design of Φ by taking the matrix elements of Φ out of a binary distribution (a Bernoulli distribution). In this case the a priori knowledge enhances the performance

¹³The results of the performance study are not published yet. Also, please notice the reconstruction performance increase due to the use of the Bernoulli distribution.

of such a measurement scheme (see e.g. [31]). Hence, there exist a trade-off between adaption to a specific signal/group of signals by including a priori knowledge into the design of Φ and the ability to sense a wide range of possible signals with high efficiency (non-adaptivity).

As part of the process of adapting the matrix Φ to the signal at hand, there is also the consideration of the noise level. Since in a real world situation noise is always present, it has to be included in the CS-formalism and adapted to the measurement conditions. The full measurement equation including noise contribution is given in equation (3.8).

$$\vec{y} = \Phi \cdot \vec{x} + \sigma_{Noise} = \underbrace{\Phi \cdot \Psi}_A \cdot \vec{a} + \sigma_{Noise} \quad (3.8)$$

σ_{Noise} in equation (3.8) describes an additive noise contribution. The noise level must be adapted to the measurement situation at hand (either by measurement of the noise level or by estimation). The adaption of the CS-measurement scheme to the specific noise level should be ensured for every CS-measurement. Deviations can have a significant effect on the reconstruction process. This will be discussed in the next section along with a few reconstruction algorithms.

3.4 Compressed Sensing Reconstruction Algorithms

Equation (3.8) describes the process of generating the measurement vector \vec{y} (measuring a scene of interest \vec{x}). The goal of this section is to explain how an estimated version of the scene $\hat{\vec{x}}$ can be derived from the measured values (\vec{y}). A straightforward solution would be to simply invert equation (3.8).

$$\begin{aligned} \vec{y} &= A \cdot \vec{a} + \sigma_{Noise} \\ \vec{y} - \sigma_{Noise} &= A \cdot \vec{a} \\ A^{-1} \cdot (\vec{y} - \sigma_{Noise}) &= \underbrace{A^{-1} \cdot A}_{=\mathbb{I}} \cdot \vec{a} \\ \implies \Psi \cdot A^{-1} \cdot (\vec{y} - \sigma_{Noise}) &= \vec{x} \end{aligned}$$

There are at least two difficulties with this simple inversion approach and both are connected to the implicit requirement of $A^{-1} \cdot A = \mathbb{I}$. For the inversion to work the existence of the inverse of A is assumed (denoted A^{-1}). For the case $m \geq n$ where the number of measurements is at least as high as the number of signal components,¹⁴ the existence of a quadratic matrix A makes the invertibility of A at least possible (it still depends on the rank of A) but as already discussed in this chapter, CS-methods try to reconstruct \vec{x} out of less measurements than signal components ($m \ll n$). In this case A is not constructable as a square matrix and an inverse matrix does not directly exist. However, this problem can still be solved if a pseudo-inverse is used. There

¹⁴The case $m > n$ is included in the considerations because of the existence of noise. $m > n$ is equivalent to the acquisition of redundant information that can be used to lower the noise level. In this, the case $m > n$ can be reduced to the case $m = n$.

are many approaches to the matrix inversion problem of non-square matrices (see e.g. [19], [17] and references given therein) but a very common approach is the use of the Moore-Penrose pseudo-inverse (A_{MP}^{-1}). This leads directly to the second aforementioned difficulty. The derivation of the Moore-Penrose pseudo-inverse is an unstable solution to the matrix equation (3.9) or equation (3.10)¹⁵.

$$A_{MP}^{-1} = (\overline{A^T} A)^{-1} \overline{A^T} \quad \text{if } (\overline{A^T} A)^{-1} \text{ exists} \quad (3.9)$$

or

$$A_{MP}^{-1} = \overline{A^T} (A \overline{A^T})^{-1} \quad \text{if } (A \overline{A^T})^{-1} \text{ exists} \quad (3.10)$$

The Moore-Penrose pseudo-inverse has some but not all properties of an inverse matrix. This causes the solution to the matrix equations to be unstable due to rank problems and numerical difficulties. The Moore-Penrose pseudo-inverse seeks to find a solution to equation (3.8) that has a minimal l_2 -norm. In that sense the solution is optimal, but in the context of THz-imaging the solution might not be optimal. However, because of the easily understood way in which the solution to equation (3.8) is produced (the solution is as before denoted \vec{x} as estimator of the scene \vec{x}), the Moore-Penrose pseudo-inverse shall serve as a gold standard to which all now considered CS-algorithms are compared to (regarding different performance indicators).

There exists a manifold of reconstruction algorithms that is still steadily increasing. In this thesis the focus does not lie on the details of the newest reconstruction algorithms. Here, the considerations concentrate on a few selected algorithms just to demonstrate the main ideas and to point out the difficulties as well as future development directions. Since all reconstruction algorithms are computer programs, the reconstruction task is formulated as a reconstruction program. In case of the Moore-Penrose pseudo-inverse, the reformulated program reads as follows (see equation (3.11)).

$$\vec{\hat{x}} = \arg \min_{\vec{\hat{x}}} \|\vec{\hat{x}}\|_2 \quad \text{subject to} \quad \vec{y} = A \cdot \vec{\hat{x}} + \sigma_{Noise} \quad (3.11)$$

In comparison, in a CS-approach the reconstruction program reads (see equation (3.12) respectively as convex program (3.13)).

$$\vec{\hat{x}} = \arg \min_{\vec{\hat{x}}} \|\vec{\hat{x}}\|_1 \quad \text{subject to} \quad \vec{y} = A \cdot \vec{\hat{x}} + \sigma_{Noise} \quad (3.12)$$

$$\vec{\hat{x}} = \arg \min_{\vec{\hat{x}}} \|\vec{y} - (A \cdot \vec{\hat{x}} + \sigma_{Noise})\|_1 \quad (3.13)$$

With the formulation as convex program, it is possible to use the very efficient and fast methods of convex programming to solve the under-determined (ill-posed) problem stated in equation (3.8). At least two development directions for the reconstruction algorithms exist. The first direction uses the classical

¹⁵This instability also exists for other pseudo-inverse approaches.

l_2 -Norm to solve problem (3.8). The l_2 -norm minimization is thereby not used in a plain classical least-squares framework but in a new and efficient manner. "Algorithms that fall in this category are often implemented as Greedy algorithms¹⁶. Here, the so called "Orthogonal Matching Pursuit" (OMP) is presented and the key ideas behind this algorithm are then discussed in more detail (see [36] for an in depth discussion of the OMP algorithm). These key ideas are in modified form also part of other CS-reconstruction algorithms. Hence, it is reasonable that the understanding of these key ideas are a suitable/sufficient foundation for the concepts presented in this thesis.

After the OMP is presented an algorithm named "Compressive Sampling Matching Pursuit" (CoSaMP) is briefly discussed (details can be found e.g. in [26]). As mentioned before, many of the ideas presented for the OMP are used in modified form for CoSaMP because, as its name already suggests, it is an extension of the OMP-algorithm with many similarities. Hence, CoSaMP is discussed here only superficially in regard to a more practical situation since it was used to reconstruct some of the results presented in this thesis. It should also be mentioned that CoSaMP is a well researched algorithm with many available performance indicators. In this, CoSaMP has established itself as a standard in the CS-community. To conclude the discussion on algorithms, a convex algorithm that uses l_1 -minimization is introduced "Basis Pursuit". Again, the key concepts discussed here are comparable to a master plate that spawned a myriad of other l_1 -algorithms. This directly leads to a brief debate on how some of the ideas presented in the Greedy algorithm- and l_1 -class discussion might be extended to construct specialized THz-reconstruction algorithms (for THz-imaging).

3.4.1 Orthogonal Matching Pursuit (OMP) - Greedy algorithms

The Orthogonal Matching Pursuit-algorithm is a class member of the matching pursuit algorithm class. The idea of matching pursuit is to find the basis elements that match the signal \vec{x} best, hence the name. The algorithmic procedure is that at every iteration the dictionary item that explains the signal best is selected via least-squares minimization. This class of algorithms is also called Greedy algorithms because at every iteration the best choice is taken without regard to the fact that a less optimal choice at one iteration step might lead to an optimal global solution. To get better insights into the workings of the algorithm, it is helpful to have a look at a pseudo-code implementation (see pseudo-code given in Algorithm 1 below).

¹⁶"A greedy algorithm is an algorithm that follows the problem solving heuristic of making the locally optimal choice at each stage" - cited after Paul E. Black, details can be found at <http://xlinux.nist.gov/dads/>

Algorithm 1 Orthogonal Matching Pursuit

Input: ► measurement matrix $\Phi \in \mathbb{R}^{M \times N}$
 ► vector of measurements \vec{y}
 ► sparsity level k of the ideal signal $x \in \mathbb{R}^N$

Output:
 ◄ an estimate $\vec{x} \in \mathbb{R}^N$ of the ideal signal \vec{x}
 ◄ a set Λ_k containing the positions of the non-zero elements in \vec{x}
 ◄ an approximation to the measurement \vec{y} by \vec{a}_k
 ◄ the residual $\vec{r} = \vec{y} - \vec{a}_k$

```

1:  $r^{(0)} \leftarrow \vec{y}$ 
2:  $\Lambda^{(0)} \leftarrow \emptyset$ 
3: for  $i = 0$  to  $k$  do
4:    $\lambda^{(i)} \leftarrow \operatorname{argmax}_{j=1,\dots,N} |\langle \vec{r}^{(i-1)}, \phi_j \rangle|$ 
5:    $\Lambda^{(i)} \leftarrow \Lambda^{(i-1)} \cup \lambda^{(i)}$ 
6:    $\Phi^{(i)} \leftarrow \lfloor \Phi^{(i-1)} \phi_{\lambda^{(i)}} \rfloor$ 
7:    $\vec{x}^{(i)} \leftarrow \operatorname{argmin}_{\vec{x}} \|\vec{y} - \Phi^{(i)} \vec{x}\|_2$ 
8:    $\vec{a}^{(i)} \leftarrow \Phi^{(i)} \vec{x}^{(i)}$ 
9:    $\vec{r}^{(i)} \leftarrow \vec{y} - \vec{a}^{(i)}$ 
10: end for
11:  $\vec{x} \leftarrow \vec{x}^{(k)}$ 
12: return  $\vec{x}, \Lambda^{(k)}, \vec{a}^{(k)}, \vec{r}^{(k)}$ 

```

As can be seen from the pseudo-code, the feature of OMP is that it uses all the identified dictionary elements to find the best new dictionary element in every iteration step. An extension to OMP is the earlier introduced CoSaMP algorithm. CoSaMP works very similar to OMP with one major distinction. CoSaMP limits its considerations to a part of the dictionary (the signal support). The signal support is chosen according to the largest $2 \cdot S_{\vec{x}}^{\Psi}$ signal components of the dictionary. This limitation is a sparsity promoting step and it can be shown that it gives tighter bounds on its convergence and performance (see e.g. [18]). Also, due to the presence of measurement noise in every experimental situation the aforementioned CoSaMP property of limiting the considerations to part of the dictionary supports the reconstruction success. It subsequently makes it also sensitive to the estimated noise level, Therefore, special care must be taken when the noise estimator is included in the CoSaMP formalism (see again [26] and references given therein).

3.4.2 Basis Pursuit (BP) - l_1 - algorithms

Basis pursuit (see the fundamental paper [14] for details) is a reconstruction principle for the expansion of a signal into an "optimal" superposition of dictionary elements from an over-complete dictionary. Optimal here means that the expansion has the smallest possible l_1 -norm (after [12]). The intended goals, stated by the authors of [12] with a Basis Pursuit decomposition¹⁷ are sparsity and Superresolution. BP is based on a global optimization and therefore it

¹⁷Since the transformation Ψ is known, a decomposition into dictionary elements (atoms) is equivalent to the reconstruction of \vec{x} .

can provide stable, superresolved reconstructions of the scene unlike for example the Matching Pursuit algorithms. Extensions of the BP-principle include noise in the considerations. One such approach is, as already introduced, the Basis Pursuit De-Noising (BPDN). It attempts to solve the modified program $\arg \min_{\vec{\alpha}} \frac{1}{2} \|y - A \cdot \vec{\alpha}\|_2^2 + \lambda \|\vec{\alpha}\|_1$, which tries to identify the dictionary elements (atoms) that form \vec{x} in the presence of noise.

3.4.3 Specialized THz-reconstruction algorithms

What distinguishes the THz-region from the VIS- and NIR-region is the large wavelength. With it come problems with diffraction effects and coherence effects of artificial radiation. The large wavelength also causes acquired images to be devoid of low-scale textures. BP and methods like Mallat's [24] multiscale edge representation as well as Rudin, Osher, and Fatemi's [32] total variation-based de-noising methods in combination with the aforementioned constraints regarding coherence and wavelength can lead to specialized THz-reconstruction algorithms. The implementation could start on two levels. The first level is the level of the dictionary. With dictionary learning techniques (see e.g. [35]) a specialized THz-imaging dictionary could be implemented. The second level involves models that represent the aforementioned constraints mathematically and make it possible to incorporate them into the established CS-framework.

1. THz-dictionary learning
2. THz-imaging model

The important thing at this point is that specialized THz-reconstruction algorithms do not exist up until now. The potential for efficiency improvements (measurement time, resolution, etc.) with such algorithms makes their development, in this author's opinion, a rewarding challenge.

3.5 Compressed Sensing and Single-Pixel THz-Imaging

With the discussion of the reconstruction algorithms, all components are given to discuss a complete THz-imaging system. In this discussion the focus lies on single-pixel THz-imaging systems (systems with only one detector). Single-pixel imaging is of such importance for the THz-region because of two reasons. First, the equipment is still rather expensive in this region. So cost considerations limit a THz-imaging system to having only a few or in most cases just a single detector. The second reason refers to the sensitivity of THz-detection systems. Multi-pixel cameras exist also for THz-radiation but their sensitivity, when measured by their NEP, is still orders of magnitude inferior to the best THz single-pixel detectors (see e.g. [5]).

As already mentioned in the previous chapters, in general, there are two possible modalities for the imaging process. All two modalities are eligible for CS-based single-pixel imaging but differ in the particularities and the boundary conditions. Every modality has its advantages and shortcomings. It therefore is helpful to briefly discuss them in the context of CS-based THz-imaging. The discussion will show that the application of CS-methods can be of great value

for THz-imaging in general and THz-security imaging (THz-security imager) in particular. The passive modality uses only the radiation coming from the scene and the natural reflections from the sun. Due to the fact that objects in the scene continuously emit radiation in the THz-region, a CS-scanning scheme is naturally suited for this modality¹⁸. As a severe shortcoming, the passive imaging modality has a limited SNR. This leads to an ever increasing effort for the development of very sensitive but in turn also very expensive detectors. In general, applications like, for example, the observation of stars/space can only be achieved in a passive imaging modality. In recent years exiting new results have been produced in this sub-field of THz-imaging (see e.g. [4]). However, from a CS point-of-view the methods employed in the passive imaging modality are similar to the methods used in active mode. Therefore, the discussion starts with the details on CS-based active single-pixel imaging and the peculiarities of the passive domain will be briefly discussed afterwards. Figure (3.10) summarizes the possible CS-based active imaging scenarios.

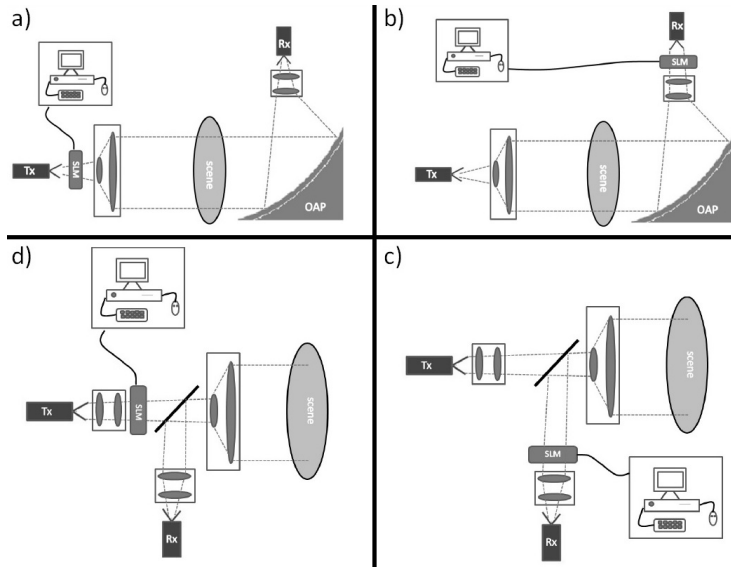


Figure 3.10: Possible CS-based active imaging scenarios.

Figure (3.10) describes schematically the different imaging settings that are possible in CS-based active THz imaging. The two dimensions are, first, the distinction between transmission geometry (top row) and reflection geometry (bottom row). The second dimension distinguishes between modulated illumination (left column) and modulated detection (right column). Let us briefly analyze what these dimensions entail in detail.

Let us start at the setting of **transmission geometry with modulated illumination** (case a) in figure (3.10)). It was already introduced in section (3.1).

¹⁸Please recall that in an active CS-scanning scheme it is necessary to illuminate the entire scene, which would potentially waste power. This is not necessary in a passive scanning scheme because the objects in the scene constantly emit THz-radiation themselves.

The modulator is placed in front of the THz-illumination source. More precisely, it is placed after some optical elements that ideally form a homogeneous parallel beam. After that the scene is illuminated. All the radiation that is not blocked by objects in the scene is then collected by suitable collecting optics. Figure (3.11) shows a schematic representation of this setting and connects the hardware components to the CS-quantities introduced throughout this chapter. Also, the figure contains a signal flow diagram indicating the different effects that can cause signal distortions and need to be taken into account. In this, the potential signal distortions are modeled using convolution blurring kernels/respective transfer functions.

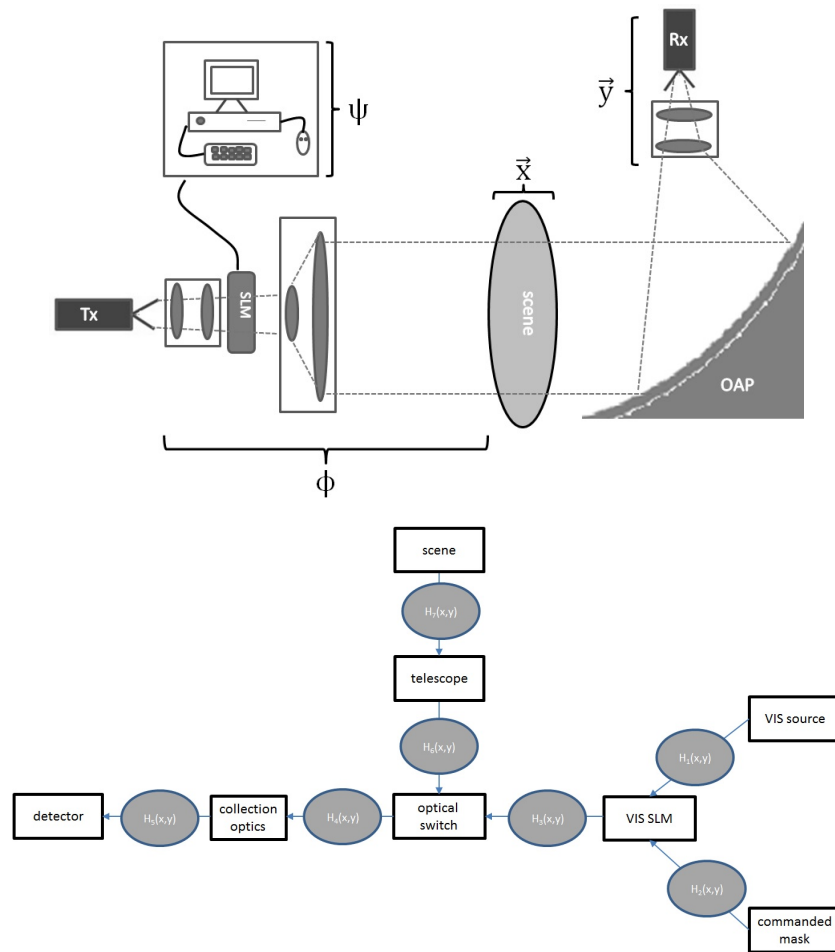


Figure 3.11: CS-based active imaging scenario in transmission geometry with modulated illumination (top) and resulting signal flow diagram in a CS-based THz-imaging scheme (bottom).

This setting is especially suited for applications where the distance between source and detector is short. The wavelength of radiation in the THz-region is

large when compared to the VIS/NIR-region. So, this setting works fine as VIS-SPC, but in the THz-region it promotes difficulties with multipath propagation and diffraction effects (modeled by blurring kernels of the signal flow diagram, details of the classification for the different blurring kernels are given in the appendix in section (A.2)). The problems stem from the pixel-size of the matrix Φ that is used to scan the scene. When the pixel-size comes in size in the order of the wavelength, the aforementioned problems are amplified (see e.g. [28]). Possible applications for such a setting are, for example, material inspections. The THz-SPC lab setup developed during this thesis is also based on this setting. The details about the THz-SPC lab setup will be given in section (6.5.1). The signal flow diagram of figure (3.11) already lists some components of THz-spatial light modulators that will be discussed in the next section. However, it is worth noting that a CS-based setting in **reflection geometry** with **modulated detection** is theoretically best suited for stand-off THz-imaging applications. It is shown schematically in figure (3.10 c)). In comparison, this setting avoids the effects of diffraction and multipath propagation best and therefore has a much simpler signal flow diagram. The modulator, which can be regarded as a dynamic filter is just in front of the detector. This setting is also similar to the setting used in passive mode. With regard to classical setups, it is most notable that for all the presented CS-based settings the used telescope does not need to have an object side focus. This becomes possible with the help of the key component of all the CS-based settings, a THz-spatial light modulator. The setup of the other two settings can be deduced from the two settings just presented. Their advantages and shortcomings can also be derived from the discussion above. At this point it is helpful to discuss the key component that is crucial for all single-pixel designs analyzed in this thesis and its relationship to the theoretical CS-framework presented in this chapter.

3.5.1 THz-Spatial Light Modulators

The classification and rudimentary make-up of spatial light modulators was already discussed in section (1.3) on page 19 and following pages. Here the physical implementation is not the main interest but the connection to the theoretical CS-framework. To support the understanding, a notion was coined in [15].

Our "single-pixel" CS camera architecture is basically an optical computer (comprising a DMD, two lenses, a single photon detector, and an analog-to-digital (A/D) converter) that computes random linear measurements of the scene under view.

The aforementioned quote refers to the VIS-SPC introduced in [15]. The VIS-SPC uses a digital micromirror device (DMD) as VIS-SLM. This SLM is used to compute the linear measurements according to the fundamental measurement equation $\vec{y} = \Phi \cdot \Psi \cdot \vec{x} + \sigma_{Noise}$. The rows of the matrix Φ (the masks) are nothing else than test patterns that measure the similarity of the signal \vec{x} to these test patterns. At this point it must also be stated that the transition to the digital domain happens already here at the VIS-SLM (DMD). The DMD can, therefore, be regarded as a digital optical element connecting the hardware level with the software level (for details on digital optical elements see e.g. [23]).

The DMD does not work directly in the THz-region and other multi-pixel THz modulators are also not available (see [30] for an overview of different modulator approaches). Even if the theory for the VIS-domain was there, for the extension of the CS-framework to the THz-region the physical implementation was the limiting factor. The very first THz-SLMs worked similar to a diascope where every mask had to be changed by hand [11]. The first dynamic and electronically controllable THz-SLMs emerged in 2012 [6] and used an optical switch to translate the modulation of visible/infrared radiation to the THz-domain. The technique of using an optical switch is extensively used in many areas of physics and engineering. The details on its mode of operation are described below. As a generic illustration of the main components of THz-SLMs, figure (3.12) shows a schematic representation of all key components of a dynamic THz-SLM.

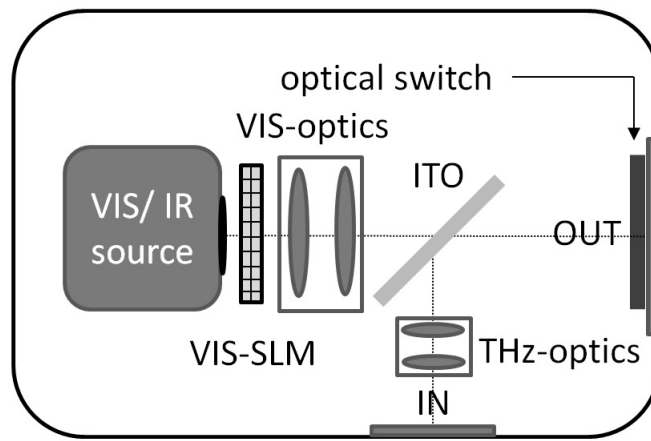


Figure 3.12: Schematic representation of a THz-SLM.

Figure (3.12) is representative for all dynamic, optically controllable SLMs published so far. The more recent designs published are [33], [13]. All designs employ the help of an optical switch to achieve the modulation of THz-radiation. In most cases the switch consists of semiconductor material but very recent results suggest also the usage of meta materials. The intermediate step of using the optical switch is on one hand an auxiliary means to achieve the modulation of radiation. The modulation could be achieved using other means (see [30] and references given therein) but the modulation of 100th, 1000th or even 10.000th of pixel, as necessary for high resolution imaging applications, is at present not possible using the aforementioned alternate means of modulation. On the hand, the intermediate step using the optical switch offers also some potential for additional functionality. One possibility is beam steering, which was already demonstrated in experiments using an THz-SLM design with optical switch (for details see [6]). The outlook to possible benefits of using the optical switch in combination with CS-methods is further discussed in section (8.2).

As described in the references given in this section, the modulation of THz-

radiation using a THz-SLM, is achieved by photo-induced illumination with a suitable light source. So, aside from the optical switch in figure (3.12), the other main components are: a VIS/IR-light source, a VIS/IR-SLM, a dichroic mirror and THz- as well as VIS/IR-optics. The VIS/IR-SLM modulates the VIS/IR-light source, which in turn illuminates the optical switch only in specific regions. The optical illumination causes the change of a property of the optical switch that in turn affects THz-radiation in these specific regions¹⁹. The dichroic mirror is then used to couple-in THz-radiation in the VIS/IR beam path.

With the help of THz-SLMs new concepts that have been reported for the VIS-part of the spectrum become possible also for the THz-region. These concepts include Superresolution [3], infinite depth of focus [38], scanning without movement of mechanical parts [1], etc. to name but a few. With THz-SLMs, methods of the digital level now become possible already on the hardware level. One example of this from the field of hardware image processing, namely hardware edge-detection, is described in [2]²⁰. To conclude this chapter on theoretical CS-methods, the next section briefly discusses CS as a method for image processing on the software level, which is achievable with the CS-framework already introduced in this chapter.

3.6 Compressed Sensing for improved image Reconstruction of THz-images

In the last section it was discussed that specific CS-algorithms allow for a superresolved reconstruction even with missing data. Although CS is inherently a new data acquisition scheme, the question comes to mind, whether CS-reconstruction algorithms can be employed to enhance the image quality of already measured images in the presence of severe noise/missing data. This reconstruction idea is illustrated in figure (3.13). In the figure it is assumed that with the help of CS-techniques, sharper edges, the interpolation of missing data and the correction of imaging artifacts can be achieved. The reconstruction using CS-techniques was already successfully achieved in the visible region of the spectrum (see e.g. [27], [16], [29]). However, at

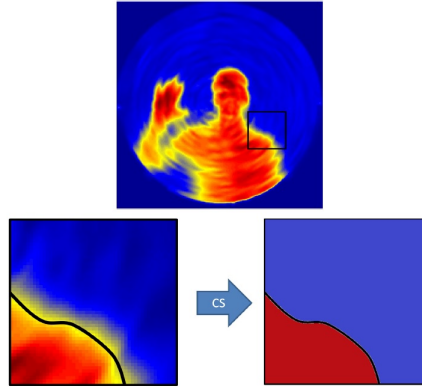


Figure 3.13: Illustrating the notion of improved image quality by CS-reconstruction.

¹⁹The theory here is that due to the optical illumination free charge carriers are generated in the conduction band of the optical switch, which in turn change the transmittance for THz-radiation. This theory has not been tested (not by this author) in experiments so far

²⁰The details on hardware image processing will be discussed in the next chapter.

present no results exist for the THz-region but first experiments on the matter²¹ suggest the possibility. The severe noise environment especially in a passive imaging modality coupled with the artifacts introduced by hardware scanning makes the implementation a challenging task. Since hardware scanning is commonly used in THz-imaging for security applications (see e.g. [25], [21], [22]), the scanning process not only introduces scanning artifacts into the acquired images, it also uses spatial undersampling to shorten the measurement time²². Some of the ideas presented in the references given in the previous sections, provide techniques to combat the challenges present in the described setting. Following the arguments in the references, a reconstruction idea is presented in this section and exemplified in figure (3.14).

The considerations start at the fundamental CS-level. As discussed in the last section the idea of l_1 -minimization is to achieve the reconstruction of a signal \vec{x} even with missing signal components. Missing signal components refers here to the spike domain (missing pixel see figure (3.14)).

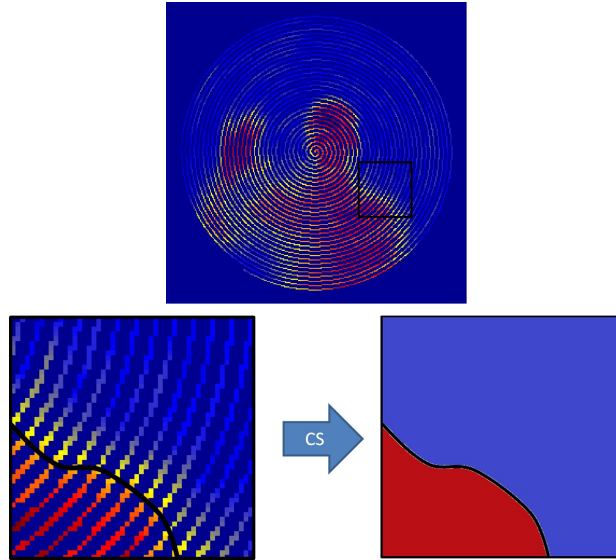


Figure 3.14: Spiral scan of a person with undersampling exemplifying the notion of interpolation using CS-techniques.

As long as the signal components in the sparse domain are measured, the signal reconstruction is unaffected by missing data²³. It, therefore, can be assumed that if the physical parameters of the acquisition process are modeled correctly and the reconstruction is then carried out in a sparse domain instead of the

²¹For details see section (6.2).

²²The concept of spatial undersampling is similar to its time domain counterpart. Here, not the sampling frequency is reduced but the sampling distance in the scene is increased. Details on spatial undersampling are briefly discussed in section (4.2).

²³This refers to the fact that, although pixel are missing, the information about the image content is still complete. More details on the information content of images is given in the next chapter.

spike domain, improved image reconstruction is achievable. The results of this enhancement methodology, applied to passive THz-images, is presented in section (6.2). It will be shown there that CS-techniques potentially offer significant improvement over established interpolation/reconstruction techniques.

This concludes the necessary basics of CS. The next chapter shows how CS as a framework refers to classical image processing and how it can extend the classical image acquisition and processing paradigm to a new paradigm combining the hardware and the software level.

References Chapter 3

- [1] S. S. Ahmed, A. Schiessl, and L.-P. Schmidt, "A novel fully electronic active real-time imager based on a planar multistatic sparse array," *IEEE Transactions on Microwave Theory and Techniques*, vol. 59, no. 12, pp. 3567–3576, 2011.
- [2] S. Augustin and H.-W. Hübers, "Phase-sensitive passive terahertz imaging at 5-m stand-off distance," *IEEE Transactions on Terahertz Science and Technology*, vol. 4, no. 4, pp. 418–424, 2014.
- [3] H. P. Babcock, J. R. Moffitt, Y. Cao, and X. Zhuang, "Fast compressed sensing analysis for super-resolution imaging using l1-homotopy," *Optics Express*, vol. 21, no. 23, p. 28583, 2013.
- [4] D. J. Benford, S. H. Moseley, G. J. Stacey, R. A. Shafer, J. G. Staguhn, R. K. Melugin, and H.-P. Roeser, "Far-infrared imaging spectroscopy with safire on sofia," in *Proc. SPIE 4857, Airborne Telescope Systems II*, February 24, 2003, vol. 4857, pp. 105–114.
- [5] S. Boppel, A. Lisauskas, A. Max, V. Krozer, and H. G. Roskos, "Cmos detector arrays in a virtual 10-kilopixel camera for coherent terahertz real-time imaging," *Optics Letters*, vol. 37, no. 4, p. 536, 2012.
- [6] S. Busch, B. Scherger, M. Scheller, and M. Koch, "Optically controlled terahertz beam steering and imaging," *Optics Letters*, vol. 37, no. 8, p. 1391, 2012.
- [7] E. J. Candes and M. B. Wakin, "An introduction to compressive sampling," *IEEE Signal Processing Magazine*, vol. 25, no. 2, pp. 21–30, 2008.
- [8] E. J. Candes and J. Romberg, "Quantitative robust uncertainty principles and optimally sparse decompositions," *Foundations of Computational Mathematics*, vol. 6, no. 2, pp. 227–254, 2006.
- [9] E. J. Candès, J. K. Romberg, and T. Tao, "Stable signal recovery from incomplete and inaccurate measurements," *Communications on Pure and Applied Mathematics*, vol. 59, no. 8, pp. 1207–1223, 2006.

- [10] E. J. Candes and T. Tao, "Near-optimal signal recovery from random projections: Universal encoding strategies?" *IEEE Transactions on Information Theory*, vol. 52, no. 12, pp. 5406–5425, 2006.
- [11] W. L. Chan, K. Charan, D. Takhar, K. F. Kelly, R. G. Baraniuk, and D. M. Mittleman, "A single-pixel terahertz imaging system based on compressed sensing," *Applied Physics Letters*, vol. 93, no. 12, p. 121105, 2008.
- [12] S. S. Chen, D. L. Donoho, and M. A. Saunders, "Atomic decomposition by basis pursuit," *SIAM Journal on Scientific Computing*, vol. 20, no. 1, pp. 33–61, 1998.
- [13] L.-J. Cheng and L. Liu, "Optical modulation of continuous terahertz waves towards cost-effective reconfigurable quasi-optical terahertz components," *Optics Express*, vol. 21, no. 23, p. 28657, 2013.
- [14] D. L. Donoho, "Compressed sensing," *IEEE Transactions on Information Theory*, vol. 52, no. 4, pp. 1289–1306, 2006.
- [15] M. F. Duarte, M. A. Davenport, D. Takhar, J. N. Laska, Ting Sun, K. F. Kelly, and R. G. Baraniuk, "Single-pixel imaging via compressive sampling," *IEEE Signal Processing Magazine*, vol. 25, no. 2, pp. 83–91, 2008.
- [16] Figueiredo, Mario A. T., R. D. Nowak, and S. J. Wright, "Gradient projection for sparse reconstruction: Application to compressed sensing and other inverse problems," *IEEE Journal of Selected Topics in Signal Processing*, vol. 1, no. 4, pp. 586–597, 2007.
- [17] Z. GAO and P. J. ANTSAKLIS, "Stability of the pseudo-inverse method for reconfigurable control systems," *International Journal of Control*, vol. 53, no. 3, pp. 717–729, 1991.
- [18] R. Giryes and M. Elad, "Rip-based near-oracle performance guarantees for sp, cosamp, and iht," *IEEE Transactions on Signal Processing*, vol. 60, no. 3, pp. 1465–1468, 2012.
- [19] G. Golub and W. Kahan, "Calculating the singular values and pseudo-inverse of a matrix," *Journal of the Society for Industrial and Applied Mathematics Series B Numerical Analysis*, vol. 2, no. 2, pp. 205–224, 1965.
- [20] S. Jafarpour, W. Xu, B. Hassibi, and R. Calderbank, "Efficient and robust compressed sensing using optimized expander graphs," *IEEE Transactions on Information Theory*, vol. 55, no. 9, pp. 4299–4308, 2009.
- [21] Jinshan Ding, M. Kahl, O. Loffeld, and P. H. Bolivar, "Thz 3-d image formation using sar techniques: Simulation, processing and experimental results," *IEEE Transactions on Terahertz Science and Technology*, vol. 3, no. 5, pp. 606–616, 2013.
- [22] B. Kapilevich, Y. Pinhasi, R. Arusi, M. Anisimov, D. Hardon, B. Litvak, and Y. Wool, "330 ghz fmcw image sensor for homeland security applications," *Journal of Infrared, Millimeter, and Terahertz Waves*, vol. 31, no. 11, pp. 1370–1381, 2010.

- [23] B. Kress and P. Meyrueis, *Applied digital optics: Micro-optics, optical MEMS, and nanophotonics*. Chichester and West Sussex and U.K and Hoboken and N.J: Wiley, 2009.
- [24] S. Mallat and S. Zhong, "Characterization of signals from multiscale edges," *IEEE Transactions on Pattern Analysis and Machine Intelligence*, vol. 14, no. 7, pp. 710–732, 1992.
- [25] T. May, E. Heinz, K. Peiselt, G. Zieger, D. Born, V. Zakosarenko, A. Brömel, S. Anders, and H.-G. Meyer, "Next generation of a sub-millimetre wave security camera utilising superconducting detectors," *Journal of Instrumentation*, vol. 8, no. 01, p. P01014, 2013.
- [26] D. Needell and J. A. Tropp, "Cosamp: Iterative signal recovery from incomplete and inaccurate samples," *Applied and Computational Harmonic Analysis*, vol. 26, no. 3, pp. 301–321, 2009.
- [27] D. Needell and R. Ward, "Stable image reconstruction using total variation minimization," *SIAM Journal on Imaging Sciences*, vol. 6, no. 2, pp. 1035–1058, 2013.
- [28] S. Priebe, C. Jastrow, M. Jacob, T. Kleine-Ostmann, T. Schrader, and T. Kurner, "Channel and propagation measurements at 300 ghz," *IEEE Transactions on Antennas and Propagation*, vol. 59, no. 5, pp. 1688–1698, 2011.
- [29] H. Rabbani and S. Gazor, "Image denoising employing local mixture models in sparse domains," *IET Image Processing*, vol. 4, no. 5, p. 413, 2010.
- [30] M. Rahm, J.-S. Li, and W. J. Padilla, "Thz wave modulators: A brief review on different modulation techniques," *Journal of Infrared, Millimeter, and Terahertz Waves*, vol. 34, no. 1, pp. 1–27, 2013.
- [31] H. Rauhut, K. Schnass, and P. Vandergheynst, "Compressed sensing and redundant dictionaries," *IEEE Transactions on Information Theory*, vol. 54, no. 5, pp. 2210–2219, 2008.
- [32] L. I. Rudin, S. Osher, and E. Fatemi, "Nonlinear total variation based noise removal algorithms," *Physica D: Nonlinear Phenomena*, vol. 60, no. 1-4, pp. 259–268, 1992.
- [33] D. Shrekenhamer, C. M. Watts, and W. J. Padilla, "Terahertz single pixel imaging with an optically controlled dynamic spatial light modulator," *Optics Express*, vol. 21, no. 10, p. 12507, 2013.
- [34] A. Srivastava, A. B. Lee, E. P. Simoncelli, and S.-C. Zhu, "On advances in statistical modeling of natural images," *Journal of Mathematical Imaging and Vision*, vol. 18, no. 1, pp. 17–33, 2003.
- [35] Z. TANG and S. DING, "Dictionary learning with incoherence and sparsity constraints for sparse representation of nonnegative signals," *IEICE Trans. Inf. Syst. (IEICE Transactions on Information and Systems)*, vol. E96.D, no. 5, pp. 1192–1203, 2013.

- [36] J. A. Tropp and A. C. Gilbert, "Signal recovery from random measurements via orthogonal matching pursuit," *IEEE Transactions on Information Theory*, vol. 53, no. 12, pp. 4655–4666, 2007.
- [37] H. Yin, "Sparse representation with learned multiscale dictionary for image fusion," *Neurocomputing*, vol. 148, pp. 600–610, 2015.
- [38] A. Zomet and S. K. Nayar, "Lensless imaging with a controllable aperture," in *IEEE Computer Society Conference on Computer Vision and Pattern Recognition*, vol. 1, 2006, pp. 339–346.

A few Words on Image Processing

Contents

4.1	The classical Image Processing Paradigm	87
4.2	Image processing techniques and the optimal digital-image pixel size	88
4.3	What is hardware image processing?	92
4.4	The information content of THz-images	96

The last chapter introduced, in the context of THz-imaging, the possibility to acquire images without the necessity for mechanical scanning. It introduced the notion of analog-to-information conversion. To conclude the theoretical considerations, this chapter briefly explains this conversion starting from the other end, the information. In the classical image processing chain the image comes first and the image processing, to extract information out of these images, comes after. However, CS goes directly after the information already on the hardware level, the stage where the images are acquired. This chapter analyzes the information content of images in a theoretical background. It also sheds light on a few image processing concepts that this thesis relies on. In a sense it is the theoretical connection of the classical hardware level with the classical software level. In the first section, it starts at the classical image processing paradigm and analyzes the shortcomings that come with it. This directly leads to a consideration on the parameters of acquired digital images and their connection to the acquisition process. This connection is investigated in the second section. The third section then explains what the paradigm of hardware image processing is and how it will improve the situation in comparison to the classical paradigm. The notion of analog-to-information conversion is theoretically established and this leads to an investigation of the information content of images that is done in the last section of this chapter.

4.1 The classical Image Processing Paradigm

It is common knowledge that image processing or to be more specific, digital image processing, can be employed on acquired images to enhance the image quality (denoising) or detect edges or use some other digital filtering technique to discover buried information. The standard digital processing chain is shown in figure (4.1).

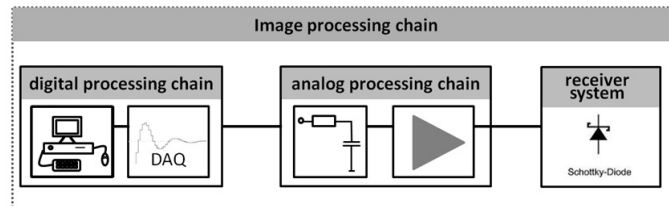


Figure 4.1: Block diagram of a generic standard digital processing chain.

Figure (4.1) shows a generic standard image processing chain. The sensor detects (receives) the signal of interest which is then (after some analog processing) digitized by the data acquisition unit (DAQ). The digitized signal is afterwards processed using a computer. Please recall the block diagram shown in figure (2.6). This block diagram depicts the generic make-up of THz-imagers. When compared with figure (4.1) it can be seen that figure (4.1) corresponds to the backend-component. In this classical image processing chain, image processing can only be done after the signal/image has been acquired and digitized. In this scenario it is not possible to establish a real-time feedback to the acquisition stage when, for example, some predefined object in the image has been detected¹.

This classical processing chain has severe shortcomings that lead to some issues especially in THz-imaging. One of those issues is the Bodyscanner-issue. It was introduced in section (1.1) on page 12. There, it was stated that although acquired THz-images that potentially reveal body parts under clothing are estranged for presentational matters, at some point of the image processing chain, potentially privacy invading images exist and may be proliferated against other intend. One way to avoid this Bodyscanner-issue would be to acquire the images already in processed/estranged form. In what way this can be achieved will be explained in section (4.3). With this solution it will be shown that theoretically a hardware-feedback-loop can be established, allowing it to adapt the resolution during measurement time and also to adapt the whole acquisition process to the acquisition environment at hand (for example the noise floor).

Following this argument, the border lines between the classical image processing chain and new hardware oriented solutions that allow many of the aforementioned techniques (and even more) are becoming more and more blurred. The next section focuses on basic image processing techniques that are needed from a hardware processing system under consideration.

¹FPGA-based methods would enable this but, as will be explained in the rest of this chapter, they also are an extremely inefficient implementation approach.

4.2 Image processing techniques and the optimal digital-image pixel size

Since the classical digital processing chain (figure (4.1)) is still the state-of-the-art in the THz-domain, the focus in this section lies on techniques implementable on a computer. The considerations then subsequently also hint to alternative implementation possibilities.

One of the most important processing techniques is the ability to reduce measurement noise. This technique is also known as denoising (see e.g. [2]). The denoising works by simply thresholding the data and in this way “throwing away” the noise components in the signal. The advantage of the computer-based post-acquisition processing is that the signal/image being processed can be transformed into another domain (expansion after certain basis vectors) and then the aforementioned noise removal technique can be applied in this domain. A wavelet expansion is particularly suited for this denoising approach because natural images² can be very efficiently represented in a wavelet basis (see e.g. [12]). There are also some other denoising techniques aside from the thresholding technique mentioned above. These other techniques involve the use of statistics, like simple averaging to reduce measurement noise (increase the SNR in the respective images). The averaging by using the mean value reduces the noise (measured by its standard deviation) according to $\sigma_{\text{Noise}} \propto \sigma / \sqrt{N}$. Here, σ describes the standard deviation of the (intensity) fluctuations before averaging and N is the number of measurements taken for one image pixel. This noise reduction strategy already shows a strong connection between the hardware level and the software level. On the hardware level the data acquisition rate determines how much averaging can be done on the software level.

Other than using averaging over time, the averaging can also be done spatially. Spatial averaging is related to the issue of the optimal pixel size. As introduced in section (2.3.2), a key factor in determining the spatial resolution (and the optimal pixel size) of a THz-imager is its telescope. For this thesis, the emphasis lies on scanning telescopes that produce a variable focus of certain dimensions. These dimensions in turn, limit the minimal achievable spatial resolution. To increase the noise performance, some of these spot sizes can be combined in the acquired THz-images for spatial averaging. This averaging will increase the SNR but, on the other hand, it leads to a reduced spatial resolution for the produced THz-images. The optimal pixel size that results from these considerations is a trade-off between the two conflicting goals. First, is a detailed consideration of the spatial resolution. The size of the telescope focus is, as already mentioned, a key indicator but spatial resolution even smaller than the geometrical size of the (Gaussian) focus is nonetheless achievable. The considerations start with the well-known Rayleigh-criterion (see e.g. [7], [17]). As is known, the Rayleigh criterion states that for the minimum resolvable detail (diffraction limit for the separation of two image points) the first diffraction minimum of one image source point coincides with the maximum of another.

²Natural images are defined by their pixel statistics (cited after [16]) so that even images taken from natural scenes in the THz-domain are defined as natural images. Even images that are not artificially created with computer-based methods but involve data acquisition with the help of a computer and produce false-color images, can, following this argumentation, be regarded as natural images.

This is a widely accepted criterion, for many imaging applications in different spectral regions. However, since it is derived for the diffraction of radiation on finite apertures (Airy-disc), it needs to be specialized for the THz-region respectively stand-off THz-imaging. The reason is that in the THz-region, due to the increased wavelength compared to the VIS-domain, a homogenous illumination is not easily achievable. This in turn makes the Airy discs, which result from a homogenous illumination of a circular aperture (e.g. a lens), not a widely encountered phenomenon. As was derived in section (2.1), the Gaussian function is ubiquitous in the THz-domain. Hence, the Rayleigh criterion needs to be specialized to Gaussian optics. For a definition of this specialization on spatial resolution inspired by the Rayleigh-criterion see figure (4.2).

Specialized for the Quasi-optical region figure (4.2) shows two Gaussian functions instead of Airy functions with a FWHM of l and a distance d , for the derivation of the minimal spatial resolution. The two peaks are distinguishable if the dip between them is $1/e^2 \cdot 100\%$ below the maximum³. Again, the dip is created when the first minimum of one image source coincides with the maximum of another. This procedure works well for higher order Gaussian functions but for the fundamental Gaussian mode, as shown in figure (4.2) a different procedure is necessary, since it reaches its minimum value only at infinity. A possibility is here to use the reversal point of the Gaussian function as in (4.2). However, the definition of the minimal spatial resolution in the THz-domain is not unambiguously discussed in the literature. The considerations presented above should, therefore, only serve as a guideline.

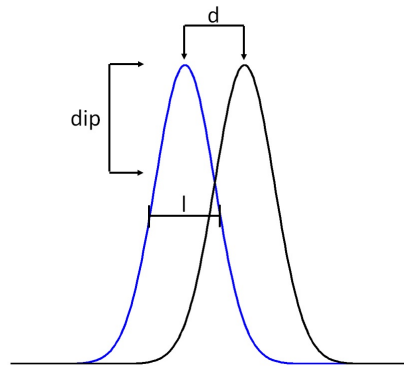


Figure 4.2: Specialized Rayleigh-criterion for stand-off THz-imaging. For this region the Rayleigh-criterion uses Gaussian functions instead of Airy functions for the derivation of the minimal spatial resolution.

Further considerations include the scanning process itself and also more subjective considerations on image quality. The scanning process, as discussed in section (2.3.2), contains deliberations on the coverage of the field-of-view with the spiral motion of the scanning telescope. This coverage is not complete. A certain degree of spatial undersampling must be accepted for the sake of reduced measurement time. Spatial undersampling here refers to the fact that when the scanning path of the telescope is combined with an one pixel small geometric dimension of the telescope focus⁴ in the image, not the entire geometric dimension of the field-of-view is covered (see figure (4.3)).

³The exact value of the necessary dip is open to interpretation.

⁴To avoid spatial undersampling, the real geometric dimensions of the telescope focus can be used. The results of this approach are given in section (6.2)

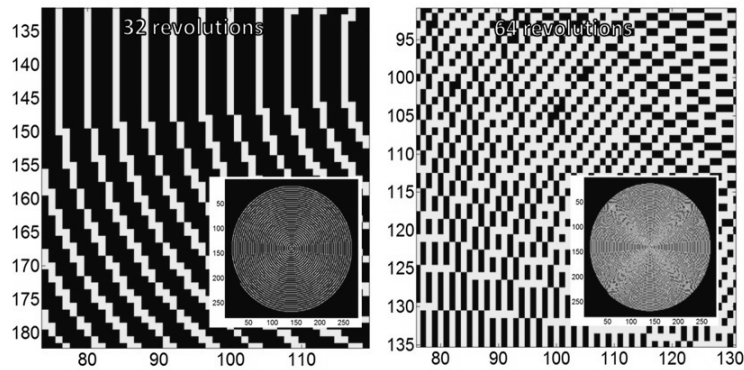
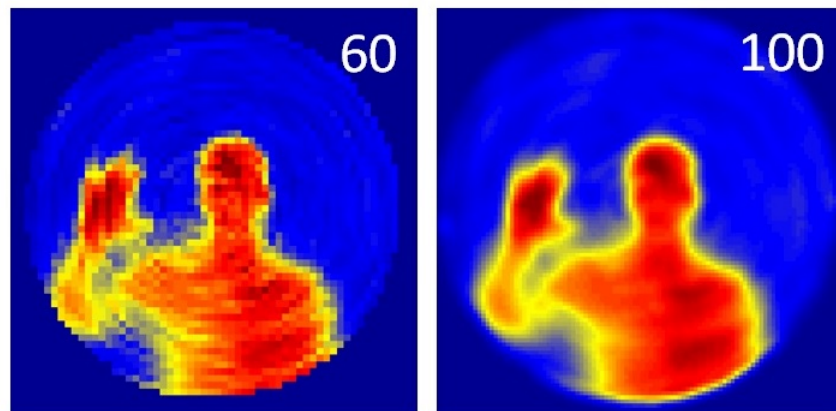


Figure 4.3: Spatial undersampling with a scanning telescope, when a spiral motion of the scanner is chosen. The amount of spatial undersampling depends on the number of revolutions of the scanner, for covering the field-of-view.

The figure shows the emergence of missing data, due to the spatial undersampling. The amount of undersampling depends on the number of revolutions that is chosen to cover the field-of-view. For a setting of 32 revolutions and a digital image size of 280 pixel, an undersampling of ≈ 4 is incurred (only every 4th pixel is really measured during a scan)⁵. The undersampling can be reduced to a value of 2 for 64 revolutions but the measurement time is also substantially increased. Accepting a certain amount of spatial undersampling, the missing pixels must then be interpolated (reconstructed) out of the measured data. This also has an influence on the decision for the optimal image pixel size. The objective aspect here, is the spatial resolution but since the images have to be interpreted by a human operator, the subjective aspect of image quality also plays a roll. The optimal image pixel size is therefore more a choice than a physical fact. Figure (4.4) illustrates this on an example image that is displayed with a differing number of pixels.



⁵The details on the properties of the ISM-imager are thoroughly discussed in chapter (5).

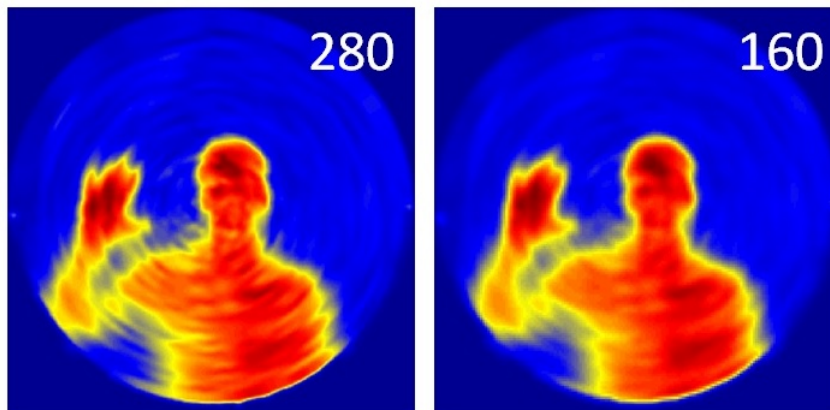


Figure 4.4: Deliberations on the optimal image pixel size

The images in figure (4.4) are labeled with the number of pixels in one direction. The image labeled 60 corresponds to a pixel size in accordance to the geometrical spacial resolution. However, it is visible that with increasing number of pixels⁶ more details become visible⁷. This directly leads to the subject of the information content of the images in question. This subject will be approached from a theoretical point of view in section (4.4). In direct relation to this subject is the detection of edges in images. This is another very important image processing technique that is briefly discussed now.

The detection of edges is equivalent to the detection of rapid changes in the pixel brightness/intensity signal. These rapid changes can easily be made visible with the help of derivatives/finite differences (see e.g. [18]). Similarly edges can be detected, when over a short distance, the intensity signal changes from above a certain threshold to below a certain threshold. At this point, again, thresholding this time in the intensity domain, is the means that is used to accomplish the objective, in this case edge-detection. Also, with the threshold method image background subtraction can be achieved (figure (4.5) demonstrates this concept). Additionally, as discussed in the last chapter, THz-images are sparse in the gradient-domain, which, therefore, leads to the applicability of CS-techniques. The importance of



Figure 4.5: Exemplifying edge-detection by thresholding.

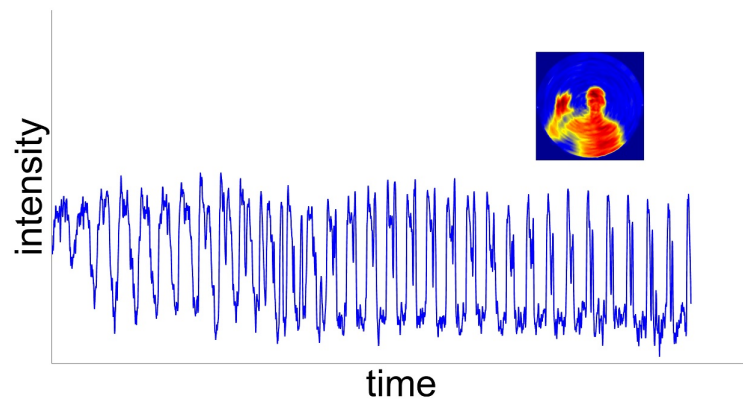
⁶The chosen number of pixels displayed is roughly chosen as a power of 2 with a little overhead taking in account the non-rectangular nature of the imaged FoV.

⁷The optimal pixel size for the ISM-imager is discussed again in section (5.3.2), in relation to the physical properties of this THz-imager.

thresholding can, in the light of the discussion above, hardly exaggerated⁸. The application of thresholding on the software level is a standard technique that is easily implemented. When implemented on the hardware level, thresholding is even more beneficial. On the hardware level, the ability to use thresholding is equivalent with the ability to relate all measurements to a specific value⁹. The next section will show at a few examples (including edge-detection) what hardware image processing is and what possibilities for future developments it offers.

4.3 What is hardware image processing?

The term hardware image processing quite literally means image processing on the hardware level. This could have been a possible title for this thesis such as: "New methods for hardware THz-image processing", but the term hardware processing is not strictly used in the literature. In the literature, terms like analog processing, optical processing or analog filtering are all used for signal processing on the hardware level, meaning signal processing at different stages in the signal path. The term optical processing comes closest to the meaning that is intended here. A few short examples are used to clarify the difference in meaning further (see figure (4.6), (4.7) and (4.8)).



⁸The choice of a threshold value is extremely important. Since the optimal value depends on the specific imaging situation, threshold-scanning offers a generic solution. Experimental details on this subject are discussed in section (6.4)

⁹This offers the possibility to relate each measurement to an absolute temperature, not only an effective temperature.

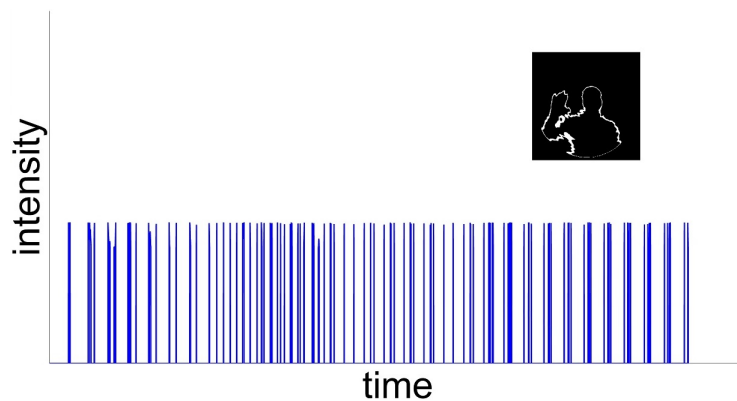


Figure 4.6: Example demonstrating the signal-change for edge-detection on the software level.

Figure (4.6) shows in the top row the original THz-image with its respective time signal (spiral-scan over time). The bottom row shows the same image digitally processed with an edge-detection filter and the resulting time signal (all values except for the detected intensity values at the edges are set to zero). Hardware processing now means that the detour step over the digital signal processing is unnecessary (see figure (4.7)).

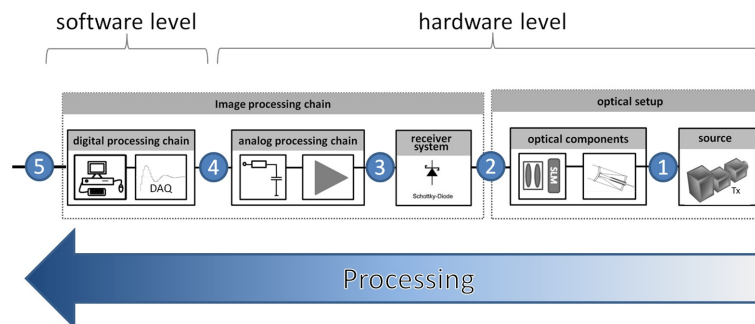


Figure 4.7: Generic block diagram for image processing systems.

Figure (4.7) covers all possible processing cases. The case of software image processing (software edge-detection) presented in figure (4.6) corresponds to the case where the respective signal is different at point ④ and point ⑤ in the processing chain. From figure (4.7) it can be seen that in a hardware image processing setting the signal of interest is already acquired in the form it assumes at the end of the processing chain (the signal is the same at point ④ and point ⑤). Without the detour step of software processing many advantages are possible. For example, in a hardware edge-detection scheme there exists on no level of the acquisition chain a clear image¹⁰. The acquisition can directly be

¹⁰This can be advantageous in regard to privacy considerations.

reduced to the information (see next section) without having to acquire details of the scene that are not used. Also, there exists a potential for speeding-up the acquisition process and by directly concentrating on the edges on the hardware level, the measurement itself can be controlled (optimized) during the acquisition.

In this, the notion of hardware image processing, as used in this text, goes beyond the established concepts of optical image processing and analog filtering. An example for optical image processing is shown in figure (4.8) [5].

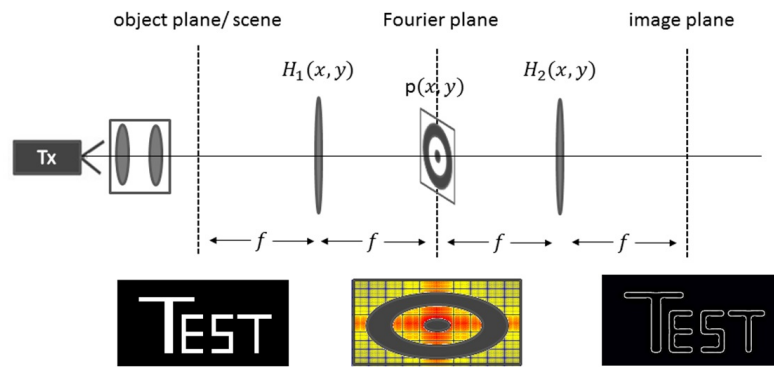


Figure 4.8: Example for optical image processing.

The example in figure (4.8) shows a classical application of Fourier-optics. It shows the filtering of an object by a zone plate. The resulting image is then presented on a screen. All the image processing is done on the hardware level but nevertheless such processing is called optical image processing in the literature. In the block diagram of figure (4.7) the processing occurs between point ① and point ②. There is also no processing beyond point ②, which in the case of this example, would be a screen. At an similar fundamental hardware level a simple anti-aliasing filter is introduced in the signal path also on the hardware level. This is normally called analog processing and corresponds to processing between points ③ and ④.

Also, combinations of the aforementioned forms of hardware processing are in use. Consider again the example described in figure (4.8). When the screen is replaced with a detector/digital camera¹¹ the respective optical processing system becomes a hybrid system, where processing can be done on the hardware level as well as on the software level (see e.g. [5] for a detailed discussion on hybrid systems).

¹¹Since THz-radiation is invisible, hybrid systems are the standard in THz-imaging.

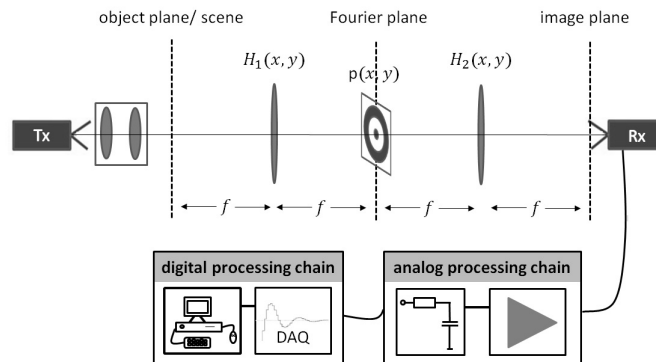


Figure 4.9: Example for a hybrid optical image processing system.

The hybrid system has already many advantages, combining some advantages of the software- and hardware-level. The hardware image processing systems described here, still go beyond the hybrid systems. The hybrid-systems lack the ability to influence the measurement process itself¹². To achieve the influence on the measurement process, the use of digital optics is proposed (see e.g. [13] for a detailed discussion on digital optics).

Digital optics, as its name suggests, is made up of a finite number of distinct elements. Examples of such optical elements are micro lens arrays or segmented mirrors. The real advantage of digital optics comes into play when the distinct elements are dynamically adjustable. As extensively described in this text, spatial light modulators fall in this category of dynamic digital optics. An example block diagram implementing the dynamic digital optic is shown in figure (4.10).

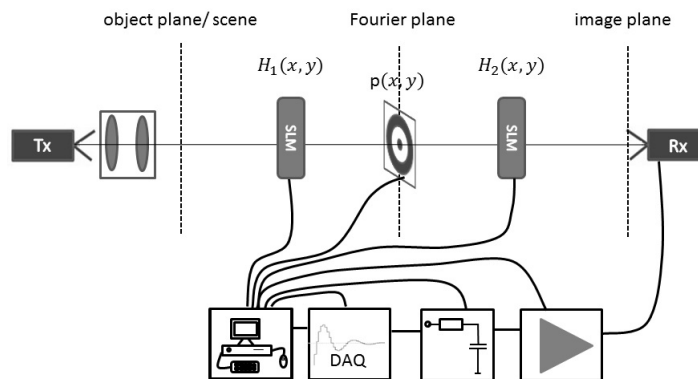


Figure 4.10: Example block diagram of a possible setup using dynamic digital optics (SLMs).

¹²With the aforementioned FPGA-based systems a feedback-loop can be implemented, which can also be used to influence the measurement itself. But the proposed hardware image processing is still more powerful than the FPGA-approach just described.

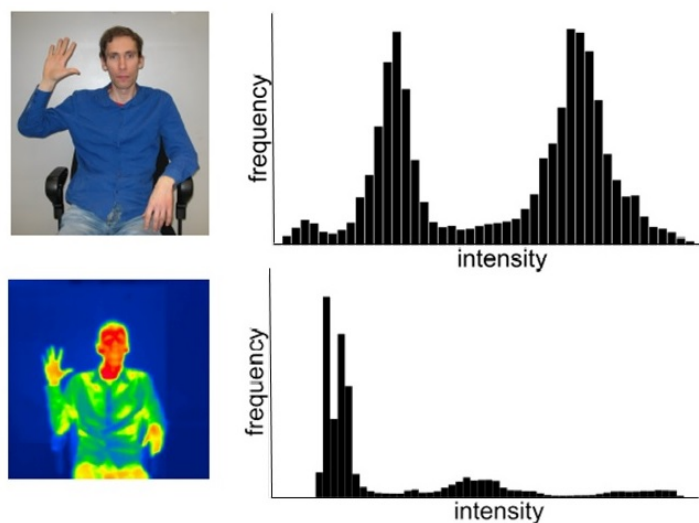
The block diagram in figure (4.10) is also generic, not specialized for a specific application. With such a setup many of the techniques that were discussed in this section are implementable on the hardware level. The setup makes the concept of direct analog-to-information conversion possible [3]. As already discussed it makes concepts like Superresolution or almost infinite depth of focus attainable. To use again the words written in [6] and translate them to the THz-domain:

The "single-pixel" THz-CS camera architecture described here is basically an optical computer (comprising a SLM with a single detector, and an analog-to-digital (A/D) converter) that computes random linear measurements of the scene under view.

The analogy to an optical computer describes best (in this author's opinion) the extend of the capabilities of SLM-based setups for THz-imaging. Only with the help of these THz-SLMs all the aforementioned methods become possible in the THz-region. Since the field of THz-hardware image processing is still in its infancy, new methods are needed that efficiently implement techniques of digital image processing on the hardware level. To efficiently translate the digital techniques to the hardware-domain, knowledge of the information content of images and especially THz-images is needed. A brief consideration on this subject is given in the next section.

4.4 The information content of THz-images

Natural images as encountered in (THz)-imaging exhibit distinct statistical properties. The knowledge of these properties can be used to aid efficient processing on both the hardware and the software level (see e.g. [14] for a discussion on the statistics of natural images). Natural images can be easily evaluated by their image histograms, thereby illustrating the difference in spectral region statistically. Figure (4.11) shows as an example of a scene captured with a digital camera, an IR camera and with a passive THz-camera (ISM-imager). As a first orientation the resulting histograms are also shown.



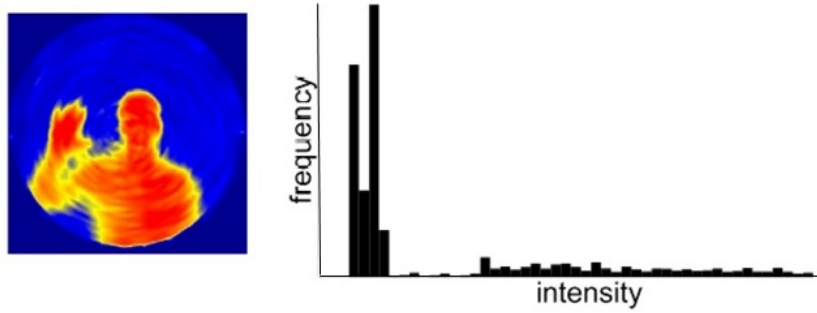


Figure 4.11: Example of a natural scene imaged in the VIS-, IR- and in the THz-region (from top row to bottom row).

The histograms in figure (4.11) give a first orientation on the statistical properties of the respective images (level of details, foreground/background separation, etc.). These statistical characteristics influence many of the possible applications presented in the previous sections, namely image compression (as used in CS), image reconstruction and image processing as a whole. In this, the image histogram is a good starting point but for more elaborate applications a more specified statistical evaluation tool is needed. This tool can be found with the Shannon-entropy (for details on the Shannon-entropy see e.g. [15]). The Shannon-entropy is not only a statistical measure (measure of randomness) it also provides a direct connection to the information content of an image (contained in the image). Interpreted for the pixels of an image \mathcal{I} , the Shannon-entropy is given by equation (4.1).

$$H(\mathcal{I}) = \sum_i p_i \cdot \log \left(\frac{1}{p_i} \right) \quad (4.1)$$

In this interpretation of the Shannon-entropy, the summation over i goes over all pixels in the image \mathcal{I} . Here, p_i is the probability that the i th-image pixel assumes its value with probability p_i ¹³. The pixel interpretation has the advantage of being the more practical interpretation, since it has the advantage of allowing $H(\mathcal{I})$ to be quantified using methods of software image processing. Also, instead of just assigning a value for $H(\mathcal{I})$ (the entire image), it is possible to restrict the definition of equation (4.1) to image parts and in this way define a local Shannon-entropy. That the local Shannon-entropy is a very useful concept is demonstrated in figure (4.12). It shows again the images of figure (4.11) and the resulting local Shannon-entropy images (patches/domains of nine pixels).

¹³Another interpretation of $H(\mathcal{I})$ is that the summation includes all possible images and p_i gives the probability of measuring the i th-image.

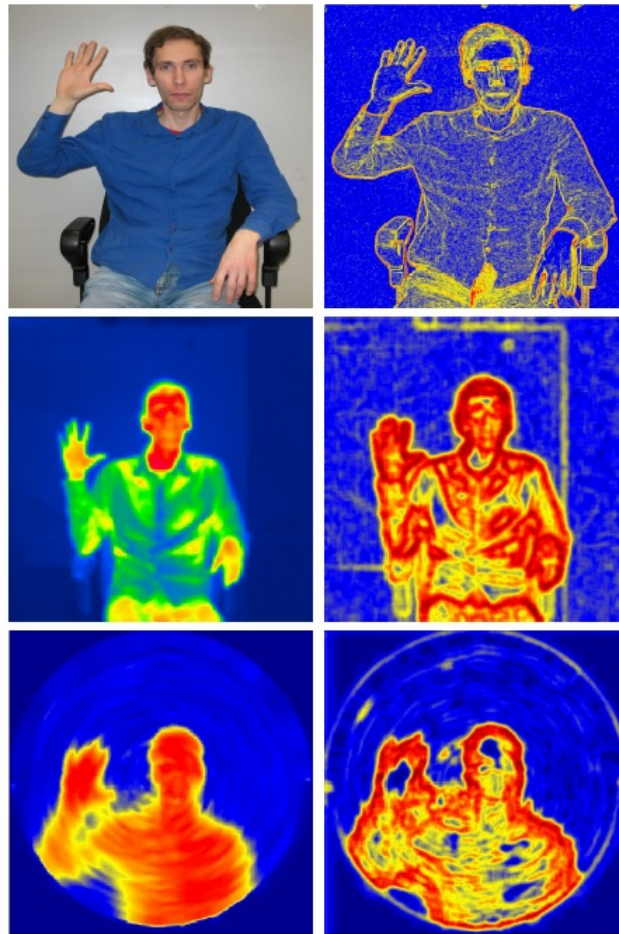


Figure 4.12: Example of the local entropy of a natural scene in the VIS-, IR- and in the THz-region.

From figure (4.12) it can be seen that the entropy is high at edges in the image, both in the image showing the VIS-scene and in the image showing the THz-scene. From this it can be concluded that the information content is concentrated around edges. This is common knowledge and is just restated here to emphasize the importance of the local Shannon-entropy as a statistical tool. It will be used in this thesis at different stages and imaging tasks.

The usefulness of Shannon-entropy/local Shannon-entropy has been proven in multiple VIS-imaging tasks. It was successfully used for image compression (see e.g. [1]) contrast enhancement [8], image quality enhancement [9] and noise reduction [4]. Especially the method of maximum entropy (see e.g. [10]) plays an important role for the implementation of specialized THz-reconstruction algorithms. In this, the method of maximum entropy is naturally suited to deal with the problems of image artifacts as introduced by mechanical scanning and the concept of blind de-blurring (see e.g. [11] and references

given therein for an introduction to the theory of blind de-blurring)¹⁴.

With this, the theoretical considerations are finished and the next part of this thesis presents results, which test the theoretical concepts presented in the first part. As this chapter discussed again, the line between hardware level and software level becomes more and more blurred. The experimental results, shown in the next part of this thesis, contribute on different levels to this process.

¹⁴Blind de-blurring refers to the process of estimating an unknown blurring kernel/transfer function from the measured data.

References Chapter 4

- [1] S. Aeron, V. Saligrama, and M. Zhao, "Information theoretic bounds for compressed sensing," *IEEE Transactions on Information Theory*, vol. 56, no. 10, pp. 5111–5130, 2010.
- [2] A. Buades, B. Coll, and J.-M. Morel, "A non-local algorithm for image denoising," in *IEEE Computer Society Conference on Computer Vision and Pattern Recognition*, vol. 2, 2011, pp. 60–65.
- [3] E. J. Candes and M. B. Wakin, "An introduction to compressive sampling," *IEEE Signal Processing Magazine*, vol. 25, no. 2, pp. 21–30, 2008.
- [4] S. G. Chang, Bin Yu, and M. Vetterli, "Adaptive wavelet thresholding for image denoising and compression," *IEEE Transactions on Image Processing*, vol. 9, no. 9, pp. 1532–1546, 2000.
- [5] G. Cristóbal, P. Schelkens, and H. Thienpont, *Optical and digital image processing: Fundamentals and applications*. Weinheim: Wiley-VCH, 2011.
- [6] M. F. Duarte, M. A. Davenport, D. Takhar, J. N. Laska, Ting Sun, K. F. Kelly, and R. G. Baraniuk, "Single-pixel imaging via compressive sampling," *IEEE Signal Processing Magazine*, vol. 25, no. 2, pp. 83–91, 2008.
- [7] FORSHAW, M. R. B., A. HASKELL, P. F. MILLER, D. J. STANLEY, and TOWNSHEND, J. R. G., "Spatial resolution of remotely sensed imagery: A review paper," *International Journal of Remote Sensing*, vol. 4, no. 3, pp. 497–520, 1983.
- [8] Guang Deng, "An entropy interpretation of the logarithmic image processing model with application to contrast enhancement," *IEEE Transactions on Image Processing*, vol. 18, no. 5, pp. 1135–1140, 2009.
- [9] S. F. Gull and G. J. Daniell, "Image reconstruction from incomplete and noisy data," *Nature*, vol. 272, no. 5655, pp. 686–690, 1978.
- [10] S. F. Gull and J. Skilling, "Maximum entropy method in image processing," *IEE Proceedings F Communications, Radar and Signal Processing*, vol. 131, no. 6, p. 646, 1984.

- [11] Haichao Zhang, Jianchao Yang, Yanning Zhang, and T. S. Huang, "Sparse representation based blind image deblurring," in *2011 IEEE International Conference on Multimedia and Expo (ICME)*, 2011, pp. 1–6.
- [12] Jिंगgang Huang and D. Mumford, "Statistics of natural images and models," in *IEEE Computer Society Conference on Computer Vision and Pattern Recognition*, 1999, pp. 541–547.
- [13] B. Kress and P. Meyrueis, *Applied digital optics: Micro-optics, optical MEMS, and nanophotonics*. Chichester and West Sussex and U.K and Hoboken and N.J: Wiley, 2009.
- [14] D. Ruderman and W. Bialek, "Statistics of natural images: Scaling in the woods," *Physical Review Letters*, vol. 73, no. 6, pp. 814–817, 1994.
- [15] C. E. Shannon, "A mathematical theory of communication," *ACM SIG-MOBILE Mobile Computing and Communications Review*, vol. 5, no. 1, p. 3, 2001.
- [16] A. Srivastava, A. B. Lee, E. P. Simoncelli, and S.-C. Zhu, "On advances in statistical modeling of natural images," *Journal of Mathematical Imaging and Vision*, vol. 18, no. 1, pp. 17–33, 2003.
- [17] Z. D. Taylor, R. S. Singh, E. R. Brown, J. E. Bjarnason, M. P. Hanson, and A. C. Gossard, "A reflection based, pulsed thz imaging system with 1 mm spatial resolution," in *IEEE/MTT-S International Microwave Symposium*, 2007, pp. 1161–1164.
- [18] R. Wang, L. Li, W. Hong, and N. Yang, "A thz image edge detection method based on wavelet and neural network," in *Ninth International Conference on Hybrid*, 2009, pp. 420–424.

Part II

Experimental Part

ISM-Imager System Evaluation

Contents

5.1	System Description	104
5.2	System Characterization	107
5.2.1	Characterization of the Tx/Rx-system	107
5.2.2	Characterization of the ISM-imager	113
5.3	Passive mode	115
5.3.1	Temperature Resolution	116
5.3.2	Spatial Resolution	118
5.4	Active mode	119
5.4.1	Tx-Rx crosstalk	123
5.4.2	Polarization effects	125
5.4.3	Off-axis illumination	127
5.5	Chapter summary	129

This chapter stands somewhat between the normally encountered chapters of theoretical basics and experimental results, because it gives measured performance parameters for the used THz-imager, the so called integrated security monitor (ISM-imager) and compares them to theoretically expected values (derived through simulation or physical estimation). The imager is briefly introduced in the first section of this chapter and then the system is evaluated in the following sections. The chapter presents measured results for the spatial- and temperature-resolution and derives what kind of THz-images to expect from the imager. The chapter ends with a short evaluation of the imagers active mode performance and concludes why this kind of THz-imager is not suited for active THz-imaging.

5.1 System Description

The idea behind the integrated security monitor was to combine information from different spectral regions to increase the detection probability of hidden threats and improve the overall image quality through image fusion techniques. To achieve that, the ISM-imager was temporarily able to use information from the visible-, the infrared- and the THz-region of the electromagnetic spectrum¹. However, the considerations presented in this thesis focus solely on the THz-part of the camera. Since the extension to the VIS- and NIR-region was achieved with two commercially available cameras that were integrated in the imager (see figure (5.1)).

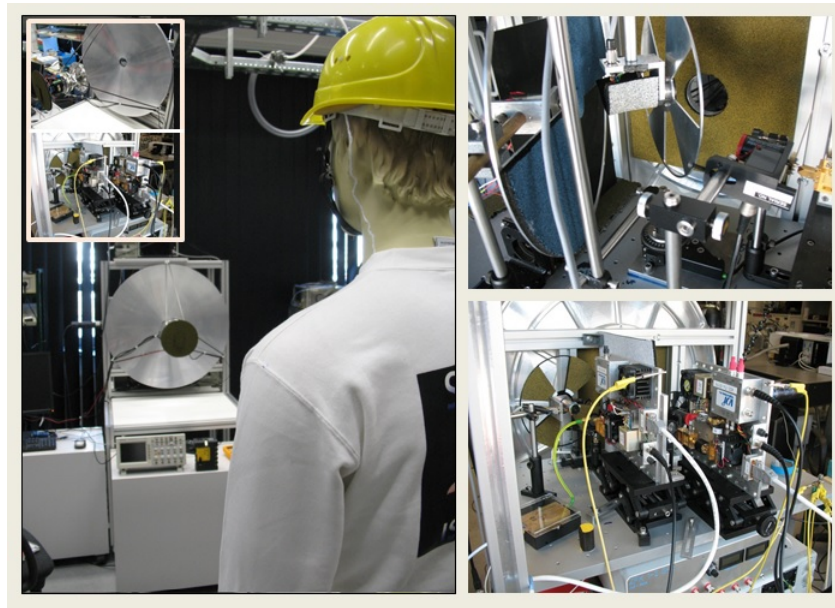


Figure 5.1: Images of the ISM-imager taken in the lab. The imager is shown on the LHS. The inset shows the tiltable secondary mirror (top) and the THz-electronics on the platform behind the primary mirror. The RHS shows again the THz-electronics (close-up).

Accordingly, the research effort focused on the THz-part of the camera and not on software development with focus on image fusion. However, when it is helpful for the respective argument, VIS- and NIR-images are shown in addition to standard THz-images. Throughout this thesis, when the term ISM-imager is used, it, therefore, refers to the THz-part of the camera.

As can be seen from figure (5.1), the ISM-imager uses a Cassegrain-type telescope (discernible by the center bore in the primary mirror). The size of its mirrors are 76 cm in diameter for the primary mirror and the secondary mirror

¹As was already stated, the ISM-imager was developed during a project of the same name. Only for the very limited time of the project was it possible to make measurements with the NIR- and VIS-camera as well. Hence, the focus, in this thesis, lies on the THz-measurements.

has a size of ≈ 18 cm in diameter. The secondary mirror is able to rotate and tilt. Its maximum velocity of rotation is 2000 rpm and its maximum tilt angle is 10° . In this way a circular field-of-view (FoV) with a diameter of 1 m can be scanned with the (spirally moving) secondary. The radiation collected by the telescope is channeled through the center bore with a diameter of ≈ 7 cm onto a platform behind the primary mirror, which holds the detection system and the electronics of the imager. The finite size of the primary mirror, as well as, the size of the center bore introduce optical aberrations into the system. These aberrations cause a varying deviation of the beam shape (from a fundamental Gaussian shape) in the center of the FoV and at its fringes. This in turn can cause image artifacts and a deviation from the "flatness" of the FoV. Both issues are addressed in the next section. In order to evaluate the severity of the deviations, a simulation of the optical properties is needed². An excerpt of the optics simulations, exemplifying the beam produced by the telescope at different tilt positions of the secondary mirror, is reproduced here and shown in figure (5.2)³.

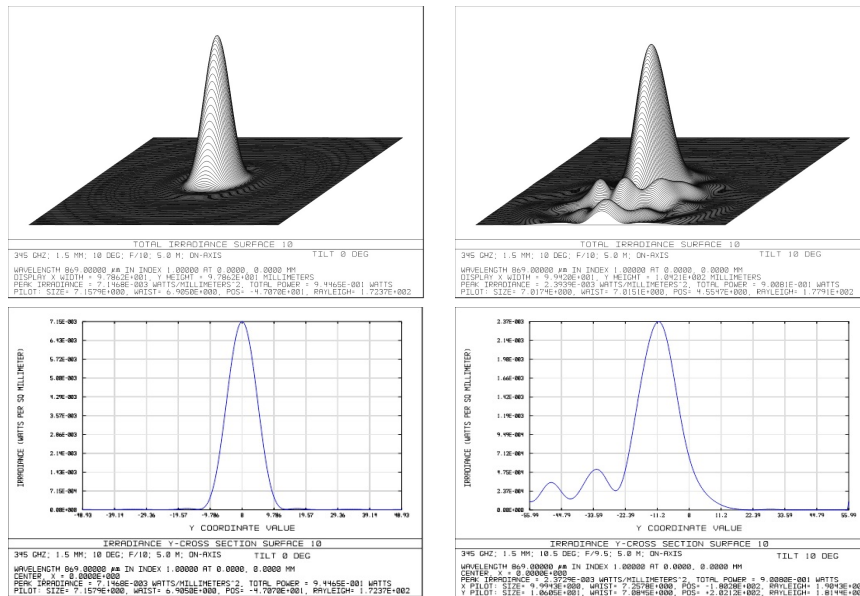


Figure 5.2: Excerpt of the theoretical optics simulations for the ISM-imager.

Even the theoretical simulation show considerable deviations from the ideal case. At 0° tilt (in the center of the FoV) the deviations are approximately ≈ 14 dB below the maximum value. At the edge of the FoV, at a tilt angle of 10° , the simulated deviations have increased to a value of ≈ 7 dB below the maximum. In addition, the beam is highly asymmetric.

²The optics simulation was supplied by the company Astro-und Feinwerktechnik Berlin-Adlershof GmbH that built the ISM-imager, according to given specifications.

³Since, figure (5.2) and figure (5.3) were supplied by Astro-und Feinwerktechnik Berlin-Adlershof GmbH the visibility of the results given in the figures is slightly limited. The images are reproduced here for sufficiency of the document

The two mirrors of the Cassegrain-type telescope channel the radiation through the center bore and bring it to a focus on the platform on the other side of the primary mirror. The geometric distances are shown in figure (5.3)

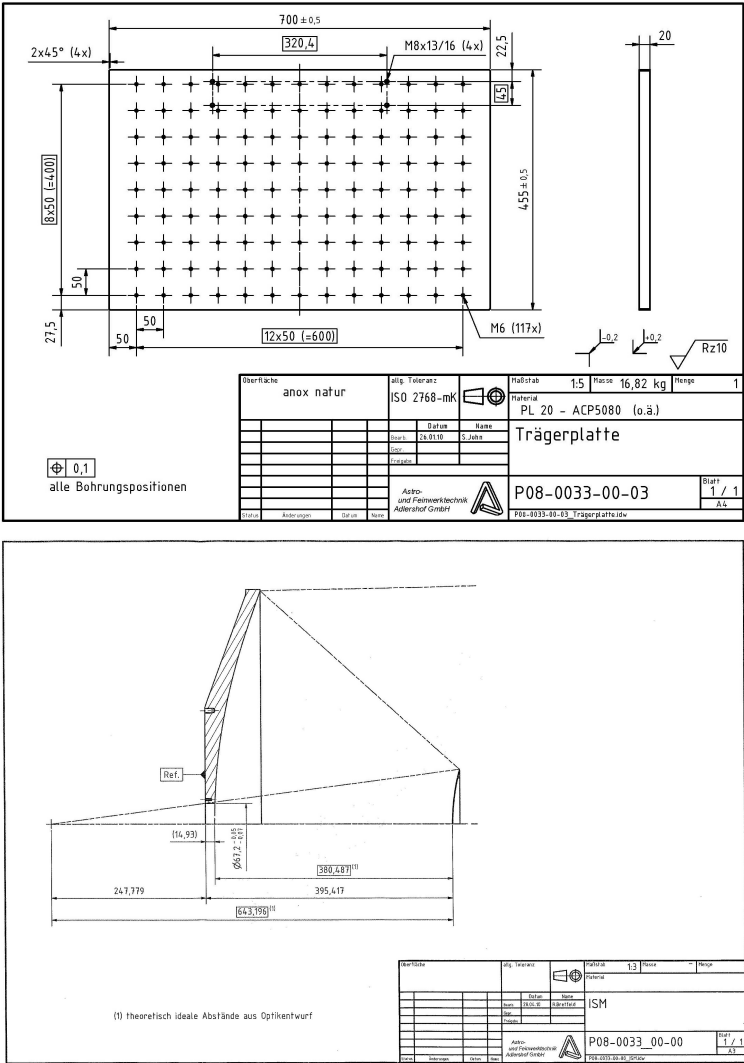


Figure 5.3: Dimensions of the platform for the THz-electronics of the ISM-imager (top) and general geometrical dimensions (bottom).

This completes the theoretical system characterization. The next section shows measurements that evaluate the major properties of the ISM-imager against the ideal state just presented. Deviations are to be expected since the Tx/Rx-system that is used in the imager already exhibits non-ideal properties (discussed in section (5.2.1)). This non-ideality as well as the deviations introduced by a real-world optical setup that is needed to adapt the Tx/Rx-system to the telescope (for details see section (5.2.2)), make the realization of the optimal

performance, shown in the optical simulations (see figure (5.2)), impossible in the first place. The next section will show with actual measurements what real-world performance was achievable with the ISM-imager⁴.

5.2 System Characterization

The system, the ISM imager, uses a Cassegrain telescope described above in conjunction with a Tx/Rx heterodyne system that will be described in the next (sub)section. The integration of the Tx/Rx system into the telescope forming the ISM-imager is discussed afterwards in section (5.2.2).

5.2.1 Characterization of the Tx/Rx-system

The Tx/Rx system consists of a YIG-based solid state transmitter (Tx) and a heterodyne YIG-based receiver (Rx). Starting with the Tx, it is shown in figure (5.4) together with its block diagram.

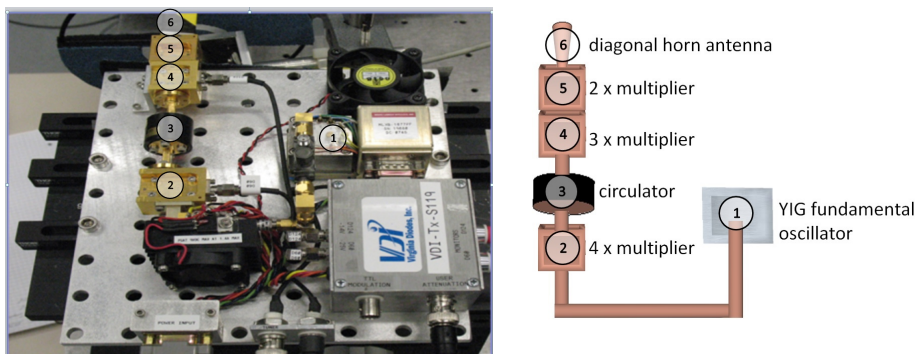


Figure 5.4: Tx (left) of the Tx/Rx-system from the ISM imager including its block diagram (right).

The Tx is a multiplier based source that uses a YIG-based fundamental oscillator whose frequency is increased in several discrete steps until exiting a diagonal horn antenna. The output radiation lies in the range from 340 GHz–360 GHz (tunable). The frequency increase is achieved with Schottky diode multipliers. The gradual process of frequency multiplication is shown in the block diagram of figure (5.4). The output frequency was indirectly verified with a measurement of the fundamental oscillator frequency in conjunction with a given multiplication factor of 24. This yields the aforementioned output frequency of ≈ 350 GHz.

For the usage in the ISM-imager, the output frequency is a parameter that is among the most important characteristics of the Tx. Additionally, the output power, beam quality and stability are also discussed as important characteristics in an imaging context in more detail. The setup that was used to

⁴This is connected to the sensitivity of the optical simulations to deviations from the ideal state. Unfortunately, a sensitivity analysis was not supplied by the manufacturer.

evaluate the aforementioned properties is shown schematically in figure (5.5)⁵. The setup was used to measure the output power of the Tx over a period of time > 5000 s determining the long-term stability of the source. For this measurement a power meter was used. Additionally, the frequency stability of the source was evaluated using a spectrum analyzer. The long term stability measurement is shown in figure (5.6) and the frequency stability measurement is shown in figure (5.7). The stability is one of the most important characteristics since the ISM-imager uses hardware scanning to acquire an image. The scanning process normally takes a few minutes depending on the integration time and undersampling factor chosen (details are discussed in the next section). After the presentation of the measurements follows a short discussion about the implications and interpretation of the results.

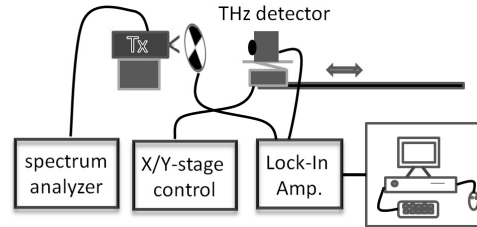


Figure 5.5: Setup used for the characterization of the source from the Tx/ Rx-system of the ISM-imager.

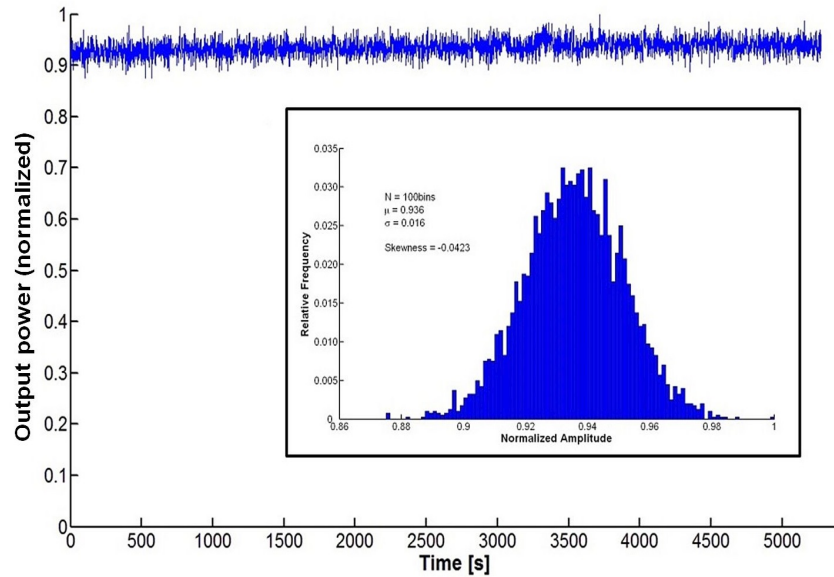


Figure 5.6: Tx long-term stability measurement and resulting histogram (inset).

Since the actual measurement was an absolute power measurement, the mea-

⁵Other important characteristics are polarization, linearity, etc. Although these characteristics were also measured in this thesis the focus lies on the aforementioned characteristics.

sured average power was ≈ 0.75 mW. However, as is known, power measurements in the THz-part of the electromagnetic spectrum are reliable only within an uncertainty of ten to twenty percent⁶. The statistical fluctuations around the average power value, as presented in figure (5.6), also contain a fluctuation component introduced by the used power meter.

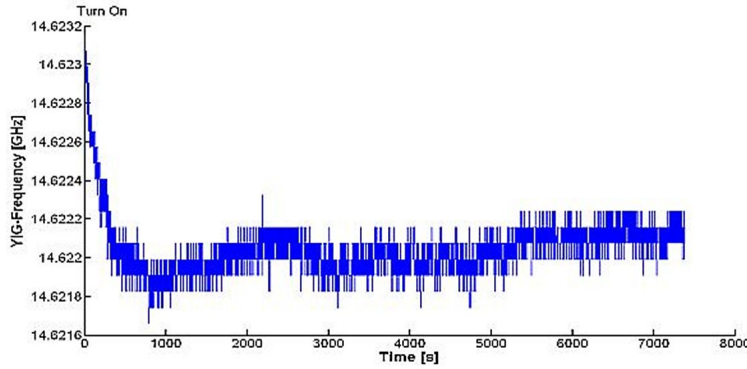


Figure 5.7: Tx frequency stability measurement.

The last characteristic that is considered for the Tx is the beam quality. For these measurements again the setup of figure (5.5) is used. This time, instead of a power meter, a Golay cell detector is used. The Golay cell is raster-scanned at varying distances from the Tx. To ensure that the distance is only varied in z-direction, a rail is used. The measurements are presented in figure (5.8) and the results are summarized in figure (5.9).

⁶The manufacturer certifies 1 mW output power for this type of source.

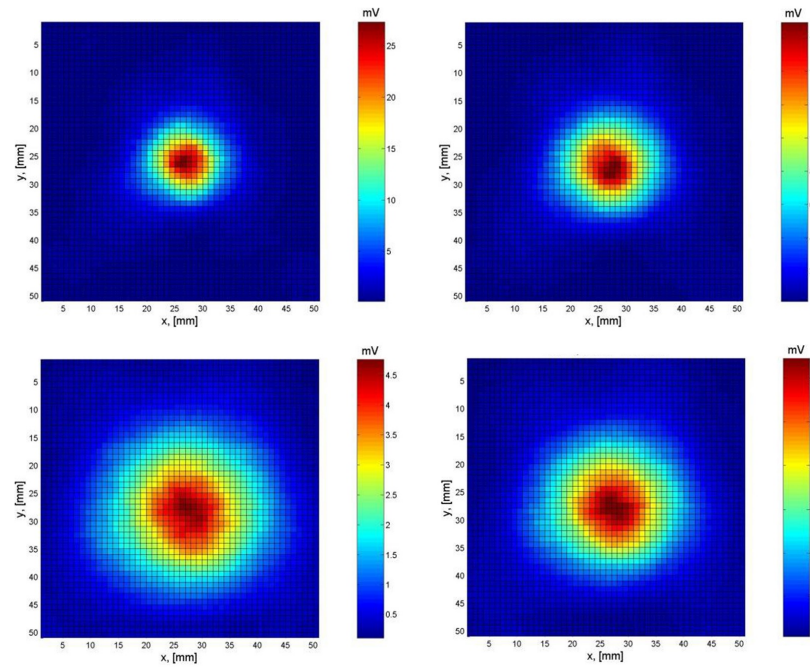


Figure 5.8: Tx beam shape measurements with varying distance Golay cell – Tx. Starting on the left in the top row with 55 mm distance and proceeding clockwise over 69 mm, 96.5 mm and 115.5 mm.

From the beam scans⁷ shown in figure (5.8), the beam waist position and radius are determined (see figure (5.9) for a graphical representation of the measured beam expansion results)⁸.

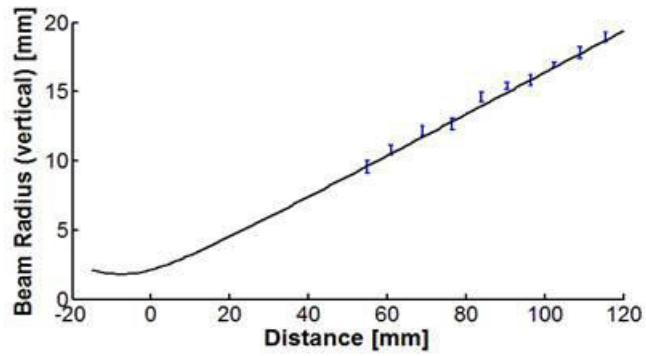


Figure 5.9: Tx determination of waist radius and position.

⁷Not all scans are shown here.

⁸Shown in figure (5.9) is just the vertical component. The horizontal component is very similar with slight deviations that are not visible in the graphical representation.

Tx characterization - results interpretation

After the characterization of the source it must be concluded that after switch-on the output radiation (frequency, power) is unstable for at least 20 min. Following these transient fluctuations, the output radiation is stable within less than 2%. The beam shape of the source is more than 80% Gaussian but still exhibits a small percentage (<15%) of higher Gaussian-modes⁹. The beam is also slightly asymmetric. It should be noted that the deviations from an ideal Gaussian-mode are significant and may be responsible for deviations in the optical setup when integrated into the ISM-imager.

The Rx with its respective block diagram is shown in figure (5.10).

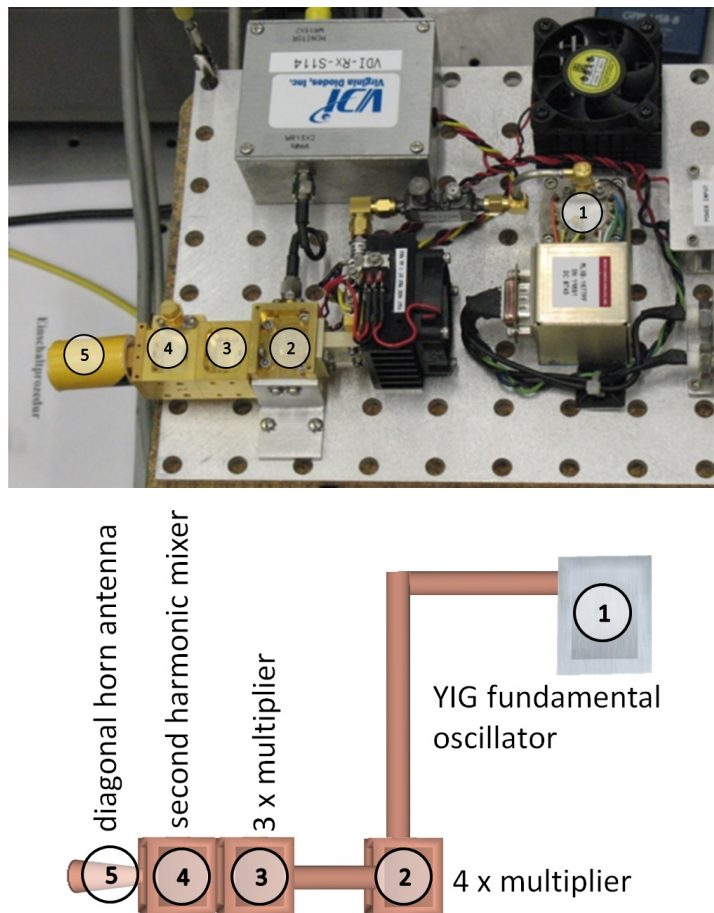


Figure 5.10: Rx (top) of the Tx/Rx-system from the ISM imager including its block diagram (bottom).

⁹The gaussicity was evaluated by taking cuts through the images of figure (5.8) and fitting a fundamental Gaussian-function (TEM_{00}) to these cuts.

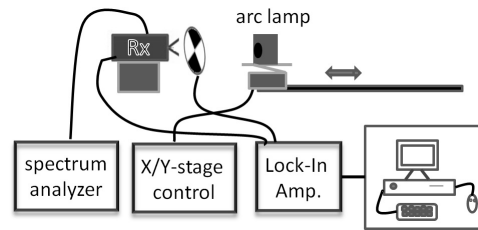


Figure 5.11: Setup used for the characterization of the receiver from the Tx/ Rx-system of the ISM-imager.

The evaluation of the Rx starts with an evaluation of the frequency dependent noise temperature. A schematic representation of the measurement setup for the Rx characterization is shown in figure (5.11). The characterization includes the frequency stabil-

ity, the noise temperature characterization and a beam shape characterization of the Rx. The frequency stability measurement uses again a spectrum analyzer. The noise temperature evaluation procedure is carried out according to the hot-cold method (details on the hot-cold method are also discussed in section (2.3.1)). The determination of the Rx beam shape is conducted using an arc lamp as radiation source, which is then raster scanned a certain distance in front of the Rx. The measured antenna profile is an important input for the ISM-imager characterization following in the next section. Additionally, as part of the characterization of the Rx, the Allan variance/time is measured. With the characterization, a statement for the optimal integration time in the presence of different noise contributions is possible.

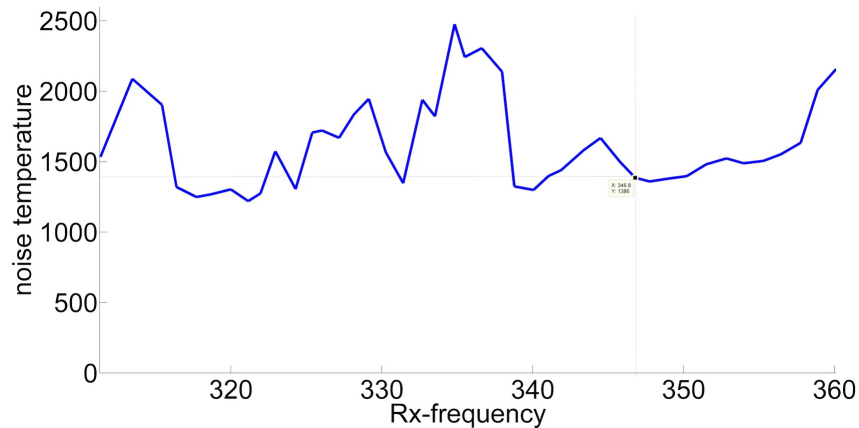


Figure 5.12: Measured frequency dependence of the Rx noise temperature using the hot-cold method.

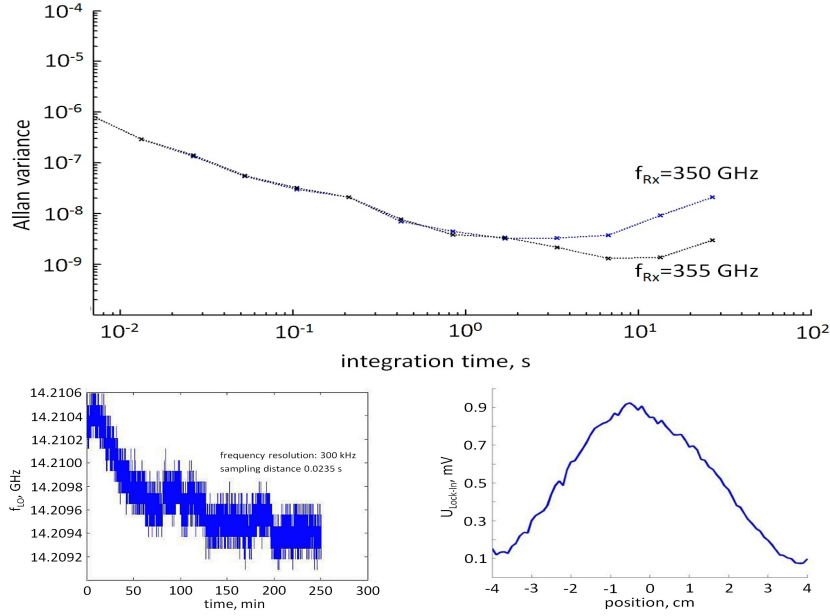


Figure 5.13: Rx measurements.

Rx characterization - results interpretation

The results for the Rx presented in figure (5.13) show again, similar to the Tx, that a stable operation is reached only after several minutes (≈ 65 min) of transient fluctuations. The beam profile of the Rx is also within some deviations of fundamental Gaussian-shape. Most notable is the Allan-time measurement which shows that the Rx allows several seconds of integration until the point of optimal integration is reached. As is shown in figure (5.12), the noise temperature, a very important characteristic for the Rx especially in passive mode, is frequency dependent. However, the point of the global minimum (320 GHz) is not chosen for the experiments since it lies too close to a water absorption line and would eventually limit the performance in a stand-off imaging setting. Instead, a local minimum around 347 GHz is chosen for the experiments with the ISM-imager.

This completes the characterization of the Tx/Rx-system. The system can now be integrated in the ISM-imager. The characterization of the entire scanner will be briefly discussed in the next section.

5.2.2 Characterization of the ISM-imager

This section deals with the necessary optical adaption to the THz electronics (Tx/Rx-system) for its use in the ISM-imager. Additionally, a few important parameters of the imager performance will be discussed. To achieve the aforementioned adaption (no loss of THz-power due to the optical mismatch between the telescope and the Tx/Rx-system), a beam adapter has to be used.

The adapter is comprised of several optical elements containing mirrors and lenses. All optical elements including the Tx/Rx-system have to be placed on the platform behind the primary mirror (shown in figure (5.3)). The choice was to implement the imager as an on-axis device, where Tx and Rx are situated on the optical axis of the imager. This choice has the advantage of making the optical components easier to align, resulting in better THz-images but it also introduces severe limitations regarding the Rx-Tx cross talk properties (details on Tx/Rx-cross talk will be discussed in section (5.4.1)).

The schematic setup of the aforementioned optical adapter is shown in figure (5.14).

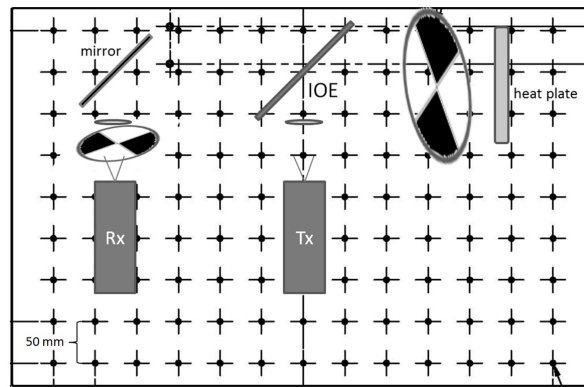


Figure 5.14: Optical adapter that allows an power efficient coupling of the Tx/Rx-system to the Cassegrain telescope of the ISM-imager.

The optical adapter facilitates measurements with the ISM-imager in very different modi. To optimize the performance in each mode, the optical adapter has to be slightly adjusted¹⁰. The optical element that has to be changed for the different modi is indicated in figure (5.14) with interchangeable optical element (IOE). In the basic configuration the IOE consists of a Mylar¹¹ beam splitter. For passive mode measurements the beam splitter is interchanged for a gold-coated mirror. These experiments are presented in section (6.1). Then, for phase-sensitive experiments presented in section (6.3), the IOE is exchanged for a metallic chopper-wheel that acts as a switchable mirror. For the last group of experiments with the ISM-imager, the optical adapter with the metallic chopper-wheel at the IOE position, is extended with another metallic chopper-wheel that is synchronized to the IOE chopper-wheel and acts as a modulator. These experiments are presented in section (6.4).

Despite the fact that the IOE has to be changed for the measurements in the different modi, the IOE's main function is to act as a mirror (switchable or not). Therefore, the performance of the ISM-imager regarding its beam

¹⁰For the experiments presented in this thesis optical elements from the adapter had to be interchanged. As the results of this thesis suggest for future experiments, the change of optical elements is no longer necessary. The measurement in a different mode can be facilitated by the use of SLMs.

¹¹Mylar is the brand name of biaxially-oriented polyethylene terephthalate manufactured by the company DuPont.

quality can be characterized for all modi together but there are slight variations of the measured values that should be taken into account. The beam size of the imager is such a key characteristic for all imaging applications that a general characterization of the beam was done as a first approximation of the achievable image quality, for a wide range of distances from the primary mirror. Thereby, the change of the beam size with varying distance and the change of overall beam quality could be measured. This was done using a rail system to ensure a fixed position in the x-y plane and a variation in the z-direction only. The results of this measurement are shown in figure (5.15).

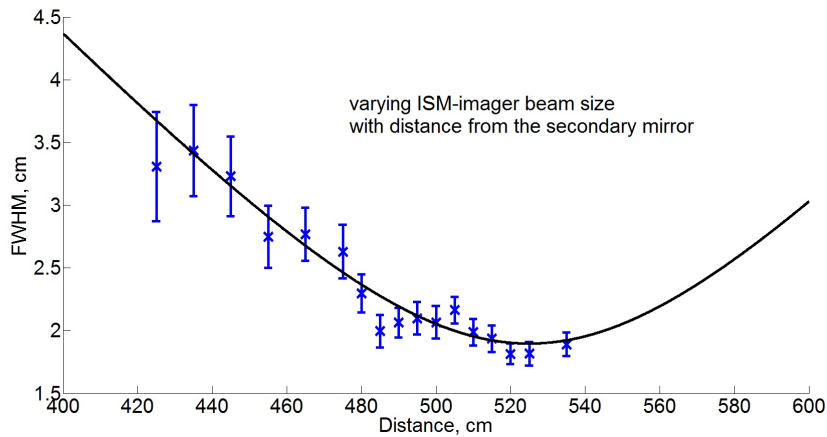


Figure 5.15: Changing spot size of the ISM-imager with changing distance from the secondary mirror (measured in passive mode, see next section for details on the passive mode).

Since most imaging was done at a distance of 5.2 m-5.4 m from the secondary mirror, a detailed evaluation of the spatial resolution and the varying beam shape at this distance (the scene distance) is added in the next section.

5.3 Passive mode

The passive mode, which is the imaging mode where only the THz-radiation that is emitted by the objects itself is of interest, is characterized in this section. In the passive mode the detected THz-signal, respective the SNR is highest when the detection bandwidth is maximal. As discussed earlier, the Rx of the Tx/Rx-system is a multiplier-based heterodyne receiver. This type of receiver has a very large bandwidth (at least several 100 GHz). The band limitation is introduced by the first amplifier following the receiver. To optimize the noise performance it is, therefore, crucial that the first amplifier has a noise temperature that is as low as possible. For the experiments presented in this thesis a low noise amplifier with a pass band from 1 GHz-2 GHz and a noise temperature of ≈ 45 K was used. Accordingly, the intermediate frequency (IF-frequency – difference frequency of the receiver mixer) was chosen in the middle of the pass band around 1.5 GHz. As mentioned above, the ISM-

imager performance changes slightly (with its parameters of operation e.g. IF-frequency) for the different modi. The two most important characteristics namely the temperature resolution and the spatial resolution are now discussed in detail.

5.3.1 Temperature Resolution

According to the Radiometer-equation and given the characteristics of the ISM-imager mentioned above, a temperature resolution of ≈ 1 K can be expected. However, the Radiometer-equation is just an orientation on what objects can be resolved in an imaging setting because of their temperature difference. The resolvable temperature difference varies over the FoV. The considerations start at the center of the FoV with an experiment shown in figure (5.16).

To determine the ISM-imager temperature resolution at the center of the FoV, figure (5.16) shows a measurement setup where a controllable temperature plate is placed at the center of the FoV. The rising temperature of the plate (U_{temp}) is measured over time as well as the detected THz-signal ($U_{Lock-In}$). With proper scaling, the THz-signal can be matched with the measured temperature of the temperature plate. With this procedure the detected THz-signal can be related to absolute temperature values. Also, the fluctuations in the THz-signal can be related to temperature fluctuations giving the imager temperature resolution. The result of this measurement is shown in figure (5.17).

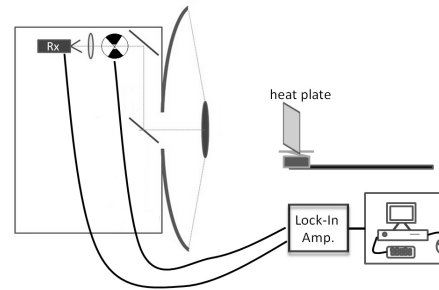


Figure 5.16: Setup used for the characterization of ISM-imager temperature resolution at the center of the FoV.

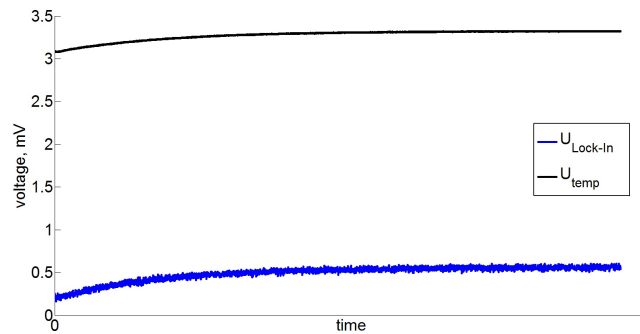


Figure 5.17: Measurement of the temperature resolution at the center of the FoV.

Measurement Procedure

1. measure $U_{Lock-In}$ and U_{temp} over time
2. scale $U_{Lock-In}$ and U_{temp} to the same value range
3. plot $U_{Lock-In}$ over U_{temp} and determine the coefficients of the linear model (input: final temperature was 44 °C and ambient temperature was 23.5 °C)
4. drift correction and determine standard variation

This measurement procedure gives only an approximate number of the temperature resolution since the heat plate is not a sufficiently stable temperature reference. Also, as already mentioned, the achievable temperature resolution is dependent on the position in FoV and also on the integration time. With an integration time (Lock-In time constant) of 100 ms the measurement procedure described above yields for the center of the FoV:

$$\Delta T_{Res}^{ISM} = 0.99 \text{ K}$$

The measured value is even better than the value derived from the Radiometer-equation but to achieve an actual estimate for an imaging setting the value for ΔT_{Res}^{ISM} (which is the value for one standard deviation) has to be adapted to a real imaging situation. To distinguish different objects in the scene due to their differing temperature, a value of 2-3 standard variations is suggested in the literature.

To arrive at a reasonable estimate for ΔT_{Res}^{ISM} , the method described above has to be conducted for every point of the FoV. This is not feasible. Therefore, a different measurement method was needed. The proposed method is a variation of the **hot-cold method**. A Siemensstar made of Eccosorb¹² glued onto a metal plate was used. The metal plate was placed in a container with LN_2 . Since Eccosorb is a poor heat conductor, the parts with the Eccosorb remained at room temperature (hot) whereas the metal plate showed a temperature gradient from 77 K at the container to almost room temperature at the top of the plate. Figure (5.18) shows a schematic representation of the setup (right) and the resulting image measured with the ISM-imager (left).

¹²Eccosorb is a RF/microwave absorber material marketed by Emerson & Cuming Microwave Products.

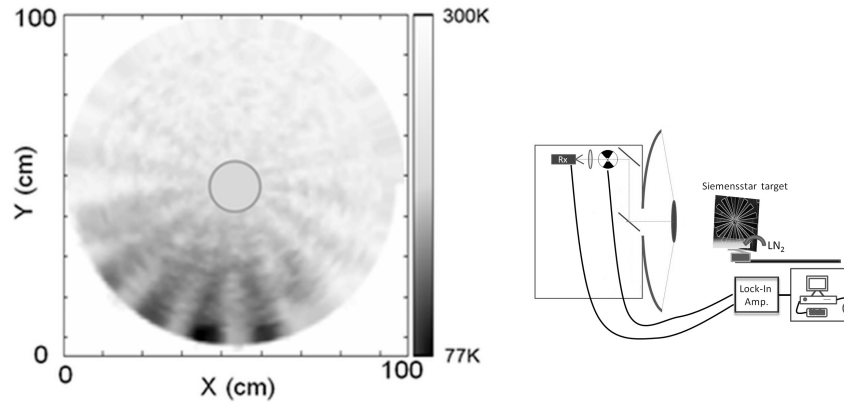


Figure 5.18: Setup (right) and measurement (left) of the temperature resolution for the entire FoV using a variation of the hot-cold method.

The measurement shown in figure (5.18) is actually a combined measurement of temperature resolution and spatial resolution in the FoV. The temperature gradient in the vertical direction causes objects in the image to eventually (with increasing y-position) become indistinguishable from the background. By measuring the temperature at different positions in the FoV an estimate for the temperature resolution ΔT_{Res}^{ISM} can be derived. For this measurement a value of $\Delta T_{Res}^{ISM} \leq 0.5$ K for an integration time of 1 s was determined. Additionally, since the imaged object was a Siemensstar, the arms of the star form wedges that eventually (with decreasing distance to the image center) become indistinguishable. Therefore, in the image center appears a "gray spot" whose dimensions determine the spatial resolution. Theoretically it is even possible to determine the entire modulus transfer function (MTF) from such a measurement but due to the poor SNR in the passive mode this is not feasible. To arrive at a characterization of the spatial resolution in the entire FoV, the next section shows beam scans at different positions in FoV, which allow a reasonable approximation.

5.3.2 Spatial Resolution

To characterize the spatial resolution of the ISM-imager (in passive mode), beam scans at different positions in the FoV were conducted. It was possible to access the different positions in the FoV by moving the secondary mirror of the telescope to a fixed position and conduct line scans with a similar setup to figure (5.11). As indicated in the setup, an arc lamp was scanned in front of the ISM-imager. This procedure allows a beam scan at certain positions in the FoV. A selection of the resulting scans is shown in figure (5.19) and figure (5.20).

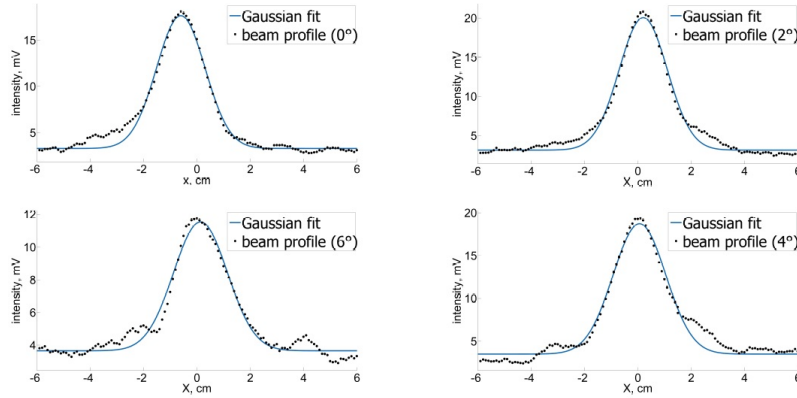


Figure 5.19: Beam Scans for the characterization of the spatial resolution of the ISM-imager in passive mode. Here, scans in horizontal direction (X) are shown.

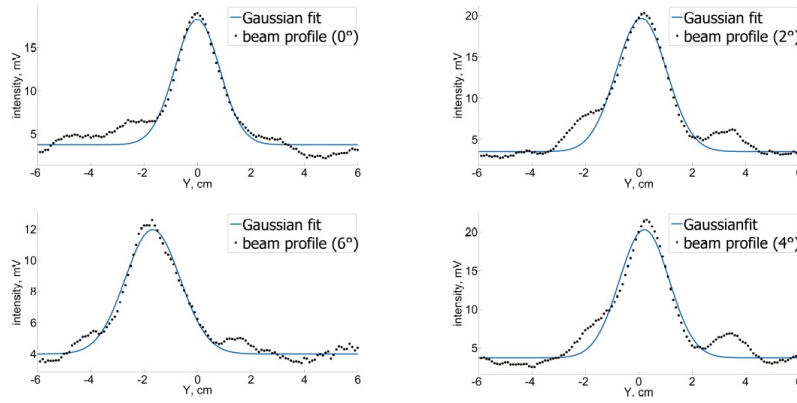


Figure 5.20: Beam Scans for the characterization of the spatial resolution of the ISM-imager in passive mode. Here, scans in vertical direction (Y) are shown.

The beam scans of figure (5.19) and figure (5.20) show the spot size at certain positions in the FoV. It is visible from the scans that the deviations from the fundamental Gaussian-shape become more and more distinctive with increasing distance from the center of the FoV. The severe deviations are caused by the up-front deviations of the Rx beam shape and optical misalignments in the optical adapter.

Since the spatial resolution in active mode is influenced by both beam profiles, that of the Rx and that of the Tx, the deviations in active mode are expected to be even more severe. Additionally, in the active mode more effects influence the image quality which are discussed in the next section.

5.4 Active mode

In active mode the IOE of figure (5.14) is interchanged for a beam splitter allowing the beam of the Tx to be coupled into the telescope and reflecting

the returning radiation from the scene into the Rx. Since beam splitter both transmit and reflect part of the incoming radiation some part of the incoming radiation can not be detected by the Rx and is lost. Ideally the ratio between transmission and reflection is $\frac{1}{2}$ but due to availability issues a ratio of 30% transmission and 70% reflection had to be chosen. This is not really an issue since the power delivered by the source is almost 1 mW, which is more than sufficient.

On the other hand, the spatial resolution in active mode can not be directly measured in ways described above, which is one of the first issues encountered in the active mode. As mentioned above, in active mode both beam profiles contribute to the resulting spatial resolution. At the scene distance from the primary mirror, the beam of the source and the beam of the receiver must be overlapping to detect the radiation coming from the overlap-area. Due to the necessary overlap, the beam can easily be distorted (see figure (5.21)).

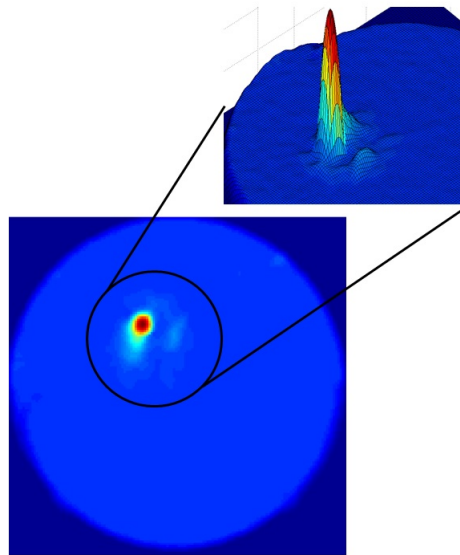


Figure 5.21: Overlapping Tx- and Rx-beams and resulting beam profile measured with the ISM-imager in active mode..

Figure (5.21) was measured by imaging the reflected radiation from a very small metallic object (point source). The spatial resolution in the entire FoV can then be determined by imaging special test objects like, for example, a Siemensstar or test patterns similar to the 1951 USAF resolution test chart. The edges in these images are then digitally line scanned and from the resulting characteristics the spatial resolution can be determined¹³. Figure (5.22) shows ISM-imager measurements of the aforementioned Siemensstar and test pattern targets, in active mode.

¹³This is similar to the knife-edge method. With a sufficient number of supporting points this procedure could even be used to determine the entire MTF of the imager.

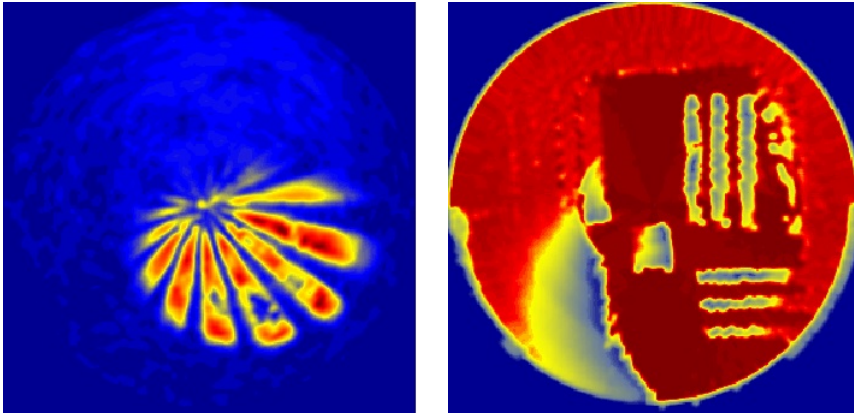


Figure 5.22: Example measurements to determine the spatial resolution of the ISM-imager in active mode in the entire FoV.

The Siemensstar and the test pattern show a spatial resolution that seems to be far better than in the passive case (indicated by the smaller gray spot). As figure (5.21) explains, this is a consequence of a poor overlap. This can create a smaller but distorted beam profile. Due to this behavior, the mapping of the scene in specific regions of the FoV can be distorted or as is the case in figure (5.22) the mapping completely fails. In addition, since the artificial illumination is highly directed illumination, the reflected (scattered) fraction of radiation coming from the scene can be very low or even undetectable. This holds especially true for metal objects where reflections play a more important role. In the case of non-metallic objects (e.g. persons) in the scene, scattering is more important but the power that is scattered back to the receiver is diminished by orders of magnitude (compared to the reflection on metallic objects).

With the diminishing detectable power, imaging artifacts that are potentially present during a measurement, now have a larger influence on the acquired THz-images. Figure (5.23) shows one such example measurement where a person/mannequin in the scene is imaged¹⁴.

¹⁴For this analysis and the analysis of the test objects a reduced image size of 150 x 150 pixels was chosen, to avoid the introduction of interpolation artifacts into the images.

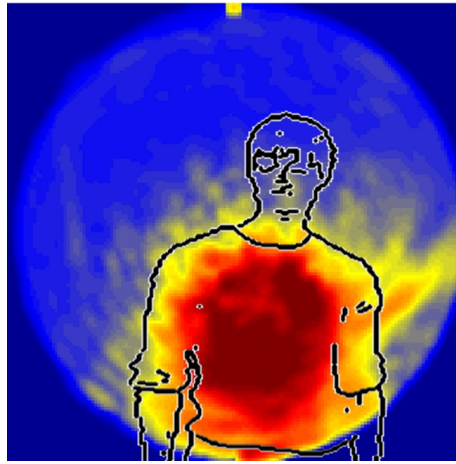


Figure 5.23: Example active measurement with a person in the scene.

The person in the scene is not clearly recognizable. The overlay suggests the contours of the person but the image is not an actual representation of the scene. In active mode, the ISM-imager is not capable of detecting a true THz-representation of the scene. To understand the reason for this behavior, the image of the Siemensstar (figure (5.22)) and of the person/mannequin figure (5.23) are analyzed in greater detail, with digital line scans and their respective time signals. Figure (5.24) shows the analysis of the Siemensstar and figure (5.25) the analysis of the scan of a person (figure (5.23))

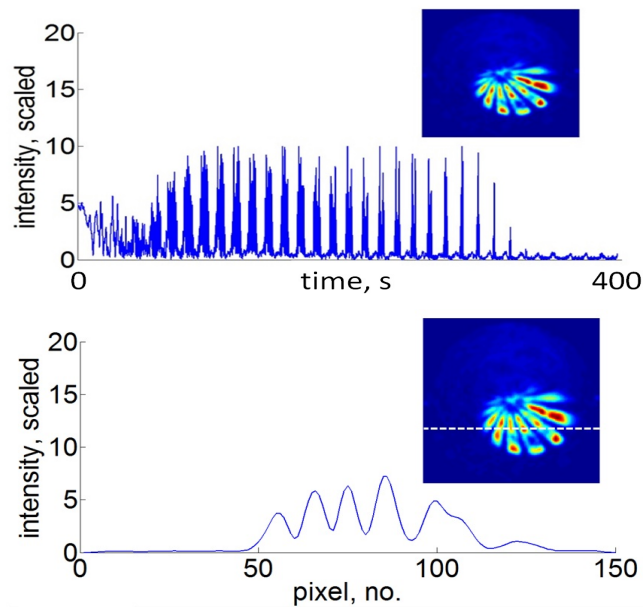


Figure 5.24: Analysis of the Siemensstar-image in figure (5.22) LHS.

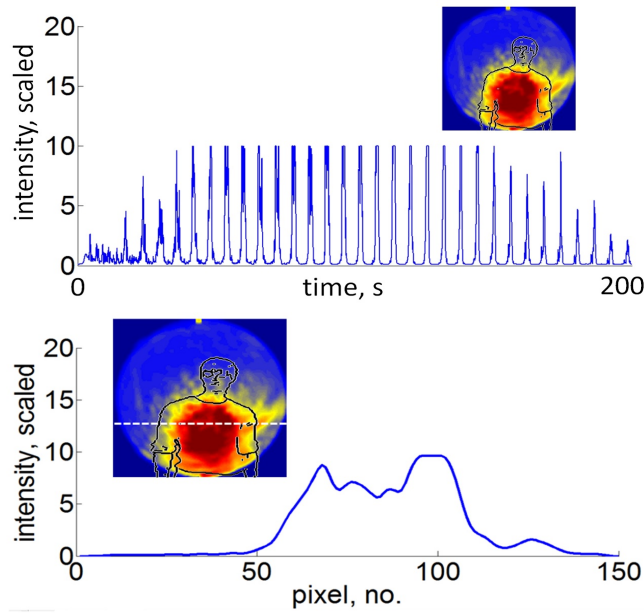


Figure 5.25: Analysis of the actively imaged person in figure (5.25).

As the analysis shows, there is a modulated signal present, whose modulation does not stem from objects in the scene. Even in regions of the images where no object is present, the modulated signal is observable. This analysis leads to the conclusion that measurement artifacts are responsible for this behavior. After the discussions in the previous chapters, two effects may be responsible, **Tx–Rx crosstalk** and/or **polarization effects**. Since it is intricate to prove these effects as the causes of the measured image artifacts, both effects will be discussed separately in more detail in the next sections.

5.4.1 Tx–Rx crosstalk

To understand the origin of the Tx–Rx crosstalk, the details of the telescope design in conjunction with the make-up of the optical adapter presented in the previous sections of this chapter need to be analyzed thoroughly. The following figure (5.26) shows a two step representation of the measurement setting.

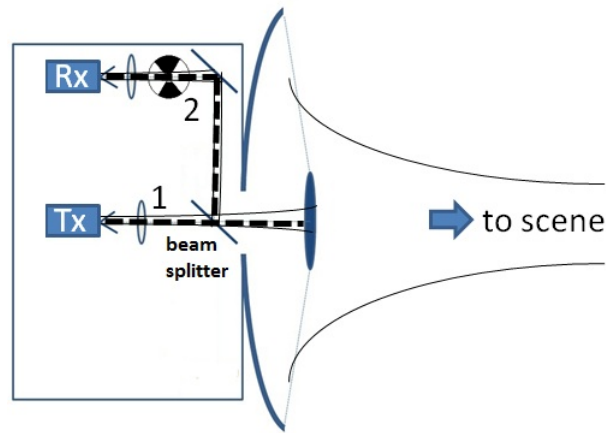
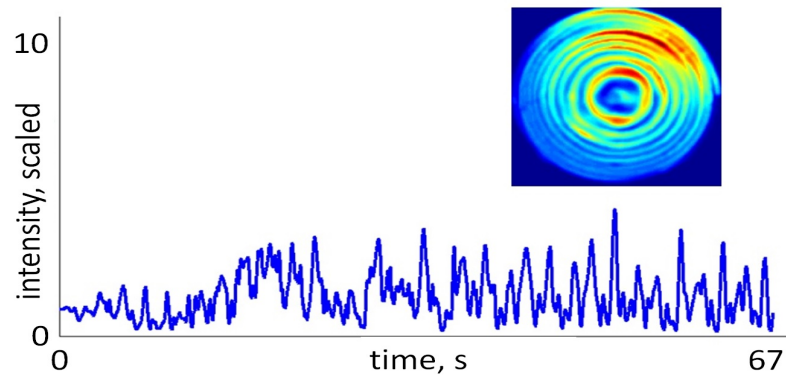


Figure 5.26: Two step measurement setting, explaining the origins of the Tx–Rx crosstalk.

As indicated in the figure, the crosstalk arises from a direct reflection at the secondary mirror, due to the fact that the used beam splitter partially transmits and reflects THz-radiation. In a first step the radiation emitted by the Tx is reflected back by the surface of the secondary mirror. Since the back-reflection travels on the same path as the incoming radiation (backwards), in a second step this radiation is reflected from the beam splitter and can enter the Rx.

If this two step process is really taking place, the Tx–Rx crosstalk can be evaluated by imaging an empty scene. In such a setting, no signal is expected to return to the Rx. In this case, any measured intensity can be exclusively attributed to a Tx–Rx crosstalk-effect. An example of such a measurement and its analysis are shown in figure (5.27).



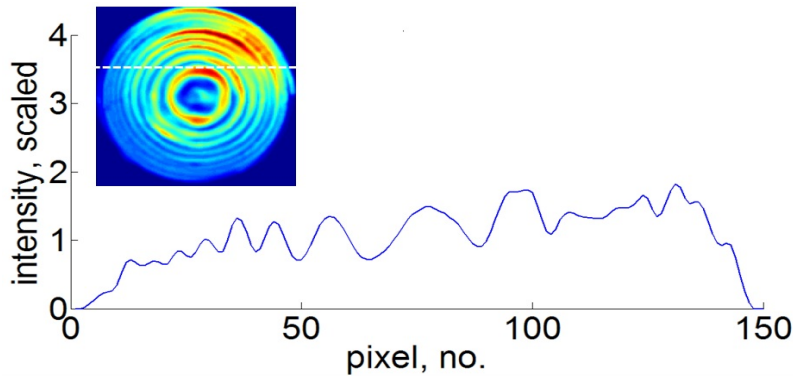


Figure 5.27: Active measurement and analysis of an empty scene.

The analysis shows that a signal can be measured regardless of an empty scene. It must be concluded that the proposed Tx–Rx crosstalk is present and if unmitigated prevents imaging in the active mode¹⁵. Additionally, the analysis shows a modulation on top of the offset caused by the crosstalk. The modulation can be attributed to the changing optical conditions during the scanning process due to the rotation and the tilting of the secondary mirror. To rule-out other measurement artifacts, the next section analyzes a measurement with a metallic object in the scene.

5.4.2 Polarization effects

As discussed in section (2.4.3), electromagnetic radiation that experiences at least three reflections during its time of flight can be subject to a rotation of its axis of polarization. Due to the scanning motion of the telescope’s secondary mirror, such a change of the axis of polarization would change over the time of a measurement causing a modulation of the measurement signal that does not stem from signal changes introduced by objects in the scene¹⁶. To investigate the aforementioned effect, a metallic object in the scene is imaged and analyzed in a cross-polarization setup (see figures (5.28)) and (5.29)).

¹⁵This is related to the subject of “flat-fielding”. Due to the strength of the cross-talk signal (orders of magnitude more powerful than a signal coming from the scene) and the fact that the cross-talk signal is not stable over time, the flat fielding can not be implemented for the ISM-imager in active mode.

¹⁶The change of the axis of polarization would only effect receivers that are polarization dependent. Since the Rx used for the measurements of this thesis is polarization dependent, the effects discussed in this section may contribute to the modulation encountered in the measurement signal (with and without objects in the scene).

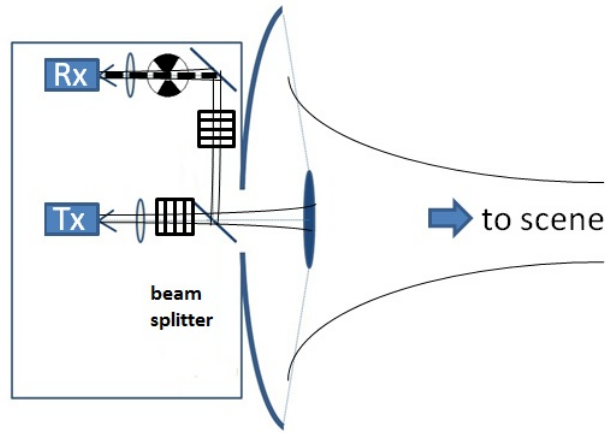
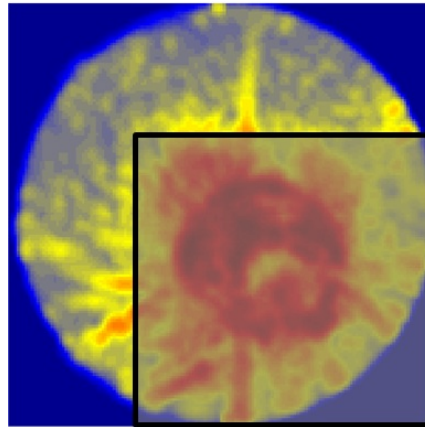


Figure 5.28: Cross-polarization setup. In the scene a metal object was imaged.

The cross-polarization setup is similar to the setup shown in figure (5.26). Additionally, it uses two identical wire grids that are placed in the beam path with a mutual orientation that allows no THz-radiation to enter the Rx due to the polarization of the radiation (see schematic representation of the wire grids in the figure). Only, if the polarization of the THz-radiation were rotated during an ISM-imager measurement, a signal would be measured. The results of this measurement are shown in figure (5.29)¹⁷.



¹⁷The overlay that is visible in the figure shows the contours of the metal plate that was imaged.

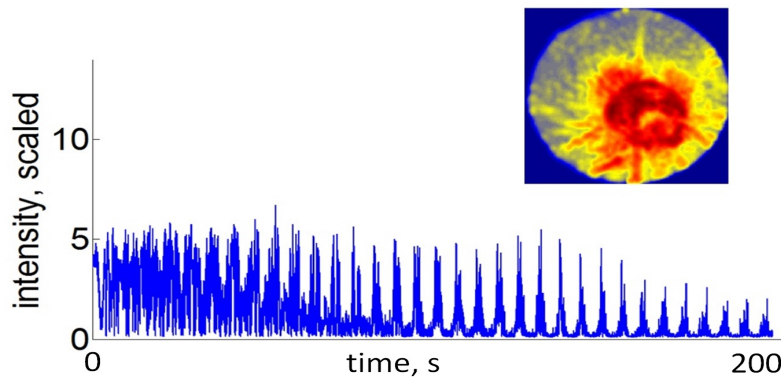


Figure 5.29: Active measurement and analysis of a metal object in the scene using a cross-polarization setup.

As visible from figure (5.29), again a signal is present which proves that also polarization effects are influencing active measurements with the ISM-imager. To verify that active measurements are indeed possible with the ISM-imager, a modified setup was adopted. The setup and example measurements will be briefly presented in the next section, also introducing a way to overcoming the problems/issues discussed in the last two sections.

5.4.3 Off-axis illumination

As already mentioned, the modified setup does not use the secondary mirror of the ISM-imager telescope to scan the scene. Also, it uses a different Tx and implements off-axis illumination. The beams of the Tx and Rx are overlapped at a distance of approximately 5.3 m in front of the primary mirror (approximately the scene distance). Then the object itself is moved (raster scanned) in an area of 0.5 m × 0.5 m. Every 0.005 m a measurement is taken. This setup is shown schematically in figure (5.30).

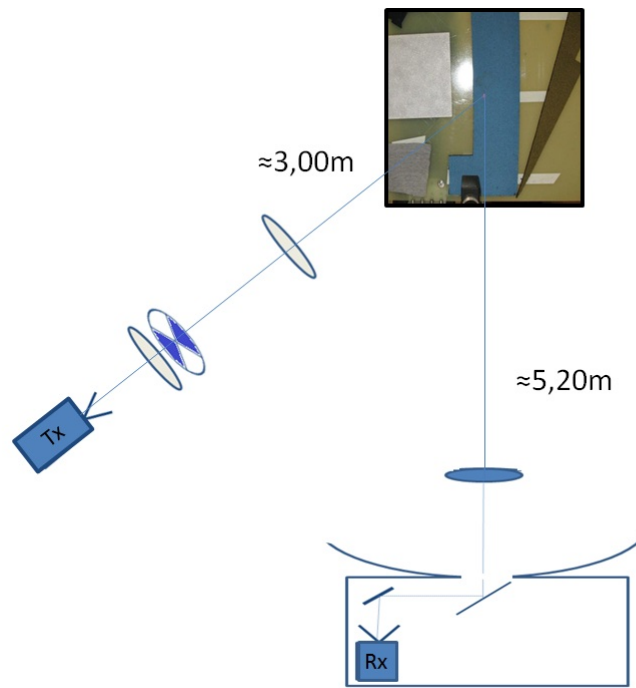


Figure 5.30: Schematic setup for the active mode raster scan measurements with the ISM-imager.

The following figure (5.31) shows an example measurement with the setup. On the LHS a digital camera image of the imaged object is shown and the RHS displays the measured THz-representation of the scene.

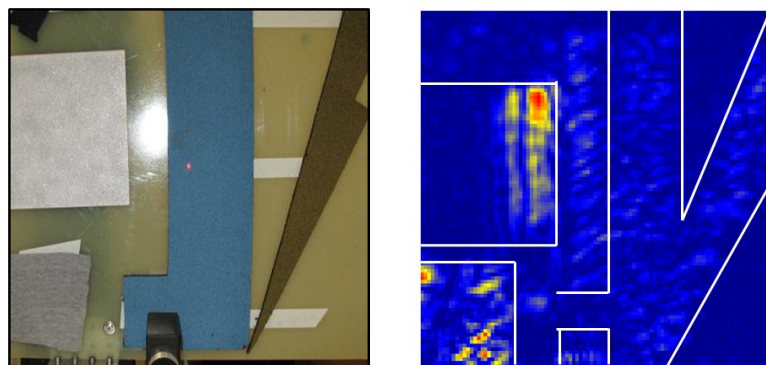


Figure 5.31: Example measurement with the active mode raster scan setup with the ISM-imager. On the LHS a digital camera image of the imaged object is shown and the RHS displays the measured THz-representation of the scene.

As can be seen from the THz-image, the imaging with this setup is quite successful. The image shows no crosstalk or polarization rotation artifacts. With this type of scan, the beam profile is not changing over time giving the same spatial resolution in every part of the image. The disadvantage of this setting is that it is not directly suited for THz-security imaging. In the setting of figure (5.30), the object has to be moved and imaging a scene of 0.5 m x 0.5 m actually took several hours. However, the general idea of scanning a scene of interest without having to move parts of the imager telescope would solve all issues described in this chapter.

5.5 Chapter summary

This chapter evaluated (characterized) some of the properties of the ISM-imager that are pertinent for the imaging process. In the passive mode the spatial resolution of the ISM-imager is limited to ≈ 1.5 cm and the temperature resolution to ≈ 1 K. On the other hand, the SNR is extremely limited (2 – 3) in passive mode due to the limited detection bandwidth available.

In active mode the SNR is limited only by the power of the THz-source, which is approximately 1 mW. The spatial resolution can not be directly measured. Instead, it has to be determined using special test patterns. In example measurements that were conducted, a spatial resolution < 1 cm was achieved but it changed dramatically over the FoV. In addition, the active mode of the ISM-imager suffers from problems with Tx–Rx crosstalk and polarization effects. It was shown that in a raster scanning setting the ISM-imager setup achieves the desired imaging capability in active mode. However, this raster scanning setting is not directly suited for THz-security imaging applications.

Due to the measurement artifacts discussed in the previous sections, the work of this thesis focuses mainly on the passive mode. However, the understanding of the cause of the image artifacts encountered in the active THz-images is essential for the extension of the novel methods described in this thesis to the active domain. The methods developed in this thesis are therefore mainly tested in the passive domain but their applicability also in the active domain is essential for a lasting contribution of the results presented in the next chapter. The discussion in this chapter leads the way for the extension of the methods to the active domain. The raster scanning setting introduced in section (5.4.3) shows no image artifacts and is the starting point for the extension. Since the raster scanning setting is not directly applicable, it has to be modified. The modifications include that objects in the scene are not scanned by moving them in a raster scan fashion, instead the scene is scanned by software scanning without any mechanical motion. This becomes possible with the help of THz-spatial light modulators. The development of a prototype THz-SLM as well as first imaging experiments are presented in section (6.5). Additionally, the off-axis illumination of section (5.4.3) is also considered in more detail in the outlook chapter in section (8.3).

Experimental Results

Contents

6.1	The experimental starting point – Passive Imaging with the ISM Imager	131
6.2	CS-based reconstruction of passive THz-Images	141
6.2.1	CS-based reconstruction of passive THz-Images - Results interpretation	152
6.3	Introducing the Lock-In Phase Space	153
6.3.1	Lock-In Phase Space - Results interpretation	163
6.4	Multinary Lock-In Phase Space	164
6.4.1	Multinary Lock-In Phase Space - Results interpretation	182
6.5	Developing a THz-SLM	183
6.5.1	Design	183
6.5.2	Optical Switching	186
6.5.3	THz-SLM imaging using CS-techniques	189
6.5.4	Developing a THz-SLM - Results interpretation	194
6.6	Chapter summary	195

This chapter could have been also entitled "Images, Images, Images", since it will present quite a lot of them taken under differing experimental conditions. The first section, like its title suggests, marks the starting point meaning the most fundamental physical ISM-imager setup is used for acquiring the images presented therein. This section will work as a reference point for the subsequent sections which will modify and enhance the fundamental setup. In the second section of this chapter, Compressed Sensing is used to reconstruct/interpolate (enhance) the image quality of some of the images acquired/presented in the first section. The third section then changes the perspective on the images a little bit. The technique presented in this section introduces the so called "Lock-In Phase Space" which offers a new view on (THz)-images by introducing a new acquisition paradigm. The following section entitled "Multinary Lock-In Phase Space" extends the introduced concept of the Lock-In Phase Space from a binary to a multinary phase space. This is achieved by extending the measurement setup with the ability of temperature threshold scanning. Many of the techniques presented in previous sections of this chapter can not reach their full potential, due

to the lack of a dynamic THz-SLM. So, in the last section of this chapter much of what was learned during this thesis is applied in an active THz-imaging lab setting to implement a first prototype of a dynamic THz-SLM. Here, the implementation process is documented and first results are presented and discussed.

6.1 The experimental starting point – Passive Imaging with the ISM Imager

This section acts as a reference for the following sections of this chapter as it presents the details on the passive measurement setting that is the starting point for the subsequent considerations. A schematic block diagram of the measurement setting is depicted in figure (6.1).

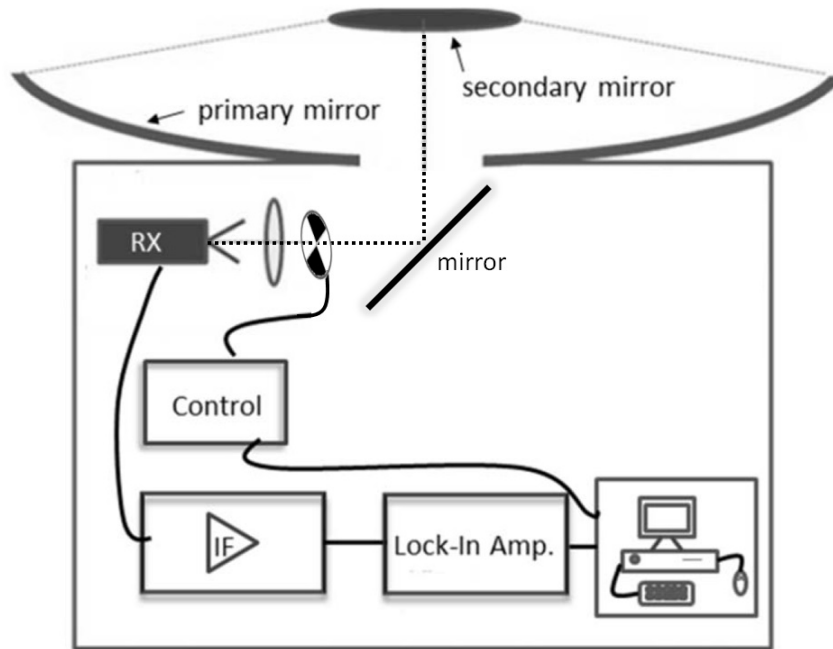


Figure 6.1: Passive measurement setting using the ISM-imager.

As already introduced in the last chapter¹, the optical system is based on a Cassegrain-type telescope with an ellipsoidal primary mirror of 76 cm diameter and a hyperboloidal secondary mirror with 18 cm in diameter. The optical system is designed in such a way that it provides an approximately Gaussian beam with its beam waist ≈ 530 cm from the secondary mirror (the scene distance). The secondary mirror can be rotated with up to 2000 revolutions per minute and simultaneously tilted by up to 10 degrees. In this way it is possible to scan a circular field of view of 1 m diameter in the imaging plane. The

¹A few key parameters of the ISM-imager are repeated here but here the emphasis lies on details of the detectable THz-power, for the derivation of the expected SNR in the images and other imaging constraints discussed in this section.

antenna beam of the Rx is imaged onto the secondary mirror by a lens made from Polymethylpentene (TPX) which is located 20 mm in front of a diagonal horn antenna. After passing the lens, the beam is redirected by a mirror. In the imaging plane the DSB noise temperature is ≈ 3850 K. The increase by a factor of about two as compared to the receiver noise temperature measured directly in front of the Rx can be attributed to different loss mechanisms (cf. section (5.2.1)). The dominant one is caused by the central blockage of the Cassegrain-type telescope. The calculations predict an increase in noise temperature caused by the central blockage by a factor of 1.9. Additional losses are due to atmospheric absorption ($<5\%$) and absorption by the TPX lens ($\approx 10\%$ loss). Beam profiles measured in the image plane at 5.3 m distance from the secondary mirror are shown in section (5.3.2).

According to the radiometer equation, the noise temperature of 3850 K corresponds to a minimum detectable temperature change of $\Delta T_{Res}^{ISM} \approx 0.3$ K. The measured value of ≈ 1 K is in good agreement with the theoretical value (see section 5.3.1 for details on the measurement). As discussed in the last chapter, the achievable temperature resolution in an imaging setting is, therefore, approximately 2 K-3 K. From the measured beam profiles a spatial resolution of $15 \text{ mm} \pm 5 \text{ mm}$ (depending on the position in the FoV) can be expected. Derived from these values, figure (6.2) depicts the passive imaging situation that is estimated according to the measured values just summarized.

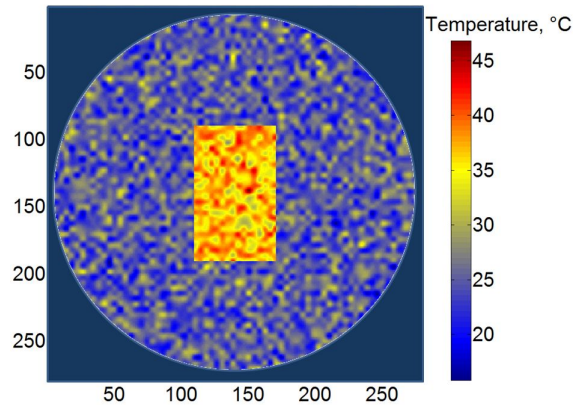


Figure 6.2: Estimation of the imaging situation derived from the passive ISM-imager setting described in this section.

The imaging situation shown in figure (6.2) is a visual estimation. It shows a 37°C object in front of a 25°C background. In the image Gaussian-noise according to the parameters given above is assumed. The calculations give a **PSNR** in the image of **5.5 dB**. In real imaging situations with the ISM-imager, the situation is worsened by the necessity to hardware-scan the scene to form an image. Due to the scanning motion the image pixels are measured on-the-fly. This causes different pixel measurements to be partly correlated and introduces motion-blur effects in the imaging process. The optimal choice for the integration time (τ_{LI}) is a trade-off between increasing PSNR and increasing

motion-blur with increasing scanning velocity. To evaluate the influence of motion-blur separately from the PSNR limitation, an object cooled to LN₂ temperature was imaged with varying τ_{LI} . The results are shown in figure (6.3).

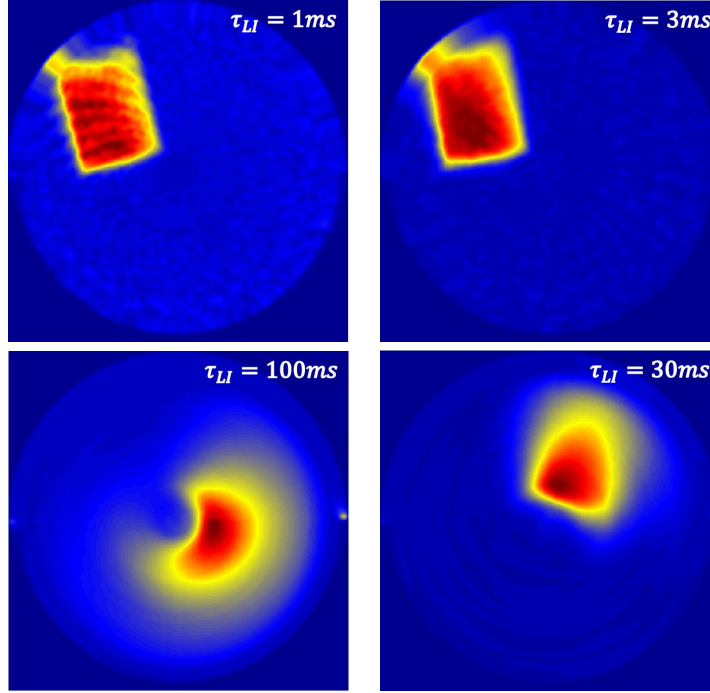


Figure 6.3: Imaged reference object cooled to LN₂ temperature for the separate evaluation of motion-blur with varying integration time. The images are taken with a constant velocity of the secondary for each image (60 rpm).

The increasing motion-blur is clearly visible in the images. Every image shown in figure (6.3) took ≈ 60 s to acquire. As can be seen, the PSNR is in the situation where a LN₂ target is imaged considerably higher². For an imaging situation with a person in the scene, the integration time has to be extended to about $30\text{ ms} < \tau_{LI} < 300\text{ ms}$. This in turn causes the measurement time to extend to $200\text{ s} < T_{meas} < 1000\text{ s}$. The exact measurement time depends on the velocity of rotation and the number of revolutions the secondary mirror uses to cover the entire FoV. To speed-up the measurement process spatial undersampling is used (see figure (6.4) (see also the detailed discussion in section (4.3)). The undersampled images presented in this chapter employ undersampling factors of 4-2. The undersampled images are interpolated (reconstructed) using classical interpolation methods of image reconstruction.³

²An estimated value for the PSNR lies between 13 dB-14 dB.

³In this chapter, an image size of 280 x280 pixels is used for the interpolation. In section (6.2) a new method of interpolation using Compressed Sensing techniques will be discussed and the first results will be presented.

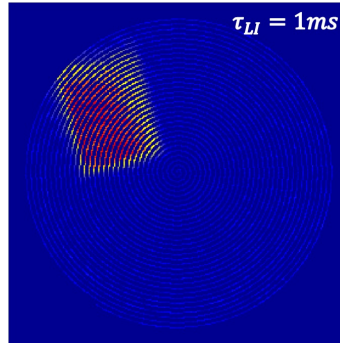


Figure 6.4: The image demonstrates undersampling for the motion of the secondary employed to speed-up the measurement process.

As can be seen in figure (6.4), the FoV is covered by 32 revolutions⁴. For an imaging situation, where a person in the scene is imaged, the situation is even more severe. This situation is demonstrated in figure (6.5).

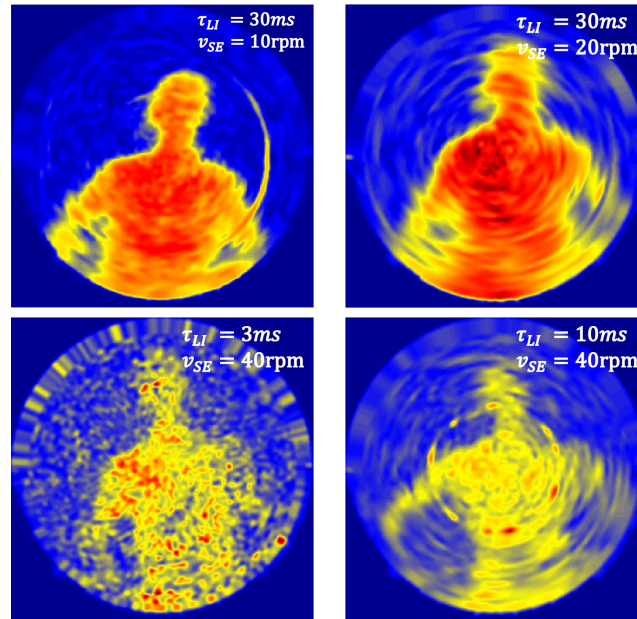


Figure 6.5: Imaged person with varying integration time and velocity of rotation the secondary mirror.

Figure (6.5) shows a scene where a person is imaged under differing acquisition conditions. It is visible that for a reliable detection $\tau_{LI} > 100ms$ has to be employed. This in turn causes a measurement to last $>400s$.

⁴In the case where the undersampling factor is chosen to a value of 2, 64 revolutions are used to cover the FoV.

The hardware used in the ISM-imager (detection system and detection bandwidth) is simply not equipped for fast image acquisition. Since the person in the scene has to not move the entire measurement time, the measurements are physically a real challenge for the person to be imaged. The prime objective for the imaging experiments presented here, is the test of new THz-imaging methods presented in the next sections, not the acquisition of high-resolution images. As long as the image quality is sufficient to demonstrate the performance of the novel techniques presented in this thesis, the image quality is only of subordinate concern. Still, to ameliorate the measurement condition, some of the new methods presented in the rest of this chapter were measured using a test object in front of a heat plate. Figure (6.6) shows a digital representation (LHS) and a THz-image of an aforementioned test object (RHS).

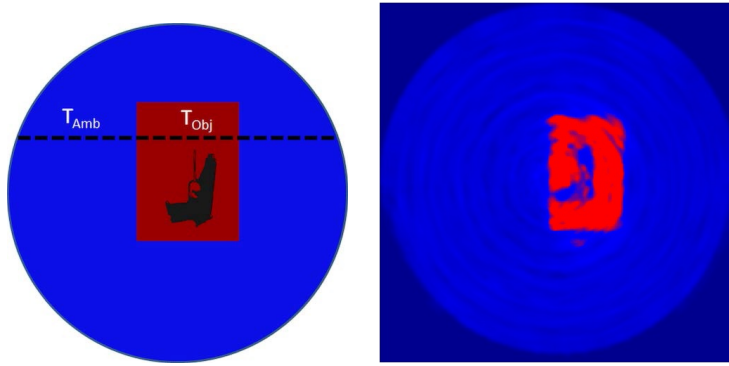


Figure 6.6: Digital representation (left) and THz-image (right) of a test object used for the passive imaging experiments.

The acquisition of the measurement shown in the RHS of figure (6.6) took 1000 s. It used an integration time τ_{LI} of 100 ms and a velocity of the secondary mirror (v_{SE}) of 4 rpm. Although the temperature of the heat plate in the image can be adjusted between ambient temperature and 40 °C, the PSNR appears to be less than in the case of an imaged person (given the same measurement conditions) due to non-homogeneous emission properties of the heat plate. However, the image quality is sufficient for the intended tests. On account of the position of the heat plate in the scene (no involuntary movements as for an imaged person), even the trigger guard of the mock-up weapon is visible in the THz-image.

Different from analyzing just the image for specific tasks, it is also helpful to analyze the time sequence of the acquired intensity measurements directly. The time sequence for the test object measurement is shown as an example in figure (6.7).

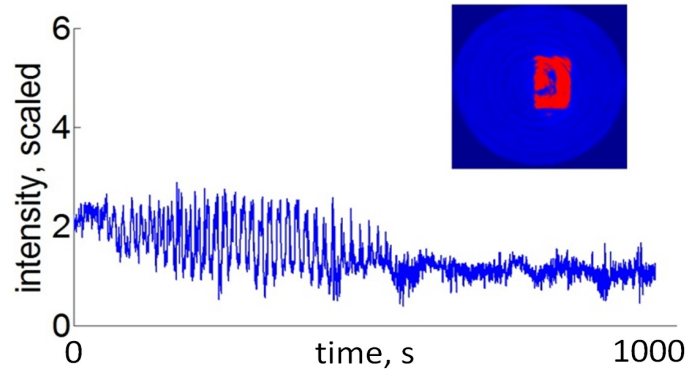


Figure 6.7: Time sequence of the intensity measurement for the THz-image in the RHS of figure(6.6).

T_{Amb} , the ambient temperature, is visible in the time sequence as offset. The temperature of the object T_{obj} in the scene is visible in the intensity time sequence of figure (6.7) as a levitation in the signal above the common offset value. The time sequence is also helpful as it provides direct access to a quantitative evaluation of the noise level. The time sequence in figure (6.7) shows measured intensity values acquired in an Lock-In amplifier (LIA) measurement scheme (see again figure (6.1)). A LIA measurement scheme also allows the measurement of relative phase information (relative to the LIA reference signal) that might offer additional information about the scene. For the measurement of the test object the phase time sequence is shown in figure (6.8).

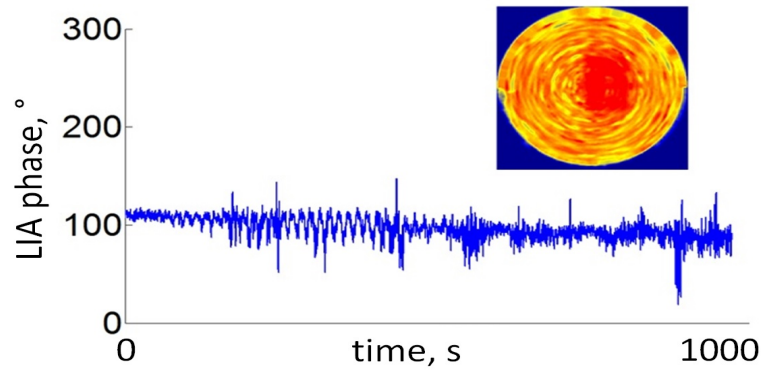


Figure 6.8: LIA phase time sequence for the THz-image in the RHS of figure(6.6).

Even in the phase domain the heat plate is clearly visible but the test object in front of the plate can not be resolved. The time sequence of the phase signal also offers no additional information that might be used to either enhance the intensity images or increase the detection probability of hidden objects. However, if the phase signal could somehow be modified during the measurement

(on the hardware level), additional useful information might become accessible. A new technique, that allows the aforementioned procedure, will be introduced in section (6.3). Also, for specific imaging situations, the knowledge of the geometric distances in the scene is helpful. To determine geometric distances in the imaging situation, digital camera images as well as IR-images are used (in specific cases) in conjunction with the THz-images. Figure (6.9) demonstrates the idea⁵.

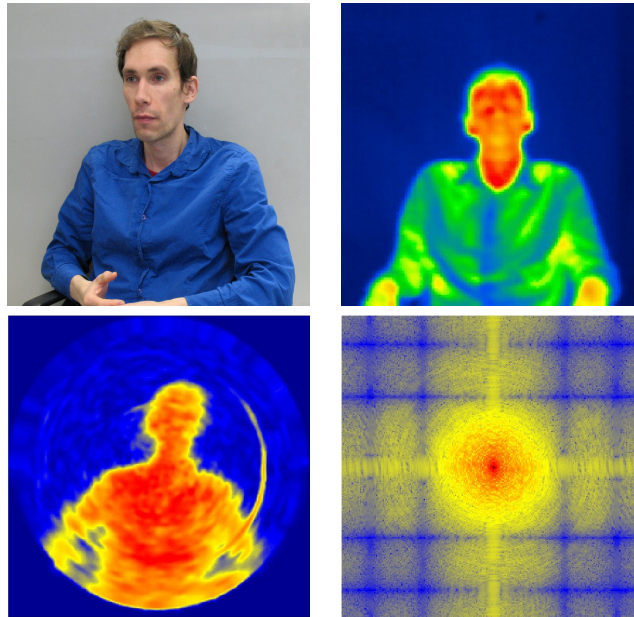


Figure 6.9: THz-, VIS- and IR-image of an example scene. Also shown is the frequency content of the THz-image (Matlab fft2 procedure - bottom row on the RHS).

The top row of figure (6.9) shows a digital camera image of the scene (LHS) and an IR-camera image on the RHS. In the bottom row the THz-information about the scene is shown. The LHS shows a THz-image taken with the ISM-imager and the RHS presents a Fourier-analysis of the THz-image on the LHS. All of these different frequency information are used to improve the image quality and detection probability for the different THz-images. Similar to the analysis of the test object it might be helpful to look at the time sequences as well. The intensity time sequence as well as the phase time sequence for the THz-image in figure (6.9) are shown in figure (6.10).

⁵Due to the fact that the IR- and VIS-cameras could not be permanently integrated into the ISM-imager, the scenes had to be reenacted, which limits the usefulness of the IR- and VIS-images a little bit. Still, the IR- and VIS- images provide valuable insights in the general setting of the scene and the geometric distances of the objects therein. In specific cases, they also supported the post-acquisition image processing of the THz-images.

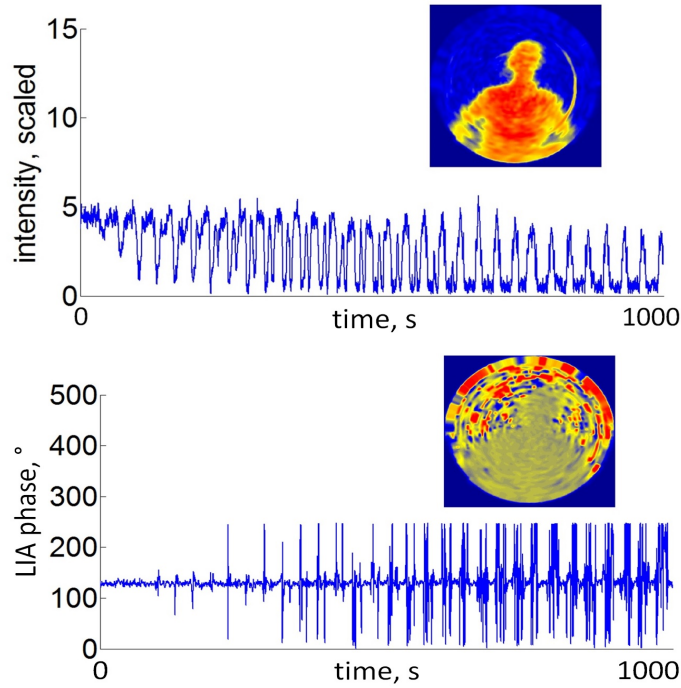


Figure 6.10: Intensity time sequence (top) and Phase time sequence (bottom) for the THz-image in figure (6.9).

As can be seen, the intensity signal shows periodic changes, whereas the phase signal exhibits mostly random behavior aside from spike like bursts. Still, an object (person) seems to be visible in the scene. In the rest of this chapter the phase analysis will prove valuable, especially when the Lock-In phase space has been introduced.

Before this section is concluded, a few passive THz-images that were acquired with the setup introduced in this section, are presented. Some of the images are used throughout this thesis and especially in section (6.2) to demonstrate some CS methods. In the next section CS-based reconstruction techniques are discussed on some of these images⁶. Here, the images will just be introduced in the spatial domain, leaving the presentation of a detailed analysis for the section in which they are used. All images exhibit certain image artifacts that will also be addressed there. The THz-images are a selection from over 2000 images acquired during the PHD-time, showing the results of varying acquisition parameters. The acquisition parameters are given in the appendix in section (A.3) as reference. The images are separated into two groups. The first group of images contains examples measured with a spatial undersampling factor of four and the second group with an undersampling factor of two⁷.

⁶These methods are developed on the software level but with the help of a THz-SLM may also be employed on the hardware level in future experiments.

⁷The distinction of the undersampling factor is of major importance for the evaluation of the reconstruction success (see section (6.2)).

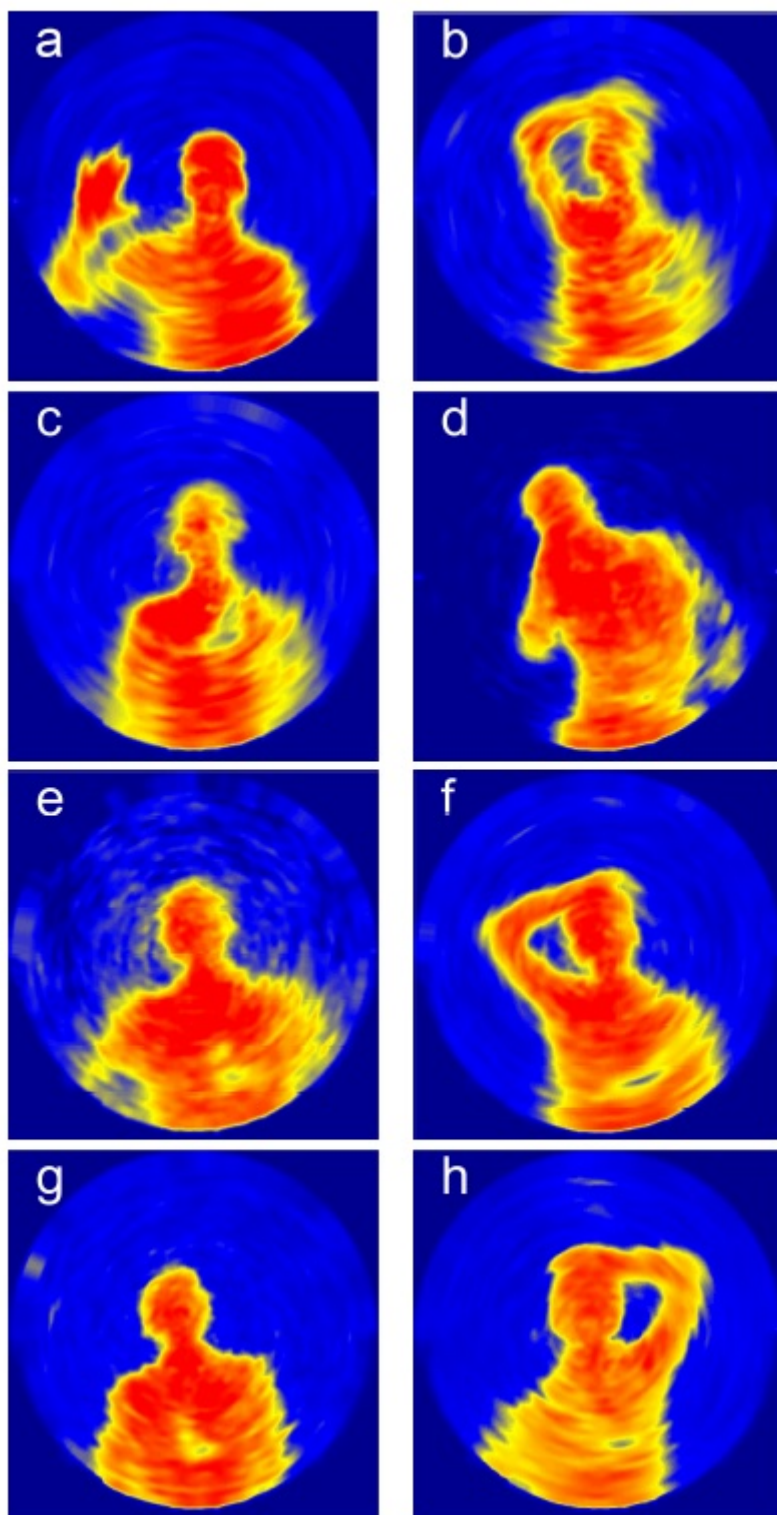


Figure 6.11: Passive THz-images with undersampling factor four.

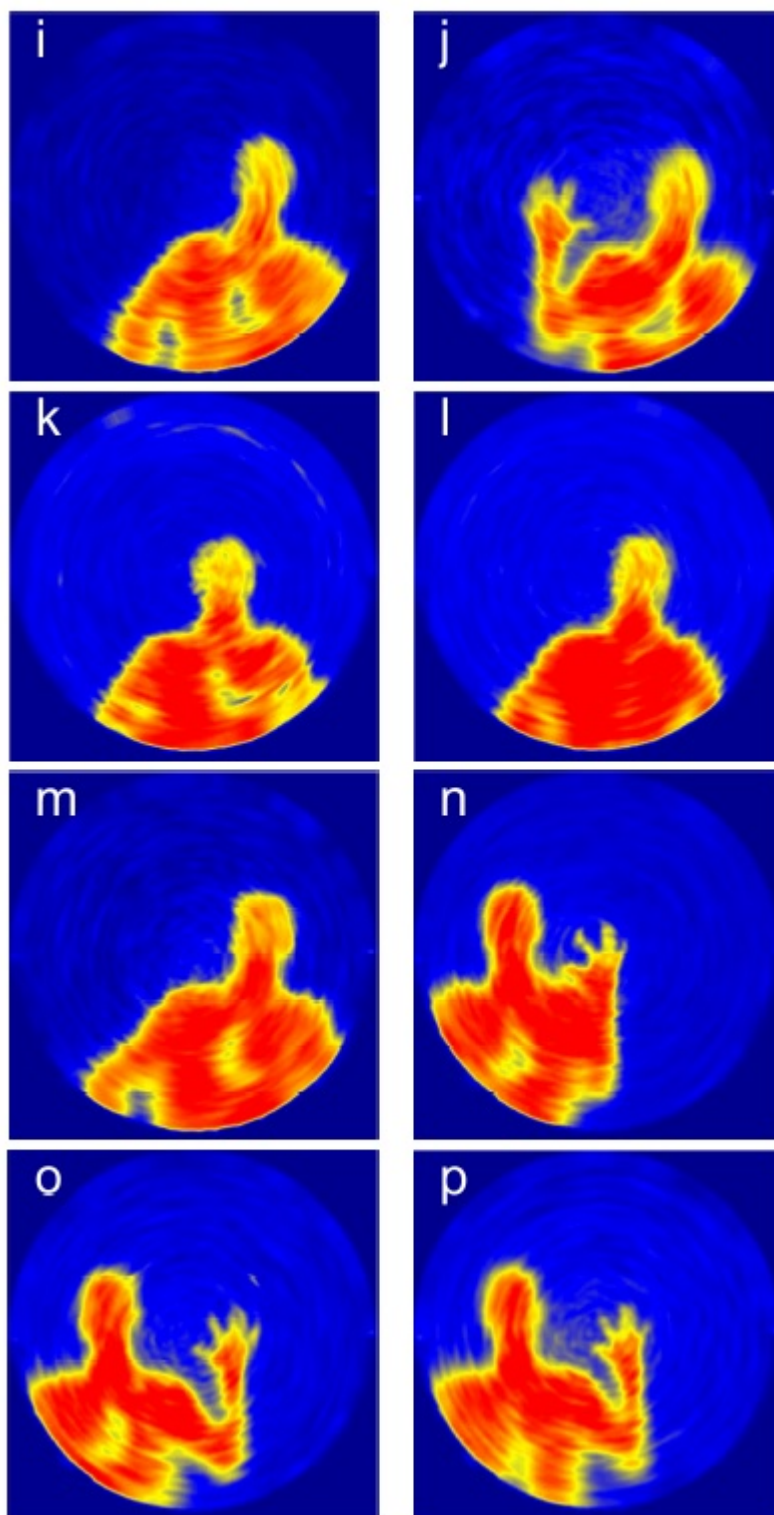


Figure 6.12: Passive THz-images with undersampling factor two.

6.2 CS-based reconstruction of passive THz-Images

The passive THz-images a-h and i-p presented in the previous section in figure (6.11) and figure (6.12) demonstrate the capability of the ISM-imager to detect hidden threats when used in a passive imaging modality. However, all images exhibit certain image artifacts that hinder automatic object detection and also reduce the detection probability. All images have been acquired with some spatial undersampling. The images a-h with an undersampling factor of four and the images i-p with a factor of two.

In this section, image reconstruction will be applied in order to ameliorate the aforementioned image quality problems. Translated into CS-terminology, the goal is to reconstruct the undistorted image designated as x that is affected by some artifacts and thereby transformed into the image x' . The aforementioned setting leads to the fundamental reconstruction equation (6.1).

$$y = \Phi \cdot B \cdot \Psi \cdot \alpha + n \quad (6.1)$$

In equation (6.1), y denotes the measured image. To simplify the notation y can be thought of as a suitably serialized⁸ column vector of size $m \times 1$. The original image x can, with the help of the transformation Ψ be expanded in a different domain, according to the equation $x = \Psi \cdot \alpha$. This transformation can be thought of as a sparsifying transformation from the spatial domain to a sparse domain, where the components of the image x are described by the column vector α . As introduced in chapter (3), Φ describes the physical setting of the imaging system, here the ISM-imager. The approach now is, to use Φ to describe the nominal behavior of the imaging system and the quantity B models deviations from that nominal behavior. With the aforementioned chosen vector approach, Φ , B and Ψ can be formulated as simple matrices. That means that the matrix Φ describes the nominal mapping process of the ISM-imager from the scene to its THz-representation x . The deviations from the nominal behavior are then modeled by the matrix B . The last component in equation (6.1) is the column vector n which models an additive noise component⁹.

Following equation (6.1) the matrices Φ , B and Ψ have to be determined for a successful reconstruction. Therefore, the rest of this section follows the path set forth by equation (6.1). The next paragraph is concerned with Φ which is equivalent with modeling the necessary physical properties of the ISM-imager and the mapping process itself. The following paragraph then focuses on the deviations from the ideal mapping process that introduce image artifacts into the resulting THz-images. Specifically, this paragraph focuses on the spatial undersampling and in turn on the so-called smearing effect. Then the matrix Ψ is discussed. As mentioned before, it is equivalent with a transformation to a domain where the image x has a sparse representation (see chapter (3) for details)¹⁰. The last paragraph of this section is then concerned with measuring

⁸There may also exist an influence on the results due to the chosen serialization procedure. This however, is not further investigated here.

⁹For the discussion in this section additive Gaussian noise is assumed. This assumption is supported by noise measurements that were done by this author but are not discussed in detail in this thesis.

¹⁰As was discussed in detail in chapter (3), the success of CS-techniques is directly linked to the sparsity of the signal.

the reconstruction success of the CS-approach using two example images.

The two example images are taken from the two lists presented in the previous section. The first one is image c from the list with an undersampling factor of four and the second is image j from the list with an undersampling factor of two. Both images are presented in their original form (without classical interpolation) in figure (6.13).

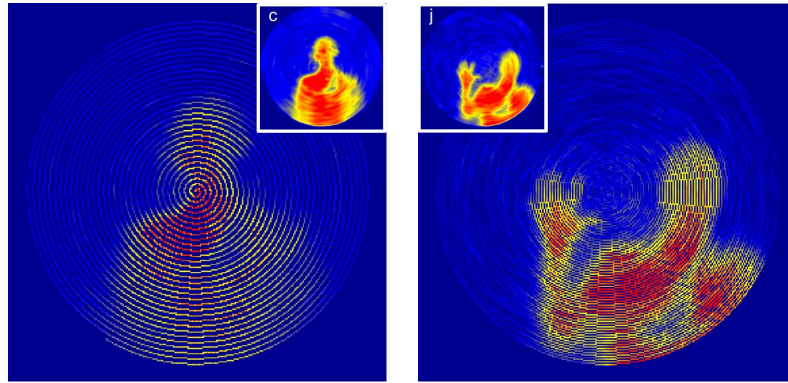


Figure 6.13: Original THz-images used for the CS-reconstruction. On the LHS the original of image c from figure (6.11) and on the RHS the original of image j from figure (6.12) are shown. In each case the insets show the images from the previous section, which are processed with a classical nearest neighbor interpolation.

As can be seen, both example images exhibit the effects of severe spatial undersampling. The amount of undersampling is defined by the chosen number of pixels for each image (refer again to section (4.2) for details on the optimal number of pixels and spatial undersampling). Also, in both original images a smearing effect is visible that most likely stems from the mechanical motion of the secondary mirror in conjunction with the chosen parameter combination for the acquired individual samples per pixel and the chosen value of the LIA time constant. The insets in figure (6.13) show a nearest-neighbor interpolation of each original image. In the insets and equivalently in the images c and j from figure (6.11) respective figure (6.12) from the previous section the aforementioned smearing-effect is even more pronounced. The nearest-neighbor interpolation uses, as the name suggests, neighboring values to interpolate missing values. Since the original values already contain the smearing-effect, the nearest-neighbor interpolation amplifies this image artifact further.

One way to overcome this image artifact is to use CS-techniques for the interpolation process. In CS-terminology one speaks of reconstruction instead of interpolation since the objective of CS is to recover/reconstruct the real image despite missing values and adverse influences by the imaging setting. One possible way to achieve this objective in a CS-framework is to use a-priori knowledge for the reconstruction process. In the case relevant here, the a-priori knowledge about the measurement process namely the mechanical scanning procedure is used. Therefore, the next step in the CS-based reconstruction is to model the mechanical scanning process. For the scanning a multitude of

possible motion patterns is imaginable. In order to optimize for measurement time two motion patterns are most prominent (as discussed in section (2.3.2)). The scanning motion used by the ISM-imager is the spiral scanning motion. For this motion the mechanical elements are optimized for a fast coverage of a large, circular field-of-view of tens of cm diameter. From a mechanical point of view such a FoV is accessible in <1 s. When the spiral motion is used, the faster measurement speed comes with a price. The image pixels no longer form a rectangular grid and the pixel itself change in size depending on their position in the field-of-view. The following image demonstrates this for a measured scanning path and a number of example pixels in the field-of-view of the ISM-imager.

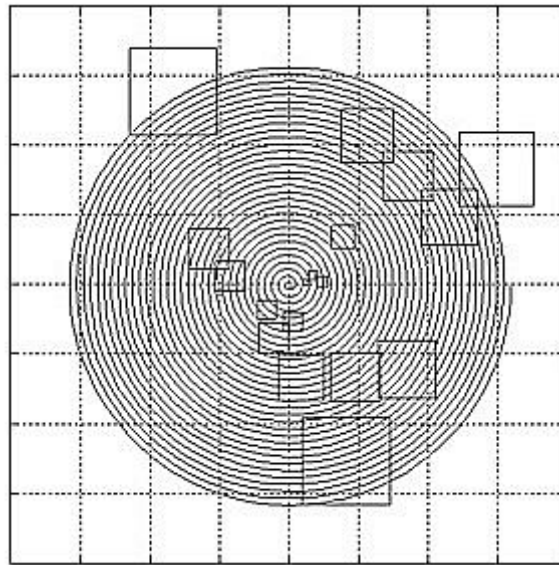


Figure 6.14: Measured spiral scanning path demonstrating the changing pixel size over the field-of-view of the ISM-imager for a number of example pixels. For each pixel shown, a constant arc length on the spiral path and a constant time per pixel is used to derive the pixel size.

In figure (6.14), it is visible that the pixel size changes multiple times from the center of the FoV to its outer rim. Following the spiral path a constant time per pixel is used as a criterion to determine the pixel size at every position¹¹. Eventually, a grid with equally sized pixels is used for the digital representation and is placed over the grid of “physical” pixels. As can be seen from figure (6.14), the physical pixel size influences multiple pixels of the equally spaced grid, depending on the position in the FoV and the number of pixels in the equally spaced grid. The optimal number of pixels respective the optimal image pixel size was already discussed in detail in section (4.2). Here, only a brief consideration on the apparent image quality of the original THz-images

¹¹The lower left corner of the square that is used to indicate the pixel size is the position for which the pixel size is computed.

is restated. A visual consideration of the optimal pixel size for the original images of figure (6.14) is shown in the following figures (6.15) and (6.16).

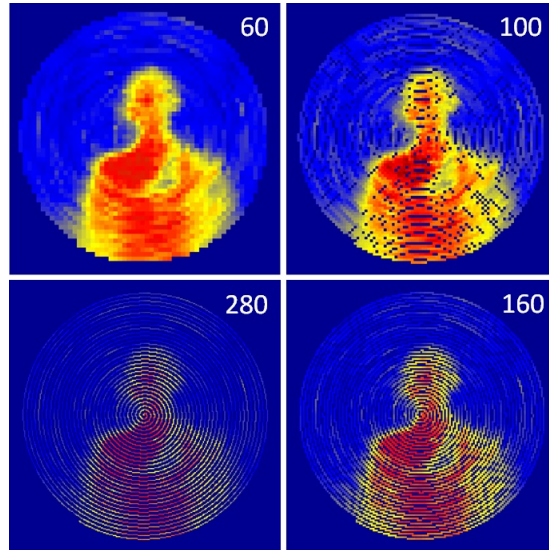


Figure 6.15: Changing number of digital image pixels (equally spaced grid) for the original image c of figure (6.13) and its influence on the general image quality.

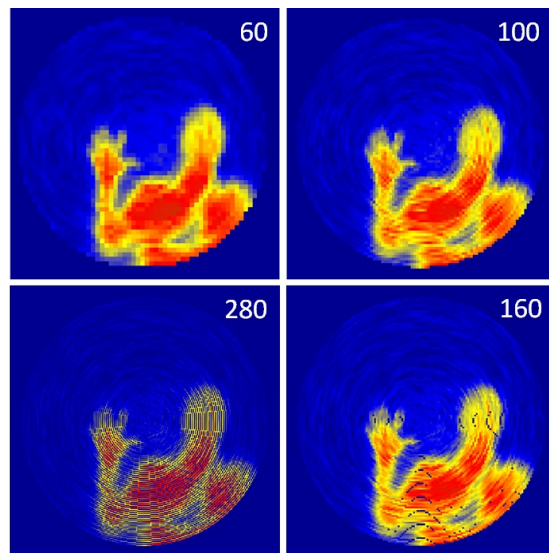


Figure 6.16: Changing number of digital image pixels (equally spaced grid) for the original image j of figure (6.13) and its influence on the general image quality.

The figures (6.15) and (6.16) show both original images with varying number of pixels. It is visible that with 60×60 pixel in the digital representation of the THz-scene no missing values exist, id est every position in the scene is measured during the data acquisition. Even when every position is measured, positions near the center of the FoV are encountered more often than positions in the outer rim of the FoV. This is illustrated in figure (6.17). Also, with only 60 pixel in one image direction not every detail in the scene is resolved.

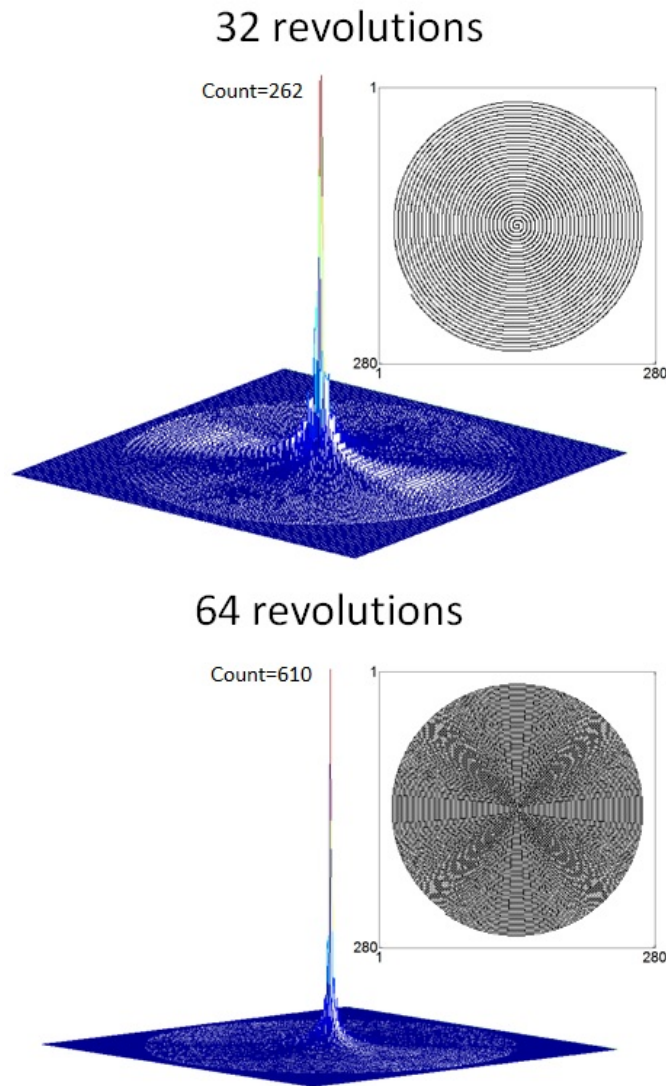


Figure 6.17: Illustration of the frequency each image pixel is encountered in the image formation process (indicated by pixel count).

As is visible in figure (6.15) and figure (6.16), by increasing the number of image pixels more details become visible (observe the facial features in figure

(6.15) and the fingers in figure (6.16)). The benefit of the obvious increase in spatial resolution is not just a question of image quality and the generation of more pleasing images alone, it also is a question of the detection probability of hidden threats. Although, with increasing number of pixels in the images not every image pixel is encountered and missing pixels have to be interpolated/reconstructed, the number of pixels comprised by a hidden object is increased and this in turn increases the probability of detection. Therefore, an optimal nominal spatial resolution in terms of number of pixels exists. This resolution should not be limited by the representation itself but instead it should only be limited by the physical properties of the imaging system. This consideration is directly connected with the information content inherent in the images in question. The basics on the information content of the passive THz-images relevant here were discussed in section (4.4). Further details are beyond the scope of this text but the basics introduced so far already allow a suitable choice for n , the number of image pixels in the digital representation of the passive THz-images. The obvious spatial resolution in figure (6.15) and figure (6.16) as well as the information content in these images suggest a choice for $n > 300 \times 300$. This in turn would lead to many missing values in the digital representation of the THz-images. In figure (6.17) the spiral path that is traversed during the image acquisition is shown. It shows the resulting pixel count for a spiral path with an undersampling factor of four (top) respective two (bottom) for an image representation size $n = 280 \times 280$. As mentioned before, an increase of n would result in more missing values (indicated by the undersampling factor). The number of missing values can be reduced when the image acquisition is set to a parameter value where more revolutions in the spiral path are traversed. This, in turn, would lead to an increase in the image acquisition time (measurement time).

Now, the question is whether passive THz-images acquired with a certain spatial undersampling factor (number of revolutions) can be reconstructed and then displayed with an optimal nominal spatial resolution in accordance with their information content? This research question can be interpreted as finding a representation for the information content of the THz-images of interest here¹² with an appropriate resolution¹³ without the need to use classical interpolation techniques¹⁴.

Since the information content is not exactly known in advance, a solution to this research question with adaptable, nominal spatial resolution is required. The optimal spatial resolution is then derived after the acquisition process by image processing techniques and the knowledge of the used acquisition parameters. The chosen approach for a solution now involves, as already mentioned, the use of a-priori knowledge. More specifically, the knowledge of the spiral scanning based acquisition process is modeled and used for the reconstruction process. As a first approximation, it is helpful to not consider image artifacts that may arise due to the acquisition process. Also, for Ψ respective a sparse domain, the Fourier domain is used. Translated into the CS-context of equation

¹²The results discussed in this section are applicable for THz-images whose acquisition involves mechanical scanning.

¹³The details on what appropriate resolution means are depending on the information content of the THz-images in question and the imaging situation itself.

¹⁴All THz-images presented in this thesis use classical interpolation techniques except the results presented in this section.

(6.1), the points discussed so far lead to equation (6.2).

$$\vec{y} = \underbrace{\Phi}_{\text{spiral scanning}} \cdot \underbrace{B}_{=1} \cdot \underbrace{\Psi}_{\text{Fourier domain}} \cdot \vec{\alpha} + \vec{n} \quad (6.2)$$

The next step in the reconstruction process is the derivation of a matrix representation for Φ . The modeling idea is demonstrated in figure (6.18).

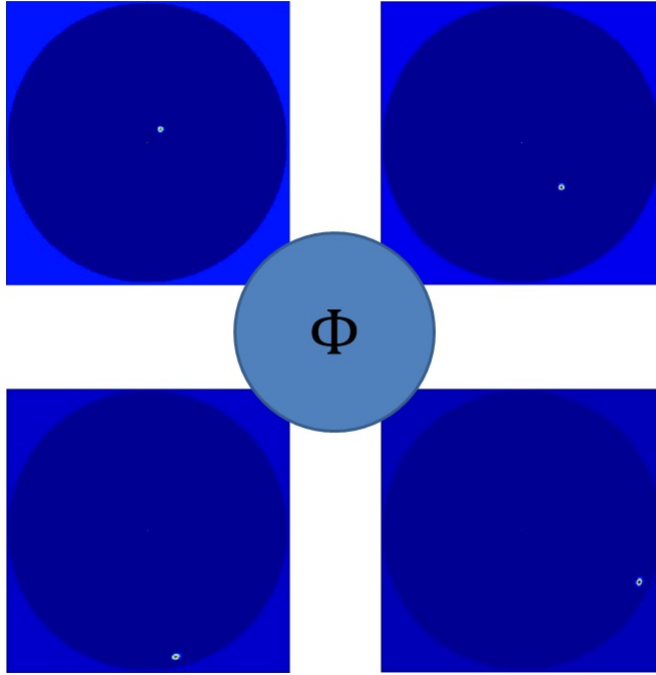


Figure 6.18: Illustration of the spiral scanning process with the changing spot of the ISM-imager at different positions in the FoV. The changing spot at every measurement position is the input for the rows of Φ .

As can be seen in figure (6.18), multiple positions in the FoV influence the measured value according to the beam shape at the measurement position. It is also visible that the beam shape changes during the image acquisition starting at the center of the FoV and ending at the rim. Since it is known, how the beam changes, this knowledge can be used directly in the reconstruction process. This idea can be straightforwardly translated into the formalism of equation (6.2). At every measurement position i a digital representation of the beam forms one row in the matrix representation of Φ ¹⁵.

¹⁵In a SLM-based context these rows are also called masks. Details are given in section (6.5)

$$\begin{pmatrix} y_1 \\ y_2 \\ \vdots \\ y_i \\ \vdots \\ y_m \end{pmatrix} = \begin{pmatrix} \Phi_{11} & \Phi_{12} & \cdot & \Phi_{1j} & \cdot & \Phi_{1n} \\ \Phi_{21} & \Phi_{22} & \cdot & \Phi_{2j} & \cdot & \Phi_{2n} \\ \cdot & \cdot & \cdot & \cdot & \cdot & \cdot \\ \Phi_{i1} & \Phi_{i2} & \cdot & \Phi_{ij} & \cdot & \Phi_{in} \\ \cdot & \cdot & \cdot & \cdot & \cdot & \cdot \\ \Phi_{m1} & \Phi_{m2} & \cdot & \Phi_{mj} & \cdot & \Phi_{mn} \end{pmatrix} \cdot \begin{pmatrix} x_1 \\ x_2 \\ \cdot \\ x_i \\ \cdot \\ x_n \end{pmatrix}$$

By using this a-priori knowledge an entire neighborhood of pixels influences the image value at the position in question. This also means that at every measurement position knowledge about an entire pixel domain is created. With that fact comes the possibility to increase the nominal resolution in the THz-representations (the number n of image pixels) until a certain limit that is given by the beam size, the number of measurement positions and ultimately the signal-to-noise ratio during the image acquisition¹⁶ is reached. Since the beam shape of the ISM-imager could not be measured for every position in the field-of-view, a model of the beam has to be used to construct the rows of Φ .

The optimal nominal spatial resolution id est n_{opt} as described above, depends on several factors (including the accuracy of the beam model) whose in detail discussion is beyond the scope of this text. In the remainder of this section different images with differing n -values and reconstruction parameters are shown and then analyzed regarding their resulting image quality. The considerations presented in this section focus on the reduction of the effects introduced by spatial undersampling. Here, only a first test of the reconstruction idea is presented, due to the necessary simplifications discussed in this section. These first results allow only for a proof-of-principle of the reconstruction idea and need to be further refined and investigated in subsequent work (after the conclusion of this thesis). The first reconstruction results are shown in figure (6.19) and figure (6.20).

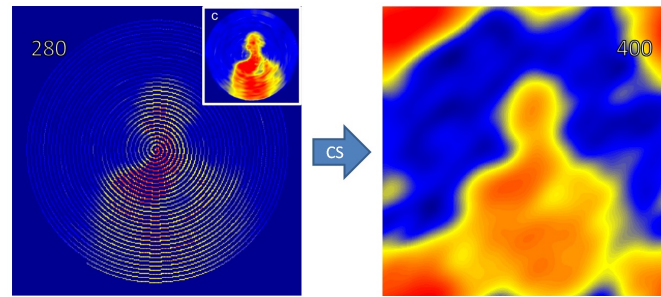


Figure 6.19: Reconstructed image using CS-methods of the original image c from the list in the previous section with a spatial undersampling factor of four.

¹⁶The assumption that the spatial resolution is only indirectly and inversely limited by the beam size is at first glance somewhat counter intuitive.

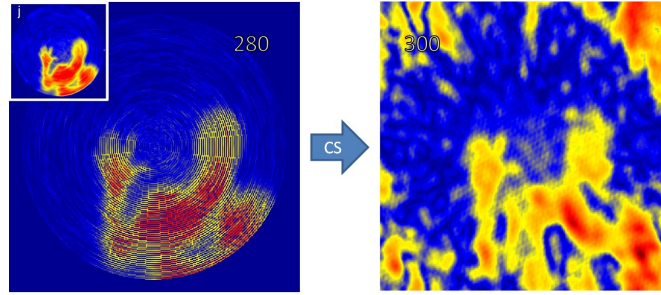


Figure 6.20: Reconstructed image using CS-methods of the original image *j* from the list in the previous section with a spatial undersampling factor of two.

The reconstruction success for image *c* is already noticeable by visual inspection. The artifact introduced due to the spiral motion of the ISM-imager is not detectable in the reconstructed version of image *c*. The reconstructed image shown in figure (6.19) has a size of $n = 400 \times 400$ pixel but despite this large magnification and accordingly the large spatial undersampling, no traces of the spiral motion are visible in the image.

The reconstruction of image *j* on the other hand exhibits some artifacts. Although the spiral scanning artifact is no longer visible, artifacts that most likely stem from the CS-based reconstruction are introduced into the image. A comparison with the original image shows that the person in the scene was also mainly but not entirely reconstructed. In some parts of the image the reconstruction completely fails whereas in other parts of the image the reconstruction successfully recovers the THz-scene without artifacts (observe the fingers of the right hand). In order to quantitatively evaluate the reconstruction success for both images a closer look at edges in the images is advisable. The following two images show digital line scans along the dashed lines in the CS-reconstruction of image *c* respective image *j*.

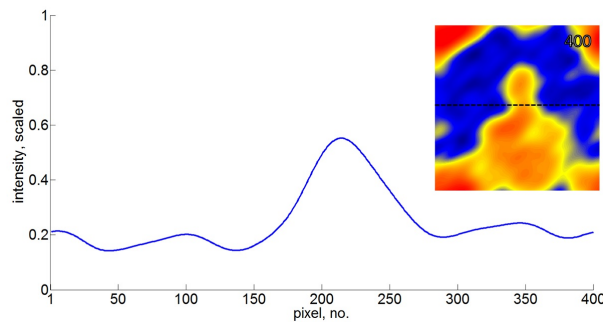


Figure 6.21: Digital line scan following the dashed line in the CS-reconstruction of image *c*.

A closer look at figure (6.21) shows that the edges encountered in the line scan

are approx. 40 pixel wide which is at least $4\times$ the intended value. The poor sharpness of edges is a first hint to problems with the model of the evolution of the ISM-imager beam profile over the field-of-view. The deviations between the model of the beam profile and its real evolution are also evident in the digital line scan of the CS-reconstruction of image j (see figure (6.22)).

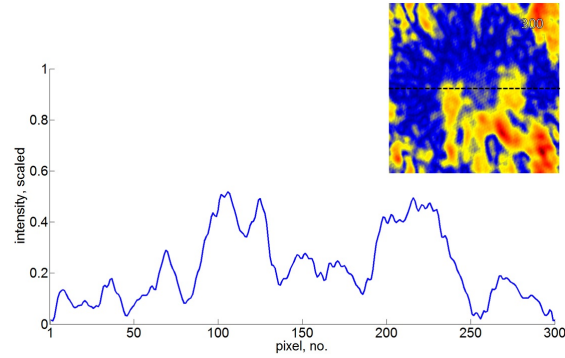
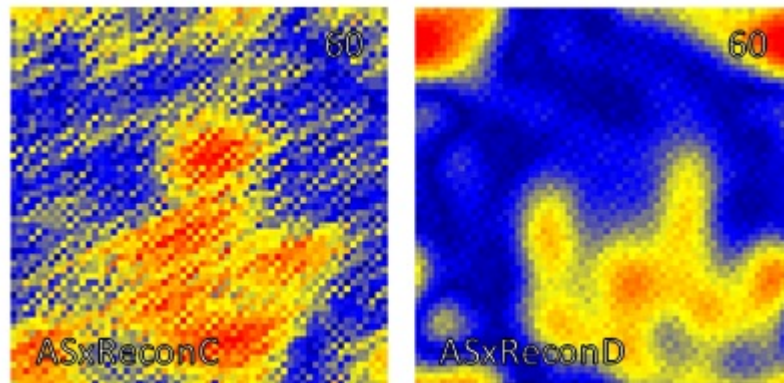


Figure 6.22: Digital line scan following the dashed line in the CS-reconstruction of image j.

As was discussed before, reconstruction artifacts are visible in this image. For the reconstruction of image j the model of the evolution of the beam profile was slightly adapted. This adaption increased the sharpness of edges in specific regions of the reconstructed image (see the line scan in figure (6.22)). In the center of the image the fingers of the right hand are resolved but a ripple-like artifact appears. Further away from the image center the reconstruction worsens and fails completely in specific image regions.

This means, that even slight modifications of the beam model have severe repercussions on the reconstruction performance. To illustrate this further, figure (6.23) shows a few additional reconstructions of image c and j with slightly modified beam model¹⁷.



¹⁷The model parameters are listed in section (A.4).

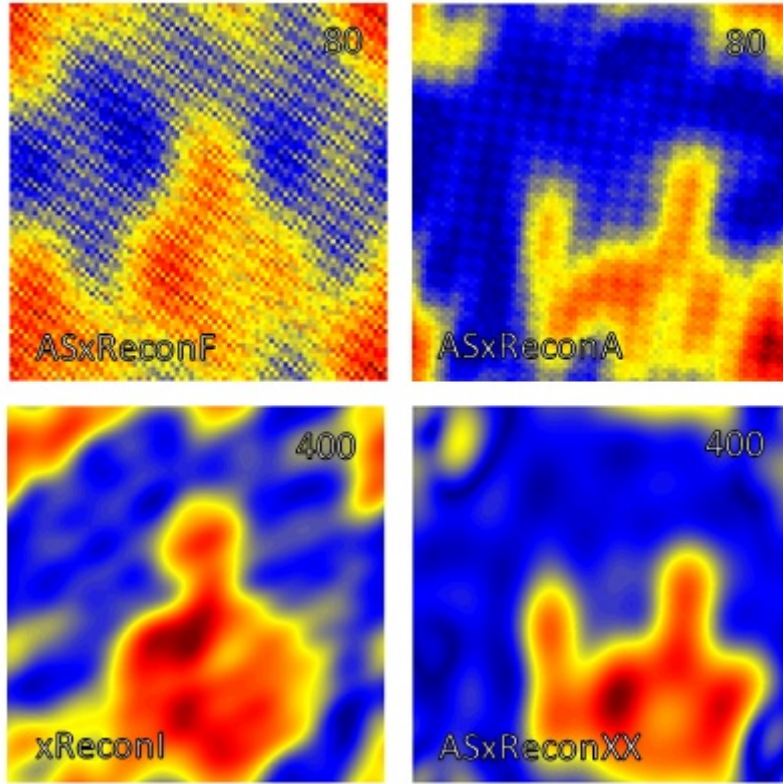


Figure 6.23: Different CS-reconstructions with slightly changed beam profile parameters in the ISM-imager beam profile evolution model (LHS image c and RHS image j).

For the images in figure (6.23) the size of the beam is increased starting with a very narrow beam in the top row and ending with a moderate beam size in the bottom row. Also indicated in each image are the name of the simulation (to identify the used beam profile parameters) and the size of the reconstructed image (indicated by the pixel value in one dimension). It is visible that with a very narrow beam missing values seem to appear in the images but due to the nature of the numeric implementation of the CS-based reconstruction the original versions of image c and image j are not reproduced. It is also visible that with increasing beam profile the reconstruction improves but still the images appear to be blurry (unsharp) with lack of details, details that are visible in the classical reconstructions but not in the CS-based reconstructions.

However, it can be concluded that the CS-based reconstruction idea presented in this section was successfully demonstrated and also that the reconstruction success is sensitively dependent on an exact model/measurement of the evolution of the beam profile at positions in the entire field-of-view.

6.2.1 CS-based reconstruction of passive THz-Images - Results interpretation

The reconstructed images presented in this section show the achieved reconstruction success of a CS-based image reconstruction procedure. The reconstruction used a-priori knowledge within a CS measurement scheme, modeling the a-priori knowledge about the measurement process (mechanical scanning) by introducing it as row vectors in the measurement matrix Φ . As the results show, a precise knowledge of the ISM-imager beam profile evolution is essential for a good reconstruction. With the complete understanding of the measurement matrix Φ all optical distortions and imaging artifacts can be moderated/overcome. The matrix Φ was derived here with a-priori knowledge of the ISM-imager's mechanical scanning process. However, the applicability of the results goes beyond the ISM-imager. The results of this section should be applicable to many mechanical scanning-based imaging applications.

In addition, with the knowledge of the image formation process using mechanical scanning, there also comes insight in the physical properties of the imaging system involved (here the ISM-imager) which may provide valuable information for software scanning applications as well.

The results presented in this section were limited by numerical considerations. The reconstruction idea outlined here is in its present implementation very demanding in its computational aspects¹⁸. This limited the investigation to a very small number of CS-algorithms and (sparse) domains Ψ . Also, the matrix B , modeling non-idealities in the image formation process, was only introduced as an identity matrix, leaving further considerations on this point e.g. the smearing effect, for subsequent investigations after the conclusion of this thesis.

¹⁸Even so the reconstruction algorithm was extended and improved with the assistance of Dipl.- Infor. Jan Hieronymus, the computational effort is still to demanding to incorporate all aspects of the CS-based reconstruction

6.3 Introducing the Lock-In Phase Space

The previous sections introduced the details and limitations of the ISM-imager when used to image objects in the scene in passive mode. Most acquired images were simply represented as measured intensity values as a function of two spatial variables x and y ($I(x, y)$). Since the measurement setup was a Lock-In amplifier based setup (cf. figure (6.1)), theoretically relative phase information can also be used and potentially contains information about the scene as well. As the analysis in section (6.1) showed, the information contained in the respective phase signals was not helpful for the imaging task at hand. This section now introduces a modified setup for passive imaging that allows the beneficial use of the LIA-based relative phase information to improve the imaging performance of the ISM-imager.

The modified setup allows for a new way in which passive THz-images are formed¹⁹. The modified setup is shown in figure (6.24).

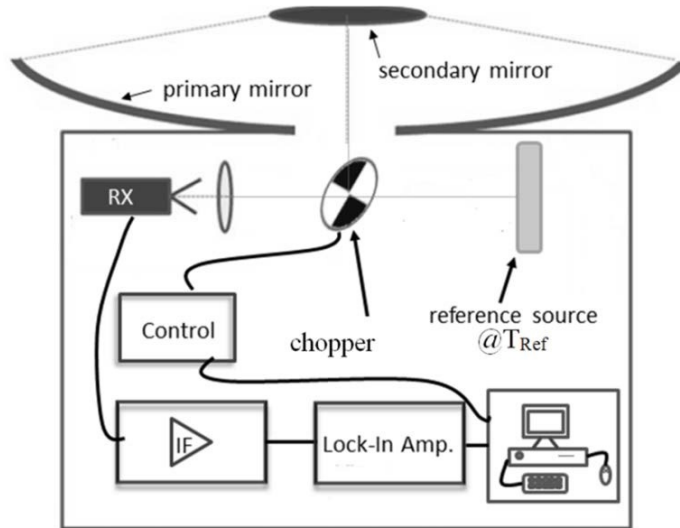


Figure 6.24: Modified setup to use LIA-based relative phase information for the formation of passive THz-images.

The modified setup of figure (6.24) uses a metallic chopper wheel as interchangeable optical element (IOE). The metallic wheel acts as a switchable mirror. Additionally a temperature reference is added to the setup. The metallic chopper wheel acting as an optical switch/switchable mirror redirects the beam from the Rx either to the image plane (scene) or to the reference source (cf. 6.24).

The chopper is made out of a flat, polished aluminum plate and has eight partitions. Four of these are open and the beam is directed through these openings onto the temperature-variable reference source, which was made from

¹⁹Although the new method is introduced here in a passive imaging modality, its extension to the active imaging modality is straightforwardly achievable. The necessary modifications for the active imaging modality will be briefly outlined in the text.

a 30 cm × 20 cm large copper plate. The plate has a roughened and blackened surface in order to achieve a homogeneous emission close to that of a black-body. The temperature of the plate can be varied between ambient temperature (≈ 293 K) and 47 °C (≈ 320 K) by a set of resistive heaters on the rear side of the copper plate.

By switching the beam, the Rx receives in one phase of the chopper the radiation from the scene and in the other phase that from the reference source. Using a lock-in amplifier (LIA) with the chopping frequency as reference, the difference signal between the object and the reference is measured. Due to the non-ideal switching properties of the chopper wheel the functionality of the implementation of the new imaging method is hardware limited. Figure (6.25) is illustrating this issue. The hardware limitation can be overcome with the help of a THz-SLM.

So, to make use of the full potential of the new imaging method, a THz-SLM has to be developed first (cf. section (6.5.1)). However, the metallic chopper wheel has sufficient functionality to introduce the general procedure of the new method in a passive THz-imaging setting and to demonstrate its benefits for specific cases. The

passive THz-images acquired with the modified setup of figure (6.24) are then generated by plotting signals of the LIA as a function of the position of the scanning secondary mirror. The LIA measures the in-phase and the quadrature components as well as the magnitude (intensity) signal and the phase between the signal and the reference simultaneously. Therefore, the LIA provides four signals: the magnitude R , the phase angle relative to the chosen reference signal Φ and the signals X and Y , which contain a mixture of intensity and phase information according to the relations $X = R \cdot \cos(\Phi)$ and $Y = R \cdot \sin(\Phi)$. The magnitude R is proportional to the difference of the intensity received from the object and the reference source. In addition, one has to take into account the emissivity of objects/reference source and the acceptance angle of the Rx optics. For simplicity in the following considerations effective temperatures, which include these effects, are used. Nevertheless, with proper calibration using a reference with precisely known temperature and emissivity, absolute temperature measurements are feasible²⁰.

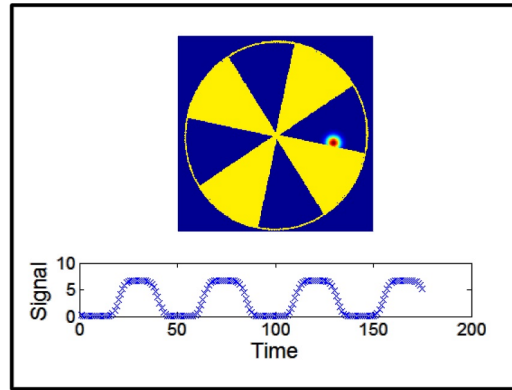


Figure 6.25: Illustration of the non-ideal switching properties of a metallic chopper wheel.

²⁰With the new imaging method, imaging that is traceable to the SI-system is possible. Here, the stability and information about the temperature reference play an even more important role.

The second signal channel of the LIA is the phase Φ . Its value is proportional to the phase difference between the signal and the lock-in reference oscillator. In a typical (passive) imaging scenario objects in the scene have a temperature which is different from the background temperature. Using the reference source, three imaging situations can occur. Case 1; the temperature of the reference source

is smaller than the temperatures of the object²¹ and the background. Case 2; the temperature of the reference source is larger than those of the object and the background. Finally in Case 3; the temperature of the reference source is in between the object and the background temperatures. In all cases the magnitude of the signal is proportional to the temperature difference between object and reference. In Case 1 and 2 the phase differs by 180° . In Case 3; the magnitude of the signal approaches a small value (around zero but not equal to zero) if the reference temperature is chosen appropriately in between the object and the background temperatures (part of the beam of the Rx covers the background while the other part covers the object). The effective temperature at the transition object/background equals the reference temperature. At this particular position the magnitude of the LIA signal is zero and the phase is undefined. A special situation occurs if the reference temperature is set to be the average of the object and background temperatures. In this case the magnitude of the signal is constant except when the beam crosses an edge in the scene. It should be noted that this case is equivalent to a **hardware edge-detection** scheme because only edges and no other details are detected. The phase signal of the LIA changes

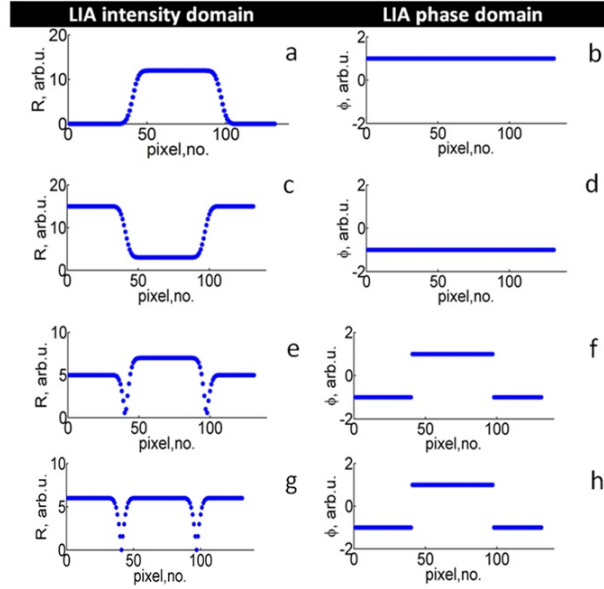


Figure 6.26: Predicted behavior for the modified ISM-imager setup presented in this section. The signal is shown as it would be measured by a LIA with a reference source at a temperature of T_{Ref} . R is the LIA magnitude/intensity and Φ is the LIA phase. Three cases are considered: Case 1 (a, b): $T_{Ref} \leq T_{Amb}, T_{Obj}$, Case 2 (c, d): $T_{Ref} \geq T_{Amb}, T_{Obj}$ and Case 3 (e, f) $T_{Amb} \leq T_{Ref} \leq T_{Obj}$. In g) and h) the special case $T_{Ref} = \frac{T_{Amb} + T_{Obj}}{2}$ is shown..

²¹Here, for simplicity it is assumed that the scene contains only one object. The situation for multiple objects in the scene can then be derived from the following considerations.

by 180° when the temperature in the image changes from below the reference temperature to above or vice versa. The outlined cases (1-3) are summarized in figure (6.26) and serve as prediction for the different measurement situations presented in this section.

As a first test of the modified setup, a test object at 5.3 m distance from the primary mirror of the ISM-imager was imaged. The test object is a gun-shaped piece of aluminum at a temperature of 37°C ($\approx 310\text{ K}$) in front of a 40°C ($\approx 313\text{ K}$) warm copper plate (cf. figure (6.6)). The temperature of the reference source was set to 25°C (298 K). This scenario corresponds to Case 1 with $T_{\text{Ref}} = T_{\text{Amb}}$ (cf. figure (6.26) a, b). It should be noted that the setup used here does not allow to realize Case 1 with $T_{\text{Ref}} < T_{\text{Amb}}$ because it was not possible to cool the reference source below ambient temperature²². The measured results are shown in figure (6.27) (magnitude/intensity signal) and figure (6.28) (phase signal).

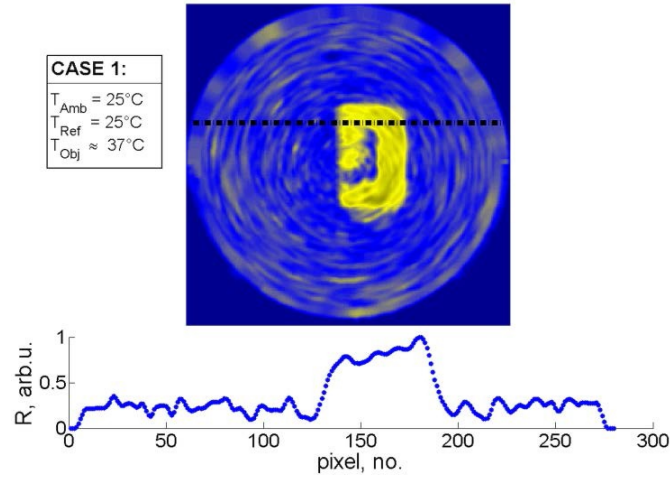


Figure 6.27: Intensity signal (R) for a scenario Case 1 with $T_{\text{Ref}} = T_{\text{Amb}} < T_{\text{Obj}}$ of the hardware edge-detection scheme. The diagram at the bottom displays the intensity signal measured along the dotted line.

²²A few experiments were conducted with LN_2 cooled objects as a temperature reference. However, this temperature was so far below the ambient temperature that the results were inconclusive.

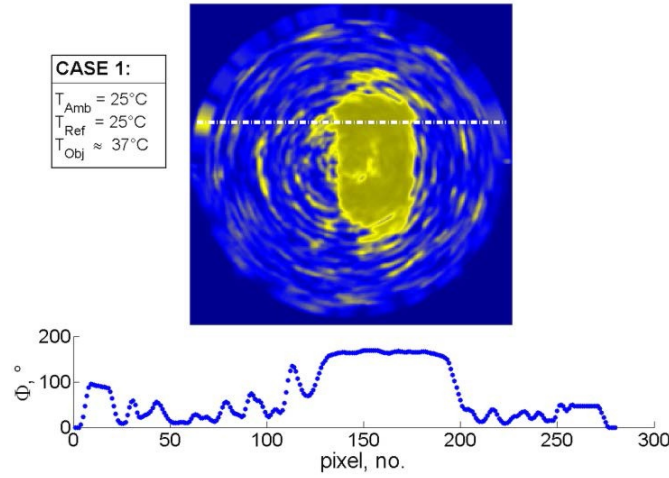


Figure 6.28: Phase signal (Φ) for a scenario Case 1 with $T_{Ref} = T_{Amb} < T_{Obj}$ of the hardware edge-detection scheme. The diagram at the bottom displays the phase signal measured along the dotted line.

The dotted lines mark cross sections through the images. Figure (6.27) shows the intensity signal R of the LIA and figure (6.28) shows the phase signal Φ . In the intensity image the hot (yellow color), rectangular plate is visible, in front of which the gun mock-up can also be seen. The mock-up is at approximately the same temperature as the rest of the background (blue color). In the phase image the warm plate has a 180° phase difference with respect to the rest of the background and the gun mock-up. The non-zero excursions of the phase signal are due to noise fluctuations, which cause the detected temperature in the scene to alternate between values above or below the threshold set by the reference temperature.

The intensity domain image looks as expected for a passive THz-image. In this case the phase domain image seems to be noisier than the intensity domain image (figure (6.27)). The noise in the phase domain is so severe that the borders of the warm object in the scene begins to vanish. This behavior is exactly as predicted by the considerations shown in figure (6.26 a, b). If the reference temperature T_{Ref} would have been below T_{Amb} , the objects in the scene would no longer be visible in the phase domain. This situation is equivalent to a standard LIA based imaging scenario.

In the scenario of Case 2 the reference temperature is raised well above the object temperature and the ambient temperature. The images of this case are presented again separately in the LIA intensity domain and in the LIA phase domain. For this measurement a piece of fabric was placed in front of the objects in the scene to lower the effective temperatures seen by the Rx further (indicated by the asterisk at T_{Obj} in figure (6.29) and figure (6.30)).

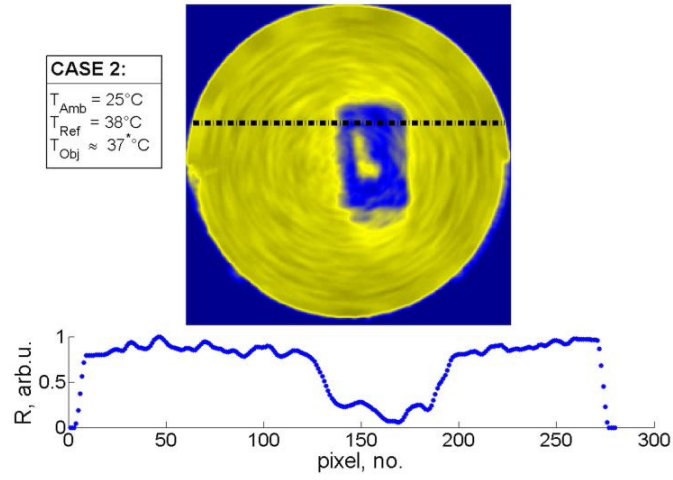


Figure 6.29: Intensity signal (R) for a scenario Case 2 with $T_{Ref} > T_{Amb}, T_{Obj}$ of the hardware edge-detection scheme. The diagram at the bottom displays the intensity signal measured along the dotted line.

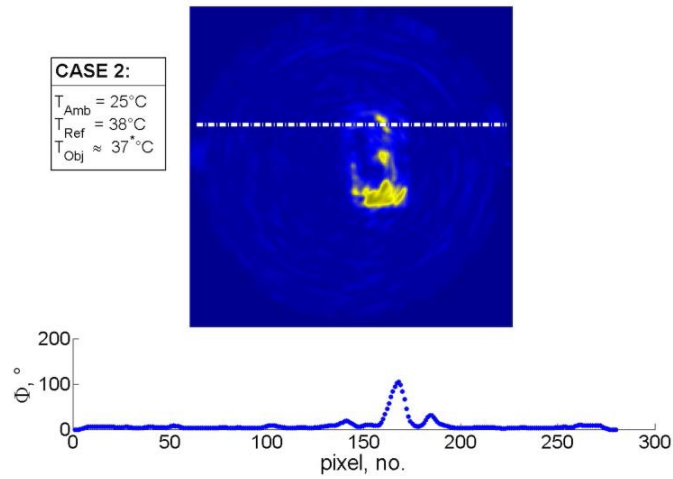


Figure 6.30: Phase signal (Φ) for Case 2 with $T_{Ref} > T_{Amb}, T_{Obj}$ of the hardware edge-detection scheme. The diagram at the bottom displays the phase signal measured along the dotted line.

Also in this case the predictions are met. In the intensity domain image (figure (6.29)) the object in the scene shows an inverted temperature difference

(indicated by the reversed colors) and in the phase domain the warm object disappears almost completely.

The images shown in figure (6.31) and figure (6.32) correspond to Case 3. The value of T_{Ref} is already close to the aforementioned special Case²³ with $T_{Ref} = \frac{T_{Amb} + T_{Obj}}{2}$. The temperature of the reference source is set to 31 °C (≈ 304 K), which is approximately the average temperature of the warm plate and the background/gun mock-up. In the image which is generated from the magnitude R the edges of the warm plate are clearly visible. The edges of the gun mock-up can also seen.

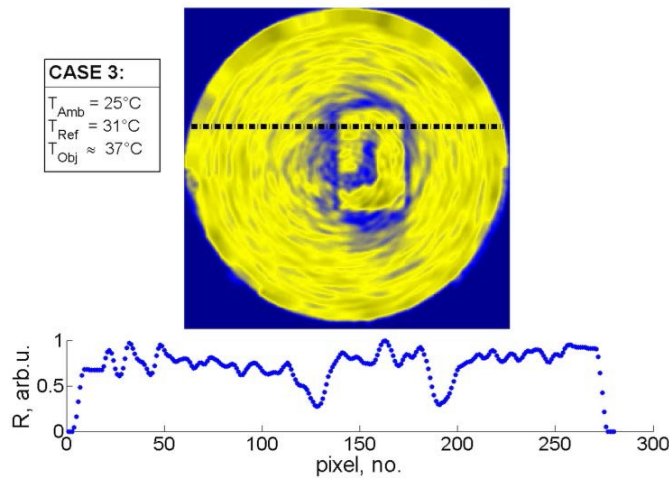


Figure 6.31: Intensity signal (R) for a scenario Case 3 with T_{Ref} close to the average of T_{Amb} and T_{Obj} of the hardware edge-detection scheme. The diagram at the bottom displays the intensity signal measured along the dotted line.

²³Since T_{Amb} can easily be measured, the edge detection method does also provide the possibility to measure temperatures of objects in the scene.

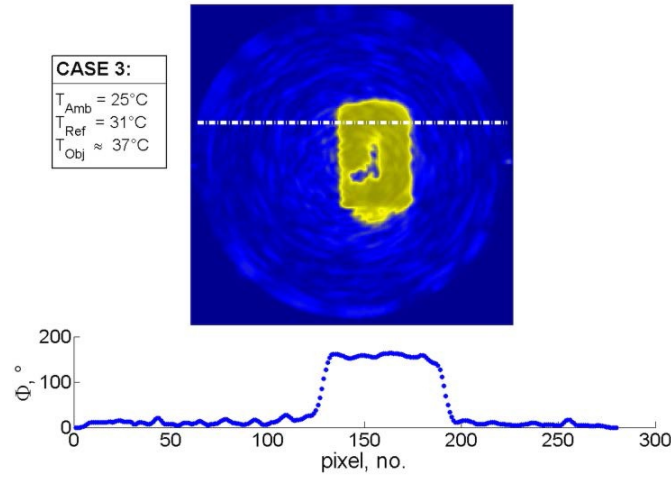


Figure 6.32: Phase signal (Φ) for Case 3 with T_{Ref} close to the average of T_{Amb} and T_{Obj} of the hardware edge-detection scheme. The diagram at the bottom displays the phase signal measured along the dotted line.

However, due to the limited spatial resolution, the edges merge and the whole mock-up appears more or less uniform. The dotted line marks again a cross section through the image. Again, R is plotted as function of the position along this line. In this plot the edges correspond to the minima. The signal depicted in figure (6.31) should theoretically be zero when the beam of the Rx traverses the edge of the hot plate. This is not the case because of noise in the image and the non-ideal switching function of the chopper. Also, due to the fact that the temperatures of objects in the scene are not known in advance, T_{Ref} can not be set exactly to the average value. This would require scanning for the exact reference temperature value. A zero signal can only be achieved if T_{Ref} is varied during image acquisition. The method of scanning for the best T_{Ref} -value (the value that produces a zero signal) will be introduced in the next section.

In figure (6.32) the phase domain of the same scene as in figure (6.31) is depicted. The signal-to-noise ratio (SNR) appears to be significantly improved compared to figure (6.31). Also, in the central part of the gun mock-up the phase changes to the same value as outside the warm plate because the image is less noisy compared to the magnitude image and edges appear sharper. This is illustrated in more detail by a cut through the image as following the dotted line. The phase changes by 180° when the beam crosses the edge between the background and the warm plate. The SNR is ~ 40 as compared to ~ 4 in the intensity-domain image. Also the edge is about three times sharper than in the intensity-domain image. This improvement is due to the fact that in the configuration used here the imaging system acts as a threshold detector with the threshold given by the effective temperature of the reference source. Since there is only one reference temperature/threshold, the signal output in

the phase domain is binary spanning a **binary Lock-In Phase Space**. To conclude this section, images which show the performance of the hardware edge-detection scheme are presented when a person is imaged at 5.3 m stand-off distance (cf. figure (6.33)).

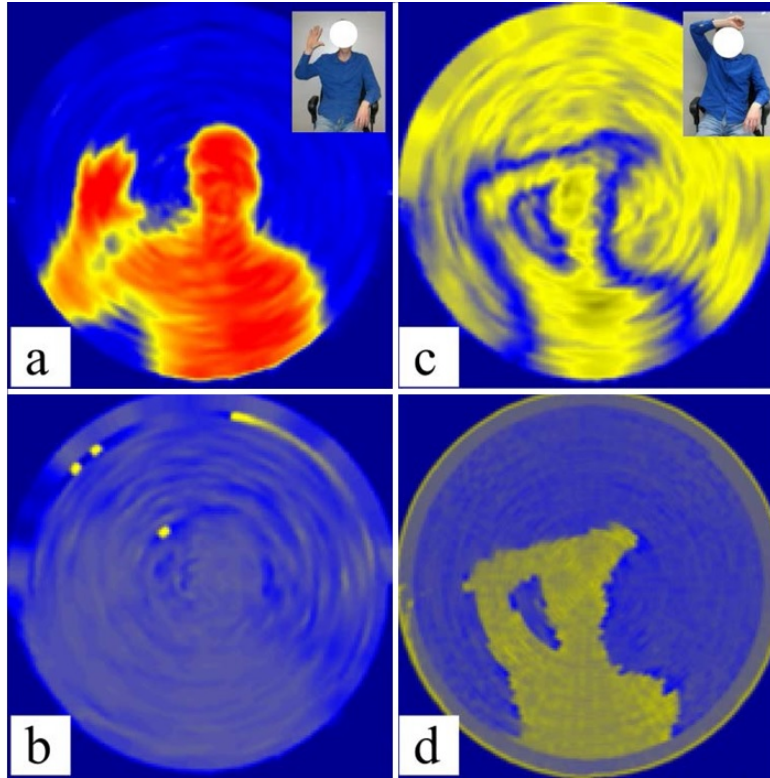


Figure 6.33: Image (a) is a normal intensity picture of a person and image (c) is taken with the hardware edge detection scheme. Image (b) is the phase picture to (a) and image (d) is the phase picture to (c).

Image (a) is acquired by plotting the magnitude without using a reference source. Image (b) shows the corresponding phase measurement. From the phase domain no information about the scene is discernible. That means, using a normal LIA measurement scheme, all information about the scene is in the intensity domain. Images (c) and (d) are taken using the hardware edge-detection scheme with LIA and reference source. The temperature of the reference source is set to a value between the background temperature and the temperature of the warm person. Image (c) shows the intensity domain. The intensity of the background and the intensity of the person are the same almost everywhere in the scene. In the image the shape of the person is nevertheless clearly visible due to the edge detection, id est at the edges of objects in the scene (person) the magnitude R of the LIA approaches values close to zero. The image labeled (d) shows the corresponding phase domain picture. In contrast to image (b) of figure (6.33), the person is here clearly recognizable. It

should be noted that the system is capable of detecting only edges and no other details. However, this is only strictly true for the phase images. Differences in temperature or emissivity across an object can still appear in the intensity images, albeit with reduced SNR compared to a normal intensity image. This can be achieved since the reference source acts as a threshold in the phase domain. With only one threshold the intensity (temperature) in the scene can be larger or smaller than the reference temperature making the modified setup a threshold detector and the resulting phase images binary images. This is the source of the improved SNR. Due to the fact that the threshold temperature is variable during image acquisition (on the hardware level), temperature resolution can be traded-off for noise robustness.

Also at detected edges in the intensity domain, where the measured signal approaches zero due to the quadratic characteristic of the integrator (the signal can not go below zero), the noise level is reduced by a factor of $\frac{1}{2}$. This improved noise performance near edges in the LIA intensity domain does manifest itself by an improved spatial resolution²⁴ (see figure (6.34) for an example measurement).

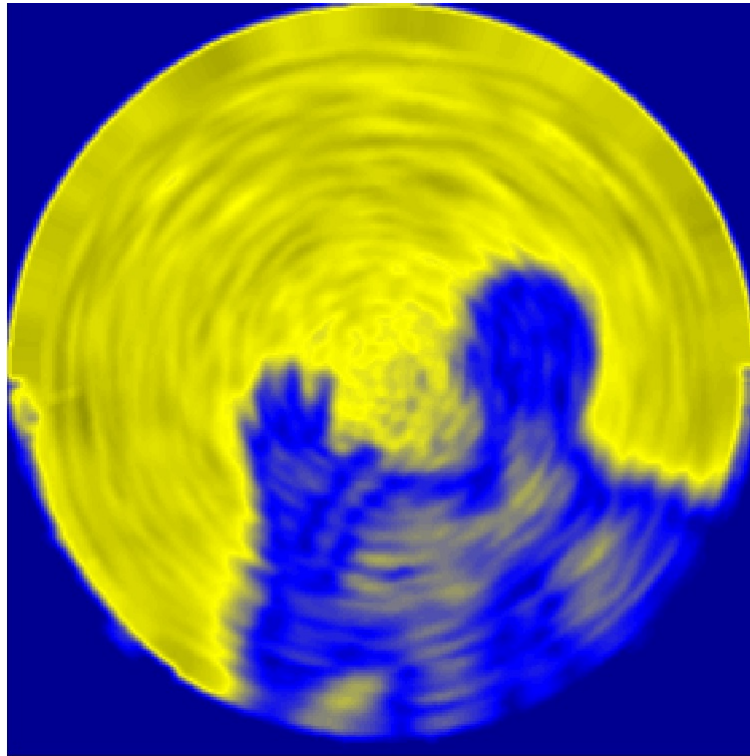


Figure 6.34: Example for the improved spatial resolution near edges in the LIA intensity domain when using the hardware edge-detection scheme.

²⁴Ultimately, the limiting factor for the spatial resolution of the ISM-imager is the noise level and not the optical properties of the telescope alone.

6.3.1 Lock-In Phase Space - Results interpretation

The experiments show that a hardware edge-detection scheme can be implemented in a passive THz imager for stand-off detection. The detection scheme relies on phase sensitive detection with a LIA and a reference source. The system is capable of detecting only edges but no other details. An additional advantage is related to the attainable SNR when measuring the intensity and the phase image simultaneously. In the phase domain the object appears with a SNR which is about a factor of 10 larger than the SNR in the intensity domain image. Also, at edges in the LIA intensity domain the edge-detection method provides an increase in noise performance by a factor of $\frac{1}{2}$. The phase sensitive detection acts as a threshold detector with a 180° phase change depending on whether the effective temperature of the reference source is larger or smaller than the object being imaged.

The heat plate used as reference source in the ISM-imager is a slow device with respect to temperature changes. Essentially, this requires the setting of the reference temperature to a fixed value at the beginning of a measurement. The T_{Ref} value detected by the Rx can be changed during image acquisition when an additional modulator is placed in front of the reference (e.g. a chopper). With this modification, T_{Ref} scanning becomes possible, making it feasible to modulate the reference temperature at every image pixel. Only with such a modification to the imaging setting the intensity domain could be scanned for a zero signal at every image pixel. With this modification, the absolute temperatures of every object in the scene within a hardware edge-detection scheme could be measured from stand-off distances. Experiments demonstrating this additional modification to the edge-detection setup will be presented in the next section. Also, the hardware edge-detection scheme could easily be used in an active imaging modality when the heat plate reference is exchanged for an electronic THz-source. In the active imaging modality a metallic chopper wheel can no longer be used as switchable mirror. An easy solution to this problem is to replace the metallic segments of the wheel with beam splitter material (e.g. Mylar). The beam splitter material then allows for a partial transmittance and partial reflectance of THz-radiation. With this modification to the switchable mirror, the setup would be equipped for the active modality without further modifications.

However, to harness the full potential of the hardware edge-detection method, respective the Lock-In Phase Space, true THz-SLMs are required. They offer advanced switching capabilities along with precise hardware synchronization abilities. To demonstrate true (real-time) hardware image processing (e.g. edge-detection), a THz-SLM needs to be exchanged for the metallic chopper wheel²⁵. In summary, already with the crude setup used for the experiments presented here, the simultaneous detection of intensity and phase has been demonstrated. It was shown that a number of advantages over pure intensity detection exist. These may lead to higher quality THz-images, improve the detection probability of concealed threats and may ease the privacy problem, which is inherent to mmW- and THz-imaging systems for security applications.

²⁵Since THz-SLMs are at the moment not readily available, the next step for the hardware edge-detection experiments after the completion of this thesis is the incorporation of a THz-SLM prototype into the ISM-imager.

6.4 Multinary Lock-In Phase Space

As demonstrated in the previous section, phase-sensitive detection offers many potential advantages to pure intensity-based imaging. It was demonstrated that the phase-sensitive detection setup acts as a threshold detector spanning a binary Lock-In phase space. The optimal value for the reference temperature is not known in advance and might also change over different positions in the scene. Therefore, the reference temperature has to be adjusted accordingly during image acquisition. For this, a modified setup is proposed here that allows scanning for the optimal reference temperature (the threshold temperature at which a phase jump occurs) at each position in the scene. The proposed setup uses an additional modulator in-front of the heat plate reference source. Unfortunately, such a modulator that can alter THz-radiation in an adequate fashion was not readily available for the experiments presented here²⁶. A simple approximation of the proposed setup that was used for the experiments presented in this section is shown in figure (6.35).

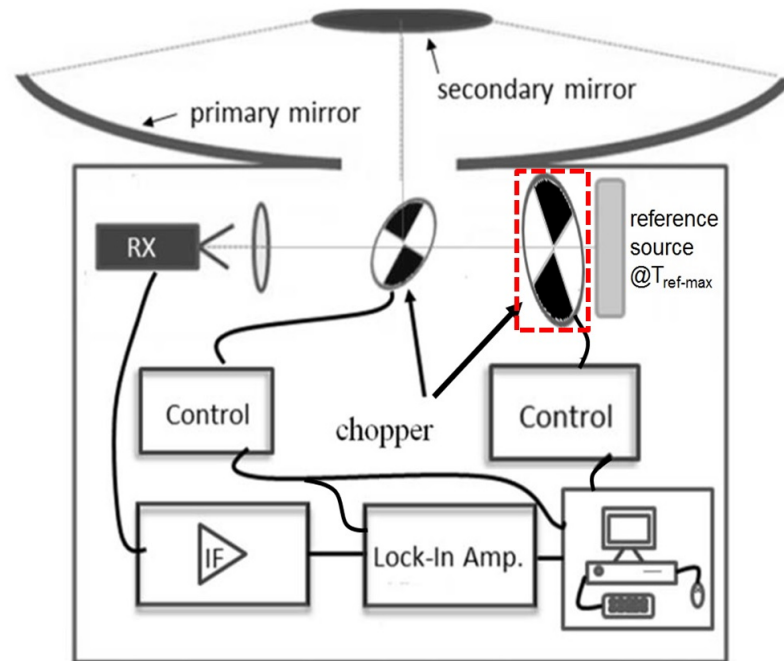


Figure 6.35: Modified setup to span a multinary Lock-In Phase Space. The modifications to the setup for a binary Lock-In phase space presented in the previous section are indicated with a dotted, red frame.

The heat plate in figure (6.35) again provides the temperature reference that acts as a threshold. Due to the fact that the temperature value of the heat plate

²⁶An adequate modulator would be a THz-SLM. A prototype of such a THz-SLM was developed during the PHD-time (see section 6.5). However, the prototype was not yet ready to be incorporated into the ISM-imager mainly due to the sheer size of the prototype.

can only be changed very slowly, an additional modulator has to be placed in front of it. In turn, the modulator adapts the temperature value detected by the Rx. In the simple setup used here, the modulator consists of a metallic chopper wheel placed between the heat plate and the Rx (cf. figure (6.35)). The modulation of the reference temperature is therefore achieved by blocking part of the heat plate and in turn the effective temperature detected by the Rx is a weighted mixture of the effective temperatures of the heat plate and the temperature of the modulator (chopper wheel).

The modulation properties (switching properties) with this simple setup are non-ideal due to the mechanical motion of the chopper wheel modulator. Another issue of the simple setup of figure (6.35) is the insufficient synchronization of the two chopper wheels. Since the scanning for the optimal reference temperature requires the modulation of the reference temperature at every image pixel, precise synchronization is needed. Due to the fact that the two chopper wheels of the setup can not be sufficiently synchronized on the hardware level, for the first experiments presented here, the synchronization has to be achieved on the software level (after the image acquisition). Accordingly, only part of the measurement time during image acquisition can be used for the formation of the passive THz-images²⁷. The aforementioned issues are illustrated in figure (6.36).

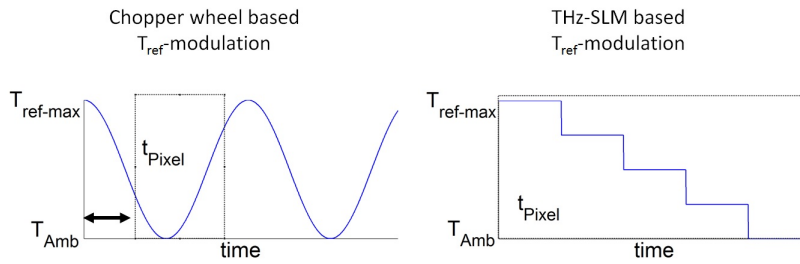


Figure 6.36: Modulation properties with a chopper wheel as approximation of a THz-SLM (left) and with a fully-fledged THz-SLM (right). A THz-SLM would provide ideal modulation capability with adaptable temperature resolution (temperature steps) and noise robustness during the measurement (on the hardware level).

Figure (6.36) illustrates the modulation properties (switching properties) with a chopper wheel as modulator and the (almost) ideal case with a THz-SLM as modulator. Due to the mechanical motion of the chopper wheel during the temperature modulation, every temperature value between the $T_{ref-max}$ (the maximum value) and T_{Amb} (ambient temperature) can be assumed by this type of modulator. The maximum temperature is given by the temperature that was set for the heat plate (a parameter that has to be set at the start of the measurement). In the setup used here, the temperature of the heat plate can

²⁷ Again, synchronization on the hardware level can be achieved if the two chopper wheels are replaced by fully-fledged THz-SLMs.

be varied only between ambient temperature and $\approx 40^\circ\text{C}$ ²⁸. Also, because of the mechanical motion the modulation can not be synchronized to the range $T_{ref-max} - T_{Amb}$ at the start of every image pixel. Therefore, the signal of the chopper motion itself has to be used to achieve proper synchronization at least on the software level.

Figure (6.36) also illustrates the (almost) ideal case where a THz-SLM is used as modulator. Here, proper synchronization can be achieved already on the hardware level. In addition, the number of temperature steps can be chosen (and changed) during the measurement providing adaptable temperature resolution vs. noise robustness. As is indicated in figure (6.36), synchronization with a THz-SLM is achievable at every image pixel providing efficient modulation with no unusable measurement time²⁹.

The on-the-fly scanning motion of the ISM-imager makes proper synchronization even more difficult (even on the software level) since the image pixels are only defined by software processing and not in hardware. Figure (6.37) shows an example temperature scan using the setup of figure (6.35).

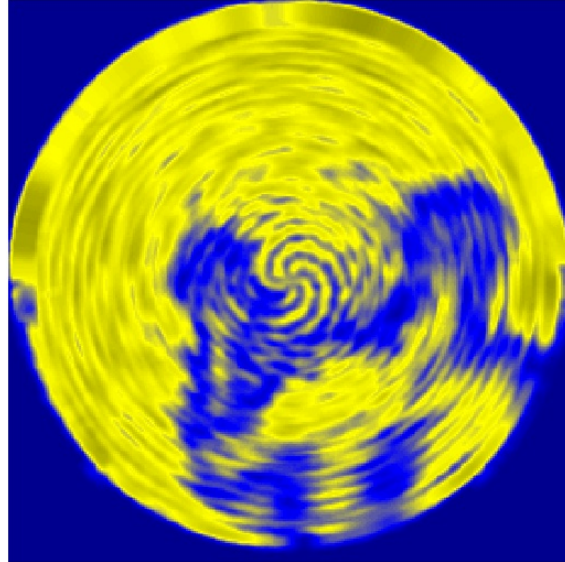


Figure 6.37: Example measurement showing the effects of temperature scanning without proper synchronization during an ISM-imager measurement.

In figure (6.37) it can be seen that the person and a hidden object (piece of wood) in the scene have been successfully detected (distinguished from the background). However, compared to figure (6.34) from the previous section the general image quality as well as the apparent spatial resolution are not as good.

²⁸The simple setup described here does not support negative $T_{ref-max}$ -values, which would be advantageous in some cases but leads to problems with water condensation during the measurement.

²⁹Unusable measurement time is caused by synchronization errors e.g. temperature modulation not starting at the start of the measurement time allotted to an image pixel and not ending at the end of the time per pixel.

Edges were detected but are smeared-out over a wider area. These edges also appear ragged and distorted. Especially in the center of the image spiral artifacts due to the scanning motion of the ISM-imager are visible. These artifacts are present in the entire image but are more severe in the center of the image since the time-per-pixel is smallest in the image center (as described in section (2.3.2)). Therefore, in the image center the aforementioned synchronization issues have the strongest effect on the generated THz-images. Here, edges were detected where no edges are present. Keep in mind that images in the case of T_{ref} -scanning are actually 4D-representations of the scene³⁰. Therefore, the representation itself is not as straightforward as in the case of simple intensity imaging. Before the details of this 4D-mapping process are discussed a closer look at figure (6.37) namely at the intensity and phase domain over time is helpful for a better understanding.

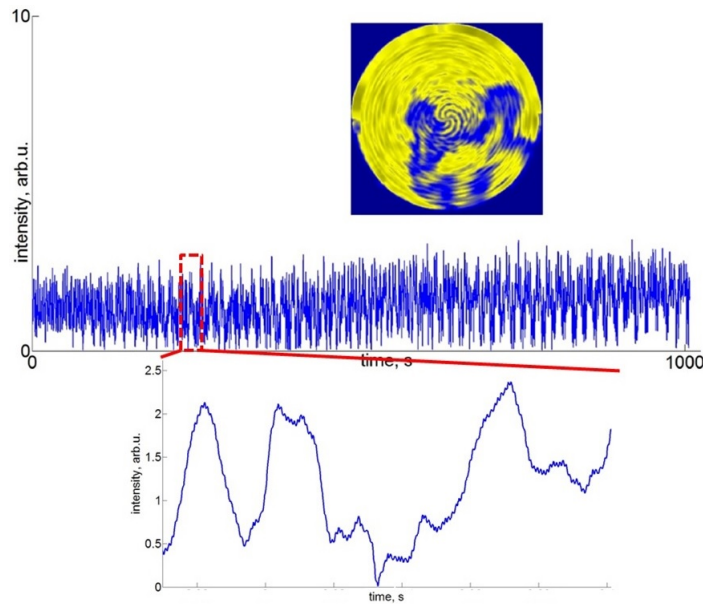


Figure 6.38: Example measurement showing the effects of temperature scanning during an ISM-imager-measurement in the intensity domain over time and enlarged version of the region around the global minimum..

Figure (6.38) shows the causes of the aforementioned effects during an ISM-imager measurement in the intensity domain over time. The region around the global minimum is enlarged and shown in the bottom part of figure (6.38). It can be seen that a zero-value is not exactly reached during the entire measurement. Still, the values reached are pretty close to zero (even allow measurements below the noise floor). Another thing that is visible are small oscillations. These oscillations are probably introduced by the mechanical motion of the

³⁰The intensity I is depicted as a function of X and Y the two spatial coordinates and the variable T_{ref} , the varying reference temperature.

modulator and the ISM-imager itself or are a result of the combination of both mechanical motions³¹. The aforementioned issues also cause effects in the Lock-In phase domain. The ISM measurement discussed in the previous paragraph (cf. figure (6.37)) is shown in the phase domain in figure (6.39). The figure shows the Lock-In phase signal over time. The bottom part of the figure shows again a magnification of an example region.

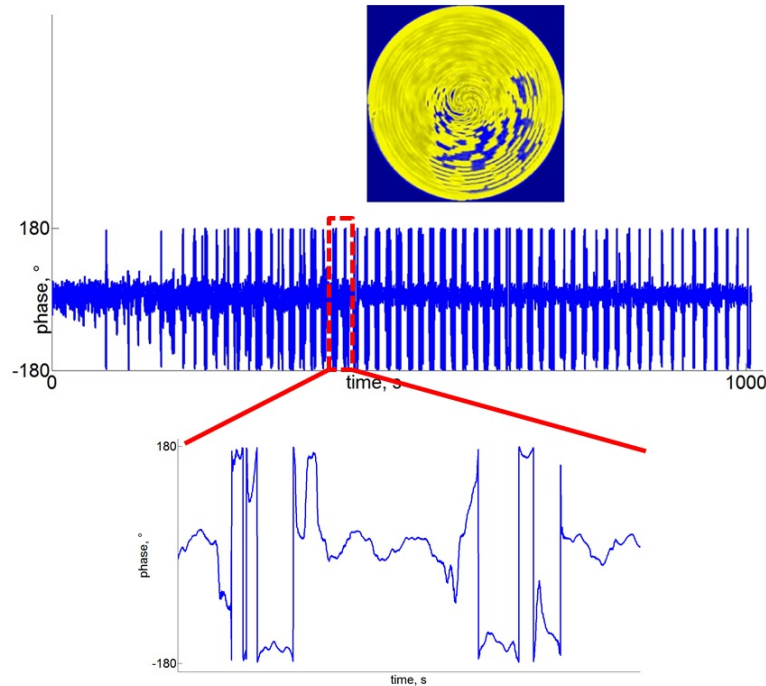


Figure 6.39: Example measurement showing the effects of temperature scanning during an ISM-imager-measurement in the phase domain over time.

180° phase jumps are clearly visible but they sometimes coincide with 360° phase jumps due to the phase space being limited to the range of 180° to -180° (folding back of the phase variations into that range). Also visible are phase jumps $<180^\circ$. These phase jumps can have multiple causes, starting from the non-ideal radiation emission characteristic of the heat plate reference over reflections respective standing waves or discontinuities in the mechanical motion of the chopper blade (modulator) etc. These issues obscure the performance evaluation of the multinary Lock-In phase space scanning scheme. Therefore, as a first step in the multinary phase space experiments, a specially designed test target was raster scanned. This means that the secondary mirror of the ISM-imager is not moving while the test target itself is moved in a zig-zag motion using a suitable raster scanner. At every image pixel the temperature is modulated using the setup of figure (6.35). The raster-scanning motion

³¹ Also, please keep in mind, that as an image pre-processing step the detected signal is averaged after the data acquisition at the start of the digital processing chain (cf. block diagram 2.6).

makes synchronization easier due to the hardware defined pixel positions. This modified setup also lessens some other of the aforementioned issues. The test pattern that was used for these experiments is shown in figure (6.40).



Figure 6.40: Test pattern used for the multinary Lock-in phase Space experiments (digital camera image).

The test pattern consists of different objects glued to an acrylic glass window about the same size as a heat plate placed behind the acrylic glass (30 cm×20 cm). The acrylic glass window is situated about 5 cm in front of the heat plate. Therefore, the test pattern never has physical contact with the heat plate (no heat conduction between the heat plate and the test pattern). In the upper left part of the test pattern three cylindrical rods made from Teflon material are glued to the acrylic glass window. The rods are of differing heights and therefore transmit THz-radiation coming from the heat plate differently (the Rx detects them with different effective temperatures). In the lower part of the test pattern a wedge made off two pieces of metal is placed. The wedge works mainly as a tool to judge the spatial resolution in the resulting THz-images and as an orientation for the position on the test pattern. The fourth object on the test pattern is a metallic disc with a hole in the middle, placed near the right edge of the test pattern, again mainly to help identify the positions of the Teflon rods but not too close to them that the metal can disturb the measurement of the rods. Due to the hole in the metal disc the effective temperature that is detected by the Rx should differ from T_{Amb} .

The goal of the experiments that will now be presented is to scan for the effective temperatures of the objects on the test pattern. The focus lies here on the three Teflon rods and whether it is possible to detect them respective distinguish between them. The imaging situation is schematically shown in figure

(6.41). As discussed above the analysis focuses on the raster scan experiments.

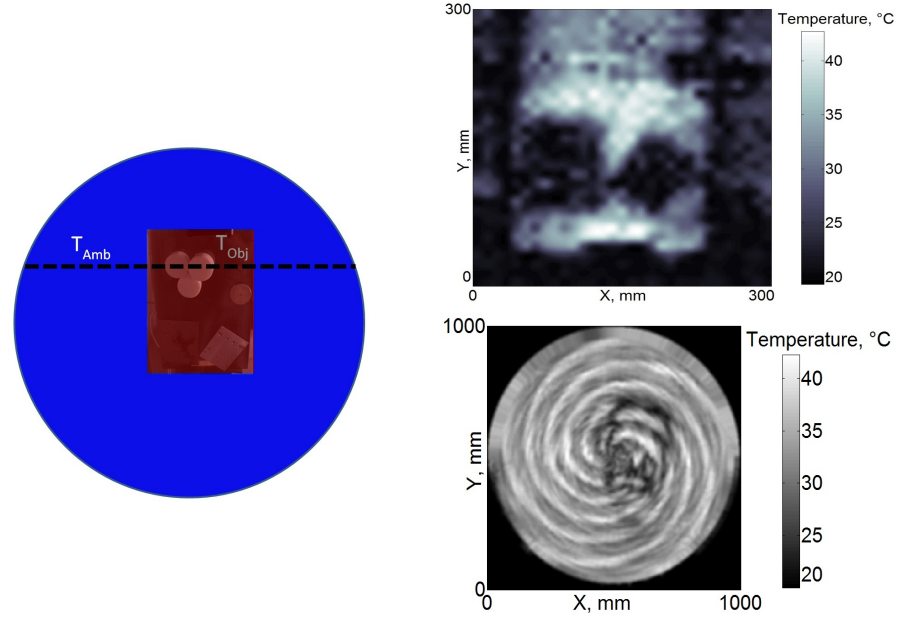


Figure 6.41: Description of the imaging situation discussed in this section (left). The dotted line indicates a cut through the image. Such cuts are used in the analysis procedure (see next paragraph). The right hand side shows in the top part a raster scan representation of the test pattern (minimum of the measured intensity value during T_{Ref} -modulation) and the bottom part shows an ISM-imager image of the test pattern (again the minimum of the measured intensity value during T_{Ref} -modulation is shown).

Again, the ISM-imager representation of the test pattern shows severe spiral artifacts. As discussed above the spiral artifacts arise from the nonsynchronous motion of the modulator chopper wheel and the secondary mirror of the ISM-imager³². Since there are no artifacts visible in the raster scan of the test image (top part RHS of figure (6.41)) the analysis of the raster scan images makes the intended proof-of-principle more straightforward to realize. Since the imaging in these cases was done with the help of a raster scanner, 4D-raster scans were acquired and then analyzed. The first two independent variables are the spatial coordinates X and Y and the third independent variable is equivalent to T_{Ref} . Given that the measurement analysis involves software synchronization, the analysis procedure is briefly explained in the next paragraph. This paragraph is a brief detour on how to analyze the results of the multinary phase space measurements just before the presentation of the measurement results.

³²Please keep in mind that the aggregation of the 4D-measurement data into the 3D-representations that are shown on the RHS of figure (6.41) introduces additional difficulties into the analysis process.

Analysis procedure

Signals for R (Lock-In magnitude/intensity signal) and Φ (Lock-In phase signal) were measured for different parameter combinations (e.g. $T_{ref-max}$, v_{mod} , etc.)³³. Therefore, two 4D-data representations for each parameter combination exist. For every image pixel these 4D-representations have to be synchronized so that the temperature modulation starts at T_{Amb} and covers the range from T_{Amb} to $T_{ref-max}$ in the measurement time allotted for each pixel. Due to the mechanical motion of the modulator chopper wheel this is equivalent to correcting a varying temporal offset at each image pixel. Additionally, the information in the 4D-representations has to be condensed into 3D/2D-agglomerations in order to allow a graphical representation. Each agglomeration shows for the LIA intensity domain the reference temperature where a minimal signal was detected and for the LIA phase domain the reference temperature where a phase jump of 180° was detected.

With this procedure the effective temperatures in the scene can be identified. The multinary character of the Lock-In phase space now stems from the fact that the phase jumps can occur at multiple reference temperatures. Since all reference temperatures between T_{Amb} to $T_{ref-max}$ are assumed, temperature steps have to be defined by software processing after the image acquisition. As discussed before, the magnitude of the temperature steps is a trade-off between temperature resolution and noise robustness. To demonstrate the aforementioned analysis procedure figure (6.42) and figure (6.43) show the procedure for one image pixel.

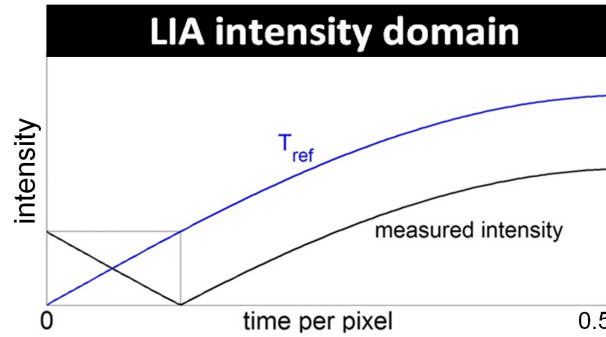


Figure 6.42: Representation illustrating the analysis procedure in the LIA intensity domain for one image pixel. The detected intensity reaches a zero value which in turn can identify effective temperatures in the scene (Details are given in the text below the figure.).

Figure (6.42) illustrates the analysis procedure for one image pixel in the LIA intensity domain. The figure shows two signals. The first signal represents the change in the detected reference temperature caused by the motion of the modulator chopper wheel and the second signal depicts the resulting change in the detected intensity signal. Measurements with the setup shown

³³ v_{mod} is the rotation velocity of the modulator chopper.

in figure (6.35) lead to the detection of an intensity signal that is the difference between the signal coming from the scene and the present, constantly changing reference temperature signal. The difference intensity signal theoretically reaches a zero signal when the detected intensity coming from the scene is equal to the detected reference temperature³⁴. This zero value can then be related to the effective temperature of the object in the scene via the second recorded signal (the acquired T_{ref} -signal which is the signal of the motion of the modulator chopper wheel and is proportional to the change in reference temperature). In figure (6.42) only the first half of a modulation period is shown. Due to the square-law behavior of the modulation the characteristic is similar to a raised-cosine characteristic ($y = 1 + \cos(\omega \cdot t + \pi)$) and the second half of the modulation period just shows the descending part of the characteristic. Other than this inversion the second half contains the same information and is redundant in the discussion of the analysis procedure. Deviations from the ideal raised-cosine characteristic will briefly be discussed at the end of this paragraph. They include also the effects of measurement noise and will be addressed by numerical estimations of the general behavior.

In the LIA phase space the situation is similar to the LIA intensity space. But unlike the intensity space, in the phase space it is not a zero-value but a phase jump that occurs when the signal from the scene and the reference signal are equal in magnitude. The situation and analysis procedure in the LIA phase space are shown in figure (6.43).

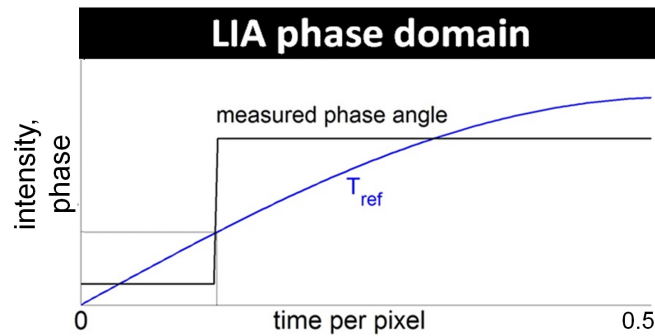


Figure 6.43: Representation illustrating the analysis procedure in the LIA phase domain for one image pixel. In the phase space 180° phase jumps occur when the signal from the scene is equivalent to the reference signal. This in turn can identify effective temperatures in the scene (Details are given in the text below the figure.).

In the LIA phase domain the phase jumps of 180° occur when the signal from the scene (the effective temperature) is equivalent to the reference signal temperature. By detecting these phase jumps and relating them to the modulator chopper motion the effective temperatures in the scene can be determined. The advantage of the LIA phase domain now is that the signal from the scene is

³⁴Please keep in mind that the detected reference temperature is a weighted average of the temperature of the heat plate and the temperature of the modulator chopper wheel due to the Rx beam shape at the position of the modulator chopper wheel.

not directly affected by noise. As discussed in the previous section, in the LIA phase domain, which becomes accessible with the use of a reference source acting as a threshold detector, rejecting all the noise below a certain threshold. In the multinary phase space multinary thresholds can be defined (hence the name) allowing for adaptable noise robustness vs. temperature resolution³⁵. Synchronization is implicitly assumed for both the LIA intensity domain as well as the LIA phase domain as can be seen from the modulation starting at the beginning of the pixel time and reaching $T_{ref-max}$ at the half of the pixel time (the time allotted to each pixel).

As we are concerned with THz-imaging here, the analysis procedure described above has to be extended to multiple pixels. The analysis procedure itself can easily be employed as described to multiple pixels, it simply has to be repeated at every image pixel. But as mentioned in the beginning of this section, this would lead to 4D representations of the measurement data. So, this paragraph briefly describes the agglomeration process from the 4D representations to 2D/3D-representations. For this agglomeration process it is necessary to condense the information in the 4D-data representations. The agglomeration condenses the measurement data at each pixel to one value that allows the identification of effective temperatures of the objects inhabiting this pixel in the scene. As discussed above, this involves the identification of zero-values (min-values) in the LIA intensity domain and phase jumps in the LIA phase domain³⁶. The agglomeration procedure described here is summarized in the following figure (6.44).

³⁵Please keep in mind that the full functionality of a multinary LIA phase space can only be realized with a fully-fledged THz-SLM as a modulator. Since in the experiments presented in this thesis a chopper wheel was used as a modulator the increased noise robustness is not achievable on the hardware level.

³⁶For a simple Lock-In amplifier, it is not possible to implement a min()-function in hardware. With the usage of FPGA-technology the methods developed in this thesis for a Lock-In amplifier can be extended further (even to incorporate Compressed Sensing techniques on FPGA's). With the use of FPGA-technology the line between the hardware level and the software level becomes blurred since here the signals would already be digitized (see again the definition of hardware level in section (4.3)).

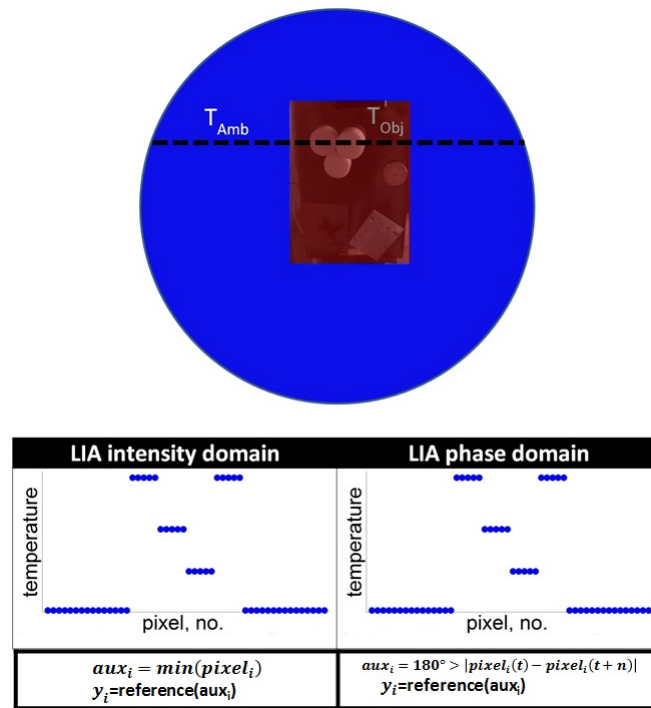


Figure 6.44: Agglomeration procedure from 3D measured data \rightarrow 2D representations for the multinary phase space measurements (one line (dotted line) in the scene).

In figure (6.44) the agglomeration procedure following the analysis procedure are shown. For both the LIA intensity and phase domain, the T_{ref} -modulation yields the effective temperatures of objects in the scene. In the LIA intensity domain the effective temperatures are determined by identifying the point during the temperature modulation when the intensity signal approaches a value of zero. To adapt the procedure to the presence of measurement noise, which inhibits the realization of a true value of zero, the procedure is adapted and determines for every pixel the occurrence of a minimal value of the measured intensity. By using the position of that minimum, the effective temperature in the scene for that pixel (reference()-function) can be determined. The procedure for the LIA phase space is similar. The only difference in the phase space is that not the position of a minimal signal is determined. Instead the occurrence of 180° phase jumps is detected. The numerical procedure is also indicated in the figure.

The inevitable presence of measurement noise now adds additional deviations from the procedure just presented for the LIA intensity space as well as for the LIA phase space. For the LIA intensity space the measurement noise directly affects the results of the measurement since no noise robustness (noise rejection) can be implemented in the LIA intensity space on the hardware level. Of course, after the image acquisition on the software level noise robustness can be implemented by binning a range of measured intensity values together

or by implementing a software threshold for the measured values.

On the other hand, the noise robustness in the LIA phase space is potentially achievable on the hardware level. Still, even measurements in the LIA phase space are not completely unaffected by measurement noise. Also, measurement noise is just one adverse effect that can influence the multinary Lock-In phase space experiments presented here. Other important effects are the deviation of the Rx beam profile from the ideal Gaussian shape. Already discussed were the effects of improper synchronization and related to this topic the unsteady motion of the modulator chopper wheel. Awareness of the other effects is important for an adequate evaluation of the measurement results presented in the next paragraph. However, adverse effects other than measurement noise are difficult to account for quantitatively. Hopefully, a brief numerical estimation of the expected behavior of the multinary phase space setup by just incorporating the additive noise effect is sufficient for a proof-of-principle (as intended here). The effects of additive noise on the LIA intensity signal are quite straightforwardly understood. For the LIA phase domain the behavior is exemplified for a specific case in figure (6.45)

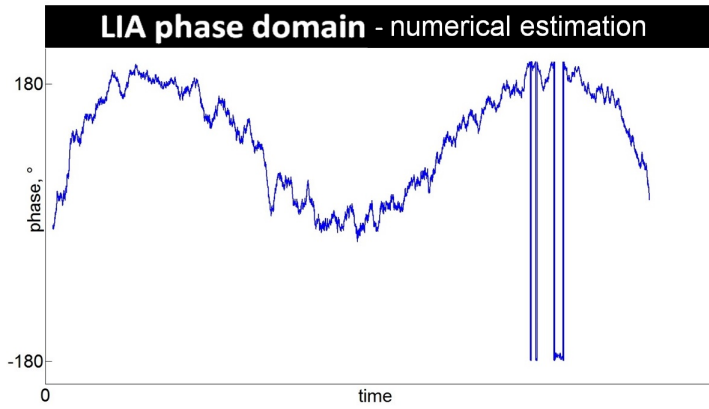


Figure 6.45: Numerical estimation (one pixel) for a measurement in the multinary Lock-In phase space for a pixel of the test pattern.

In the case of a metallic chopper wheel as modulator every T_{ref} -value between T_{Amb} and $T_{ref-max}$ is assumed. When combined with measurement noise the phase jumps are no longer 180° . Because of the multiple occurrences of phase jumps during the T_{ref} -modulation and the smoothing effect of the Lock-In time constant τ_{LI} the behavior in the Lock-In phase space deviates from the ideal case shown in figure (6.43). This behavior is reflected in the numerical estimation shown in figure (6.45). For the numerical estimation an object at a constant temperature T is assumed and measured over time at a fixed spatial point (one pixel). The reference temperature is then modulated between T_{Amb} and $T_{ref-max}$. In the figure additive Gaussian noise and a value for the Lock-In constant τ_{LI} that corresponds to an averaging over 10-15 measurement values is assumed. Due to the fact that the phase space is confined to phase angle values between $-\pi$ and π , phase angle values beyond this range are "folded-back" into this range. This introduces discontinuities in the evaluation process (cf.

(6.45) for an example.). Also, due to averaging during the image/signal acquisition, the expected phase jumps of 180° are moderated to less than 180° . These problems arise in addition to the problems discussed in the last paragraph. In light of all the discussed problems, the goal of the experiments is as mentioned before just a proof of the theoretical considerations and a proof-of-principle of the multinary Lock-In phase space. The next paragraph presents the results of the multinary LIA phase space measurements on the test pattern introduced above.

Results

As a first step, a $31\text{ cm} \times 31\text{ cm}$ section of the test pattern was raster scanned with a step size of 1 cm. At every step (image pixel) the reference temperature was modulated for 3 s. The results for this initial experiment are shown in figure (6.46).

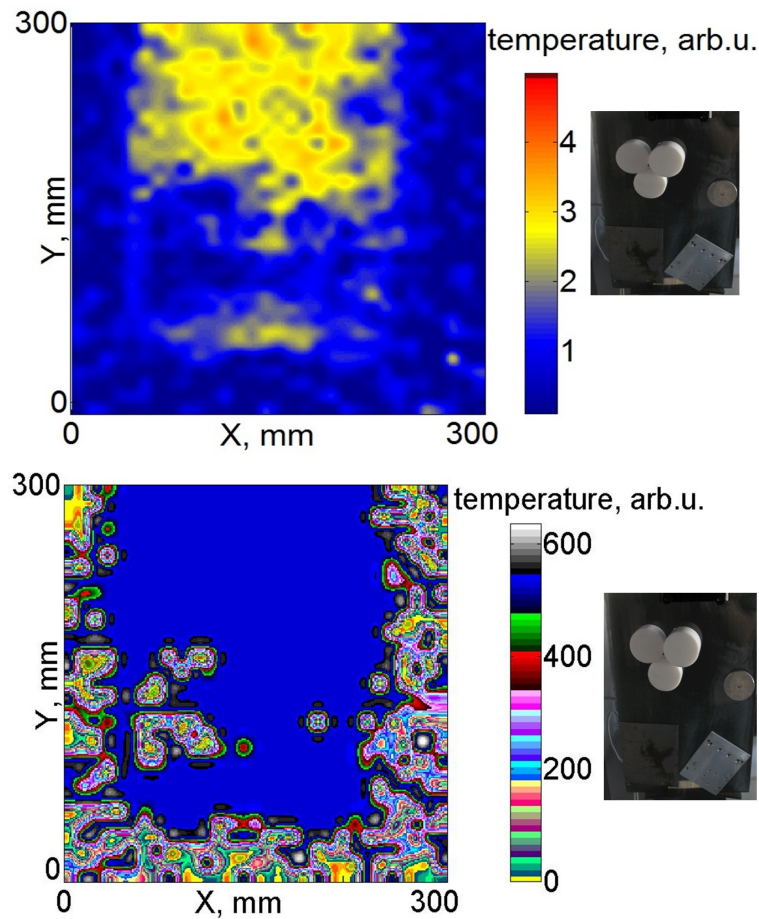
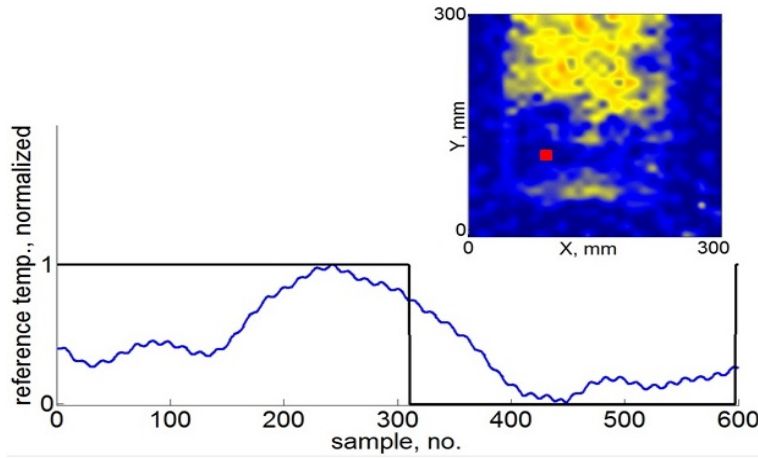


Figure 6.46: Raster scanned section of the test pattern top row in the LIA intensity space and bottom row LIA phase space. Also shown is a digital camera image of the test pattern for a straightforward comparison.

Figure (6.46) shows in the top row the image for the LIA intensity space and in the bottom row for the multinary LIA phase space. The multinary character of the phase space is achieved by binning a number of measured temperature values together (cf. the color code used). Additionally, a digital camera image of the test pattern is shown in each representation to promote a straightforward comparison. The objective is to identify the detected objects in the scene for both the LIA phase space and the LIA intensity space and to relate an effective temperature to the objects in the scene.

In the LIA phase space only a few objects were detected with the chosen parameter combination v_{mod} , $T_{ref-max}$ and f_{mirror} , namely the velocity of the reference temperature modulation v_{mod} the maximum reference temperature $T_{ref-max}$ and the velocity of the switching mirror chopper wheel f_{mirror} . However, the edges of the heat plate in the scene were identified correctly. One of the pieces of metal in the scene was also detected with roughly the same temperature as the surroundings (T_{Amb}). For the detection only 45° phase jumps were used. Due to the aforementioned effects the theoretically expected phase jumps of 180° were reduced to this smaller value. Also, already in the LIA intensity domain not all objects were detected correctly. This might indicate that also other effects negatively influence the results. Therefore, it seems prudent to have a closer look at the signals over time for a specific image pixel.³⁷ Figure (6.47) shows the results of the temperature modulation for a specific image pixel³⁷.



³⁷To be representative the specific pixel was chosen in the middle of a detected object in the scene.

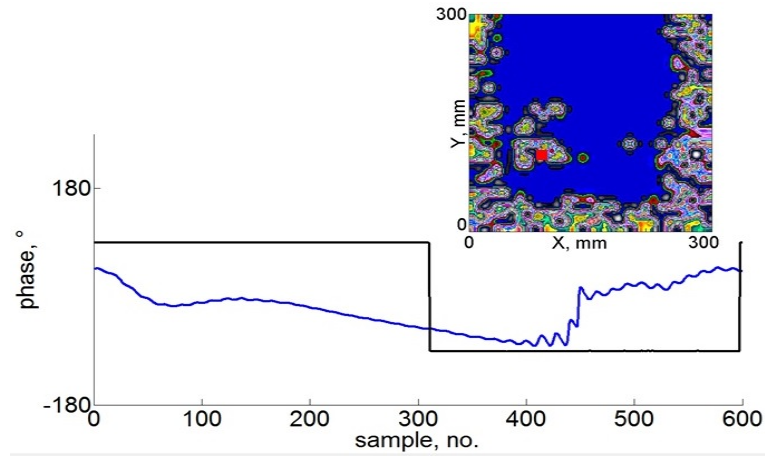
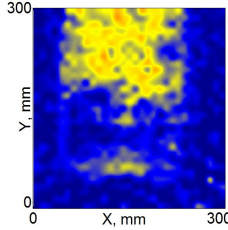
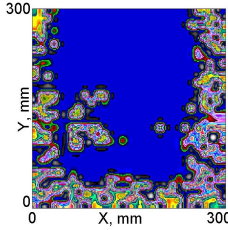


Figure 6.47: Signals over time for a specific pixel in the raster scanned section of the test pattern top row in the LIA intensity space and bottom row LIA phase space. The position of the specific pixel is indicated with a red square in the inset.

The results for one specific pixel presented in figure (6.47) show the deviations from the theoretical expectations for this specific pixel. For both domains the figure shows the measured signal (intensity top row respective phase bottom row) (blue signal) and for synchronization purposes the detected chopper signal (black). In the LIA intensity domain (top row in figure (6.47)) the signal minimum is reached in the second half of the modulation whereas in the first half of the modulation a maximum signal was assumed. This behavior is not expected, according to the theoretical considerations presented earlier. The briefly discussed additional effects might account for this behavior e.g. deviations from the ideal Gaussian Rx beam shape, etc. Also, in the LIA phase domain the expected phase jumps of 180° are considerably reduced and the phase signal shows additional fluctuations that are spread-out over an extensive period of time (no. of samples). To better understand the deviations from the theory, it seems helpful to investigate the behavior of the multinary LIA phase space setup for different parameter combinations of the three main parameters namely v_{mod} , $T_{ref-max}$ and f_{mirror} . Therefore, different parameter combinations were measured and are shown as an overview in the following figure (6.48).

LIA intensity space	LIA phase space	Parameters
		$v_{mod} = v$ $T_{ref-max} = 34.5^\circ\text{C}$ $f_{mirror} = 14\text{ Hz}$

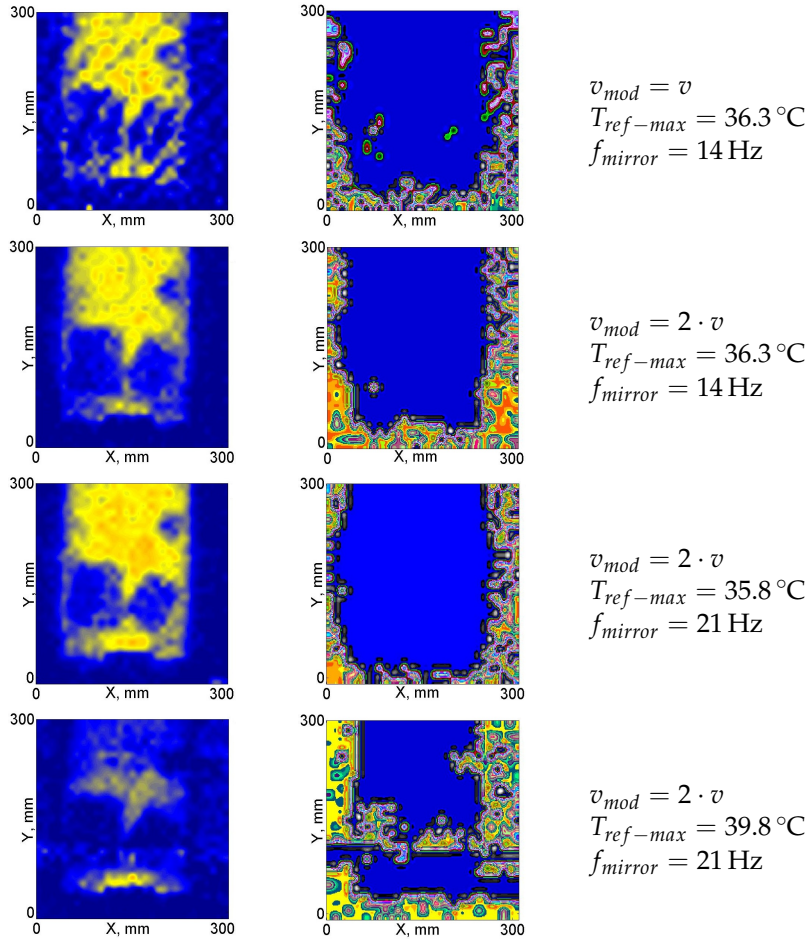


Figure 6.48: Overview of the multinary LIA phase space experiments with differing parameter combinations.

From the overview in figure (6.48) it can be reasoned that with increasing modulation velocity objects in the LIA intensity space are better detectable but the quality of detection in the LIA phase space is not increasing. The third parameter combination for example allows detection of almost all objects in the intensity space. Even the outline of the Teflon rods in the test pattern seem to be detected. However, to increase the detection quality in the LIA phase space, the last parameter combination seems to offer the best results. To evaluate the performance in detail the signals over time for this parameter combination are shown in figure (6.49).

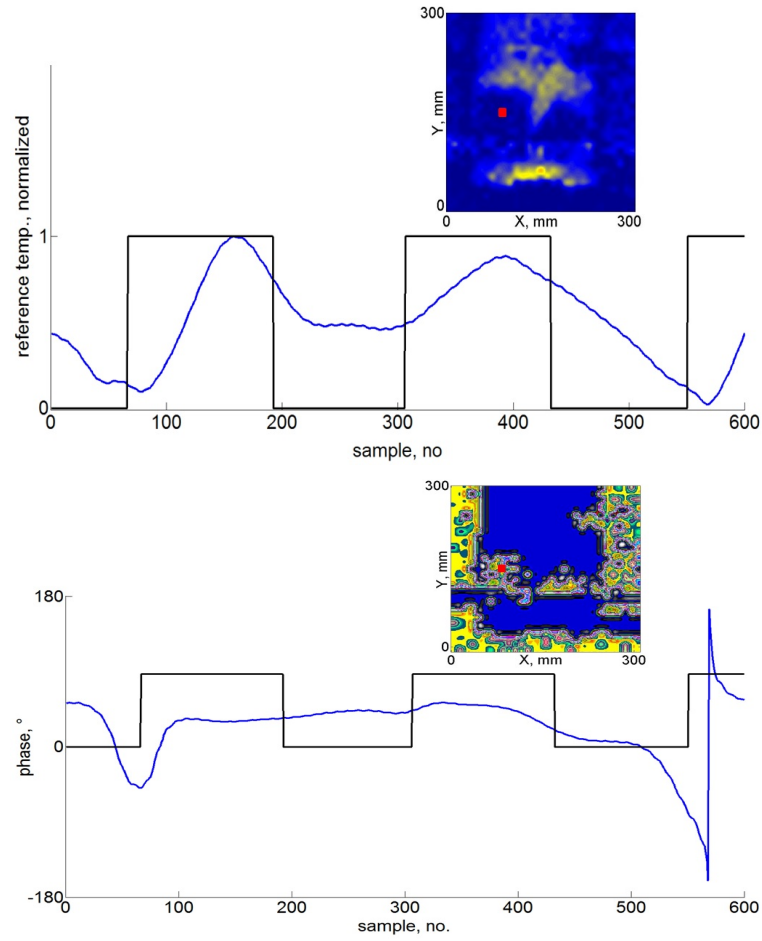


Figure 6.49: Signals over time for a specific pixel in the raster scanned section of the test pattern for the 6. parameter combination $v_{mod} = 2 \cdot v$, $T_{ref-max} = 39.8^\circ\text{C}$ and $f_{mirror} = 21\text{ Hz}$. The top row shows the LIA intensity space and the bottom row the LIA phase space. Again, the position of the specific pixel is indicated with a red square in the inset.

The results in figure (6.49) show that the theoretical expectations for a multinary LIA phase space are indeed correct. In the LIA intensity space the reference temperature modulation produces a minimal signal at a certain reference temperature and in the LIA phase space 180° phase jumps occur when the effective temperature in the scene is equal to the reference temperature. But, figure (6.49) also shows that the mechanical modulation of the reference temperature, using a metallic chopper blade, can cause significant deviations from the expected behavior of the setup.

The periodicity of the modulation is not as expected (raised cosine characteristic). Instead, the periodicity appears to be much longer. Additionally a time jitter is present in the results. As expected, a smear-out effect is present due to the LIA time constant and additional averaging. This also causes some

time delay that is visible in figure (6.49). Specifically, in the figure it is visible in the LIA intensity space that the time characteristic is reproducible when several periods are measured. However, aside from the aforementioned deviations, the characteristic shows also slight differences in its absolute value in subsequent periods. This effect might be caused by deviations in the Rx beam shape. In the LIA phase domain the aforementioned effects can also cause the reduction of the detected phase jumps (see the two detected phase jumps in the characteristic).

To better judge the reproducibility, it seems prudent to extend the time characteristics shown in figure (6.49) to several pixels. Therefore, the following figure (6.50) shows the time characteristics for an entire line of pixels.

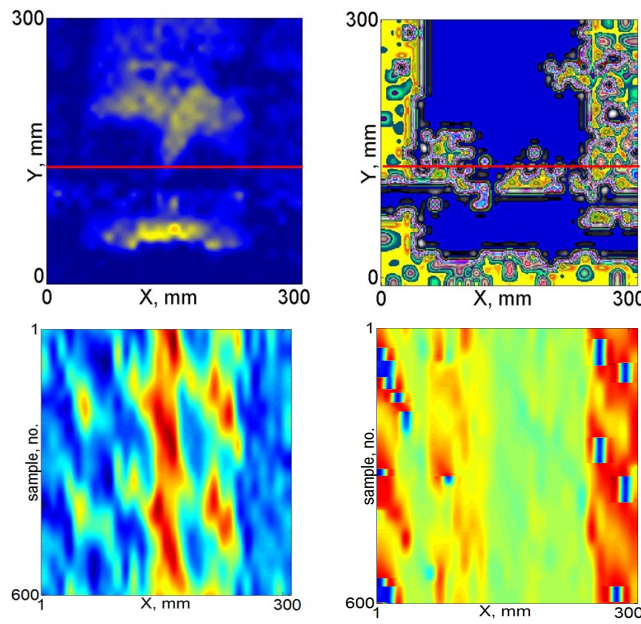


Figure 6.50: Signals over time for a line of pixels in the raster scanned section of the test pattern for the 6. parameter combination. The top row shows the LIA intensity pattern (left) and the line of pixels chosen. The same line is shown for the LIA phase space on the right. The bottom row shows for each case a representation over time for every pixel in the line.

It can be seen in figure (6.50) that the characteristic is reproducible for image pixels that belong to the same object in the scene. It is also visible that the synchronization problems cause distortions in the acquired time characteristics, for both in the LIA intensity and phase domain. In the LIA phase domain these synchronization problems seem to have a more significant effect. Still, the edges of the reference heat plate are clearly distinguished even clearer than in the LIA intensity domain. It seems likely that with an optimized parameter combination for v_{mod} , $T_{ref-max}$ and f_{mirror} even better detection results are achievable in the LIA phase space. This concludes the presentation of the results for the multinary LIA phase space measurements.

6.4.1 Multinary Lock-In Phase Space - Results interpretation

Here, a modified setup that enables measurements in a multinary LIA phase space, instead of a binary LIA phase space, was introduced. The modification is achieved through the introduction of a modulator in front of the reference heat plate (cf. figure (6.35) and figure (6.24)). The introduction of a separate modulator was necessary because the reference heat plate is only able to change its temperature value very slowly. As a modulator a simple metallic chopper blade was used. The chopper blade blocked the reference as seen from the position of the Rx. Due to the mechanical motion of the chopper blade the portion of the reference seen by the Rx was constantly changed allowing for a continuous change of the reference temperature in the range T_{Amb} to $T_{ref-max}$. The simple mechanical nature of the modulator caused problems that limited the capabilities of the modified setup. Problems arose due to the unsteady motion of the modulator chopper wheel, which in turn caused synchronization problems. This synchronization problem could not be overcome on the hardware level and even on the software level the applicability of the simple multinary phase space setup discussed in this section, was significantly diminished. However, the results presented in this section show that a proof-of-principle of this novel imaging method was successful. The true advantage of a multinary phase space comes with the ability to do hardware image processing. It was demonstrated that this is only possible with a fully-fledged THz-SLM³⁸. Since the usage of a THz-SLM would lessen many of the aforementioned issues. However, experiments with the simple setup used here demonstrated the feasibility of a multinary LIA phase space.

³⁸See section (6.5) for details.

6.5 Developing a THz-SLM

Because it was shown in the previous sections that an even greater potential for a phase space exists with the application of a fully-fledged THz-SLM, the next logical step is the development of such a device. Therefore, the last section of this chapter is concerned with the details of its development. SLMs as introduced in section (1.3) are devices that are readily available in the VIS- and NIR-region of the electromagnetic spectrum. In these parts of the electromagnetic spectrum they are employed as dynamic, digital, optical elements (cf. section (4.3)) and allow for the manipulation of electromagnetic waves on the hardware level. The full potential of the new methods presented in this chapter, namely the Lock-In phase space and Compressed Sensing for THz-imaging, is only achievable with a THz-SLM. Therefore, a natural next step was the development of a THz-SLM that could be integrated into the ISM-imager.

6.5.1 Design

Generally speaking, a SLM intended for imaging applications can be characterized as an array of thousands of pixels that are individually controllable via a computer. The pixels either control the amount of the reflected radiation (mirrors) or the amount of transmitted radiation. SLMs for the VIS- and NIR-region are commercially available but for the THz-region commercially available devices do not exist.

The problem of building a THz-SLM mainly stems from the fact that for imaging applications thousands of pixels are needed. Building devices that have the capability to modulate THz-radiation with only a couple of pixels are relatively straightforward. Such devices are very well established and readily available for years. They use different approaches to achieve the modulation of THz-radiation. The modulation can be achieved with electric or magnetic fields using liquid crystals or metamaterials. In the last three years THz-SLM prototypes that used optically-induced modulation emerged and the research efforts to develop THz-SLMs for imaging applications mainly focused on this approach. The optically-induced modulation of THz-radiation is achieved using an **optical switch** as a **mediator**. The optical switch consists of semiconductor material. When the semiconductor is illuminated with light (electromagnetic radiation of certain frequencies), its physical properties change. In the illuminated regions of the semiconductor free charge carriers are generated. This leads to a transition from a semiconducting state to a metallic state depending on the spectrum and power of light it is exposed to. In regions which become metallic the semiconductor is no longer transmissive but reflects or absorbs THz-radiation. So, if the illumination of the semiconductor with light can be spatially modulated³⁹, a THz-beam subjected to the semiconductor is in turn spatially modulated as well. To use the mediating step of the semiconductor/optical switch, offers additional advantages. First, the number of pixels of the THz-SLM is defined by the number of pixels that are used to modulate the light that is subjected to the semiconductor to trigger its transition to a metallic state. Additional advantages stem from the fact that such a THz-SLM

³⁹The device that spatially modulates the radiation on the optical switch is a commercially available VIS/NIR-SLM (TFT-LCD).

design is not only affecting a THz-beam in two spatial dimensions but in three (details on this subject are briefly discussed in section (8.2)). So, the use of the optical switch is not just a means to an end, it offers additional benefits that can be useful for imaging applications⁴⁰. With the description given above a prototype setup of a THz-SLM can be derived and is shown in figure (6.51).

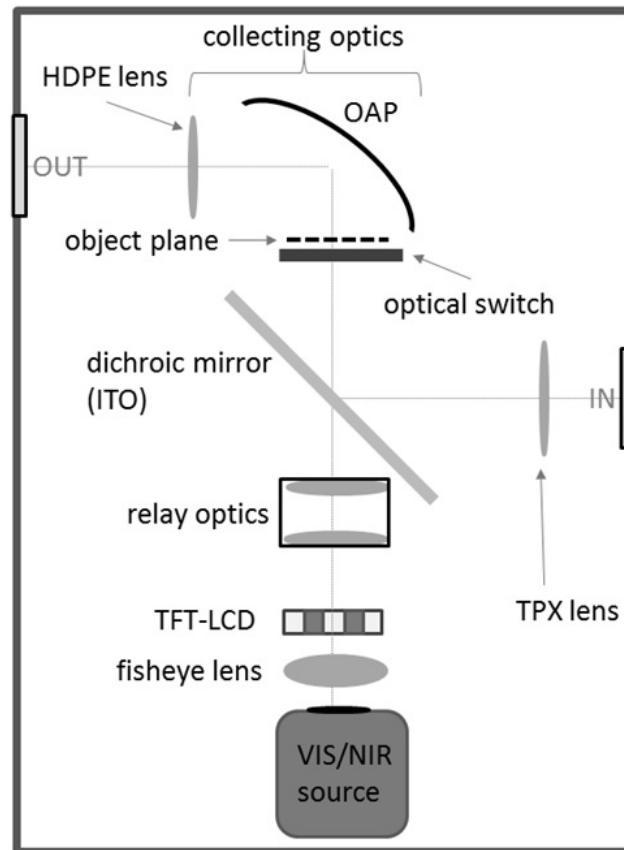


Figure 6.51: Lab prototype setup of a TFT-LCD-based THz-SLM.

The main components are: VIS/NIR source with optics, a fisheye lens, a TFT-LCD acting as VIS/NIR spatial light modulator, relay optics, a dichroic mirror, a semiconductor disc acting as optical switch for THz radiation and collecting optics.

The VIS/NIR light source is an OSRAM HLX 64657 (250 W at 24 V) halogen lamp, which provides a radiation spectrum that is close to a blackbody with a temperature of ≈ 3000 K. The TFT-LCD (Electronic Assembly EA DOGM128W-6) acts as a VIS/NIR-SLM and has 128×64 individually-controllable pixels. It is back-illuminated through a fisheye lens. Having a good homogeneity (flat intensity distribution) of the back-illumination is advantageous, as it diminishes the need for additional characterization of the optical setup. The

⁴⁰e.g. beam steering, dynamic Shack-Hartmann sensors, etc.

concentration of optically excited charge carriers in the semiconductor disc increases with the amount of light with photon energies larger than the band gap energy of the semiconductor. Therefore, good mapping of the VIS/NIR source onto the TFT-LCD and the semiconductor as well as high modulation of the transmitted light by the TFT-LCD are important. The depth of modulation of the TFT-LCD as a function of the incident wavelength was measured with a Fourier Transform spectrometer. It is illustrated in figure (6.52), which shows the TFT-LCD's modulation depth M .

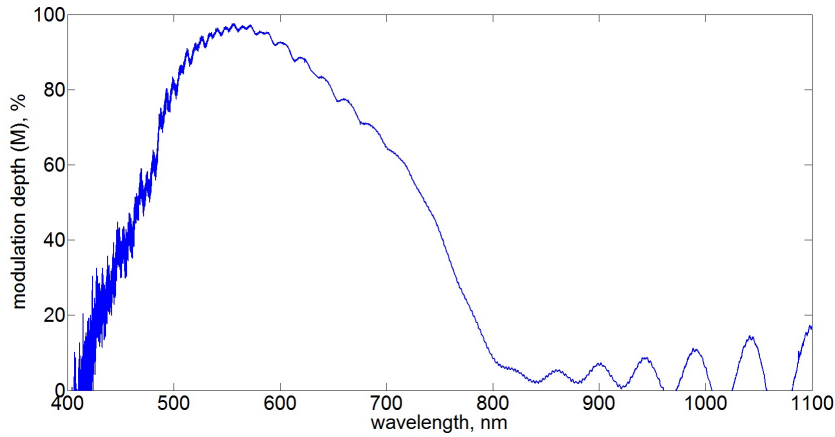


Figure 6.52: TFT-LCD modulation (M) of the transmitted VIS/NIR light when all TFT-LCD pixels are set to black respective white for different wavelengths. The results were measured using a Fourier transform spectrometer.

The relay optics projects the part of the TFT-LCD that was illuminated with VIS/NIR light through a dichroic mirror made of indium tin oxide (ITO) onto a semiconductor disc. An optical setup is used which provides approximately a 1:1 mapping of the VIS/NIR illumination pattern onto the semiconductor. The relay optics is placed approximately 35 cm away from the TFT-LCD⁴¹.

The quality of the optical mapping onto the semiconductor is very important for the success of the reconstruction process. The mapping was found to be free of distortion by naked eye inspection. The precise knowledge of the THz-intensity distribution resulting from each commanded mask is mandatory for a successful reconstruction. However, these patterns are not directly accessible in a straightforward manner. Therefore, the approach chosen here was to assume that the intensity distribution of VIS/NIR light on the semiconductor can directly be used to derive the THz-intensity distribution for each mask. Later, the validity of this assumption is discussed in more detail. The optical switch is a semiconductor disc of 35 mm diameter. The material is single-crystalline Germanium with an impurity concentration less than 10^{-10} per cm³. Germanium was chosen in favor of Silicon because it has a smaller

⁴¹The TFTs can be stacked to increase the depth of modulation further. The depth of modulation of n stacked TFT is $M_{sum} = 1 - (1 - M_{sing})^n$ when the depth of modulation of a single TFT is M_{sing} . A necessary condition for the equation is that the amount of light that is transmitted by the n TFT for the all transmissive state is kept constant.

band gap, which should increase the spectral range of light usable for optical excitation of free charge carriers. Illuminating the Germanium disc with the maximum available (limited by the used VIS/NIR source) amount of light changes its state partially from semiconducting to metallic (the amount of free electrons in the conduction band is significantly increased), which dampens the transmittance of THz radiation. If the semiconductor is illuminated with a pattern of VIS/NIR light, this pattern is, therefore, transformed into a similar pattern of free charge carriers. This creates a dynamic spatial filter for THz-radiation. Using this procedure, a so called mask is transformed from the VIS/NIR domain into the THz-domain. Commanding a mask consisting of black pixels only, the negative-transmissive (inverting logic) TFT-LCD will be set to transmit the VIS/NIR light completely. The transmitted VIS/NIR light will excite charge carriers in the semiconductor turning it non-transmissive for THz-radiation. Vice versa, commanded white pixels will translate to VIS/NIR non-transmissive pixels on the TFT-LCD and non-illuminated parts on the semiconductor keeping it transmissive for THz radiation in these regions. Subsequently, the depth of modulation of the VIS/NIR-SLM together with the excitability of the Germanium determine the depth of modulation of the THz-SLM. The setup presented here is able to achieve 3% - 5% depth of modulation for the transmitted THz-radiation.

The next component is the collecting optics consisting of an off-axis parabolic mirror (OAP) and a lens made from high density polyethylene (HDPE). The optics is used to collect the entire THz-radiation that passes through the optical switch and that is not blocked by objects/targets in the scene. It has to be large enough to accommodate the size of the scene, which is approximately 35 mm in diameter. In addition, the collecting optics has to be able to collect all radiation redirected by diffraction effects arising from objects in the scene and the patterns induced by the optical switch.

6.5.2 Optical Switching

The performance of the THz-SLM prototype critically depends on the type of the semiconductor used as optical switch and on the light source used to modulate the optical switch. Here, especially the delivered optical power and the spectrum are of prime importance. The experiments presented in this section focused as a proof-of-principle on blackbody light sources. For future experiments specialized light sources like LEDs or Lasers might give better results. With the aforementioned blackbody sources and Germanium as optical switch (semiconductor), the optically-induced modulation was successfully demonstrated in an early stage of the development process. This measurement is shown in figure (6.53).

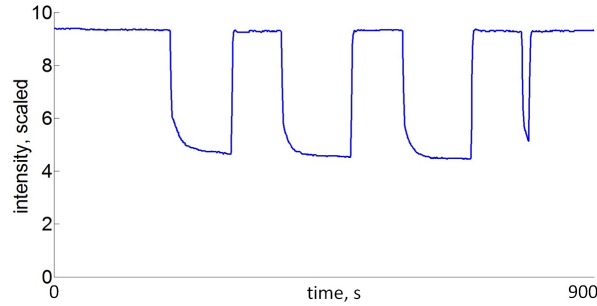


Figure 6.53: Measurement demonstrating the switching of THz-radiation by illuminating a Germanium disc with light from a blackbody using the setup shown in figure (6.51) without the TFT-LCD.

The optically-induced switching is clearly visible in figure (6.53). The depth of modulation is around 50%. For the measurement the halogen light source was used with maximum power (250 W) in the ON-state and was manually blocked in the OFF-state. As is visible, even with full illumination the THz-signal does not vanish completely. This is an indicator that the amount of light illuminating the optical switch was not sufficient to cause a complete transition of the semiconductor to a metallic state. Another thing that is notable in the figure are the transient effects reminiscent of an exponential decay/rise. These are most likely caused by the low pass characteristic of the measurement electronics (time constant of the LIA). Due to the severe noise during the measurement the time constant had to be chosen as $\tau_{LI} = 1$ s. The challenging measurement conditions are not recognizable from figure (6.53) since the switching was done here manually. The full situation can be recognized from figure (6.54) as it shows the modulation of a THz-signal by setting the entire TFT to black respective white (performance of the THz-SLM).

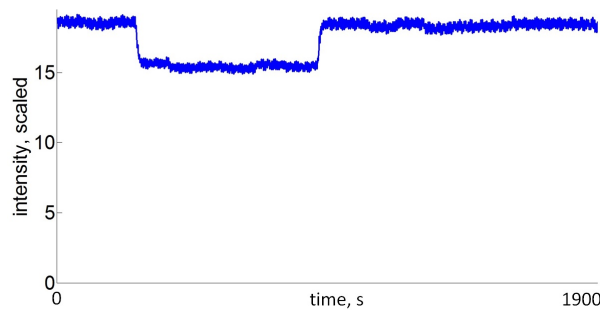


Figure 6.54: Measurement demonstrating the switching of THz-radiation by illuminating a Germanium disc with light from a blackbody using the complete setup shown in figure (6.51) (performance of the THz-SLM lab prototype).

As is visible, the modulation depth is limited to a maximum of $\approx 5\%$. Also visible is the severe noise situation. The switching time of the THz-SLM is

mainly limited by the LIA time constant of 1 s and is approximately of the order of a few seconds (rise/fall time). A full measurement with the SLM-setup now uses projected patterns ("MASKS") that cause a known spatial distribution of free charge carriers in the optical switch. The measurement process with the THz-SLM is as follows:

An object is placed approximately 2 cm behind the Germanium disc. A mask is commanded to the TFT-LCD by LabVIEW™ based control software. The VIS/NIR illuminated TFT-LCD is mapped onto the semiconductor using the relay optics. For every commanded mask, 20 detector readings (measurements) are taken. In addition, 20 measurements are taken with the entire TFT-LCD set to white (increased blocking of VIS/NIR radiation) and another 20 measurements with the TFT-LCD set to black (reduced blocking of VIS/NIR radiation) in order to track a scaling factor and an offset for each mask. In figure (6.55) the measurements for one sequence of "MASK", "Light ON" (TFT-LCD black) and "Light OFF" (TFT-LCD white) are illustrated. The scaling factor represents the ratio between the transmitted THz-radiation when the TFT-LCD is set to black, respective white. The offset is the part of the transmitted THz-radiation, which is not modulated by the optical switch. Both the offset and the scaling factor have to be tracked during the measurements in order to keep track of measurement artifacts like, e.g., temperature drifts.

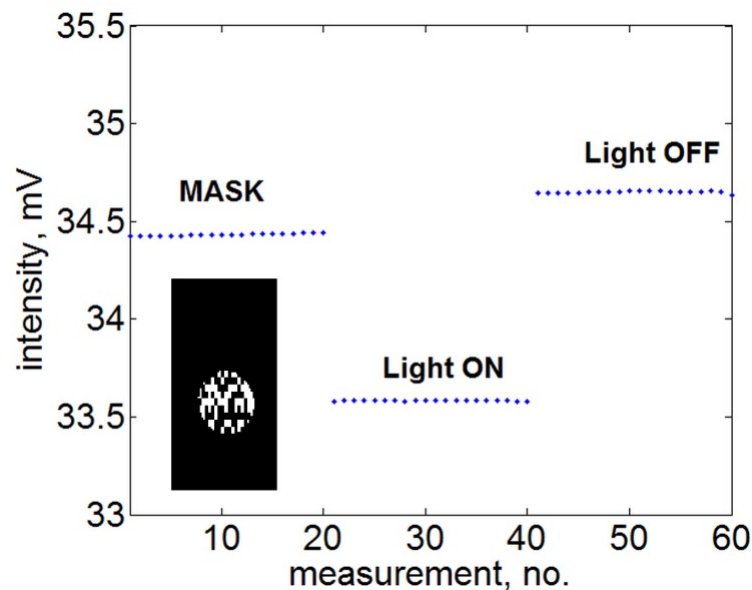


Figure 6.55: Example of a measurement sequence with the THz-SLM setup. The y-axis is the detector signal and the x-axis is the number of the measurement within one sequence. The inset shows the commanded mask of the sequence.

In order to measure all objects in the scene with the THz-SLM multiple masks and the resulting transmitted signal have to be measured. The measurement process of a simple object will be presented in the next paragraph.

6.5.3 THz-SLM imaging using CS-techniques

For the imaging experiments discussed now, the THz-SLM setup has to be extended by a THz-source and a THz-detector. For the experiments a YIG based multiplier source was used to illuminate objects in the scene. The source delivers a continuous wave illumination of approximately 10 mW output power at a frequency of 345 GHz with an almost Gaussian-shaped beam. For a successful reconstruction, the shape of the source beam should be homogeneous, id est a constant power distribution across the scene (equivalent to a top-hat beam profile). However, the real beam is, as mentioned above, of Gaussian-shape. Therefore, its power distribution needs to be known in advance. Because the source beam is further modified by a beam shaping lens and the dichroic mirror a characterization of the beam shape in the imaging plane is necessary. The shape of the beam in the plane of the optical switch, measured by a mechanical/hardware scan using a Golay cell detector, is depicted in figure (6.56). A single Golay cell detector in conjunction with a Lock-in amplifier was also used for the THz-imaging experiments with the THz-SLM setup.

For the imaging experiments presented now, objects made of Eccosorb material were used as targets in the scene. This material is non-transparent for THz-radiation. Targets made of this material are, therefore, binary with respect to THz-radiation. The size of observable objects in the scene is limited by the field-of-view (FoV) of the setup. The FoV itself is limited by the size of the Germanium disc. Another limitation arises from the size and the shape of the THz-beam.

This setup is shown in figure (6.57). The THz-source and the single Golay cell detector together with the THz-SLM described in the last section form an active single-pixel THz-camera⁴².

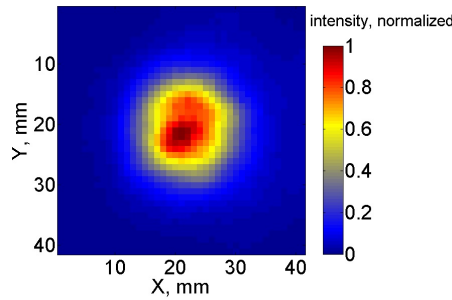


Figure 6.56: Shape of the THz-beam after modification by beam shaping lens and dichroic mirror (ITO) without the optical switch approximately in the imaging plane. The figure shows the view into the beam.

⁴²This setup is similar to the SPC-setup described in section (1.4) but extends the concept of the SPC to the THz-region.

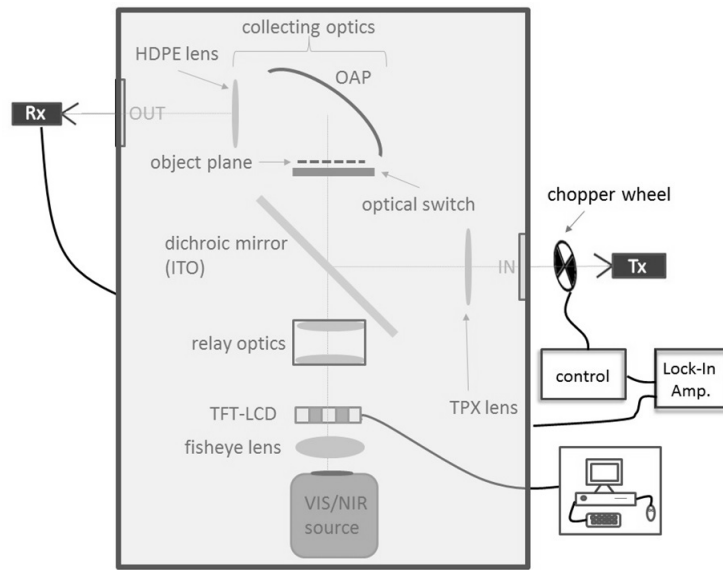


Figure 6.57: Setup showing the extension of a THz-SLM to an active THz single pixel camera (THz-SPC).

As a first step, the beam profile was measured with the setup. In total 1024 i.i.d. 0/1-masks were used for this measurement. For evaluation purposes, the beam reconstruction was done using the Moore-Penrose pseudo-inverse as implemented in MATLAB instead of a CS algorithm. This choice was driven by the requirement to have a reliable and CS independent measurement of the beam in the correct coordinate system. The goal of the measurements presented in this section is to evaluate CS techniques in the THz-domain (CS techniques with a THz-SLM). Therefore, the characterization of the beam should be independent of CS-approaches. However, this type of scan must be transformed into the correct coordinate system, i.e. the coordinate system of the software scan with the THz-SLM. As this transformation is not precisely known, a characterization of the method is prone to offset-errors. The result of the beam

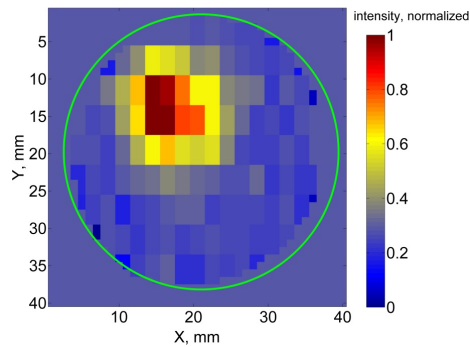


Figure 6.58: Software scanned (1024 i.i.d. 0/1-masks) and reconstructed beam using the pseudo-inverse. The green circle marks the boundary of the Germanium disc.

characterization using software scanning with 1024 random Bernoulli masks and the pseudo-inverse for reconstruction is shown in figure (6.58).

The software scanned image in figure (6.58) exhibits a lateral offset and the spatial resolution is not as good as for the hardware scan of figure (6.56). The spatial resolution in the software scanned image is given by the pixel size of the masks. It was chosen to be $2\text{ mm} \times 4\text{ mm}$. This is significantly larger than the wavelength of the transmitter in order to minimize diffraction effects at the pixel boundaries. The beam profile measurements (hardware as well as software scan) were done at the position of the Germanium disc. Concerning the shape of the beam, it must be stated that this is important insofar as the whole object plane should be illuminated with sufficient power. In this experiment the ratio between the maximum power (red) and minimum power (blue) regions is approximately 18:1. This poses significant difficulties for the reconstruction of objects, as will be seen in the following paragraph.

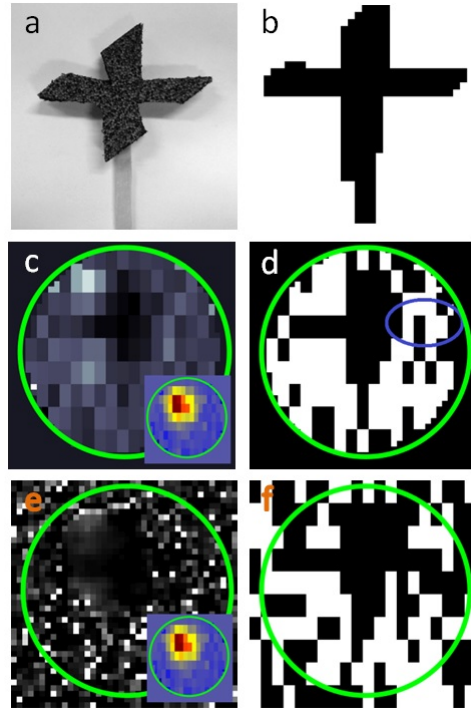


Figure 6.59: Digital camera image of the object, b) binarized object, c) software scanned and pseudo-inverse reconstructed object using 1024 masks, d) binarized version of c), e) software scanned and CoSaMP reconstructed object using 300 masks, only pixels inside the green circle (edge of Germanium disc) are to be considered, f) binarized version of e) with pixel aggregation to adapt to the pixel size of c) and d). The insets in c) and e) show the beam profile. The green circles indicate the edge of the Germanium disc. All images show a portion of $40 \times 40\text{ mm}^2$.

In figure (6.59), a pseudo-inverse reconstruction (center row) and a CS reconstruction (bottom row) of a single object (top row: a) digital camera image of the object, b) binarized version) are compared with respect to the quality of reconstruction and necessary number of measurements (masks). It should be mentioned again that the depth of modulation is quite low with 3% - 5% and that the center of the THz-beam is located mostly in the upper left portion of the scene. Therefore, the SNR on the right side of the object is too low for a successful reconstruction. Both reconstructions recovered the central and left part of the cross but fail to recover the right arm of the cross. As can be seen from the inset, the THz beam illuminates the right arm with significantly less power than the left and center parts of the cross. The ratio between the signal power of the beam on the left arm and on the right arm is approximately 18:1⁴³. The reconstruction shown in the center row of figure (6.59) is based on the pseudo-inverse with 1024 measurements (masks). As is known, the pseudo-inverse minimizes the l_2 -norm as compared to most CS-algorithms e.g. CoSaMP⁴⁴ which minimize the l_1 -norm. The goal in a CS-scanning scheme now is to achieve a similar or better quality of reconstruction with significantly reduced number of measurements (masks). The reconstruction result presented in the bottom row of figure (6.59) used a standard CS algorithm (CoSaMP) with only 300 measurements (masks) for the reconstruction. The number of necessary masks is significantly reduced for this CS-reconstruction compared to the pseudo-inverse reconstruction (300 vs. 1024). The image quality of the two different reconstruction approaches is fairly similar, in particular when considering the binary images. In order to evaluate the image quality quantitatively, the number of correctly reconstructed pixels for the pseudo-inverse as well as the CoSaMP approach was determined. The results of this evaluation are shown in figure (6.60).

⁴³It can be assumed that either using a detector with lower NEP or a higher depth of modulation will yield a better reconstruction. Another possibility to improve the reconstruction is to use a less absorbing optical switch, resulting in a higher SNR without the need to increase the absolute signal power.

⁴⁴As introduced in section (3.3), CoSaMP is a very prominent CS-algorithm.

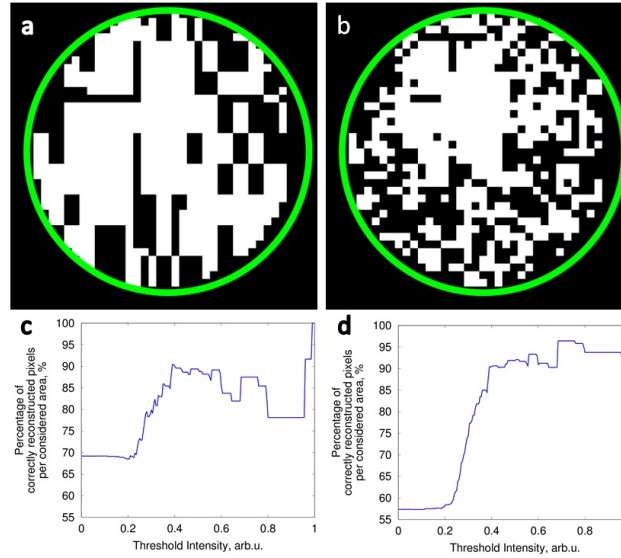


Figure 6.60: In a) (pseudo-inverse reconstruction) and b) (CoSaMP reconstruction, only pixels inside the green circle are considered) the correctly reconstructed pixels are shown in white and the incorrectly reconstructed pixels are shown in black. In c) (pseudo-inverse reconstruction) and d) (CoSaMP reconstruction) a quantitative analysis is shown.

Figure (6.60) shows in the top row the correctly reconstructed image pixels for the pseudo-inverse reconstruction (LHS) and for the CoSaMP reconstruction (RHS). A white pixel indicates a correctly reconstructed pixel while a black pixel indicates a wrongly reconstructed pixel. For both approaches most of the correctly reconstructed pixels are in the region with significant intensity (cf. figure (6.58)). In turn, the bottom row shows a quantitative evaluation on the intensity that is needed for a successful reconstruction. Here, the percentage of correctly reconstructed pixels is plotted as a function of the threshold intensity. In this the threshold intensity is the percentage of the maximum detected intensity in the scene. For the representation in (c) and (d) only those pixels are considered which are illuminated with an intensity equal or larger than the threshold intensity. It should be noted that both reconstructed images have been binarized prior to comparison with the expected image (figure (6.59) b)). This introduces small binarization artifacts that cause for example a slight shift in the position of edges. When comparing the reconstructed image of the object to the expected image (figure (6.59) b)), these artifacts become visible as incorrectly reconstructed pixels (see figure (6.60) a)) black right angle in the upper left part). This shift (the resulting “incorrectly” reconstructed pixels) is responsible for the drop of the correctly reconstructed pixel percentage in the high intensity region between ~ 0.8 and ~ 0.95 . However, this is not an inherent effect of the measurement and the reconstruction. In summary it can be stated that good reconstruction is achieved for both approaches in regions that are illuminated with intensities $> 40\%$ of the maximum intensity (yellow to reddish areas in figure (6.56) respective figure (6.58)).

6.5.4 Developing a THz-SLM - Results interpretation

The measurements presented in this section showed that already with a low-cost TFT-LCD based THz-SLM, software scanning using CS-techniques was successfully implemented. It was demonstrated that already with standard CS-algorithms a reconstruction can be achieved using only 300 instead of 1024 measurements as needed for pseudo-inverse reconstruction. This is a reduction to less than 30 %. The use of CS-methods became possible only with the help of a THz-SLM prototype. The new design, which used the aforementioned TFT-LCD and a Germanium disc, offers possibilities for very compact implementations with significantly reduced cost compared to approaches using, e.g., a digital micro-mirror device. The presented setup also allows for improvements like increased depth of modulation, larger field of view and improved compactness. Additionally, the correlation between the commanded masks, its optical representation, and the effective THz-masks was investigated. It was found that the initial approach using the commanded masks for the reconstruction was sufficient for a successful reconstruction. However, some of the deviations in the reconstruction may be attributed to a difference between the commanded masks and the THz-masks. An investigation on the exact structure of the THz-masks may offer potential to increase the image quality and imaging speed further. Additionally, several possibilities for structural design-improvements have been identified, which are also relevant for other SPC designs. In summary, the combination of a THz-SLM with CS and a sensitive single-pixel detector is a promising alternative to large format THz-array detectors.

6.6 Chapter summary

This chapter presented the main body of the results attained during the work on this thesis. The first section served as a reference point for all the following sections, presenting a selection of images measured with the ISM-imager. It showed the imaging capabilities of the ISM-imager when used in a passive imaging modality using only intensity information from the scene. It showed the practical limits regarding spatial- and temporal resolution with the given hardware of the THz-imager. The presented passive THz-images while of good quality exhibited some artifacts stemming from the hardware scanning nature of the image acquisition. However, it was demonstrated that under certain conditions the spatial resolution limit set forth by the scanning telescope could be exceeded. In that way, it was shown that the ISM-imager is well-suited for the demonstration of the new imaging methods that are the core of this thesis.

In the section "CS on passive THz-images" the passive THz-images presented in the first section of this chapter were improved/analyzed using methods normally applied in CS-applications. The section showed that the image artifacts commonly encountered in passive THz-imaging using only a few or just a single-detector can be addressed with these techniques. The section presented the possible benefits CS has when applied on the software level and at the same time demonstrated the potential CS-methods hold for THz-imaging when applied on the hardware level using a THz-SLM. The first of the new methods was presented in section (6.3) introducing the so-called Lock-In phase space. The LIA phase space is a new way to acquire passive THz-images enabling the use of Lock-In phase information. The results presented in this section discussed three possible theoretical cases which were successfully tested in a passive imaging setting. The advantages of the new method, which include hardware image processing, increased noise performance and increased spatial resolution, were demonstrated and possible extensions were pointed-out. Although the method was demonstrated here in a passive THz-imaging setting, its extension to an active THz-imaging domain was also outlined.

In section (6.4) the method introduced in the previous section was extended from a binary phase space to a multinary phase space. It was demonstrated how the extended method of a multinary phase space can be used to adapt the acquisition process to the measurement situation at hand. It was shown that temperature resolution can be traded-off for increased noise robustness during the measurement (on the hardware level). It also was discussed that the natural extension of a binary phase space to a multinary phase space would offer even more potential when implemented with THz-SLMs.

The last section of this chapter was concerned with software scanning using a THz-SLM. It presented a way to achieve the combination of software scanning with a single detector using THz-SLMs. The section discussed a THz-spatial light modulator lab prototype and demonstrated SLM-based image acquisition (software scanning) with CS-techniques. It was shown that the new, dynamic software scanning design based on a low-cost TFT-LCD provides the capability to change the transmittance of an array of pixels and in this way enables single-pixel THz-imaging without hardware scanning.

Conclusions and New Developments

Contents

7.1	Active vs. Passive THz-Imaging	197
7.2	Hardware vs. Software Scanning	197
7.3	Lock-In Phase Space vs. Lock-In Intensity Space	198
7.4	Hardware vs. Software Image Processing	198
7.5	THz-Imaging vs. THz-Imaging with CS	199
7.6	Spatial undersampling vs. Information content	199
7.7	SNR vs. Scanning Time	200

This chapter summarizes the conclusions that can be drawn from the results presented in this thesis (theoretical and experimental). Every section is concerned with a specific topic that will be addressed therein. The specific topics are formulated as research questions that will be answered referring to a certain result discovered during the work on this thesis. The results usually pertain to the ISM-imager but in this chapter a generalization of the results for all THz-imager/THz-imaging as a whole is attempted.

7.1 Active vs. Passive THz-Imaging

Is active THz-imaging or passive THz-imaging better suited for security imaging applications?

Answer: The ISM-imager is not well-equipped for THz-imaging in the active domain. However, the results suggest that with certain modifications active imaging is possible with the ISM-imager and that it holds promising advantages over passive imaging for the solution of the imaging scenario at hand. The most important advantage is the almost unlimited SNR in active mode, which is only limited by engineering considerations (output power of the artificial source(s)). Also, due to the fact that artificial illumination is used, the illumination source(s) can be modulated to further improve the imaging capabilities. Nonetheless, it was shown that in the active mode resolution well beyond the spatial resolution limit set forth by the scanning telescope is possible and that even the scattering/reflection from radar absorption material can, under certain conditions, be sufficient for the imaging task. The results also suggested that the directional illumination of artificial sources is not well-suited for stand-off imaging. Accordingly, different illumination scenarios are better equipped for the imaging scenario in security imaging and should be employed.

Bottom line: With the outlined solution (FMCW-radar with software scanning) for the problems encountered in the active imaging domain, namely polarization effects and Tx-Rx crosstalk as well as the directional illumination, the advantages of an active imaging domain outweigh the advantages of a passive imaging modality and therefore an active imaging modality is recommended for the solution of the security imaging scenario discussed in this thesis.

7.2 Hardware vs. Software Scanning

What are the advantages/disadvantages of software scanning compared to hardware scanning?

Answer: A scan of the imaging scene is only necessary when the number of available detectors is not sufficient for the aspired spatial resolution of the resulting images. If hardware scanning is chosen, it comes with the necessity to physically move considerable masses, which makes the scanning motion relatively slow. When the scanning process is accelerated by using an on-the-fly mode, the scanning introduces image artifacts in the resulting images. This was well observed and analyzed in this thesis. On the other hand, in a software scanning mode, no physical masses have to be moved, which makes the imaging process considerably faster. In addition, it was shown that if the software scanning process is implemented correctly, no image artifacts are introduced during the acquisition process. In an active imaging modality, software scanning requires the illumination of the entire scene, which potentially wastes power emitted by the source(s). Also, the software scanning requires SLMs, which are not yet readily available. The lab prototype presented in this thesis

is also not yet ready to be implemented in the ISM-imager.

Bottom line: The imaging scenario for security imaging discussed in this thesis requires very fast real-time capability for the image acquisition. Therefore, hardware scanning solutions can not be chosen. When the potential waste of power in an active software scanning scenario is overcome by, e.g. beam steering solutions, the benefits of software scanning far outweigh the advantages of a hardware scanning approach. In addition, the potential measurement time reduction software scanning offers with the application of CS-techniques (as demonstrated in this thesis) is not achievable in a hardware scanning setting.

7.3 Lock-In Phase Space vs. Lock-In Intensity Space

What are the merits of the Lock-In phase space compared to the Lock-In intensity space?

Answer: As demonstrated, the Lock-In phase space offers an alternative way to implement the imaging process. By choosing a modified setup with a reference source and Lock-In detection, the phase space becomes available and offers the possibility for an increased noise performance/robustness and under certain conditions also increased spatial resolution. The usage of an Lock-In amplifier is obligatory for this new imaging setting because the Lock-In reference source provides a phase reference. In addition, the reference source opens-up the possibility of image processing on the hardware level. As discussed in earlier chapters, thresholding is a very useful method of image processing and with a reference source in a modified imaging setup, thresholding is already possible on the hardware level.

Bottom line: In the Lock-In phase space temperature resolution can be traded-off for noise robustness. Since the trade-off can be changed during a measurement, the measurement setting can be adapted to the imaging conditions at hand. Since the only requirements for the new method are a temperature reference and the use of a Lock-In amplifier, the advantages of the Lock-In phase space far outweigh the Lock-In intensity space where measurements can be directly corrupted by noise.

7.4 Hardware vs. Software Image Processing

What are potential gains of hardware image processing compared to software image processing?

Answer: Hardware image processing as introduced here offers many possibilities. Among them is edge-detection on the hardware level. It was shown that this can lessen and in some cases even solve the Bodyscanner-issue. Hardware image processing uses THz-SLMs to achieve filtering of the THz-signal on the level of the radiation itself. This is equivalent with extracting directly the information content from the signal. With hardware (image) processing it is possible to detect the information content in signals better and make content visible that would not be retrievable in a classical processing chain where the

(image) processing is only conducted after the acquisition on the software level.

Bottom line: Hardware image processing makes the discovery of information content possible that would not be retrievable on the software level or it can prevent the proliferation of unintended content.

7.5 THz-Imaging vs. THz-Imaging with CS

How will CS affect the future of THz-imaging for security applications?

Answer: The advantages of CS were amply demonstrated on the hardware level in the VIS- and IR region of the electromagnetic spectrum. In this thesis the advantages of CS were demonstrated both on the hardware and on the software level. On the hardware level it was shown that the number of necessary measurements can be substantially reduced when CS-methods are used. On the software level it was shown that CS-techniques can improve the image quality and combat measurement artifacts. This only shows the tip of the iceberg of what is possible with CS for THz-imaging. For the THz-region the potential advantages are even greater than for the VIS- and NIR-region since THz-hardware is much bulkier and much more expensive. In future applications CS will result in new imager designs that make Superresolution and an almost infinite depth of focus also possible in the THz-region.

Bottom line: CS is already changing the paradigm of THz-imaging (for security applications).

7.6 Spatial undersampling vs. Information content

Can passive THz-images acquired with a certain spatial undersampling factor be reconstructed and then displayed with an optimal nominal spatial resolution in accordance with their information content?

Answer: Reconstruction success is achievable with the help of CS-based image reconstruction procedures. This approach uses a-priori knowledge to reconstruct the THz-representation of the scene without missing values. This reconstruction approach is trying to reconstruct the THz-scene in accordance with its information content going beyond the physical limitations of the imaging system itself. However, the implementation of this approach is computationally demanding and sensitively dependent on the exact knowledge of the imaging process.

Bottom line: CS offers the possibility for super-resolved passive THz-images.

7.7 SNR vs. Scanning Time

Is the SNR the main factor for the determination of the image acquisition time (measurement time)?

Answer: The classical formula for the sequential measurement of an image is number of pixels multiplied with the integration time per pixel. Many of the images presented in this thesis were acquired according to this formula. However, in a software scanning setting this formula no longer applies. Due to the fact that in a software scanning approach multiple pixels can be active at the same time, the derivation of the measurement time depends on the measurement algorithm (the sequence of active pixel). When software scanning is combined with CS-methods, the necessary measurement time can even be reduced further. Also, in a software scanning approach, the measurement SNR is greatly improved by the number of active pixel. Due to that reason, a simple relation of SNR and measurement time no longer holds.

Bottom line: In a software scanning approach the SNR is no longer the main factor for the determination of the measurement time.

Outlook

Contents

8.1	Using Compressed Sensing with a THz-SLM for THz-security Imaging	202
8.2	3D-THz-SLM	203
8.3	Towards BRDF enhanced THz-security imaging	205

This concluding chapter is devoted to application examples of the new developments in THz-imaging, which are demonstrating the potential for further improvements of some of the results gained in this thesis. The first section expands the concept of "THz-SLM based imaging" introduced in the text and shows how it will be possible to adapt the THz-SLM lab prototype for the ISM-imager by combining it with the method of frequency modulated continuous wave-radar (FMCW-radar) to overcome the issues encountered with the ISM-imager in active mode. The second section then extends the lab prototype THz-SLM from a 2D-SLM to a 3D-SLM presenting one possibility of overcoming the mentioned waste of power encountered in active mode THz-SLM based imaging. The last section then discusses different illumination scenarios in the context of an optimized detection of reflected/back-scattered radiation. The discussion is guided by the concept of the bidirectional reflectance distribution function.

All examples discussed are extensions of the results presented in previous chapters and therefore give an outlook of how the work on the subject of THz-security imaging might continue in the future.

8.1 Using Compressed Sensing with a THz-SLM for THz-security Imaging

It was shown that the THz-SLM lab prototype has the necessary functionality to be included into the ISM-imager. However, (at least) two points that need improvement still remain. Firstly, the depth of modulation of the prototype while sufficient should be improved for the measurements with the ISM-imager. The improvement, as was already discussed, is easily achievable with the use of stacked TFT-LCDs. The depth of modulation increases with the number n of stacked TFT-LCDs according to equation (8.1) when the depth of modulation of a single TFT is M_{sing} . A necessary condition for equation (8.1) is that the amount of light that is transmitted by the n TFT-LCDs for the all transmissive state is kept constant.

$$M_{sum} = 1 - (1 - M_{sing})^n \quad (8.1)$$

According to equation (8.1), the depth of modulation of for example three TFT-LCDs is in the range of 8.6% - 14.3%. The stack of much more than three TFT-LCDs would require too much illumination with VIS/NIR light and, therefore, would be unfeasible to implement. To stack multiple TFT-LCDs, the illumination source has to be optimized. Corresponding experiments have already been conducted and suggest that for Germanium the modulating wavelength lies in the NIR-region of the spectrum. Since a TFT-LCD is an optimized modulator for VIS-wavelength, a possible solution here would be to choose a different semiconductor as optical switch. Another option for improving the depth of modulation would be to choose a different kind of VIS-SLM. Experiments have already been conducted with a digital micromirror device (DMD)¹. With a DMD as VIS-SLM more than 30% depth of modulation was achieved.

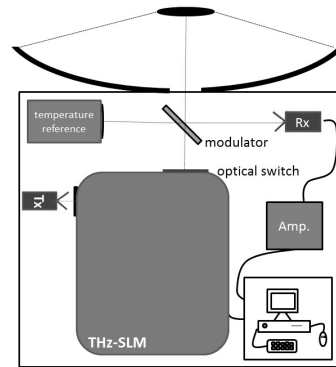


Figure 8.1: Schematic setup for THz-SLM based imaging with the ISM-imager in a modulated illumination setting.

It is then straightforward to implement the THz-SLM into the ISM-imager. As already discussed in section (3.5), two setup alternatives are possible in active mode. Figure (8.1) shows a schematic setup implementing THz-SLM based imaging with the ISM-imager in a modulated illumination setting. The schematic setup of figure (8.1) shows a setting where the illumination is modulated by the THz-SLM. The setup also depicts the necessary modifications for a Lock-In phase space detection.

¹A DMD is a digital light processing device manufactured by Texas Instruments Inc. details can be found at www.dlp.com.

As a simple solution, the modulator would in this case consist of a Mylar chopper wheel and the temperature reference has to be a calibrated THz-source. Since synchronization with the chopper wheel would be an issue in this setting, a second THz-SLM replacing the chopper wheel (modulator) would be advisable.

As already discussed in section (3.5), a modulated illumination setup is more suited for short-range applications (like demonstrated for the lab prototype experiments). For a stand-off application a modulated detection setup is more advisable. The modulated detection setting is shown as schematic representation in figure (8.2). The modulator can be implemented as before in the modulated illumination setting. Again, synchronization is an issue with the setup. To overcome the synchronization issue, the modulator could

be replaced with the optical switch of the THz-SLM making the setup a combination of the modulated illumination setup and the modulated detection setup. This is up until now a setup that has not been studied by any research group. The possible advantages of this setup are very promising. However, it is also a very challenging implementation of THz-SLM-based imaging since it inherits the possible problems of both the modulated illumination setup and the modulated detection setup. To fully understand the physical basics of this implementation, the THz-SLM must not be thought of as a 2D-device but instead as a 3D-device. What is exactly implied by the notion of a 3D-THz-SLM is discussed in the next section.

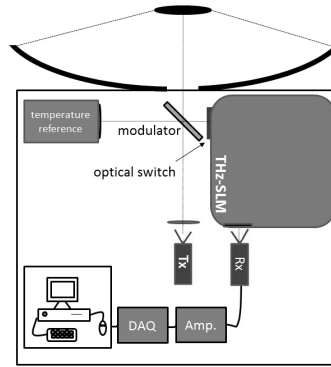


Figure 8.2: Schematic setup for THz-SLM based imaging with the ISM-imager in a modulated detection setting.

8.2 3D-THz-SLM

To understand the notion of a 3D-THz-SLM, the notion of a 2D-THz-SLM has to be considered first. The description of the THz-SLM given in previous chapters names the optical switch as a main component that facilitates the spatial filtering of an incident THz-beam. In the 2D-picture, the optical switch can be regarded as consisting of multiple 2D-pixels (length and width but no depth). The individual pixels exhibit either a metallic or non-metallic behavior. When the behavior of the pixel is metallic, incoming THz-radiation in the spatial region of the respective pixel is not transmitted through the optical switch. In the other case of non-metallic pixels, THz-radiation is modeled to pass-through such pixels without change in its direction of propagation. In the 2D-picture the pixels are either transmissive or non-transmissive and the

optical switch is modeled as infinitely thin.

The 3D-picture now models the optical switch as having finite thickness and also as allowing interim values between a fully transmissive and fully non-transmissive state. Due to the finite thickness of the optical switch, deviations from the original direction of propagation of incident THz-radiation are caused. The general notion of a 2D- and 3D-THz-SLM are visualized in figure (8.3).

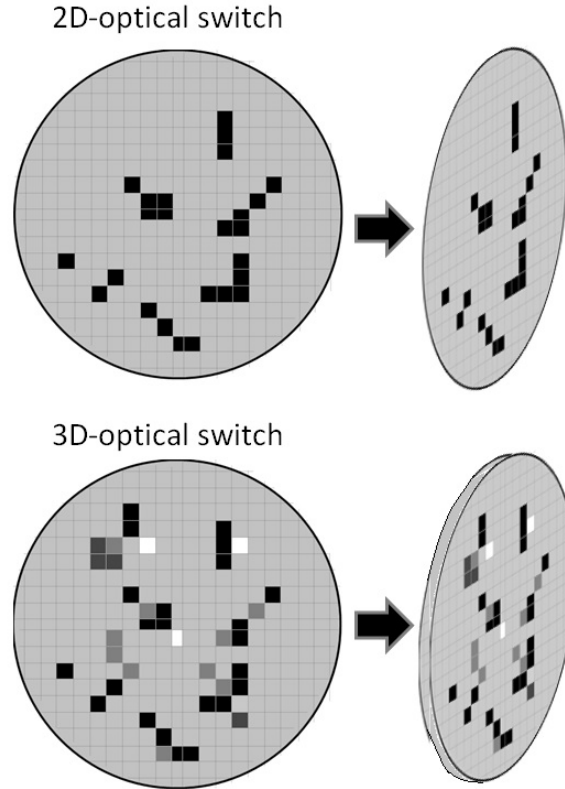


Figure 8.3: Visualization of the notion of a 2D- and 3D-THz-SLM (optical switch).

The notion of a 3D-THz-SLM is connected to the modeling of the behavior of the optical switch and the influence of the blurring kernels in THz-SLM-based imaging discussed in section (3.5) and section (A.2)². For a full understanding of the 3D-nature of the optical switch in a THz-SLM, additional studies are necessary. The research done on this subject in other research groups has only scratched the surface. For the modeling of the optical switch which is needed for almost all software scanning applications in THz-imaging, a fundamental physical understanding of the processes involved is necessary.

²The modeling of the optical switch in the lab prototype used a scaling factor and an offset that globally considered a not-fully transmissive/non-transmissive optical switch. For a 3D-THz-SLM this behavior has to be modeled locally on a pixel by pixel basis.

8.3 Towards BRDF enhanced THz-security imaging

In the last section of this thesis, the directional properties of the radiation involved are discussed. In a passive imaging scenario the objects in the scene itself emit THz-radiation³. In such a setting the radiation exhibits almost no dependence on the angle of detection (ϕ), meaning the THz-radiation does not change in strength when ϕ is changed. That is one of the reasons the passive imaging modality is so useful for the test of new imaging techniques. However, a real-world THz-security imaging scenario, as extensively discussed in this thesis, is an active imaging scenario. In this scenario, the incident Tx-beam and the outgoing Tx-beam (after reflection/scattering) form a plane that is schematically shown in figure (8.4). This plane defines the angle of detection ϕ and the signal strength changes when ϕ is changed. This situation is also shown in figure (8.4).

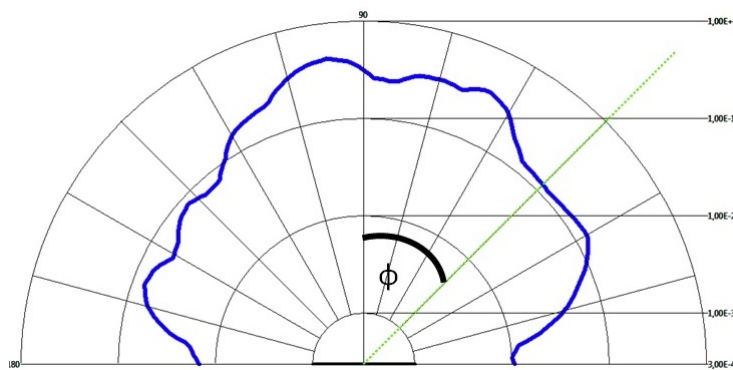


Figure 8.4: Definition of the angle of detection (ϕ).

The situation described in figure (8.4) has been extensively studied for all kinds of materials that are encountered in THz-imaging, namely human skin, optical obscurants and all kinds of possible hidden objects (metallic, non-metallic). Also, other research groups have studied the subject known as the bidirectional reflectance distribution function (BRDF) which quantitatively describes the physical quantities in the aforementioned scenario.

Now, a totally different situation arises when the entire scene is illuminated with artificial THz-radiation. This illumination scenario is encountered in the software scanning approach. Here, no data for the BRDF of possible objects in the scene exists. Future research on this subject may offer potential benefits for software scanning solutions. Telescopes used in this approach do not focus the radiation on the side of the scene. Here, the light gathering ability of such telescopes is of main importance. The combination of the software scanning approach in conjunction with BRDF considerations might lead to entirely new telescope designs for THz-security imaging.

³Outdoors the reflection of the sky (the sun) is also relevant and introduces a dependence on the detection angle (ϕ).

Summary - Contributions of this Thesis

Summary of contributions

This section briefly summarizes the main contributions of this thesis and gives an overview of the published work stemming from the work presented herein. The overall motivation for this thesis was to contribute to the solution of the imaging scenario shown again in figure (1.1)⁴.



Figure 8.5: Potential scenario for THz-security imaging (reproduced from section (1.1)).

⁴The image is reproduced here in figure (4.12) for ease of reading.

As discussed in section (1.1), the imaging scenario poses a significant challenge that can not be met with established methods and technology. The particular challenges of the scenario are:

1. capability of detecting hidden metallic/non-metallic threats under optical obscurants
2. providing a field-of-view of at least a few square meters
3. a large depth-of-focus of at least a few meters
4. video capability
5. privacy problems (Bodyscanner-issue)

The list of the first four challenges are technical issues and the fifth challenge is mainly a political/societal issue. The given order of the list does not reflect an order of importance. Every point needs to be addressed to solve the imaging task at hand. This thesis contributes to all five challenges of the list and offers new techniques that ameliorate or potentially even solve the respective challenge.

In particular the thesis presents measurements that use a novel phase-sensitive detection technique that is described in section (6.3) and published in [AH14]⁵. The new method was also presented at the International Conference on Infrared, Millimeter, and Terahertz Waves (IRMMW), which was held September 1st - 6th, 2013 in Mainz, Germany. In extension the new method offers the possibility for absolute measurements traceable to the SI-system as well as additional noise reduction properties. The successful implementation of the new method enabled the participation in the European metrology research program (EMRP) joint research program THz Security Microwave and terahertz metrology for homeland security (JRP-NEW07) under a researcher excellence grant. A summary of the project can be found under the following URL:

[Summary Report for JRP NEW07](#)

The work done in this project was also presented in a poster at the International Workshop on Terahertz Technology and Applications in Kaiserslautern, Germany (see figure (8.6) for a miniaturized poster version.).

⁵The citation style of this section was deliberately chosen differently from the rest of the text to distinguish the references given therein.

Phase sensitive passive THz Imaging at 5m stand-off distance

Author: Sven Augustin email: sven.augustin@dlr.de

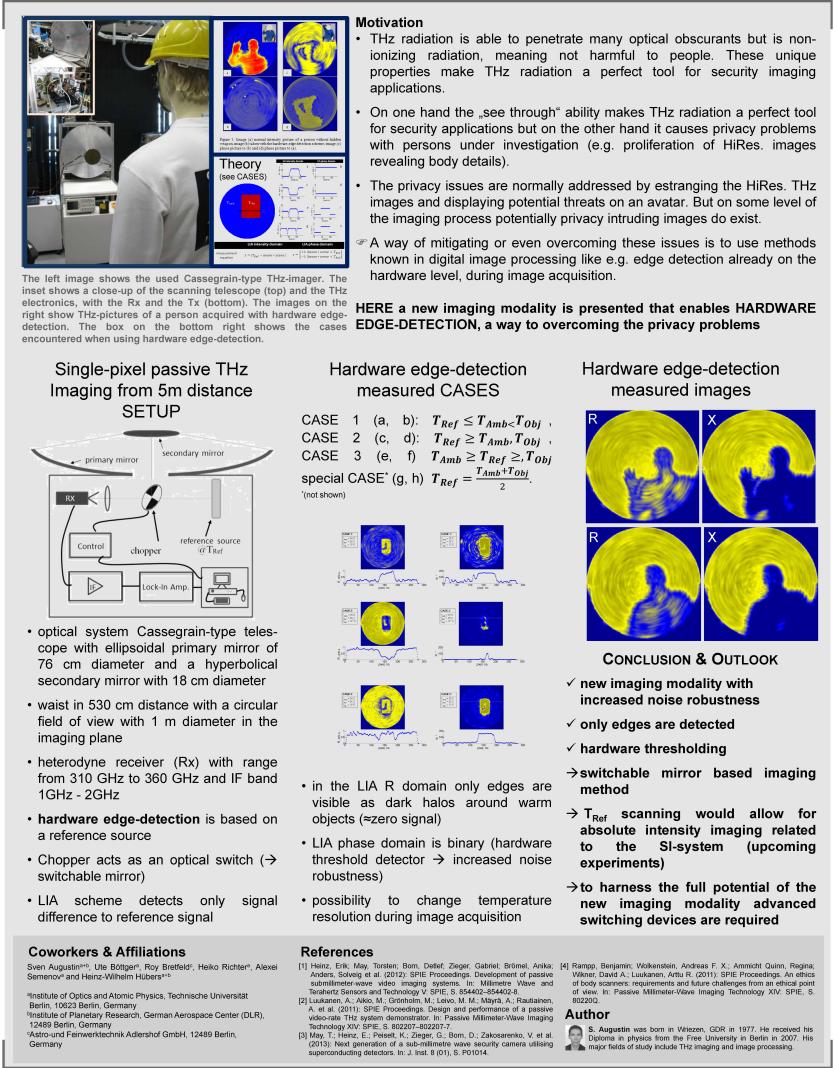


Figure 8.6: Miniaturized version of the poster presented at the International Workshop on Terahertz Technology and Applications in Kaiserslautern, Germany.

The method proved to be very useful and innovative and therefore was

filed for patent application (Amtliches Aktenzeichen: 10 2013 217 314.8 - "Vorrichtung und Verfahren zur Erzeugung von Terahertz Bildern"-patent pending). As described in section (6.3), the first implementation of the new phase-detection method uses a metallic chopper wheel as switchable mirror. An extension to the first implementation uses two synchronized chopper wheels and extends the phase-sensitive method from a binary implementation to a multinary one. The details are described in section (6.4) and a publication of these results is in preparation.

A chopper wheel is just a crude approximation of a THz-SLM as described in this thesis. Since a fully-fledged THz-SLM is necessary to harness the full potential of the new LIA phase space method, the logical next step was to combine the new phase detection method with a fully functional THz-SLM. The first THz-SLMs are at present in the early research stages. The design of a THz-SLM prototype for the security imager used in this thesis is described in section (6.5.1). For the test of the new design a binary object is imaged using a CS-scanning scheme. This is described in section (6.5.3) and the results are published in [AHJH15]. With the identified connection between the phase-sensitive hardware image processing method and the theory of Compressed Sensing, both subjects are able to benefit from one another. CS provides the means to combat the challenges 1-4 introduced in the beginning of this section. The work on this subject lead to a priority program proposal (DFG priority program 1798) that was granted in January 2015. CS also offers improvements on the software level with the enhancement of the acquired THz-images regarding image noise and overall image quality. This improvement on the software level is advantageous for the detection of hidden threats. It is described in section (6.2) and the first results were presented in a poster on the Matheon Workshop 2013 Compressed Sensing and its Applications in Berlin, Germany (see figure (8.7) for a miniaturized poster version.).

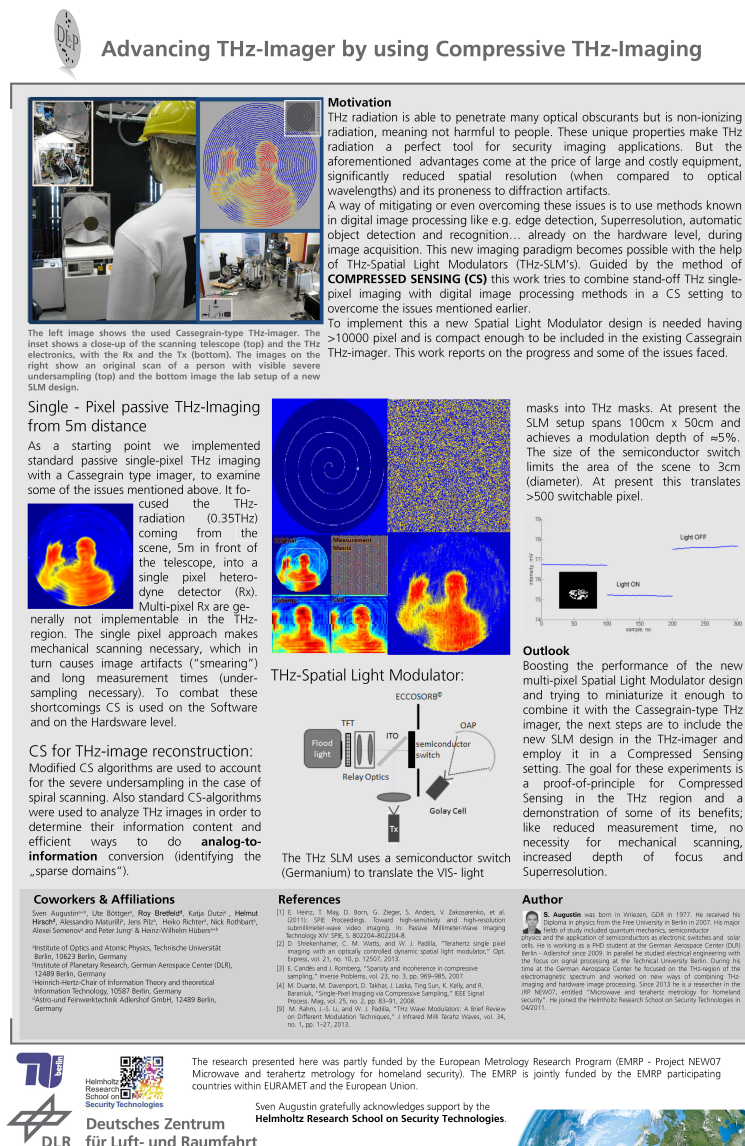


Figure 8.7: Miniaturized version of the poster presented at the Matheon Workshop 2013 Compressed Sensing and its Applications in Berlin, Germany

In short, rather than hardware development the research in this thesis focused on new scientific methods on the subject of hardware THz-image processing. The research goal was to contribute to finding a solution for the imaging task exemplified in figure (8.5). To that end, the aforementioned publications document the successful research effort that is presented in detail in this thesis. For a full list of publications during the PHD-time see the next pages.

Own Publications

- [ABB⁺13] S. Augustin, R. Bretfeld, U. Bottger, H. Hirsch, H. Richter, A. Semenov, and H.-W. Hubers. Passive stand-off thz imaging using lock-in phase information. In *38th International Conference on Infrared, Millimeter, and Terahertz Waves (IRMMW-THz 2013)*, pages 1–2, 2013.

Oral presentation: Introduced the Lock-In phase space in a passive THz imaging setting.

- [AH14] Sven Augustin and Heinz-Wilhelm Hübers. Phase-sensitive passive terahertz imaging at 5-m stand-off distance. *IEEE Transactions on Terahertz Science and Technology*, 4(4):418–424, 2014.

Journal article: Introduces hardware edge-detection by using phase sensitive detection.

- [AHJH15] S. Augustin, J. Hieronymus, P. Jung, and H.-W. Hübers. Compressed sensing in a fully non-mechanical 350 ghz imaging setting. *Journal of Infrared, Millimeter, and Terahertz Waves*, 36(5):496–512, 2015.

Journal article: Introducing a THz-SLM lab prototype and showing the feasibility of software scanning with Compressed Sensing.

- [AH30] S. Augustin and H.-W. Hübers. Vorrichtung und verfahren zur erzeugung von terahertz-bildern, August 30.

Patent: Measurement technique that allows phase-sensitive detection (patent pending).

- [Aug09] S. Augustin. Poster presentation. In *European Summer School on New Trends in Terahertz Imaging*, 2009.

Poster presentation: Introduced the objectives during the PHD.

- [Aug10a] S. Augustin. Poster presentation. In *456. WE-Heraeus-Seminar on THz Radiation*, 2010.

Poster presentation: Discussed the concept and first results of BRDF for different obscurants (e.g. clothing).

- [Aug10b] S. Augustin. Thz-sicherheitstechnik für den einsatz im zivilen transport: Oral presentation. In *DLR - Next Generation Forum 2010*, 2010.

Poster presentation: Discussed the potential of THz-radiation for security imaging applications.

- [Aug11] S. Augustin. Poster presentation. In *DLR-Doktoranden-Symposium*, 2011.

Poster presentation: Presented some results from the doctoral studies on THz-security imager.

- [Aug12a] S. Augustin. Oral presentation:. In *JRP NEW07 - THz Security Microwave and terahertz metrology for homeland security*, 2012.

Oral presentation: Introduced the work of REG(TUB) on a THz-calibration source.

- [Aug12b] S. Augustin. Thz scanner für sicherheitsanwendungen: Oral presentation. In *6. Terahertz Frischlinge Treffen*, 2012.

Oral presentation: Introduced the concept of Compressed Sensing for THz-security imaging.

- [Aug13a] S. Augustin. Poster presentation. In *Matheon Workshop 2013*, 2013.

Poster presentation: Showed first results of the application of CS-techniques for the reconstruction of passive THz-images.

- [Aug13b] S. Augustin. Poster presentation. In *HRSST evaluation*, 2013.

Poster presentation: Summarized the work during the doctoral studies.

- [Aug14a] S. Augustin. Poster presentation. In *International Workshop on Terahertz Technology and Applications*, 2014.

Poster presentation: Discussed the the theoretical background and experimental results of phase-sensitive detection.

- [Aug14b] S. Augustin. Towards security imaging using software scanning with compressed sensing: Oral presentation. In *Joint PTB and R&S workshop Security Scanners*, 2014.

Oral presentation: Showed the first results measured with an THz-SLM prototype for future application in THz-security imaging.

- [CSA13] *Matheon Workshop 2013: Compressed Sensing and its applications (CSA2013)*, 2013.

- Conference: Interdisciplinary conference on new aspects and applications of Compressed Sensing.
- [DAG11] Volker Dworak, Sven Augustin, and Robin Gebbers. Application of terahertz radiation to soil measurements: Initial results. *Sensors*, 11(12):9973–9988, 2011.
- Journal article: Evaluates the applicability of THz-radiation for stand-off imaging in agricultural employments.
- [DLR11] *DLR-Doktoranden-Symposium*, 2011.
- Conference: Exchange between different disciplines on a PHD-student level.
- [Fri12] 6. *Terahertz Frischlinge Treffen*, 2012.
- Workshop: Presentations on different applications of THz-radiation.
- [Her10] 456. *WE-Heraeus-Seminar on THz Radiation*, 2010.
- Workshop: Generation, Detection and Applications of THz-radiation
- [HRS13] *HRSST evaluation*, 2013.
- Evaluation: Performance evaluation of the Helmholtz research school on security technologies to assess the successful operation of an interdisciplinary doctoral program.
- [IRM13] *38th International Conference on Infrared, Millimeter, and Terahertz Waves (IRMMW-THz 2013)*, 2013.
- Conference: Forum devoted to the science and technology of long-wavelength radiation. The scope of the conference includes all scientific and technological activities which involve the long-wavelength region of the electromagnetic spectrum.
- [IWT14] *International Workshop on Terahertz Technology and Applications*, 2014.
- Workshop: Focused on Non-destructive Testing, Technology for Homeland Security, Communications, Health and Social Aspects of Terahertz Technology and new THz system technologies
- [JRP12] *JRP NEW07 - THz Security Microwave and terahertz metrology for homeland security: Kick-off meeting*, 2012.
- Kick-off meeting: Joint research project (JRP) international kick-off meeting.
- [NGF10] *DLR - Next Generation Forum 2010*, 2010.

Forum: New developments in public transport.

[NTT09] *European Summer School on New Trends in Terahertz Imaging*, 2009.

Summer school: Methods for THz-imaging

[RSw14] *Joint PTB and R&S workshop Security Scanners: Adequate Methods to Measure the Exposure*, 2014.

Workshop: Discussed new ways to accurately measure the exposure in THz-security imaging.

Appendix

A.1 Motivation of the Radiometer equation

The goal of this section is to give a mathematical motivation of the Radiometer equation and to provide an understanding of the assumptions in its derivation as well as conditions that are necessary prerequisites for its validity. The Radiometer equation reads:

$$\Delta T = \frac{T_{sys}}{\sqrt{2 \cdot \Delta\nu \cdot \tau}} \quad (\text{A.1})$$

The Radiometer equation gives the temperature resolution (the sensitivity limit) that is achievable given certain conditions of the detection system. T_{sys} is the system noise temperature, $\Delta\nu$ is the detection bandwidth and τ is the time constant of the integrator used. T_{sys} can be thought of as consisting of two contributions T_N the noise temperature of the receiver/detection system (including electronics) and the antenna noise temperature T_A .

$$T_{sys} = T_N + T_A \quad (\text{A.2})$$

Fundamental assumptions now are that the radiation that is to be detected is statistical in nature and that the detection bandwidth is small against the center frequency of the incoming radiation. Following these assumptions, it can be stated that the power spectrum of the incoming radiation can be treated as constant over the detection bandwidth (**white noise**). According to these assumptions, the Radiometer equation is only accurate in a passive modality. Implicitly, the aforementioned equations also assume the validity of the **Nyquist theorem** which relates the noise temperature to the noise power.

$$P_N = k_B \cdot T_N \cdot \Delta\nu \quad (\text{A.3})$$

The useable bandwidth of the detection system exhibits bandpass character with the pass band frequencies between f_1 and f_2 . The center frequency of this pass band is denoted f_C . With these assumptions the detected signal voltage U_R is given by equation (A.4).

$$U_R(t) = U_0(t) \cdot \cos(2 \cdot \pi \cdot f_C \cdot t + \phi(t)) \quad (\text{A.4})$$

In equation (A.4), $U_0(t)$ and $\phi(t)$ characterize statistical amplitude- and phase-fluctuations. The detected voltage now has to be integrated to produce a readable signal. The integration over a time τ_I yields a value U_{DC} with standard deviation ΔU_D . U_{DC} is an offset value and ΔU_D is the sensitivity limit. When the standard deviation is expressed in temperatures instead of voltages, the Radiometer equation is obtained with the equivalence of equation (A.5).

$$\frac{\Delta T}{T_{sys}} = \frac{U_{NF}}{U_{DC}} \quad (\text{A.5})$$

In this, ΔT is equivalent to 1 standard deviation of $T_{sys} + \Delta T$. U_{NF} is the detected voltage with a signal present whose power spectrum is constant over the detection bandwidth ($1/\tau_I$) and U_{DC} is the constant offset caused by T_{sys} with no additional signal. According to the aforementioned assumptions, the sensitivity limit is equivalent to a detection probability of 68%, since the detector voltage follows a Gaussian distribution.

A.2 Classification of blurring kernels

The blurring kernels were introduced in figure (3.11) of section (3.5). The classification of the kernels is listed below.

Table A.1: Classification and model functionality of blurring kernels in SLM-based THz-imaging

$H_1(x, y)$	homogeneity blur	considers inhomogeneities in the VIS/NIR-illumination
$H_2(x, y)$	geometric blur	considers magnification factors and geometric deviations for the commanded masks
$H_3(x, y)$	mapping optics blur	considers deviations in the mapping of the commanded masks onto the optical switch
$H_4(x, y)$	diffraction blur and multipath blur	considers the effects of diffraction and multipath propagation
$H_5(x, y)$	diffraction blur and multipath blur	considers the effects of diffraction and multipath propagation
$H_6(x, y)$	diffraction blur and multipath blur	considers the effects of diffraction and multipath propagation
$H_7(x, y)$	motion blur	considers the effects of movement of objects/persons in the scene

A.3 Passive THz-images and their acquisition parameters

Table A.2: Measurement parameters for the used passive THz-images with undersampling factor 4.

Image a	ISM Scam 01.09.2011_2348	Lock-In TC: 100 ms Lock-In range 500 μ V scan velocity 5 rpm measurement time \approx 400 s target: me on chair chopper frequency: 62 Hz
Image b	ISM Scam 08.09.2011_1939	Lock-In TC: 100 ms Lock-In range 500 μ V scan velocity 5 rpm measurement time \approx 400 s target: me on chair + plastic mock-up weapon chopper frequency: 299 Hz
Image c	ISM Scam 08.09.2011_2245	Lock-In TC: 100 ms Lock-In range 500 μ V scan velocity 5 rpm measurement time \approx 400 s target: me on chair + metallic mock-up weapon chopper frequency: 62 Hz
Image d	ISM Scam 30.03.2012_1451	Lock-In TC: 100 ms Lock-In range 10 mV scan velocity 5 rpm measurement time \approx 400 s target: me on chair in portal chopper frequency: 266 Hz
Image e	ISM Scam 26.03.2012_1836	Lock-In TC: 100 ms Lock-In range 10 mV scan velocity 5 rpm measurement time \approx 400 s target: me on chair + metallic mock-up weapon chopper frequency: 267 Hz
Image f	ISM Scam 08.09.2011_2213	Lock-In TC: 100 ms Lock-In range 500 μ V scan velocity 5 rpm measurement time \approx 400 s target: me on chair + metallic mock-up weapon chopper frequency: 299 Hz
Image g	ISM Scam 02.01.2012_1455	Lock-In TC: 30 ms Lock-In range 10 mV scan velocity 10 rpm measurement time \approx 200 s target: me on chair + metallic mock-up weapon chopper frequency: 249 Hz

Image h	ISM Scam 11.01.2012_2239	Lock-In TC: 100 ms Lock-In range 500 μ V scan velocity 5 rpm measurement time \approx 400 s target: me on chair + metallic mock-up weapon chopper frequency: 186 Hz
---------	--------------------------	--

Table A.3: Measurement parameters for the used passive THz-images with undersampling factor 2.

Image i	ISM Scam 05.07.2013_2046	Lock-In TC: 100 ms Lock-In range 20 μ V scan velocity 4 rpm measurement time \approx 1000 s target: me on chair + metallic mock-up weapon chopper frequency: 14 Hz
Image j	ISM Scam 05.07.2013_1953	Lock-In TC: 100 ms Lock-In range 20 μ V scan velocity 4 rpm measurement time \approx 1000 s target: me on chair + metallic mock-up weapon chopper frequency: 14 Hz
Image k	ISM Scam 24.06.2013_2246	Lock-In TC: 100 ms Lock-In range 10 μ V scan velocity 4 rpm measurement time \approx 1000 s target: me on chair + metallic mock-up weapon chopper frequency: 14 Hz
Image l	ISM Scam 24.06.2013_2309	Lock-In TC: 100 ms Lock-In range 10 μ V scan velocity 4 rpm measurement time \approx 1000 s target: me on chair + metallic mock-up weapon chopper frequency: 14 Hz
Image m	ISM Scam 05.07.2013_2114	Lock-In TC: 100 ms Lock-In range 20 μ V scan velocity 4 rpm measurement time \approx 1000 s target: me on chair + metallic mock-up weapon chopper frequency: 14 Hz
Image n	ISM Scam 15.07.2013_1821	Lock-In TC: 100 ms Lock-In range 20 μ V scan velocity 4 rpm measurement time \approx 1000 s target: me on chair + metallic mock-up weapon chopper frequency: 14 Hz

Image o	ISM Scam 15.07.2013_1849	Lock-In TC: 100 ms
		Lock-In range 20 μ V
Image p	ISM Scam 15.07.2013_1918	scan velocity 4 rpm
		measurement time ≈ 1000 s
		target: me on chair + metallic mock-up weapon
		chopper frequency: 14 Hz
		Lock-In TC: 100 ms
		Lock-In range 10 μ V
		scan velocity 4 rpm
		measurement time ≈ 1000 s
		target: me on chair + piece of wood
		chopper frequency: 14 Hz

A.4 CS-based reconstruction beam model parameters

Table A.4: Beam profil model parameters

ASxReconC beam size	0.003(in) & 0.002(out)
ASxReconD beam size	0.003(in) & 0.002(out)
ASxReconF beam size	0.003(in) & 0.002(out)
ASxReconA beam size	0.003(in) & 0.002(out)
xReconI beam size	0.02(in) & 0.02(out)
ASxReconXX beam size	0.03(in) & 0.02(out)

*all sizes are given in relative units of n (image size in one dimension) **scaling constant 3 used $\rightarrow 3*n$

This page is intentionally left blank.

